ACADEMIC REGISTRY
Research Thesis Submission

Name*:*	Lisa Therese Bergendahl		
School/PGI:			
Version: *(i.e. First, Resubmission, Final)*	Final	Degree Sought (Award **and** Subject area)	PhD Chemistry

Declaration

In accordance with the appropriate regulations I hereby submit my thesis and I declare that:

1) the thesis embodies the results of my own work and has been composed by myself
2) where appropriate, I have made acknowledgement of the work of others and have made reference to work carried out in collaboration with other persons
3) the thesis is the correct version of the thesis for submission and is the same version as any electronic versions submitted*.
4) my thesis for the award referred to, deposited in the Heriot-Watt University Library, should be made available for loan or photocopying and be available via the Institutional Repository, subject to such conditions as the Librarian may require
5) I understand that as a student of the University I am required to abide by the Regulations of the University and to conform to its discipline.

* *Please note that it is the responsibility of the candidate to ensure that the correct version of the thesis is submitted.*

Signature of Candidate*:*		Date:	

Submission

Submitted By *(name in capitals):*	
Signature of Individual Submitting:	
Date Submitted:	

For Completion in the Student Service Centre (SSC)

Received in the SSC by *(name in capitals):*			
Method of Submission *(Handed in to SSC; posted through internal/external mail):*			
*E-thesis Submitted (**mandatory for final theses)***			
Signature:		Date:	

Please note this form should bound into the submitted thesis.

Updated February 2008, November 2008, February 2009, January 2011

Computational Photochemistry of Heteroaromatic Biomolecules: Photodynamic Therapy and Ultrafast Relaxation

L. Therese Bergendahl

Institute of Chemical Sciences

Heriot Watt University

Submitted for the degree of Doctor of Philosophy (Chemistry)

Oct 2014

It is also a good rule not to put too much confidence in experimental results until they have been confirmed by theory

– Sir Arthur Eddington

Acknowledgements

This thesis, and the work underlying it, would not have been possible without the help and guidance of Prof. Martin Paterson. His expertise, enthusiasm and generally good humour sets him apart in the field of PhD supervisors and highlights his status as Great Guy in general.

The good laughs and discussions with my colleagues and good friends at Heriot Watt have also been invaluable for my progress. Russel, Justyna, Dan, Divya, Peter, Nuno, Jeremy, Pini and Paul: Cheers!

Above all I would also like to thank my family, and especially Kenny. Your support has not only made this thesis, but my whole career and everyday happy life, possible. Thank you.

Publication List

Hadden, D. J.; Wells, K. L.; Roberts, G. M.; Bergendahl, L. T.; Paterson, M. J.; Stavros, V. G. Time Resolved Velocity Map Imaging of H-atom Elimination From Photoexcited Imidazole and its Methyl Substituted Derivatives. *Phys. Chem. Chem. Phys.* 13: 10342, 2011

Livingstone, R.; Schalk, O.; Boguslavskiy, A. E.; Wu, G.; Bergendahl, L. T.; Stolow, A.; Paterson, M. J.; Townsend, D.; Following the Excited Relaxation Dynamics of Indole and 5-Hydroxyindole Using Time-Resolved Photoelectron Spectroscopy. *J. Chem. Phys.* 135: 194307, 2011

Bergendahl, L. T.; Paterson, M. J Two-photon Absorption in Porphycenic Macrocycles: The Effect of Tuning The Core Aromatic Electronic Structure. *Chem. Commun.* 48: 1544, 2012

Paterson, M. J.; Bergendahl, L. T. *Computational Modelling of the Steps Involved in Photodynamic Therapy*: in Molecular Photochemistry, edited by S. Saha, In-Tech (Rijeka), 2012, Chapt. 8 (p. 161).

Bergendahl, L. T.; Paterson, M. J. A Two-Photon Absorption-Molecular Structure Investigation Using a Porphycene Chromophore With Promising Photodynamic Therapy Characteristics. *J. Phys. Chem. B* 116: 11818, 2012

Roberts, G. M.; Hadden D. J.; Bergendahl, L. T.; Wenge, A. M.; Harris, S. J.; Karsili, T. N. V.; Ashfold, M. N. R.; Paterson, M. J.; Stavros, V. G. Exploring Quantum Phenomena and Vibrational Control in the UV Photodissociation of Thioanisole. *Chem. Sci.* 4: 993, 2013

Bergendahl, L. T.; Paterson, M. J. Influence of Electronic Effects on One- and Two-Photon Absorption in Porphyrin Isomers. *RSC Advances* 3: 9247, 2013

Bergendahl, L. T.; Paterson, M. J. Excited States of Porphyrin and Porphycene Aggregates: Computational Insights. *Comput. Theor. Chem.* 1040: 274, 2014

Abstract

This thesis focuses on the photochemistry of *heteroaromatic biomolecules*. These molecular systems have a rich photochemistry and take part in photochemical reactions that have many very topical applications. Small heteroaromatics constitute important biological building blocks and are therefore a fundamental components of living organisms. Even though these compounds absorb light very efficiently, they also have *ultrafast* relaxation processes available to them. This means that they can remove the absorbed energy very fast and avoid harmfull photoproducts forming, which can lead to cell damage. Larger heteroaromatics have a similarly efficient absorption of electromagnetic light, and are present in compounds that are responsible for the harvesting of energy in nature, for example the chlorophyll molecule in green plants and bacteria. If large heteroaromatics are artificially presented to living cells however, the excess energy absorbed by these systems may also cause cell damage. This destructive force can however be utilised in therapy forms where there is a need to get rid of unwanted cells, such as in anti-cancer therapy. A form of therapy based on this principle is *photodynamic therapy*.

The use of *computational chemistry* in the investigations of photochemical phenomena has increased following the improvements in the efficiency of computers and algorithms. Modern techniques have now reached a stage where ultrafast relaxation processes can be calculated for small heteroaromatics. As the experimental community has also reached a stage where these compounds can be probed using ultrafast laser experiments, there is a need for computational input to aid in the interpretation of the data of these phenomena. This thesis will present computational results concerning the relaxation dynamics of important small heteroaromatic

biomolecules, and discuss them in terms of experimental data collected by collaborative groups.

For the development of molecules to be used in photodynamic therapy, a lot of work is needed to ensure safety for use in human beings. With the computational chemistry community now being able to carry out absorption studies for large heteroaromatics, computational structure-absorption relationships can aid the development of this form of therapy. At the limits of modern photochemistry, methods are also appearing that can be used for studies of ultrafast relaxation in larger systems. These computations could contribute hugely to the understanding of the behaviour of these types of systems and aid their development. In a large component of this thesis, new structure-absorption relationships are presented for interesting heteroaromatics with potential for use in photodynamic therapy. One section is also devoted to exploratory work using methods that have not before been used in systems that are larger in size, and presents some promising results as well as current challenges in the field.

Contents

Chapter 1

Introduction

Photochemistry is the study of the chemistry that results from a molecular system absorbing light. This light absorption generally leads to the molecule existing in an excited state, which can go on to form new products as well as having its energy redistributed or emitted from the original system. The main goal of the photochemist is to gain a structural and dynamical description of the absorption process as well as an understanding of the pathways available to the excited molecule. In order to reach this goal a thorough understanding of various fields, such as quantum mechanics, spectroscopy, molecular structure and chemical dynamics, and their integration is needed.

Recent improvements in the tools for the computational modelling of molecules in their excited states have been under rapid development in the last couple of decades, and accurate simulations of molecules of considerable size are now possible. Hardware and software developments have also lead to supercomputers with extraordinary power that can compute accurate descriptions of light- induced pathways at a molecular level. In particular the modelling of the spectroscopy and photochemistry of relatively large molecular systems are now routine and has an accuracy that was not possible only a few years ago.

The aim of the work presented in this thesis is centred around the use of computational techniques to aid the interpretation of photochemical observable events. As well as direct collaboration with experimental photochemists carrying out ultrafast spectroscopic experiments, this work has been centered on evaluating the contribution of computational chemistry to the development of the field of photodynamic ther-

apy (PDT) . Before introducing the theoretical background needed for a thorough description of the computational aspects involved in this task, this chapter will serve as an introduction to the molecular systems, as well as the general photochemical processes, that are at the core of PDT.

1.1 Photochemistry of Heteroaromatics

This first section introduces the set of molecular systems that the following chapters are focused on. In principle the ground state of *any* compound can give rise to a large number of excited states when absorbing light. Each of these states can then be characterised by their unique properties and electron distribution and each can have chemistry just as varied as the ground state.[1] One set of molecules that has an especially rich photochemistry in the ultraviolet (UV) and visible part of the light spectrum is the family of organic *heteroaromatics*. These molecules are classed as aromatic and have heteroatoms (e.g. O, N, S) as part of their cyclic conjugated π-system.[2] Examples range from smaller ring systems such as *imidazole* and *indole* to macrocyclic molecules such as *porphyrin*, as illustrated in Figure 1.1.

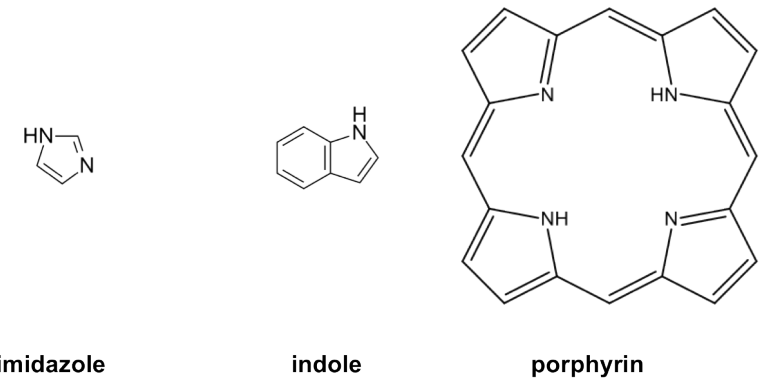

Figure 1.1: Molecular structures of example heteroaromatics: the five-membered ring system, imidazole, a bicyclic heteroaromatic, indole, and a macrocycle, porphyrin.

The strive to gain a deeper understanding of the photochemical behaviour of heteroaromatics has largely been motivated by the many interesting processes they take part in. Examples range from practical ways of transforming sunlight into high

quality fuels to replace fossil fuels, [3] to the development of optical compounds that efficiently emit photons for use in biological imaging.[4]

Figure 1.2 is a common pictorial representation of photochemical events, called a *Jablonski* diagram. A Jablonski diagram is a convenient way of describing the energy flow of a molecular system after it has absorbed light and will be used extensively in this thesis. The basis of the Jablonski diagram lies in the description of discrete states that are available to the molecular system, a concept that will be introduced in detail in the Theoretical Background section of this thesis. In the diagram the excited states available to a system are illustrated by horizontal lines, labelled with their spin multiplicity, and organised vertically with respect to their potential energy. Organic heteroaromatics are commonly found in a singlet electronic ground state configuration (S_0) and absorption of UV or visible light, for example through a one- or two-photon absorption process (OPA or TPA, respectively), can result in the molecule being in some singlet excited state (S_N). The non-linear process of TPA was first proposed by Göppert-Mayer in 1931, but not observed until after the development of lasers with high photon flux in 1961.[5] This process has numerous advantages with respect to the applications discussed in this thesis, and will therefore be introduced in depth further on in this chapter. If the excited state is created in the condensed phase, the energy can often be transferred through various processes to nearby systems. The energy is however often first re-distributed through very fast non-radiative processes, termed internal conversion (IC), if within the same spin manifold, or intersystem crossing (ISC), if between states of different spin multiplicity. Internal conversion can also lead to new photoproducts being formed (not shown in Figure 1.2) or the emitting of a photon, through fluoresence (FL), especially if the molecule is in the gas phase. If the molecule has ISC pathways available, a triplet state can also be generated that, if there are no energy transfer pathways available, can lead to an emitted photon through a process termed phosphoresence (PH).

One important photochemical process with large impact on everyday life is the absorption of UV light by heteroaromatic compounds found in the human body, such as the nucleic acids of the DNA oligomer and amino acid residues. [6] The DNA bases for example have large UV absorption cross sections and excitation is very effective.[7] There are however curiously low yields of any, potentially harmful, photo-products (around 1%). This suggests that there are very effective IC pathways back

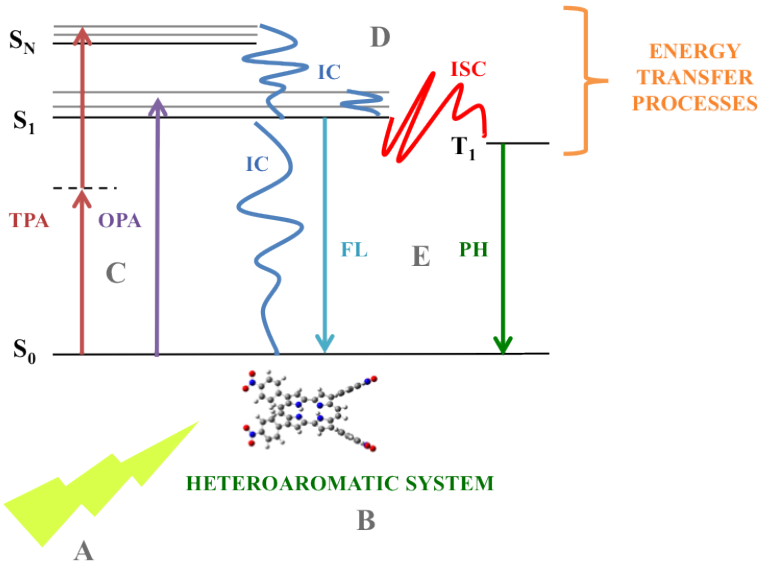

Figure 1.2: A Jablonski diagram illustrating the photochemical pathways available to common heteroaromatics. Light (**A**) that reaches a heteroaromatic compound (**B**) can be absorbed through various processes (**C**). The energy can then be dissipated through various non-radiative processes (**D**) within the molecule or transferred to a nearby system. The energy can also be given off through radiative pathways (**E**).

to the ground state available to these molecules.[8] These relaxations can take place within the timescale of molecular motion ($10^{-12} - 10^{-14}$ s), and are therefore termed *ultrafast* relaxation processes. Due to the medicinal importance of photochemical reactions of heteroaromatic biomolecules, such as the building blocks of DNA, it is of great interest to be able to determine both the reactive and non-reactive pathways which these chromophores have available to them.

Practical photochemistry experiments have had interesting recent developments in the ever-increasing speed at which chemical processes can be investigated. Spectroscopy laboratories with lasers that can produce pulses of a few femtoseconds (10^{-15} s) are now routine, and phenomena such as formation and breakage of chemical bonds can be monitored in real time. However, when excited state dynamics are concerned, such as those of the DNA building blocks, experimental data can only infer the presence of certain mechanisms, and a thorough investigation of the excited states themselves are needed in order to confirm the precise character of such photochemical pathways. Laser excitation by femtosecond pulses also results in a coherent excitation that potentially could lead to control over chemical reactions by steering them towards specific reaction pathways. This is however a very challenging task which also requires an intimate knowledge of the character of the states of the excited species, specifically with regards to the modes of any internal vibrational distribution. Despite the many developments in practical experimental techniques a *computational* input is therefore crucial in order to gain a thorough understanding of all the aspects of a photochemical reaction pathway. The use of computational photchemistry as a tool for the understanding of experimental data obtained from ultrafast photochemistry experiments is one of the key concepts of this thesis.

1.2 Photodynamic Therapy

Apart from an understanding of the dynamics of photoproducts that can be harmful to organisms, there is also scope for the utilisation of photochemical processes in the treatment of various diseases through PDT.[9] This form of therapy is a branch of phototherapy that requires UV or visible light as well as the presence of a chemical compound, a so-called *photosensitiser*, and molecular oxygen. In the Jablonski diagram in Figure 1.3 the photochemical pathways of PDT are outlined. The ideal

photosensitiser (as will be introduced in the next section) has large OPA and/or TPA transition strengths and very efficient IC and ISC relaxation processes to a triplet excited state manifold (T_1). An energy transfer process can then take place to a nearby molecule of oxygen in its triplet ground state, which leads to the generation of singlet oxygen species. Singlet oxygen is extremely reactive and has been linked to numerous reactions which, if taking place within a cell, cause significant damage that can ultimately lead to apoptotic cell death. This destructive force can be utilised as an anti-tumour or anti-bacterial strategy, and an in-depth knowledge of the reactivity of the excited states of the photosensitisers will play a crucial role in making this relatively side-effect free treatment more routinely used.

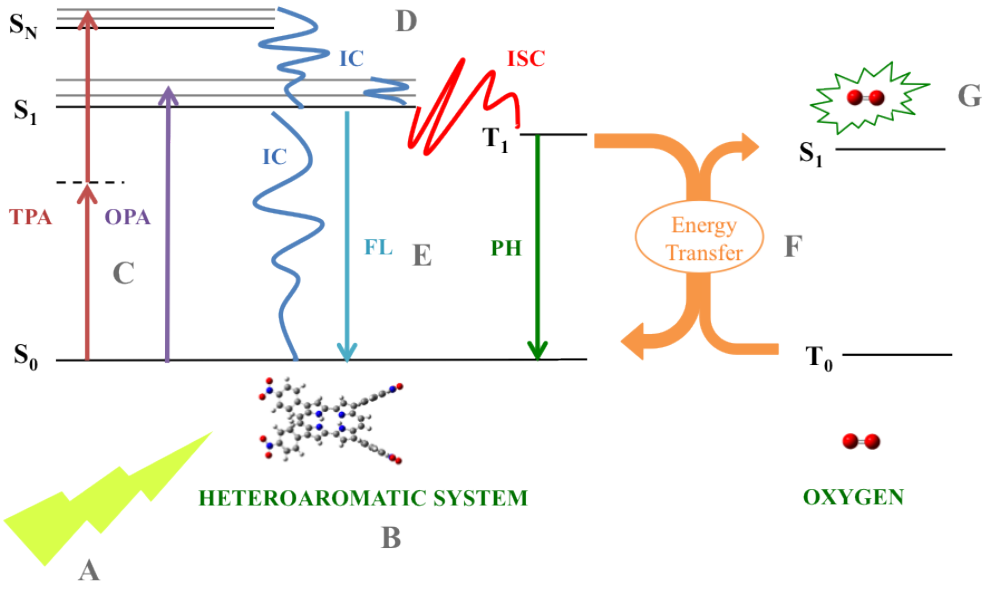

Figure 1.3: Heteroaromatics that are used as photosensitisers in PDT (**B**) have efficient absorption (**C**) and relaxation processes (**D**) to reach a triplet excited state manifold (T_1). Energy transfer can then take place (**F**) to nearby oxygen molecules, creating extremely reactive, and potentially destructive, singlet oxygen species (**G**).

The knowledge of the benefits of sunlight on general health has been traced back over 5000 years with references to, for example, Egypt and India. Ancient Greek texts also mention both Herodetus and Hippocrates recommending "heliotherapy" to their fellow Greeks and documenting the benefits of sunlight on bone growth.

[9] The development of PDT as we know it today has been in progress on and off since the early 1900s, with an example being the 1903 Nobel Prize in Physiology or Medicine awarded to the Danish scientist Niels Rydberg Finsen for his work in the use of light as a form of therapy for *Lupus vulgaris*. Finsens work was the first to use light actively and directly as a treatment of disease.[10] The first descriptions of the use of a *chemical* photosensitiser in light therapy are also from the early 1900s through the observations of Raab as well as Jasionek and Von Trappen. [11] Raab's work involved the investigation of bacterial cultures and their reaction to an added porphyrin dye. He was surprised to observe unexpected cell death in the experiments, but only if they were carried out in the daytime. Experiments carried out in the evening (or possibly during Scottish autumn) showed no such effects. He concluded that the light activated his dye molecules and changed their therapeutic behaviour. [12] One of the more notable examples of photosensitisation from this period is the 1913 experiment by the German scientist Meyer-Betz. In the true spirit of discovery he decided to inject himself with 200 milligrams of haematoporphyrin, a carbonyl functionalised porphyrin derivative (Figure 1.4). Meyer-Betz felt absolutely no effect until he went out for a walk, exposing himself to radiation in the form of sunlight. After instantly suffering extreme swelling he experienced photosensitivity for several months after the experiment. [13]

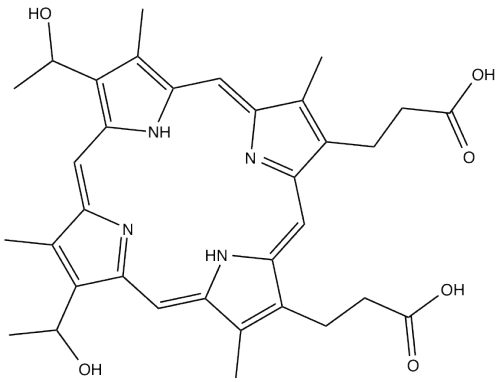

Figure 1.4: The porphyrin derivative haematoporphyrin is functionalised with carbonyl units. Photofrin^{TM}contains oligomers of haematoporphyrin of varying size.

The field lay largely dormant after this point until the 1950s and 60s, when Tom Dougherty essentially re-discovered PDT and contributed to the realisation that

the heamatoporphyrin derivative in fact has tumour localising properties as well as being photo-toxic.[14] This discovery prompted a spur of photosensitiser development between 1960s and 1980s, which ultimately led to the first clinically approved PDT drug: *Photofrin* ^{TM}, based on the haematoporphyrin derivative. This discovery is also considered the starting point for the development of PDT as a promising tool in cancer treatment, and Tom Dougherty is often referred to as the father of PDT. [15–17]

The attractiveness of PDT as clinical therapy is due to several aspects that could, at least in principle, place it above current treatment methods. First of all it is a non-invasive therapy that has little toxicity in the absence of a light source, and compared to surgery it has excellent outcome with respect to scarring and other cosmetic considerations. Secondly, as the technique generally requires light in the ultraviolet to infrared region the radiation damage is minimal compared to other forms of radiotherapy. It has in fact also been suggested that PDT can trigger and help mobilise the immune system against the tumour. [18] One major advantage of PDT in comparison to other forms of chemotherapy is the inability of the body to develop resistance to the treatment, as there is not necessarily a specific target biomolecule involved in the mechanism of its cytotoxicity. Despite these attractive attributes, the current use of PDT in cancer treatment is typically only for palliative and very advanced stages of skin, bladder, lung and oesophageal cancers. It has been a success in the treatment of age-related macular degeneration, which is a leading cause of blindness in the western world, but this unfortunately still represents the only area where PDT is the first treatment of choice. [19]

Clearly PDT is a very attractive therapy in theory, and it has many advantages that are too major to ignore. The improvement and development of ever better photosensitiser molecules therefore remains an attractive research goal. Apart from the synthetic and pharmaceutical considerations in photosensitiser development, a deeper insight into the photochemical pathways available for these systems has the potential to accelerate PDT development. This also requires intimate knowledge of the character of the excited states and hence the photochemical pathways available to the photosensitiser, a task that computation could be of great help to complete. The bulk of this thesis will be concerned with the various photochemical pathways involved in PDT, and the role computational chemistry has in their understanding,

and possible improvement.

1.3 Photosensitisers for PDT

All modern photosensitisers used in clinical practice today are based on the porphyrin macrocyclic structure, and PDT with porphyrin derivatives have been under active development since the 1960s. [12, 20] Possibly the most recognisable porphyrin derivative is found in the human body coordinated to Fe in *haem*, responsible for the function of the haemoglobin protein. The unchelated porphyrin structure in haem is protoporphyrin IX (PpIX) and this molecule has been shown to be a very effective photosensitiser. [21] When treating with PpIX the strategy is to administer a synthetic version of β-Aminolaevulic acid, the biosynthetic precursor to PpIX, which leads to a build-up of PpIX. In Europe, PpIX is approved for use in topical PDT of for example basal cell carcinoma. [22] The most common photosensitiser in use today, however, is still the heamatoporphyrin derivative (Figure 1.4) used in Photofrin^{TM}in a mixture of oligomeric porphyrin chains. [23] Photofrin is approved in Europe, the USA, Canada and Japan and is used mainly for cervical, bladder and gastric cancers. Although heamatoporphyrin and other porphyrin derivatives show excellent singlet oxygen quantum yields, the longest wavelength at which they are excited is at 630 nm.[24] This is pertinent in that it indicates the level of access the light has to the tumour. Even though the specifics of the interaction of light with human tissue is not completely unraveled, it is well known that an optical window of tissue penetration exists at 600 nm to about 1000 nm, as illustrated in Figure 1.5.[25]

It is expected that, at the porphyrin maximum wavelength of 630 nm, the tissue penetration level is in the order of 0.5 cm.[26] Clearly this is a very limiting factor, and indeed the cancers that can currently be treated with modern PDT are all situated so that the light source can be positioned physically close to the tumour. If the treatment could take place using light of a longer wavelength however, the clinical use of the photosensitiser would be expanded as cancers that were located deeper in the tissue could be treated as well. With this in mind, extended research has been carried out into ways of manipulating the wavelength of maximum absorption in porphyrin related molecules. [20]

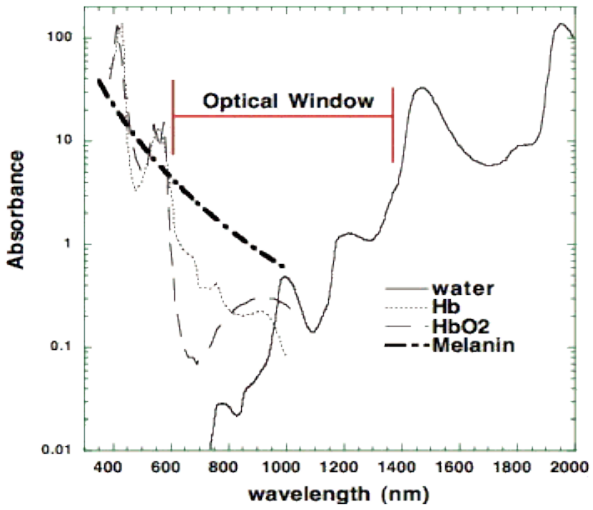

Figure 1.5: The optical window of tissue penetration shows the region where the tissue is most transparent and the absorption due to common tissue absorbers (such as the melanin pigment, haemoglobin **Hb** and **HbO2** and water) is at a minimum. Figure adapted from [25].

1.4 Two-Photon Absorption

One research avenue that has the potential of being especially promising is the utilisation of higher order absorption events in existing photosensitiser molecules. The non-linear absorption response is normally small in most systems unless the light source can administer a large number of photons, *i.e.* has a high photon flux. The advent of lasers in the 1960's however has lead to a lot of research involving non-linear optical events for use in many attractive applications, for example dye-sensitized solar cells for use in artificial photosynthesis, molecular semiconductors in photovoltaic cells, photo catalysts and biological imaging dyes. [27–34]

The use of a non-linear optical excitation technique such as TPA in PDT does not necessarily have an impact on the subsequent photochemical pathways. If the state reached after the simultaneous absorption of two photons relaxes into the same singlet state reached during a conventional one-photon absorption (OPA) transition, the subsequent pathway could indeed remain identical. Nevertheless, even if it does not have an impact on subsequent ISC or singlet oxygen generation by the molecule,

TPA can still provide numerous advantages in this field. [35–38]

First, as will be introduced further in the Theoretical Background section of this thesis, a molecule with a particular symmetry might have states available for TPA that diverges from those available for conventional OPA, resulting from a change in the selection rules for the transition. This leads to potential access to states that are *dark* with respect to OPA, meaning that TPA efficiency can be improved as OPA pathways does no longer compete. A further advantage with a non-linear excitation process is the fact that the probability of TPA falls off quadratically with respect to the focus of the excitation source, e.g. a focused laser beam. The singlet oxygen production can therefore be restricted to a very small volume, and extremely high spatial resolution for PDT treatment can be achieved. However, with the previous discussion in mind, the main advantage of using TPA is arguably the fact that the non-linear absorption process takes place using two photons to achieve an excitation that normally requires one higher energy/ shorter wavelength photon. This highlights an avenue that can be used to develop photosensitisers that are designed towards absorption in the optimum position in the optical window of tissue penetration.

There are numerous investigations into porphyrin type systems and their OPA and TPA spectra.[37, 39–47] The probability of TPA in any molecular system is defined through its TPA transition strength, δ^{TPA}, which is controlled by the molecular electronic structure. The reason for the organic aromatic chromophores large non-linear optical responses, lies in the inherently large polarisability of their delocalised π-electron cloud. A general strategy to enhance these properties in porphyrin-type compounds have so far been focused on the chelation of the macrocyclic unit to a metal centre, a modification of the heteroatoms in the macrocyclic core and, mainly, the addition of electron donating (pushing) and electron withdrawing (pulling) groups. As these "push-pull" systems have large charge-transfer absorption transitions they also exhibit large molecular *hyper*polarisabilities, which are directly related to macroscopic non-linear optical properties. [40, 41, 48–57]

Clearly there are a large number of research avenues to adress in this area of photosensitiser development. Considering the many issues involved before any promising photosensitiser reaches the clinic, PDT development could benefit hugely from automation in the form of a computational chemistry input into the process. The accurate modelling of a non-linear absorption process has great potential in the de-

velopment of ideal photosensitiser molecules, and has been a key aspect of the investigations carried out in the work of this thesis.

The main focus of the synthetic developments of more effective photosensitiser system has been dominated by porphyrin related systems (commonly referred to as First and Second generation photosensitisers), and this is also the avenue that recent computational efforts have gone down. Therefore the computational studies in the following chapters of this thesis have been designed with systems like these in mind. It is however important to keep in mind that non-porphyrin photosensitisers also are being investigated, including various dye molecules and systems on the nanoscale such as semiconductor quantum dots and fullerenes.[58, 59] The calculation of properties of molecules of the size of porphyrins is a challenging task and with computational chemistry having reached a stage where important contributions can be made, systematic studies of molecular structure-properties relationships can hopefully aid in the design of drug molecules for future applications.[60–65]

As the field of theoretical chemistry develops, with improvements in algorithms as well as advances in computational hardware, the input into PDT research has the potential to become very important in the future.

In this thesis the theoretical background needed for a computational description of the photochemical pathways of heteroaromatics will be introduced. The Jablonski diagram in Figure 1.3 will then be used as a guide, following the vertical one- and two-photon absorption processes and leading to the excited state relaxation pathways.

Chapter 2 introduces the quantum mechanical tools needed for a thorough understanding of photochemical pathways, and the computational strategies used in this thesis to predict these. It will focus on the advances and challenges in the field of computational photochemistry.

In Chapter 3 the absorption and relaxation pathways of small heteroaromatics of the imidazole and indole families presented in Figure 1.1 will be introduced. The work underlining this chapter was carried out in collaboration with experimental groups carrying out ultrafast spectroscopy measurements and serves as an illustration of the importance of practical and computational photochemists working together to gain a

deeper understanding of the excited state dynamics of these important biomolecules.

Chaper 4 introduces the computation of one- and two-photon absorption processes in a substituted macrocycle related to the porphyrin system. It focuses on the use of two-photon absorption as a tool for achieving optimum absorption wavelengths for the improvement of photodynamic therapy.

In Chapter 5 the effect of various substitution patterns on the one- and two-photon absorption of porphyrin and a related macrocycle is investigated. The focus is on non-linear optical properties for use in PDT as well as techniques involved in biological imaging.

Following on from the investigation into substituted macrocycles, Chapter 6 focuses on the electronic structure of the macrocyclic core molecule, and how its manipulation affects non-linear optical properties.

Chapter 7 will take the step towards the modelling of photochemistry not only isolated in the gas phase, but with interacting neighbouring molecules. The formation of macrocyclic aggregates, and their absorption characteristics, will be investigated.

In chapter 8, the computational description of the reactive chemistry and excited relaxation, including non-radiative processes, of macrocycles is introduced. This is a challenging field, and the results achieved so far will be introduced together with a discussion of the abilities and limitations of current computational techniques.

The concluding Chapter 9 summarises the work of this thesis, and describes the future challenges involved in gaining a deeper understanding of the photochemistry of heteroaromatic biomolecules from a computational perspective.

Chapter 2

Theoretical Background

The foundation of a computational description of photochemistry, from first principles, lies in the understanding of quantum mechanics. We can see the need for a quantum mechanical description when we look at various photochemical phenomena, as illustrated in the the Jablonski diagram presented in the Introduction to this thesis (Figure 1.2). The obvious example from this diagram is the fact that we can describe the system as having discrete allowed energy values, i.e. *quantised* states, available for the energy to be distributed into after absorption of light. Further examples are the wave-particle duality of matter and light, which are fundamental quantum mechanical effects that needs to be accounted for when analysing and developing a computational description of photochemical phenomena.

Quantum mechanics is a tool used to describe all chemical phenomena that can be observed, and it was formulated around a set of fundamental *postulates* in the early parts of the twentieth century.[66] Despite the fact that these postulates have not been rigorously derived from more basic principles they have stood the test of time, and quantum mechanics is used routinely as an accurate tool in the description of chemistry.

2.1 Molecular systems

2.1.1 The Schrödinger Equation

One important postulate of quantum mechanics describes how the mathematics varies from that used to describe classical mechanics. The key difference lies in the description of observable quantities. These could be any measurable quality, such as position as a function of time or polarisability in the presence of a field (such as the electromagnetic field of light). Whilst classical mechanics deals with observables in terms of functions, quantum mechanics represents observables by *operators*. The most important example of such an operator, when dealing with the quantum mechanical description of chemistry and photochemistry, is the Hamiltonian operator, $\hat{H}$. This is the operator related to the absolute energy of a molecular system of N electrons and M nuclei:

$$\begin{aligned}\hat{H} = &- \sum_{i=1,N} \frac{\hbar^2}{2m_e}\nabla_i^2 - \sum_{i=1,M} \frac{\hbar^2}{2m_{nuc}}\nabla_i^2 - \sum_{i=1,M}\sum_{j=1,N} \frac{Z_i e^2}{4\pi\varepsilon_0 |r_j - R_i|} \\ &+ \sum_{i<j=1,M} \frac{Z_i Z_j e^2}{4\pi\varepsilon_0 |R_j - R_i|} + \sum_{i<j=1,N} \frac{e^2}{4\pi\varepsilon_0 r_{i,j}}\end{aligned} \tag{2.1}$$

where m is a mass, $\hbar$ is the reduced Plancks constant, e is the elementary charge, r and R are electronic and nuclear positions, and Z the nuclear charge. The first and second term describe the kinetic energy of the electrons and nuclei respectively, whilst the third term describe nuclear and electron attraction. The final two terms are repulsive in nature and describe the nuclear-nuclear repulsion and the electron-electron repulsion. Further terms can be added on if the system is perturbed, for example by an electromagnetic field.

The Hamiltonian operator is used in the non-relativistic time-independent *Schrödinger Equation*:

$$\hat{H}\Psi_i = E_i\Psi_i \tag{2.2}$$

where E_i is the energy of the stationary state i that we are investigating and the *wavefunction*, Ψ_i, accounts for the wavenature of the system at hand. One of the quantum mechanical postulates states that a wavefunction for a molecule exists that

contains all the information that can be known about the molecular system that is being investigated. It therefore depends on various variables that describe the system, such as its wavenature through a wavelength and frequency. In order to represent a system that is physically observable, the form of the wavefunction is also constrained to certain behaviours and boundary conditions. An important postulate that greatly aids the selection of a suitable wavefunction is that it must be square integrable, single valued, and finite everywhere:

$$\int \Psi^* \Psi d\tau = \langle \Psi | \Psi \rangle = 1 \tag{2.3}$$

where *Dirac* bracket notation has been used to simplify the notation of integrals.

The wavefunction does however not in itself contain information that relates to a measurable quantity. Instead its square is interpreted as the probability of finding a particle in a particular volume element - a probability density, ρ:

$$\rho(r) = |\Psi(r)|^2 \tag{2.4}$$

In the Schrödinger equation the wavefunction is constructed such that it is an *eigenfunction* of $\hat{H}$. In fact, it is postulated that for every observable quantity there is a quantum mechanical operator that can be applied to the wavefunction to yield a corresponding observable *eigenvalue*. The mean of the measured quantity will be equal to the *expectation value* of the operator:

$$\langle O \rangle = \langle \Psi | \hat{O} | \Psi \rangle \tag{2.5}$$

where $\hat{O}$ is an arbitrary operator related to the quantity we are interested in measuring, O, and the wavefunction is normalised.

After introducing the components of the Schrödinger equation, we seem to have reached a point where all the information of the various states of the system we desire could in principle be solved exactly. However, as seen from the components contained in the Hamiltonian (Equation 2.1), a second-order differential equation in $3N + 3M$ coordinates needs to be evaluated. We also need to identify the form of the wavefunction itself. Neither of these are trivial, if at all possible, tasks for systems that have more than one electron and nucleus, and we therefore need to introduce

some approximations at this stage in order to be able to describe systems of chemical interest.

2.1.2 The Adiabatic and Born-Oppenheimer Approximations

As chemists, the very first simplification to the Shrödinger equation that we can identify becomes apparent when considering the separation of the terms in the Hamiltonian according to the *timescales* at which they operate. A vibration and rotation of a chemical bond in a molecular system are of the order of $10^{14}\ s^{-1}$. As an average chemical bond is in the order of 1 Å, and an electron travels on average 10^{16} Ås^{-1}, the electron has plenty of time to readjust its position in the timescale of the molecular motion. This suggests that the second term in the Hamiltonian operator in equation 2.1, the kinetic energy of the nucleus, which is only needed to characterised nuclear dynamics, can be left out when investigating the majority of chemical problems of interest. Simplifying in such a manner leads to a so-called *clamped nuclei* or *electronic* version of the Hamiltonian, $\hat{H}_{el}$:

$$\hat{H}_{el} = -\sum_{i=1,N} \frac{\hbar^2}{2m_e}\nabla_i^2 - \sum_{i=1,M}\sum_{j=1,N} \frac{Z_i e^2}{|r_j - R_i|} + \sum_{i<j=1,M} \frac{Z_i Z_j e^2}{|R_j - R_i|} + \sum_{i<j=1,N} \frac{e^2}{r_{i,j}} \quad (2.6)$$

The resulting electronic Shrödinger equation using this Hamiltonian is:

$$\hat{H}_{el}\Psi(r;R) = E_{el}(R)\Psi(r;R) \quad (2.7)$$

The components still depend parametrically on the position of the nuclei through the denominators of the potential terms, but the problem has been reduced to a second-order differential equation in $3N$ coordinates. The next approximation step is to make an assumption that the total wavefunction can be described in terms of an electronic and nuclear wavefunction *separately*, through what is known as the Born-Oppenheimer ansatz:

$$\Psi(r,R) = \sum_k \chi_k(R)\psi_k(r,R) \quad (2.8)$$

where the total wavefunction is described as a *product* of an electronic wavefunction, ψ, and a nuclear wavefunction, χ. This is a basic simplification at first glance, but it has recently been suggested that the exact total wavefunction can be written as such a product. [67] This factorised wavefunction can then be inserted into the full Schrödinger equation, and rearranged to yield:

$$(\hat{H}_{el} - \sum_{i=1,M} \frac{\hbar^2}{2m_{Nuc}} \nabla^2 - E) \sum_k \chi_k(R) \psi_k(r,R) = 0 \tag{2.9}$$

If the electronic wavefunction is truly decoupled from the nuclear motion, as assumed at the start of this section, we can now integrate out the electronic contribution from the above expression, and evaluate the (expectation) value of $\hat{H}$, i.e. the total energy of the molecular system we are interested in. To evaluate the energy of an arbitrary state, ψ_L, perhaps some photochemically relevant excited state, we multiply the above expression with ψ_L* on the left, and integrate over the position of all electrons, as per Equation 2.5. The resulting expression has three terms:

$$0 = (E_L(R) - \sum_{i=1,M} \frac{\hbar^2}{2m_i} \nabla^2 - E) \chi_L(R) \tag{2.10}$$

$$+ \sum_K \langle \psi_L(r,R) | \sum_{i=1,M} \frac{\hbar^2}{2m_i} \nabla^2 | \psi_K \rangle \chi_k(R) \tag{2.11}$$

$$+ \sum_k \langle \psi_L(r,R) | \sum_{i=1,M} \frac{\hbar^2}{m_i} \nabla | \psi_K(r,R) \rangle \nabla \chi_K(R) \tag{2.12}$$

The final two terms are non-orthonormal terms that couple states L and K, (2.11) and (2.12), the non-adiabatic coupling terms. When investigating chemical problems we can assume that the states will be well separated on the energy scale in many situations. This is especially true in the ground state manifold. We can therefore set the non-adiabatic coupling terms to zero for all $K \neq L$. The full approximated treatment introduced so far is called the *adiabatic approximation*, and results in a Schrödinger equation of the form:

$$0 = (E_L(R) - \sum_{i=1,M} \frac{\hbar^2}{2m_i} \nabla^2 - E + \langle \psi_L(r,R) | \frac{\hbar^2}{2m_i} \nabla^2 | \psi_L \rangle) \chi_L(R) \tag{2.13}$$

where only the diagonal correction term remains from the coupling terms.[68]

When looking at this remaining diagonal term, we see that the operator depends inversely on the mass of the nucleus, m_{Nuc}. As a nucleus is at least 1867 times larger than any electron, we realise that the contribution from the coupling elements are likely to be very small in most instances and could be neglected. Neglecting this contribution results in what is known as the *Born-Oppenheimer* (BO) *approximation* leading to:

$$0 = (E_L(R) - \sum_{i=1,M} \frac{\hbar^2}{2m_{Nuc}} \nabla^2 - E)\chi_L(R) \tag{2.14}$$

The Adiabatic and BO approximations are fundamental in the understanding of any chemical property or reaction, as they result in expression for the total electronic energy of state L, $E_L(R)$, as a function nuclear motion, R. This means that the nuclei move in a potential provided by the electronic energy, which can be used to rationalise the appearance of quantised states in photochemical spectra. Each state can in fact be described fully by a function, commonly known as a *potential energy surface* (PES), which also provides a crucial tool for evaluating conformations of a molecular system. Through the evaluation of critical points on the surface conformations for transition states as well as ground and excited state minima can be located. A common two-dimensional cut out of a PES, describing a discrete state of a chemical molecule is shown in Figure 2.1, and describes the energy of the system as a function of a molecular motion, for example a vibration. The nuclear Schrödinger equation, using the nuclear wavefunction component $\chi_L(R)$, can then be used to evaluate vibration, as well as rotation, of the system at hand.

Despite research constantly striving for improvements in the description of a total wavefunction, the adiabatic and BO approximations hold their ground and is used as a standard reference that is widely applied and extremely useful in a variety of descriptions of chemistry.

2.2 Computational Strategies

So far in this chapter a quantum mechanical representation of electronic states has been introduced, through the adiabatic and BO approximations to the time-

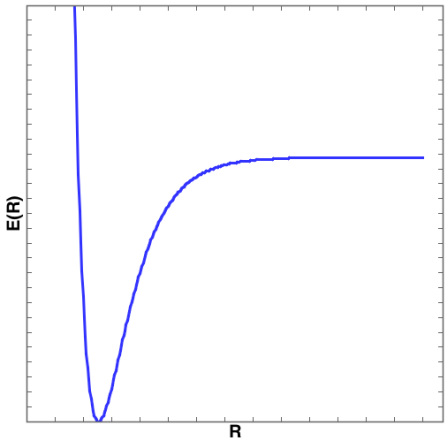

Figure 2.1: Illustration of a typical potential energy curve

independent Schrödinger equation. The appearance of discrete, quantised, states rationalises the appearance of spectra as well as the use of a Jablonski diagram, such as in Figure 1.3, to explain photochemical phenomena.

What still remains is an introduction to the computational strategies that are currently in place for the evaluation of the concepts introduced so far with respect to heteroaromatic biomolecules, which will ultimately lead to a description of the photochemical pathways available to them.

2.2.0.1 Variation Principle

One fundamental principle that greatly aids the computation of general eigenvalue problems, such as the Schrödinger equation, is the *variation principle*.[68] Given a wavefunction that is constructed both to be normalised and follows some appropriate boundary conditions, then

$$\langle \Psi | \hat{H} | \Psi \rangle \geq E_0. \tag{2.15}$$

where $\hat{H}$ is any Hamiltonian (or indeed any operator) that has a complete set of functions, $|\Psi\rangle$, and E_0 is the exact energy (or property associated with the operator) of the state.

The variation principle is extremely powerful, as it provides a measurement of

how appropriate an approximate wavefunction can be. Any improvement to the approximated wavefunction will mean a lowering of the energy, until it reaches a minimum. This minimum will then be used as the variational estimate of the exact energy of the state.

2.2.0.2 Orbitals

So far we have illustrated that the Schrödinger equation can potentially be greatly simplified through the Adiabatic and Born-Oppenheimer approximations, introducing an electronic Hamiltonian. The fact remains that it is a many-body problem, through the electron-electron interaction term in Equation 2.1:

$$+ \sum_{i<j=1,N} \frac{e^2}{r_{i,j}} \tag{2.16}$$

The variables in this term can not be separated, as they describe the instantaneous interactions between all electrons in the system. One strategy to overcome this many-body situation is to approximate the electron-electron interaction term to be *additive* for every particle, through a so-called *mean-field* approach.[69] However, if the Hamiltonian is to contain terms for single particles only, the wavefunction also needs to be adjusted to suit single particles. This leads to a crucial concept in chemistry, namely the association of electrons in discrete *spin-orbitals*, $\phi(r)$:

$$\psi(r_1, r_2 \ldots r_N) = \phi_i(r_1)\phi_j(r_2)\ldots\phi_k(r_n) \tag{2.17}$$

A spin-orbital is a wavefunction for one particle that describes both its spin and its spatial distribution. The spin functions correspond to spin up, α, and spin down β. The description above is termed a *Hartree* product, and it is a fairly severe approximation to the total wavefunction as it does not take into account any specific couplings between electrons in specific orbitals. At this stage it is also crucial to remember that the statistics in the quantum chemistry world differs from classical situations. Not only will identical particles, such as electrons, be considered indistinguishable, they will also behave differently according to the value of their spin. Electrons will follow Fermi-Dirac type statistics, due to their non-integer spin, (they are therefore commonly referred to as *fermions*) which essentially boils down to the fact that the

wavefunction will have to be *antisymmetric* with respect to permutations of electrons. A better description than the Hartree product can therefore be a *Slater*-determinant:

$$\psi(r_1, r_2 \dots r_N) = (N!)^{-1/2} \begin{vmatrix} \phi_i(r_1) & \phi_j(r_1) & \dots & \phi_k(r_1) \\ \phi_i(r_2) & \phi_j(r_2) & \dots & \phi_k(r_2) \\ \vdots & \vdots & & \vdots \\ \phi_i(r_N) & \phi_j(r_N) & \dots & \phi_k(r_N) \end{vmatrix} \tag{2.18}$$

where $(N!)^{-1/2}$ is a normalisation factor. One convenient outcome of the antisymmetrization of the wavefunction in this way is that it captures the effect of the Pauli exclusion principle automatically - If two electrons occupy identical states, the determinant will be equal to zero. One convenient way of expressing a normalised Slater determinant, which includes the normalisation constant, is to only write out the diagonal element:

$$\psi(r_1, r_2 \dots r_N) = |\phi_i, \phi_j \dots \phi_k\rangle \tag{2.19}$$

where the order of the electrons are assumed to be numerical from 1 to N.

Having approximated the wavefunction as above we can now attempt to solve the Schrödinger equation, using the tools introduced so far; the Born-Oppenheimer approximation and the variational principle.

2.2.1 Hartree Fock Theory

A variational treatment, using the electronic Hamiltonian, leads to the *Hartree-Fock Equations*, which can be conveniently expressed in atomic units:[69]

$$\hat{h}\phi_i = \varepsilon_i \phi_i = \hat{h}_i(r_i)\phi_i(r_i) + \hat{J}\phi_i(r_i) - \hat{K}\phi_i(r_i) \tag{2.20}$$

The switch to atomic units to describe the Hamiltonian essentially means that the constants in front of the kinetic and potential energy operators in Equation 2.1 have been set to 1, providing an expectation value for the energy with the unit *Hartree*.

The first term in the Hartree-Fock (HF) equation contains the one electron terms:

$$\hat{h}_i(r_i)\phi_i(r_i) = (-\frac{1}{2}\nabla_i^2 - \sum_{alpha} \frac{Z_\alpha}{|R_\alpha - r_i|})\phi_i(r_i) \tag{2.21}$$

The second term contains the *Coloumb Operator*, $\hat{J}$, which describes how electron i gets repelled by the mean-field charge distribution of all other electrons:

$$[\sum_j \langle \phi_j(r_j)| \frac{1}{r_j - r_i} |\phi_j(r_j)\rangle]\phi_i(r_i) = \hat{J}\phi_i(r_i) \tag{2.22}$$

where μ is used to indicate that the sum is running over all possible electrons. As the sum runs over ALL electrons, an error gets introduced as the term also describes the electron interacting with itself. The self-interaction problem gets counteracted in the final term, which involves the *Exchange Operator*, $\hat{K}$:

$$[\sum_j \langle \phi_j(r_j)| \frac{1}{r_j - r_i} |\phi_i(r_j)\rangle]\phi_j(r_i) = \hat{K}\phi_i(r_i) \tag{2.23}$$

This term is a by-product of the antisymmetrisation of the wavefunction. The concept of exchange is completely mathematical in nature, and not easily described, but can be thought of as the specific repulsion between two electrons of the same spin. Due to the Pauli principle, which is accounted for by the Slater determinant, electrons with the same spin should not occupy the same space and are therefore kept apart. This does however mean that the Coloumbic repulsion between them is weaker. Hence the Coloumb and exchange operators together assures that the electrons are behaving correctly in response to the mean-field, spread out charge of all other electrons.

The main issue with the Coloumb and exchange operators is that they contain the correct orbitals for all electrons in the system. This essentially means that, in order to solve the HF equation and reach a good eigenvalue (ε_i), we already need to know the correct eigenfunctions (ϕ_i). In order to deal with this situation a guess is made as to the orbitals shape, and the eigenvalue problem is solved using these. The new orbitals generated are then fed back in, creating an iterative process that proceeds until the orbital shape stops changing. This is termed the *self-consistent field* (SCF) approach.

2.2.1.1 Linear Combination of Atomic Orbitals (LCAO)

One issue that needs to be dealt with is the description of the one-electron orbitals of the molecular system. A function that behaves well in three dimensions is needed, which also describes all parts of the molecule well. Such a function can quickly become very difficult to compute. One solution to this issue is to expand the molecular orbitals into a set of *atomic orbital* basis functions, using a linear combination of atomic orbitals (LCAO):

$$\phi_i = \sum_{\mu} c_{i,\mu} \chi_\mu \tag{2.24}$$

Apart from giving the chemist in charge of the calculation more flexibility to describe the electron movement, the introduction of a set of basis functions also reduces the HF differential equation, 2.20, to a matrix eigenvalue equation, after multiplication on the left by $\chi_\nu*$ and integrating:

$$\sum_{\mu} \langle \chi_\nu | \hat{h} | \chi_\mu \rangle c_\mu = \varepsilon \sum_{\mu} c_\mu \langle \chi_\nu | \chi_\mu \rangle \tag{2.25}$$

These equations are called the *Roothaan*-equations and define two matrices, the *Fock matrix* and the *overlap matrix*. [70] The Fock matrix,

$$\mathbf{F} = \langle \chi_\nu | \hat{h} | \chi_\mu \rangle \tag{2.26}$$

contains the one-electron integrals (for the kinetic energy and the nuclear attraction), which are fixed for a given basis set, as well as the two-electron Coloumb and exchange integrals. The manipulations of the two-electron integrals are the most difficult and computationally expensive step in Hartree-Fock calculations, as well as any post-HF method. If the basis functions were orthonormal, we could now retrieve the eigenvectors (the expansion coefficients, $\mathbf{C}$) and the eigenfunctions (the energies, ε) by diagonalisation of the Fock matrix. However, even though the basis functions are normalised, they are not necessarily orthogonal to each other. This gives rise to the overlap matrix, $\mathbf{S}$,

$$\mathbf{S} = \langle \chi_\nu | \chi_\mu \rangle \tag{2.27}$$

This means that the basis set need to be orthonormalised, before the Roothaan equations can be solved as a usual matrix eigenvalue problem. The Roothaan equations are normally written in the compact form:

$$\mathbf{FC} = \mathbf{SC}\varepsilon \tag{2.28}$$

As the Fock matrix is dependent on the matrix of expansion coefficients, **C**, the Roothaan equations are actually pseudo-eigenvalue equations that need to be solved by an SCF procedure.

2.2.1.2 Basis sets

It is clearly a benefit to select a good set of atomic orbital basis functions in order to achieve a flexible description of the movement of the electrons in the LCAO molecular orbitals. In the 1930s John Slater introduced a function for the electron of the form $e^{-\zeta r}$ that behaves well at short distances from the nucleus (it has a cusp at small r) as well as having an exponential decay at long range.[71] These two conditions corresponds well to the eigenfunctions of the Schrödinger equation for one-electron systems, and would therefore be ideal to use as atomic orbitals in the LCAO for molecular orbitals of atoms and molecules. However, the evaluation of integrals over Slater-type orbitals are very difficult to compute. Gaussian-type primitive functions however, with the form $e^{-\alpha(r-R)^2}$, where R and α are the centre and exponent of the Gaussian function, are routinely coded for. The general strategy that is used in computational chemistry calculations is to create the type of functions that are desired, such as Slater-type functions for atoms and molecules, using a linear combination of contracted Gaussians. Instead of using one Gaussian function per occupied orbital centred on each atom in the system, more flexibility is introduced when the basis space is increased. This leads to more variational flexibility. The terminology used in the description of a set of basis functions uses the term *zeta* (as it is commonly used for the Slater-type orbital exponent) as follows:

double-zeta

A double-zeta basis set has *twice* as many contracted Gaussian functions as there are core and valence orbitals.

triple-zeta

A triple-zeta basis set has *three times* as many contracted Gaussian functions as there are core and valence orbitals.

Another strategy to increase the basis space is to include so called *polarisation functions*. These describe orbitals of higher angular momentum than the atoms orbital space. This leads to more angular space becoming available for the electrons to minimise in to, and hence a more flexible description. Conversely to the angular space, the radial space available for the electrons can also be increased using so called *diffuse functions*. These functions are of the same angular momentum, but belonging to a higher shell, giving the electrons more radial freedom. The latter can be crucial for the description of photochemical events as these require a good description of excited states, which are often diffuse in nature. One specialist case for small organic molecules that require the use of diffuse functions is for *Rydberg* molecules. These systems have low lying states of Rydberg character, i.e. states resulting from an excited electron interacting with the rest of the system in a similar way to a proton in a Rydberg atom. This leads to diffuse states of atomic character requiring diffuse basis functions, or possible even specialist Rydberg-functions [72], for a correct description.

As valence orbitals normally are crucial in the description of chemical phenomena, such as bonding, a good strategy is to use more functions to describe them as accurately as possible. Families of basis sets from various research groups, such as the Pople and Ahlrichs groups, have created so called *split valence* basis sets with this in mind, where the orbitals are further divided into core and valence.[73–75] Examples of split valence basis sets are:

6-31+G*

A Pople-type double-zeta basis set with added diffuse functions (+) and polarised functions (*) on heavy (non-hydrogen) atoms. It has 6 primitive Gaussians for each core atomic orbital, 3 Gaussians for the inner valence and 1 for the outer valence.

(Def-2) TZVP

An Ahlrichs-type triple-zeta basis set with polarised valence. Def-2 specifies a newer formulation. [75]

In order to improve further on the form of the basis functions the Dunning group have developed a series of functions that have been fitted to behave well when comparing to experimental data.[76, 77] These are termed *correlation-consistent* basis sets and are abbreviated as below:

aug-cc-pVDZ

A Dunning-type double-zeta (DZ) basis set with polarised functions (p), correlation-consistent (cc) fitting and diffuse augmented functions (aug)

The Dunning-type basis have the advantage that they can be rigorously increased by adding contractions, leading to the ability to extrapolate the value of the energy given with these functions towards the basis-set limit. The fitting does however mean that these sets are not always suitable for all methods.

For atoms further down than the first row of the periodic table, it is common to use an effective core potential (ECP). An ECP method replaces the core electrons of a heavier element with a pseudopotential in order to approximate them. The version of pseudopotential used in this thesis, is of the Stuttgart/Dresden type (SDD).

The more basis functions (of a suitable shape and size for the problem at hand) that is used the better the description of the chemical structure or behaviour will be. However, for large molecular systems the limit is very quickly reached when calculating two-electron integrals, such as in the Hartree-Fock matrix eigenvalue equation.

2.2.2 Electron Correlation

The Hartree-Fock method, used with a suitable set of basis functions, has been shown to be remarkably successful for singlet ground state energies and in most cases it recovers up to 99.9% of the ground state energy.[69] However, treating the motion of electrons in a mean-field approach means that any description of events that involve the specific interaction of one electron with the other will not be described at all. As most interesting chemical events involves such specific electron interactions, a description of the *correlated* electron motion is highly desired. The definition of the electron correlation energy is the energy that is missing from the HF treatment compared to the true energy from the Schrödinger equation, E:

$$E_{corr} = E - E_{HF} \tag{2.29}$$

Since the development of the HF method, the efforts of the computational chemistry community has been mainly focused on the development of methods that captures this electron correlation energy. The way this problem has been approached has divided the computational methods available into two broad categories, depending on the strategies used to describe the specific electron correlation energy:

Wavefunction Methods

Methods that use the Hamiltonian from HF as a base, and tailor the description of the *wavefunction* to recover E_{corr}

Density Functional Methods

Methods that uses the electron *charge density* to describe electrons, and then tailor the description of the Hamiltonian to recover E_{corr}

These two strategies, and the most common methods resulting from them, are introduced in the following sections.

2.2.3 Wavefunction Methods

Hartree-Fock theory has many very powerful advantages. It is very well behaved for atomic properties and is also self-interaction free, from the cancellation of self-interaction terms in the Coloumb term by the exchange term. Crucialy it is also very well defined as a variational method. This means that any improvements made to the wavefunction, making it more flexible, will be systematic. The HF wavefunction is therefore an excellent starting point for systematic improvements in the endeavour to retrieve electron correlation effects. Before moving on in the description of some of the wavefunction methods used in this thesis, it is first important to make a distinction between the two general types of correlation; *dynamic* and *static* correlation. Whilst the former deals with the instantaneous correlation between electrons, the latter is a more permanent, static, type that comes into play when one can use more than one determinant to describe the same state. When dealing with photochemical events, which often involves areas where states are very close, or even cross, the static correlation becomes a very important effect.

2.2.3.1 The Second Quantisation formalism

The language of *second quantisation*, first introduced by Dirac in the 1920s, is an extremely useful approach to the discussion of many methodologies and will therefore be introduced briefly before moving on.[78]

In second quantisation all operators as well as wavefunctions are described by the same elementary operators that changes the number of electrons in the system. Elementary operators are *creation operators*, $a_i^\dagger$, and *annihilation operators*, a_i, for each spin-orbital i and they are each others adjoint. For a Slater determinant of N orthonormal spin-orbitals, the operation of the elementary operators are:

$$a_i^\dagger|\phi_j,\ldots,\phi_k\rangle = |\phi_i,\phi_j,\ldots,\phi_k\rangle \tag{2.30}$$

$$a_i|\phi_i,\phi_j,\ldots,\phi_k\rangle = |\phi_j,\ldots,\phi_k\rangle \tag{2.31}$$

The order of the elementary operators are crucial, as can be seen by their anti-commutation relationships:

$$a_i^\dagger a_j^\dagger + a_j^\dagger a_i^\dagger = 0 = [a_i^\dagger, a_j^\dagger]_+ \tag{2.32}$$

$$a_i a_j + a_j a_i = 0 = [a_i, a_j]_+ \tag{2.33}$$

We can now define standard operators from first quantisation using these elementary operators. The *excitation operator* for example, $\hat{X}_i^a$, anihilates the ground state and creates the excited state by essentially exciting (or substituting) an electron from an occupied spin-orbital, i, to an un-occupied one, a.

$$\hat{X}_i^a = a_a^\dagger a_i \tag{2.34}$$

2.2.3.2 Configuration Interaction

One solution to the problem of electron correlation is to generate more determinants to describe the trial wavefunction by promoting electrons in occupied orbitals to virtual, unoccupied, orbitals. This means that the system is described by a linear combination

of all substituted configurations, which is termed the Configuration Interaction (CI) method.[79, 80] This method generates an exact solution to the non-relativistic BO Schrödinger equation, i.e. capture *all* correlation effects, within the particular basis set.

Using the second quantisation formalism the full CI wavefunction is:

$$\Psi^{CI} = (1 + \sum_{a}\sum_{i} c_i^a a_a^\dagger a_i + \sum_{a>b}\sum_{i>j} c_{ij}^{ab} a_b^\dagger a_j a_a^\dagger a_i + \dots)\psi_0 \tag{2.35}$$

$$\Psi^{CI} = (1 + \hat{C}_S + \hat{C}_D + \dots)\psi_0 \tag{2.36}$$

where ψ_0 is a reference wavefunction, S and D stands for single and double excitations and c are the expansion coefficients. The reference wavefunction can be constructed using Slater determinants as in HF theory, or using so-called *Configuration State Functions* (CSFs). The latter is a linear combination of Slater determinant, where the expansion coefficients have been evaluated so that the CSF are eigenfunctions both the spin operator and its z-projection; $\hat{S}^2$ and $\hat{S}_z$. Therefore CSFs are referred to as being *symmetry adapted*. The use of CSFs or Slater determinants as a basis depends on the problem at hand (and the size of the system).

If an optimisation of the expansion coefficients were to be carried out over all possible configurations the CI wavefunction would be equal to the exact wavefunction, within that basis set. This is termed the *full* CI wavefunction and is used, when it can be obtained, as a standard reference in quantum chemistry. A full CI treatment is however a difficult task as the number of possible configurations will grow very fast when the basis functions used to describe the orbitals are increased. The full CI wavefunction therefore normally needs to be truncated for it to be used on most systems of chemical interest. There is however a problem associated with a truncated CI wavefunction. This becomes apparent when considering that the total wavefunction of any molecular system is an asymmetric product of individual wavefunctions;

$$\Psi_{A,B\dots} = \hat{A}\Psi_A\Psi_B\dots \tag{2.37}$$

where $\hat{A}$ is an anti-symmetrizer. If we for example look at a situation where we would want to include only double excitations in the HF wavefunction for two systems, A

and B, the resulting CID wavefunction should have the form:

$$\Psi_A \Psi_B = (1 + \hat{C}_{D,A} + \hat{C}_{D,B} + \hat{C}_{D,A}\hat{C}_{D,B})\psi_{HF} \tag{2.38}$$

However, the wavefunction truncated at CID will actually be:

$$\Psi_{A,B}^{CID} = (1 + \hat{C}_{D,A} + \hat{C}_{D,B})\psi_{HF} \tag{2.39}$$

which are missing contributions from quadruple excitations that are there in an ideal multiplicative treatment. Because of this missing component the result will no longer be *size extensive*. Crucially, the energy will no longer scale linearly with the number of particles, or molecules, of the system. A size extensive treatment requires full CI.

2.2.3.3 CASSCF

There is one method that includes a full CI to some extent; the Complete Active Space Self Consistent Field method (CASSCF).[81, 82] This method utilises the fact that some parts of the CI expansion contributes more to the total wavefunction, depending on the problem at hand. By biasing the system, depending on what part of the PES is investigated, the power of a full CI can be utilised for the most important components of the determinant. Molecular orbitals, for example Hartree-Fock orbitals, are selected according to their importance in the description of the system, or the chemical event, at hand and divided into three categories depending on their expected importance based on electron occupation. Orbitals that are expected to stay either fully occupied or un-occupied in all determinants, for example the orbitals of the inner shell or the high-energy un-occupied orbitals of the molecule, will be kept unchanged. The remaining orbitals will be considered to be active, and a full CI will be carried out on this subset.

As all determinants in the active space are treated equally, all static correlation effects will be accounted for. Any dynamical effects from the electrons in orbitals outside of the active space will not be included however. This means that the main advantage of the CASSCF method is the construction of *qualitatively* correct wavefunctions, rather than minimum energy wavefunctions. Additionally to optimising the coefficients of the determinant the CASSCF procedure also optimises the MOs that are used to make the determinants. The specific MOs used are the so-called

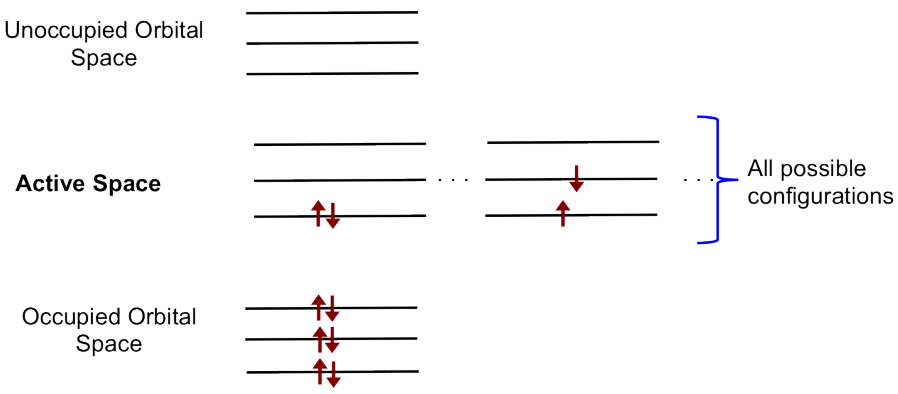

Figure 2.2: In CASSCF occupied and unoccupied orbitals are considered to be *inactive*, whilst the *active* space gets a full CI treatment.

natural orbitals(NOs) . The NOs are orbitals that are unique to a wavefunction, i.e. the resulting orbitals of the orbital optimisation step, and can be defined as the eigenorbitals of the first order reduced density operator ρ of the wavefunction.

$$\rho = \sum_{i,j} p_{ij} |\psi\rangle_i \langle\psi|_j \tag{2.40}$$

The diagonal elements, p_{ii}, are referred to as the orbital occupation numbers. In a multi-determinant wavefunction $0 \leq p_{ii} \leq 2$, and the occupation number can therefore provide a convenient measure of the importance of the particular orbital in the wavefunction for each state. CASSCF is therefore exceptionally flexible and can be used to compute a qualitative picture of essentially any part of the PES of excited as well as ground states and, as the active orbitals get a full CI treatment, the results will also be size extensive.

These facts makes CASSCF a very important tool for computational investigations in photochemistry, and has been used in the work that constitutes this thesis. The common nomenclature, CAS(n,m), where n and m are the number of electrons and orbitals respectively selected for the active space, has been used throughout.

2.2.3.4 RASSCF

When looking at the construction of a CASSCF wavefunction we realise that the larger the molecule the larger the active space we are likely to want. As with full CI, the computational effort will increase very fast with an increase in orbitals and electrons. For a system as large as some heteroaromatics, especially of the type commonly used as photosensitisers in photodynamic therapy, we therefore need to bias the system further. One variation of CASSCF that achieves this is the Restricted Active Space Self-Consistent Field method (RASSCF).[83] Here the orbitals in the active space are divided into three sections, termed RAS1, RAS2 and RAS3. Whilst the RAS2 space gets full CI treatment the remaining spaces have a restricted number of excitations, as illustrated in Figure 2.3. This method has been applied for the use of calculations of the relaxation pathways of porphyrins, and the standard nomenclature CAS(n,m,RAS(a,b,c,d)) has been used where a and b are the number of holes and orbitals incorporated in RAS1 and c and d are the number of electrons and orbitals in RAS3.

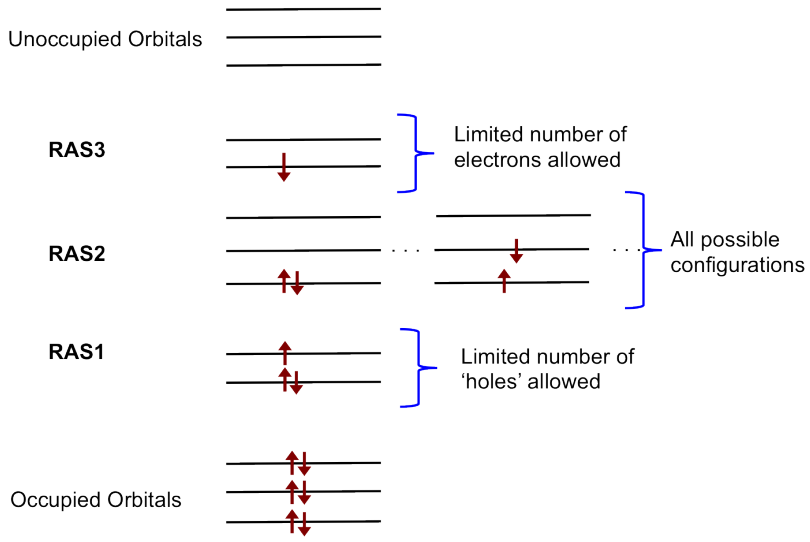

Figure 2.3: In RASSCF occupied and unoccupied orbitals are considered to be *inactive*, just as in the CASSCF treatment. The *active* space however gets divided into sections that get a full CI treatment, RAS2, or have a restricted number of excitations allowed, RAS1 and RAS3.

The drawback of CASSCF and RASSCF, apart from neither including dynamical

correlation to a large extent, is the orbital selections themselves. As there are a limited number of orbitals to chose from, before the active space/RAS2 becomes too computationally expensive to evaluate, good knowledge of the chemistry that underlies the problem is needed. Unlike many other methods, especially density-based methods, the set-up and result analysis of CAS and RASSCF calculations are far from straight forward.

2.2.3.5 Coupled Cluster Method

One alternative to biasing the CI wavefunction, so as to avoid having to truncate it, and still achieve size extensive results is to use a different approach all together in order to mimic the multiplicative behaviour of the wavefunction that was illustrated in Equation 2.38. This can be achieved through an exponential ansatz, commonly known as the *coupled cluster* (CC) method.[84, 85]

Analogous to the CI wavefunction we write the CC wavefunction, in second quantisation formalism, as:

$$\Psi^{CC} = (1 + \sum_{a}\sum_{i} t_i^a a_a^\dagger a_i + \sum_{a>b}\sum_{i>j} t_{ij}^{ab} a_b^\dagger a_j a_a^\dagger a_i + \dots)\psi_0 \tag{2.41}$$

$$\Psi^{CC} = (1 + \hat{T}_S + \hat{T}_D + \dots)\psi_0 \tag{2.42}$$

where ψ_0 is a reference wavefunction, analogous to the CI case it is normally a Hartree-Fock wavefunction, S and D stands for single and double excitations and t are the expansion coefficients. The reason a different label is introduced is that the *cluster* operator, $\hat{T}$, is now treated using an exponential, rather than a linear treatment:

$$\Psi_{EXP} = exp(\hat{T})\psi_0 \tag{2.43}$$

Expanding the exponential function as a Taylor series results in:

$$exp(\hat{T}) = 1 + (\hat{T} + \frac{\hat{T}^2}{2!} + \frac{\hat{T}^3}{3!} + \dots + \frac{\hat{T}^n}{n!} + \dots) \tag{2.44}$$

and we are therefore automatically including all the higher order terms needed for a proper expression of the wavefunction, even when it is truncated, as illustrated in Table 2.1

Table 2.1: Comparison of CC and CI wavefunctions at various levels of truncations

$\Psi_{CC} = exp(\hat{T})\psi_0$		$\Psi_{CI} = \hat{C}\psi_0$
$\hat{T}_1\psi_0$	singly excited	$\hat{C}_1\psi_0$
$(\hat{T}_2 + \frac{\hat{T}_1^2}{2!})\psi_0$	doubly excited	$\hat{C}_2\psi_0$
$(\hat{T}_3 + \hat{T}_2\hat{T}_1 + \frac{\hat{T}_1^3}{3!})\psi_0$	triply excited	$\hat{C}_3\psi_0$

The coupled cluster method truncated at the double excitation level and with added triplet components through a perturbative treatment, CCSD(T), is commonly referred to as the *gold standard* in ground state computational chemistry.

2.2.4 Density Functional Methods

One very popular alternative to using the wavefunction to try to capture the electron correlation is to use the electron density as a starting point. The first attempt was introduced by Fermi as early as in the 1920s, and it was a very attractive approach as both electron-nuclear energies and electron-electron repulsion energies can be written *exactly* in terms of the electron density, $\rho(r)$.[86] The kinetic energy on the other hand has a very complex relationship to the density and, at the time, it was not yet known if such a relationship even existed. Without a rigorous theoretical development, DFT would have limited applicability for electronic structure calculations of atoms and molecules.

2.2.4.1 Hohenberg-Kohn Theorems

When looking at the electronic Hamiltonian in atomic units at a specific nuclear-nuclear distance,

$$\hat{H}_{el} = -\sum_{i=1,N}\frac{1}{2}\nabla_i^2 - \sum_{i=1,M}\sum_{j=1,N}\frac{Z_i}{|r_j - R_i|} + \sum_{i<j=1,N}\frac{1}{r_{i,j}} \tag{2.45}$$

we realise that the Schrödinger equation depends fundamentaly only on two variables; the number of electrons, N, and the external potential, V_{ext}, i.e. the electron-nuclear

attraction term:

$$V_{ext} = -\sum_{i=1,M}\sum_{j=1,N}\frac{Z_i}{|r_j - R_i|} \tag{2.46}$$

As the Schrödinger equation uniquely defines a wavefunction for each problem, which can then be used to determine the energy as well as any other property, the energy (or property) is a *functional* of both N and V_{ext}.

The first step that was taken towards the development of a rigorous theory for the use of DFT in computational chemistry calculations was the formulation of the first Hohenbergh-Kohn Theorem:[87]

First Hohenberg-Kohn Theorem

> A unique external potential directly determines a unique electronic charge density , $\rho(r)$.

As the electron density also determines the number of electrons, N, through:

$$\int \rho(r)dr = N \tag{2.47}$$

it is clear the the electron density in fact must be a variable as fundamental to the energy of a system as N and V_{ext}.

The next step in the rigorous theoretical description of DFT is the introduction of a variational approach in the second Hohenberg-Kohn Theorem:

Second Hohenberg-Kohn Theorem

> For any given external potential, V_{ext}, and charge density, ρ, an energy functional exists that is minimised variationally by the *ideal* electron density, ρ_0:
>
> $$E[\rho(r)] = F[\rho(r)] + \int V_{ext}(r)\rho(r)dr \geq E[\rho_0(r)] = E_0 \tag{2.48}$$
>
> where E_0 is the exact energy, and $F[\rho(r)]$ is the so-called *universal density functional*

All the components in the second theorem are well defined and proven to be exact. However, we *do not know* the form of the universal functional, $F[\rho(r)]$, so an approximation strategy has to be used.

2.2.4.2 Kohn-Sham Theory

The strategy developed by Kohn and Sham for an approximate form of the universal functional has been called genius in quantum chemistry textbooks.[68] Its foundation lies in the realisation that a system of non-interacting electrons has *exactly the same* density as a real system.[88] Essentially the non-interacting electrons in the fictitious Kohn-Sham (KS) system are described by an effective external potential that is defined so that the electron density is the same as in the real, interacting, system. This realisation means that a description of the kinetic energy of these electrons becomes a well defined trivial term. For the KS system a Slater determinant is not only a good approximation but the *exact* wavefunction, meaning that the exact kinetic energy for the KS system can be defined as:

$$T^{KS} = \sum_{i=1,N} \langle \phi_i^{KS} | -\nabla^2 \frac{1}{2} | \phi_i^{KS} \rangle \tag{2.49}$$

The KS orbitals, ϕ_i^{KS} are defined as the orbitals which corresponds to the ground state density ρ_i that would gives us the exact ground state energy, if the universal density functional was known:

$$\rho(r) = \sum_{i=1,N} (\phi_i^{KS})^2(r) \tag{2.50}$$

The electrostatic interactions is also straight forward, and can be written down as a Hartree term (essentially a Coloumbic repulsion term):

$$E_H[\rho(r)] = \frac{1}{2} \iint \frac{\rho(r_1)\rho(r_2)}{|r_1 - r_2|} dr_1 dr_2 \tag{2.51}$$

With these defenitions in mind, Kohn and Sham defined the universal functional:

$$F[\rho(r)] = T^{KS}[\rho(r)] + E_H[\rho(r)] + E_{XC}[\rho(r)] \tag{2.52}$$

where an *exchange-correlation* energy term has been introduced. This term essentially collects all the components that we can not calculate exactly, i.e. the missing contribution to the kinetic energy term from the kinetic energy of the real system as well as the missing components in the Hartree term from the real electron-electron potential.

In order to evaluate what the charge density must look like in order to be variational, the KS energy expression is minimised with respect to the electron density, with the number of electrons as the constraint. Incorporating the KS orbitals (from Equation 2.50) and evaluating the energy, this yields the Kohn-Sham equations, which are the fundamental equations in DFT:

$$[-\frac{1}{2}\nabla^2 + V_H(r) + V_{ext}(r) + V_{XC}(r)]\phi_i^{KS}(r) = \varepsilon_i \phi_i^{KS} \tag{2.53}$$

where $V_H(r)$ is the Hartree potential:

$$V_H(r) = \frac{\delta E_H(r)}{\delta \rho(r)} \tag{2.54}$$

and $V_{XC}(r)$ is the Exchange-Correlation Potential:

$$V_{XC}(r) = \frac{\delta E_{XC}(r)}{\delta \rho(r)} \tag{2.55}$$

The KS equations strongly resembles the Hartree-Fock equations (Equation 2.20) apart from the crucial issue that the HF exchange operator, $\hat{K}$, has been replaced by an exchange-correlation potential. As the latter is multiplicative in nature this means that we have an *in principle* simpler term to solve. The only remaining issue is that we still do not know the form of the exchange-correlation energy.

The KS equations are solved analogously to the HF equations. After LCAO MOs are introduced to form a matrix eigenvalue problem, an SCF procedure is carried out until the DFT energy is minimised.

2.2.4.3 The DFT Exchange-Correlation Energy

The way in which the exchange-correlation energy functional is approximated in DFT is what differs the various methods available to the computational chemist today, and development has been focused on finding a good "guess" for the term. The first port of call in the functional development was to use an approximation of electrons in a system in the form of a homogenous electron gas, introduced in the early days of DFT. This is the foundation of a family of so called *Local Density Approximated* (LDA) functionals. These all assume that, in a local small volume of the molecular system, the electron density is homogenous and can therefore be solved as a sum of

small contributions, as if it was a homogenous electron gas problem. A number of LDA exchange and correlation functionals has been developed,[89] but most generally overbind molecular systems and have limited applicability in chemical calculations outside the solid state community.

Improvements to the LDA include accounting for the fact that E_{XC} not only depends on the local $\rho(r)$. To this end so-called *Generalised Gradient Approximated* (GGA) functionals were developed to improve the LDA by including more long-range behaviour of the density, through the addition of the first derivative (gradient) of the density functions. The famous Becke 88 exchange functional (B88 or B)[90] is of GGA type and is commonly used in combination with various correlation functionals, such as LYP[91] and P86[92] just to mention a few.

One improvement that can be realised straight from the form of the KS equations, is that the Hartree term will carry with it an inherent self-interaction error. In Hartree-Fock treatments this self-interaction is directly cancelled by the exchange term. Could the addition of some HF exchange lead to a better results compared to experiment? One extremely popular functional that seems to prove this point is the B3LYP functional, which uses amongst others, both the Becke exchange and LYP correlation in an interesting mixture:[93]

$$E_{XC}^{B3LYP} = E_{XC}^{LDSA} + 0.20(E_X^{HF} - E_X^{LSDA}) + 0.72E_X^{B88} + 0.81E_C^{LYP} + 0.19E_C^{VWN} \quad (2.56)$$

Functionals of the type that includes exact exchange from HF (evaluated with KS orbitals) are called hybrid functionals and have been shown to have plenty of advantages for many applications, including photochemical properties. However, even though the temptation would be to add 100% HF exchange, and cancel the self-interaction problem completely, this has been shown to be incompatible with general correlation functionals. The 20% exact exchange incorporated in the B3LYP functional seems to symbolise the most balanced amount for reaction energies, at least in the ground state.

A further improvement in functional development is to incorporate spin kinetic energy density for occupied KS orbitals, as well as higher order derivatives of the density, into the functional expression in order to capture more non-local effects .[94]

Fitting to empirical data from large datasets in combination with various additions, such as exact exchange from HF, has lead to a series of meta-GGA functionals, for example the M06 series by Truhlar et al..[95]

So-called double hybrids are a recent addition to the plethora of functionals, and have been shown to be the most successfull approach currently available. Apart from including exact exchange from HF, double hybrids also incorporate correlation energies from a method known as MP2.[96] MP2 is the wavefunction-based Moller-Plesset perturbative approach to retrieving the correlation energy, truncated at the second order term. The main drawback from the point of view of the work carried out for this thesis however, is the fact that the method scales as MP2 rather than DFT, making it difficult to apply to many larger heteroaromatic molecules, such as porphyrins.

The DFT approximations introduced so far can not accurately describe dispersion interactions, a crucial issue in systems with more than one molecule, which has lead to a recent addition in the functional collection. The strategies to achieve this include the successful approach of adding a correction term to the existing DFT mean-field energy, which has been shown to describe the correct binding energy for a large range of weakly bound complexes, including large systems with π-interactions, such as heteroaromatics. [97–100]. Successful functionals include Grimme's B97-D functional series [101].

All of the improvements to the exchange correlation functional that has been described so far are commonly referred to as being rungs of a *Jacob's ladder* to a quantum chemical "heaven" (in computational accuracy terms).[102] The order of the rungs of the ladder are LDA, GGA, meta-GGA, hybrid and, recently added to the last rung, double-hybrids. This description is however only true in terms of ground state chemistry of single molecules.

2.3 Non-Adiabatic Events

The methods introduced so far are all based on the initial approximations made. The BO approximation is valid, and indeed essential, for an accurate theoretical description of most areas of chemistry but there are certain cases where it does break down. The breakdown is caused by the assumptions used in the derivation of these

approximations, such as the states at hand being well separated, no longer being valid and is a common result of efficient coupling between the electronic and nuclear motions. This means that the non-adiabatic coupling terms in Equations 2.11 and 2.12 no longer can be ignored. To account for the breakdown of these approximations is especially important in situations where polyatomic molecules are in their excited state manifold, with many electronic eigenstates that are close to each other in energy as well as many nuclear degrees of freedom, where electronic state PESs often come close to each other or even cross. The crossing of a system from one PES to another was introduced in the introductory session as internal conversions (IC) and inter-system crossings (ISC) (depending on their spin manifold, as illustrated in Figure 1.2) and are fundamental concepts that are needed in the description of photochemical pathways.

Two N-dimensional PESs, where N is the number of degrees of freedom in the molecule, intersects on a N-2-dimensional surface in an intersection space where the non-adiabatic coupling terms are infinitely large. In Figure 2.4 a more accurate representation of IC after OPA is illustrated, where the energies are plotted against the two remaining coordinates, x_1 and x_2, in what is known as the *branching space*. In the branching space the two PESs form a double cone, and meet in a point as shown. Due to the shape of the surfaces when plotted in this space, these types of crossing points are termed Conical Intersections (CIns).[103–105]

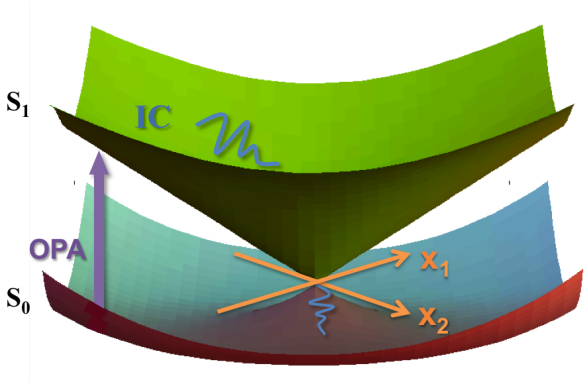

Figure 2.4: The conical intersection coupling S surfaces, as described in the space of the gradient difference (x_1) and derivative coupling (x_2) vectors

Conical intersections are mathematical objects that have been known since the

1930s, and many excellent reviews exist on the topic.[103–106] They were well known early on to exist in high symmetry species, and manifest through phenomena like the Jahn-Teller effect, showing that molecules in orbitally degenerate states undergo non-totally symmetric distortions to remove the degeneracy.[107] However, advances in electronic structure theory in the last 20 years or so have highlighted that accidental conical intersections, not requiring high symmetry, are also exceptionally common in polyatomic systems, and especially in heteroaromatic molecules, which is of interest from a photosensitiser point of view.

The two coordinates x_1 and x_2, which lift the degeneracy of the states and thereby define the branching space, are termed the energy gradient difference (GD) vector and the derivative coupling (DC) vector, respectively and have the form:

$$x_1 = \frac{\delta(E_L - E_K)}{\delta R} \tag{2.57}$$

$$x_2 = \langle \psi_L | \frac{\delta \hat{H}_{el}}{\delta R} | \psi_K \rangle \tag{2.58}$$

where R describes the nuclear motion, $\hat{H}_{el}$ is the electronic Hamiltonian and E_L and ψ_L denotes the energy and the adiabatic wavefunction for the electronic state L respectively.

A comparison of the gradients of the two vectors in the branching space will give information of the exact topology of the CIn, which can lead to conclusions as to the outcome of the photochemical reaction. A peaked CIn (as the example shown in Figure 2.4) between an excited state and the ground state for example, have non-parallel vectors that are of opposite sign and therefore suggest that the IC will lead to formation of photoproducts as well as regeneration of the reactants. A sloped CIn, however has near parallel vectors and is considered to be a feature of photostable compounds as it will mainly lead to the regeneration of the reactants. Any movement in the branching space will lift the degeneracy. However, a more accurate description of the CIn is achieved by considering movement along any of the other remaining internal coordinates in the intersection space. Then the degeneracy is not lifted and it is realised that the intersection is in fact a hyperline, or a seam, consisting of an infinite number of conical intersection points. A deeper knowledge of the form of the seam has been shown to lead to many important realisations with respect to the

outcome of photochemical reactions.[108]

If the two PESs that cross belong to different spin manifolds, the crossing is an ISC, and is illustrated as in Figure 2.5 for an ISC between the first singlet and triplet states. The DC term will then become zero, as electronic states of different spin-symmetries do not couple through the electronic hamiltonian, and only the GD coordinate represent a break in degeneracy. The PES crossing therefore appears as a seam in the ISC crossing space when the GD is plotted against another arbitrary nuclear coordinate. As the crossing-point involves a change in spin of one electron in the system, it is mainly seen in molecular systems that have efficient spin-orbit coupling (SOC), such as those containing large atoms.[109] When it comes to the family of heteroaromatics SOC is generally weak and involvement of a triplet state is mainly seen in large systems such as porphyrins or systems with large heteroatoms.

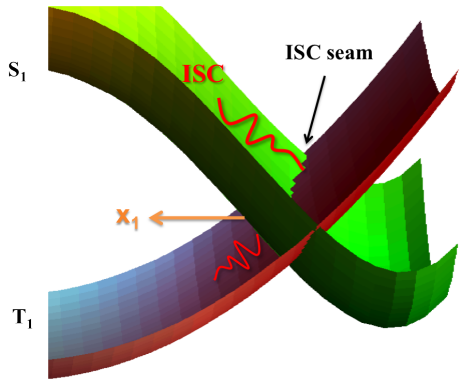

Figure 2.5: Intersystem crossing between two states differing in spin multiplicity. Plotted in the branching space, the crossing takes place along a seam.

2.4 Time-Independent Molecular Properties

The methods introduced so far have been concerned with the correct estimation of the energy of a molecular system through the solution of the Schrödinger equation. The BO approximation means we have a way of describing the molecular energy of a system as a function of the position of the nuclei. The resulting PES can then be used as we turn to the calculation of the properties of the molecules of interest.

Property calculations are centred around the *change* in energy under some form of perturbation. For the molecular geometry, the energy can be expanded in a Taylor series about the coordinates of the initial molecular structure we are interested, X:

$$E(x) = E^0 + E^1\Delta x + \frac{1}{2}E^2\Delta x^2 + \dots \tag{2.59}$$

As the perturbation is static, it can can be estimated by differentiating, so that:

$$E^1 = \frac{dE}{dx} \tag{2.60}$$

is the molecular gradient, and:

$$E^2 = \frac{d^2E}{dx^2} \tag{2.61}$$

is the molecular Hessian (the matrix of second derivatives). These derivatives are used for the location and characterisation of minima and saddle points points on the BO surface as well as localisation of CIns and minimum energy reaction paths.

2.5 Time-Dependent Molecular Properties

In the classical view of photochemistry and the absorption of light by molecular systems, the electric field, $E(t)$, of the light causes an oscillation of the charges in the molecule, which gives rise to an induced polarisation, $\mu(t)$ in the system. [110] How well the field manages to set these charges in motion is related to the *polarisability* of the molecule itself. The rich colours of molecules such as porphyrins, with highly polarisable electrons in large π-systems, is evidence of effective absorption of visible light. General molecular properties in the presence of the field can be derived through an expansion of the polarisation in orders of the electric field:

$$\mu(t) = \mu_0 + \alpha E(t) + \frac{1}{2}\beta E^2(t) + \frac{1}{6}\gamma E^3(t) + \dots \tag{2.62}$$

where α is the polarisability and β and γ are the first- and second order hyperpolarisabilities respectively. Whilst α will give an indication of OPA cross sections, γ is related to the molecule's ability to undergo TPA.

From a quantum mechanical point of view, however, the probability that a molecule

will transition from one state to another after absorption of the oscillating field is proportional to the square of the transition moment integral, M:

$$M = \langle \psi_0 | \hat{\mu} | \psi_k \rangle \tag{2.63}$$

for a transition between state 0 and k, where $\hat{\mu}$ is the transition dipole moment operator. By dividing $\hat{\mu}$ into two components, one for the electronic, including spin ($\hat{\mu}_{es}$) and one for the nuclear coordinates ($\hat{\mu}_n$), M can be written as:

$$M = \langle \psi_{n_0} | \psi_{n_k} \rangle \langle \psi_{e_0} | \hat{\mu}_e | \psi_{e_k} \rangle \langle \psi_{s_0} | \psi_{s_k} \rangle \tag{2.64}$$

The first integral is referred to as the Franck-Condon factor and describes overlap between two vibrational wavefunctions in the two electronic states. The second and third integral are the orbital and spin integrals respectively, and highlight a crucial point in photochemistry: the importance of *symmetry* in the observation of photochemical transitions. If the transition takes place between states of differing spin, or between orbitals whose symmetry operations do not include the totally symmetric irreducible representation of the group, the total transition moment integral will be zero. The calculation of transition moment integrals is far from trivial when we realise that, as the electric field is not static, we need to find an alternative to a straight forward gradient calculation, as in the case of geometry optimisations.

2.5.1 Response Theory

If the molecular perturbation is not time-dependent, the wavefunction as well as the energy can be expanded in terms of the operators describing the perturbation, as discussed for geometry optimisations using a gradient approach. In a time-dependent case there is however no well-defined function describing the energy, and instead we have to turn to the special case of *response theory*. In response theory it is assumed that the TD change is small. This means that the solution can be written in terms of the eigenstates of the *unperturbed* system, and express how the system responds to the perturbation.

The time-dependent perturbation is expressed by an interaction operator, $\hat{V}(t)$

which is added on to the unperturbed Hamiltonian $\hat{H}_0$:

$$\hat{H}(t) = \hat{H}_0 + \hat{V}(t) \tag{2.65}$$

As the exact solutions to $\hat{H}_0$, ψ_n, form a complete set, we can use those to express the perturbed state $\psi(t)$:

$$\psi(t) = \sum_n c_n \psi_n \tag{2.66}$$

Interaction with light means that the TD perturbation is of the form of an oscillating electric field, and the interaction operator is described as:

$$\hat{V}(t) = \sum e^{-i\omega t} \hat{Q} F \tag{2.67}$$

where ω and F denotes the frequency and strength of the field, respectively, and $\hat{Q}$ is the perturbation operator, which describes the nature of the perturbation.

The expectation value of any operator $\hat{P}$ can be expanded in order of the perturbations $\hat{Q}$ and $\hat{R}$ as:

$$\langle \hat{P} \rangle(t) = \langle \hat{P} \rangle + \sum_k e^{-i\omega_k t} \langle\langle \hat{P}; \hat{Q} \rangle\rangle_{\omega_k} F_k + \sum_{k,l} e^{-i(\omega_k + \omega_l)t} \langle\langle \hat{P}; \hat{Q}, \hat{R} \rangle\rangle_{\omega_k, \omega_l} F_k F_l \tag{2.68}$$

The first term is then the static expectation value whilst the following are the *linear* and *quadratic* responses.[111] As the operators $\hat{P}$, $\hat{Q}$ and $\hat{R}$ can be any operators, a large selection of properties can be calculated. In terms of photochemistry however, we deal with the electric dipole moment operator, $\hat{\mu}$. When $\hat{P} = \hat{Q} = \hat{R} = \hat{\mu}$ the linear response term, $\langle\langle \mu; \mu \rangle\rangle_\omega$, term is the frequency dependent polarisability, α_ω, which gives information on OPA transitions. In the energy representation it has the form:

$$\langle\langle \mu_a; \mu_b \rangle\rangle_\omega = -\hat{\Pi}^{ab} \sum_{k \neq 0} \frac{\langle \psi_k | \hat{\mu}_a | \psi_0 \rangle \langle \psi_0 | \hat{\mu}_b | \psi_k \rangle}{\omega - \omega_k} \tag{2.69}$$

where $\hat{\Pi}^{ab} f_{ab} = f_{ab} + f_{ba}$. The poles correspond to excitation energies and the residues gives OPA transition moments (and hence subsequently oscillator strengths) between the reference state ψ_0 and excited states ψ_k.

Analogously the quadratic response term, $\langle\langle \mu;\mu,\mu\rangle\rangle_{\omega}$, corresponds to two dipole perturbations, one of frequency ω_1 and one of frequency ω_2:

$$\langle\langle \mu_a;\mu_b,\mu_c\rangle\rangle_{\omega_1,\omega_2} = -\sum \hat{\Pi}^{abc} \sum_{k,l\neq 0} \frac{\langle\psi_0|\hat{\mu}_a|\psi_k\rangle\langle\psi_k|\hat{\mu}_b|\psi_l\rangle\langle\psi_l|\hat{\mu}_c|\psi_0\rangle}{(\omega_k-\omega_1+\omega_2)(\omega_k-\omega_2)} \tag{2.70}$$

The latter describes properties related to the first hyperpolarisability, β. It can involve several different frequencies, depending on the property of interest, such as $\beta_{-2\omega;\omega,\omega}$, which determines the response due to the second harmonic generation (SHG) of a photon.

It is expected that even higher order response terms have to be evaluated in order to estimate the TPA response. However, if there is a resonant absorption of two photons of equal frequency, the residues of 2.70 is in fact identical to the TPA transition moment tensor, $M_{\alpha\beta}$ between states ψ_0 and ψ_l through an intermediate state, represented by ψ_k,

$$M_{\alpha\beta} = \sum_k \frac{\langle\psi_0|\hat{\mu}_\alpha|\psi_k\rangle\langle\psi_k|\hat{\mu}_\beta|\psi_l\rangle}{\omega_k-\omega} + \frac{\langle\psi_0|\hat{\mu}_\beta|\psi_k\rangle\langle\psi_k|\hat{\mu}_\alpha|\psi_l\rangle}{\omega_k-\omega} \tag{2.71}$$

where α and β refers to the cartesian coordinates of the TPA tensor. As the intermediate state, ψ_k, is a linear combination of all real eigenstates of the system, this expression for the TPA transition moment might look like a tedious summation to carry out computationally. It will become apparent however, that the machinery of modern response theory evaluates this quantity without the need to carry out the summation.

2.5.2 Photochemistry of Heteroaromatics

The photochemistry of heteroaromatics in the UV-visible region is generally dominated by electronic transitions between occupied and un-occupied molecular orbitals of π-character of the aromatic system; so-called $\pi-\pi^*$ transitions. As the heteroatoms involved also commonly have lone pair electrons that are not part of the aromatic system, these can also take part in electronic transitions, which are then referred to as $n-\pi^*$ character transitions.[1] Modern photochemical studies normally

refer to this terminology when describing the photochemistry of these systems. However, molecular systems that have been known for a long time sometimes uses older terminology. This is especially true for systems where the older nomenclature can shed light on the specific nature of the absorption, which is the case for molecules in the porphyrin family. Porphyrin-type molecules, with a tetra-pyrrole moiety as its core, has been known for its rich photochemistry for decades. In the 1960s Martin Goutermann used the frontier molecular orbitals to draw conclusions on the appearance of the absorption spectra in his Gouterman Four Orbital (GFO) model.[64, 112] In general absorption spectra of porphyrin-type molecules with D_{2h} symmetry two dominant regions of absorption are commonly observed, one in the 200-350 nm region and one at 470-570 nm regions. The shorter wavelength transitions are in the so called Soret-region whilst the transitions into the longer wavelength region are termed Q-region transitions. Any absorption at shorter wavelengths than these are normally weak so-called N-type transitions that are not caused by transitions amongst the frontier orbitals. According to the GFO model the two dominant regions of absorption are caused by transitions that arise through mixing of a limited number of configurations consisting of the HOMO-1, HOMO, LUMO and LUMO+1 orbitals. In the porphyrin molecule the transition moments between the orbitals involved, which are of equal and opposite direction due to degeneracy of the LUMO and LUMO+1 orbitals, lead to a cancellation in the two transitions (to the 1^1B_{2u} and 1^1B_{3u} states) of the Q-band in the visible region and a strengthening in the two transitions of the Soret-band (to the 2^1B_{2u} and 2^1B_{3u} states) in the visible region. This is not necessarily the case in all related systems however. An example output from a frontier orbital calculation of the orbitals involved in the Gouterman model are presented in Figure 2.6, where the expansion coefficients indicate orbital importance in the first (Q-type) transitions for the porphyrin and its reduced isomer porphycene at the Time-Dependent ωB97XD//TZVP level of theory.

The GFO model was developed with the porphyrin core in mind and there are plenty of theoretical results that support the use of the GFO model for the assignment of the transitions into these regions in porphyrins. [46] It might however not apply for all related isomers of the family. In the case of the porphycene macrocycle for example, the degeneracy of the LUMO and LUMO+1 is lifted as the symmetry of the aromatic system is lowered to C_{2h}, as illustrated in Figure 2.6. This leads to a

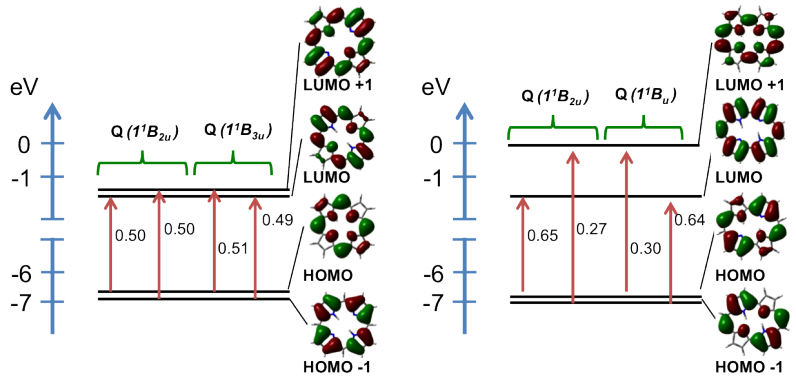

Figure 2.6: Frontier ωB97XD//TZVP orbitals of porphyrin (left) and porphycene (right) involved in the first two transitions into the Q-band. The calculated orbitals illustrate the Gouterman-model well, and can be used to characterise low energy states of porphyrin-type macrocycles.

significant increase in the oscillator strength of transitions to the Q-type states, as there is no longer a cancellation of transition moments. In experimental data the Soret-band of the porphycene monomer is generally comparable to that of porphyrin. [113, 114]. However, there is some debate whether the Gouterman model is in fact useful with regards to the analysis of the porphycene system in more detail. It has been suggested that the model needs to be expanded and involve further orbitals in order to describe higher lying states in the porphycene macrocycle. The presence of so called N-type transitions, involving lower lying molecular orbitals as well as the Gouterman set, has been shown in theoretical studies to be incorporated to a large degree into the Soret-band.[115, 116]

Just like for the porphyrin macrocycle, the transitions in indole-type systems have also been investigated for a long time, and already back in the 1940s Platt introduced a nomenclature for describing the character of this set of systems[117]. His work was based on what was known as the free-electron orbital model, and essentially boils down to a description of the $\pi - \pi^*$ states with respect to the frontier orbitals. The two lowest lying $\pi - \pi^*$ states of indole are characterised depending on whether the state originates from excitation from the HOMO, the so called ^1L_a-state, or from the HOMO-1, the ^1L_b-state.

2.6 Computational Photochemistry

In this section, the computational methods introduced earlier will be evaluated with respect to their photochemical applications. Earlier on in this chapter the concept of response theory was introduced as a tool for evaluating transition moments between photochemical states of a molecular system. The linear and quadratic response functions, $\langle\langle \mu;\mu \rangle\rangle_\omega$ and $\langle\langle \mu;\mu,\mu \rangle\rangle_\omega$, were introduced as they provide information on the OPA and TPA transition moments, respectively. These response functions are sometimes referred to as *polarisation propagators* (if the operator, in this case μ, is number conserving). So far the properties provided by these propagator functions are in principle *exact*, meaning that they will deal with all possible excitation and de-excitation amplitudes. This essentially means a "full-CI"-type treatment of the photochemical transition. As in the case of CI calculations, this is a task that very quickly becomes expensive, from a computational point of view, and the method needs to be approximated. The simplest method of approximation is to truncate the propagator to only include single excitations and de-excitations. This approximation and is commonly referred to the *Random Phase Approximation* (RPA) for HF or DFT references, or the *Equation of Motion* (EOM) approximation, if a CC reference wavefunction is used.[118, 119] Splitting the excitations from de-excitations allows the poles of the linear response function to be written in matrix form: [120]

$$\begin{bmatrix} A & B \\ B & A \end{bmatrix} \begin{pmatrix} X \\ Y \end{pmatrix} = \omega \begin{bmatrix} 1 & 0 \\ 0 & -1 \end{bmatrix} \begin{pmatrix} X \\ Y \end{pmatrix} \tag{2.72}$$

where the A matrix consists of energy differences between the orbitals as well as an exchange-type matrix that couples occupied and un-occupied molecular orbitals, the B matrix is a coupling matrix and the vector (X,Y) contains the MO coefficients. By writing the new excited state in terms of new configurations obtained by substituting an electron in an occupied orbital for an electron in a virtual one, each state is then written as a linear combination of all these configurations with the expansion coefficients being the unknowns. This means that the method is very efficient as there is no need to construct all the excited states explicitly, such as in the sum-over-state expressions for the response functions in Equation 2.69.

The RPA can be used with a number of references, including HF (in TD-HF),

DFT (in TD-DFT) and CC wavefunctions (EOM-CC).[121–124] If the RPA is to be improved however, one strategy is to look at the expansion of the propagator as a function of the *fluctuation potential*. This potential is the difference between the exact potential for electron-electron repulsion and the HF potential. It is then realised that the RPA is equivalent to truncating this expansion at first order, incorporating only single excitations and de-excitations. By including higher order terms the accuracy of the properties may improve as higher order excitations and de-excitations contribute to the expression. For CCSD reference wavefunctions for example, the propagator expansion is truncated at second order. The expansion in terms of the fluctuation potential is also a useful tool when dealing with coupled cluster excitations as it provides a way of systematically improving excitation energies using a coupled cluster wave function. [125] This approach introduces a hierarchal ladder that extends the improvements to include not only ground state energies but also excitation energies and transition moments. The rungs of the ladder, within a specific set of basis functions, in order of improvement is: CCSD - CCDR(3)/CCSD(T) - CCSDT. Note here that CCSD(T) is for use on ground state wavefunctions only, as it already contains perturbative CC poles as well as HF poles, and therefore is unsuitable as a response reference. This approach introduces a systematic convergence in not only ground state energies but also excitation energies and transition moments as a function of both basis and electron space of the correlated wavefunction.

For molecules the size of large heteroaromatics, such as porphyrins, the use of TD-DFT is crucial in studies such as those in this thesis. With regards to which exchange-correlation functionals that are suitable, there is unfortunately no corresponding Jabos-ladder type argument in the evaluation of excited states using TD-DFT. Being a variational method based on ground state density, information on the excited state is very much dependent on the specific state investigated and its relation to the ground state. Even the very popular B3LYP functional has been shown to behave better than more recent methods including the CC2 level, for localised states without charge transfer character, in nucleic acid bases.[126]

The central issue that DFT is struggling with when calculating photochemistry is the presence of charge transfer characters in some excited states. A correct description of transitions to these states requires the use of long-range corrected (LC) functionals that can deal with small orbital overlap .[127–129] The CAM-B3LYP functional of

Yanai et al. adds LC through a Coloumb attenuated method.[130] This functional is comparable to B3LYP in many properties, without any additional computational cost, but crucially out-performs with respect to polarisabilities and charge transfer excitation energies.[131] The long-range behaviour of the CAM-B3LYP has also been shown to affect the description of non-linear optical effects, such as TPA, and benchmark studies have shown it to behave as well as CC methods for small molecules. This opens up for accurate TPA calculations of molecules of considerable size. [132]

Double-hybrids, such as Grimme's B2-PLYP functional also behave very well for excited states as well as ground states, and produce excellent excitation energies and state orderings for the first few states of organic chromophores. They do however fail to describe transition energies for CT states, where LC functionals such as CAM-B3LYP still preforms the best. The performance of double hybrids in non-linear absorption studies is not yet known.[133]

The development of analytical derivatives also means that critical points of PESs of the excited states can be evaluated using DFT response theory. As the response is dependent on a good description of the ground state, i.e. a state written as a single Kohn-Sham determinant, it is important to point out that TD-DFT will not be able to describe more than a semi-qualitative picture of points of degeneracy between states with the same spin, such as IC relaxation pathways between PESs. Double-Hybrid functionals have been shown to be marginally better than other functionals when used with response theory to evaluate crossings between states with same spin. This is thought to be due to the fact that the MP2 correlation adds a portion of double excitation correlation.[134] As DFT has the ability to find critical points on triplet ground state surfaces, it can however localise minimum energy ISC crossing points. Hybrid crossing point methods, which combine various levels of theory to make the calculations more effective for large systems, has been developed to locate the geometry of ISC points using DFT. [135]

2.6.1 Excited State Relaxation Pathways

In order to describe such relaxation pathways in general, and evaluate ICs, it is clear that we need to be able to describe situations where more than one determinant can be used to describe the state. Hence methods that incorporate full-CI, such as

CASSCF or RASSCF (for large molecules) are ideal for these situations. Setting the evaluation of critical points to be carried out within the branching space (i.e. applying the constraint that the energy difference between the two surfaces go to zero) means that information on the geometries, and therefore also access to information as to what vibrational modes makes the crossing, can be realised.

Modern computational codes can straightforwardly locate stationary points on a surface, but in the case of two surfaces crossing, the actual crossing point is not a stationary point of either of the surfaces. The intersection seams are of dimension 3N-8 for an N-atom molecule (every point on the seam being a conical intersection geometry). Modern optimisation algorithms optimise to points of zero gradient in this so-called intersection space, generating minimum energy crossing points.[136, 137] These act as photochemical funnels for the reaction in the upper electronic state. It is important to note however that this minimum energy crossing point might not be the only one of importance when it comes to the generalisation of various reaction paths, but a good characterisation of the full seem is crucial. [108] The procedure that is needed to find the minimum energy crossing point is actually fairly straight forward, at least in principle, and involves computing both the energy and its gradient on both surfaces, as well as the non-adiabatic coupling, which essentially describes the extent to which the electronic states are coupled by nuclear motion (i.e., a break-down of the BO approximation discussed earlier).

Multiconfigurational methods are the most common, and appropriate, for the calculations of the IC pathways, as they can handle the multi state character needed near a crossing point. However, as the ubiquitous nature of conical intersections, and their importance in the description of photochemistry, in molecules with biological importance, such as photosensitiser molecules, becomes more evident there is a need to develop methods that can handle systems of a larger size. The use of TD-DFT, which is successful for excited states in the vertical region, in the characterisation of crossing points have been investigated, and has been shown to be of some use for the location of minimum energy crossing points between excited levels (i.e., not with the ground electronic state) They can not yet describe excited state surfaces accurately in general, so care must be taken in their application to problems in reactive photochemistry as opposed to spectroscopy. [138]

2.7 The Presentation of Computational Photochemical Data

In order to compare computational absorption stick-spectra with experimental spectra one can obtain the true vibronic absorption peaks through the calculation of the nuclear wavefunction overlaps. This is a laborious task for large molecules, and a common strategy is to homogeneously add artificial broadening, for example using a Gaussian function. This strategy can greatly aid comparison with experimental data, and has been used when needed for the presentation of results in this thesis.

Results from a linear response calculation, apart from excitation energies, are a set of excitation amplitudes that describes the contribution of a particle-hole pair to the specific transition. In order to analyse the nature of the electronic transitions in detail Natural Transition Orbitals, NTOs, were calculated for each transition. A NTO is a calculated orbital representation of the electronic transition where that transition amplitudes have been reduced to a set of particle-hole amplitudes, in terms of eigenvectors of the transition density matrix, which gives a more intuitive picture of the nature of the transition[139]. The NTO representation of the nature of the excitation is complementary to the response eigenvectors using the Kohn-Sham orbitals but generally gives a more compact representation of the state.

Armed with the knowledge of the underlying theory of photochemical events, as well as the computational methods used to estimate them, we can now move on to the evaluation of their use with respect to heteroaromatics. The starting point is the smaller compounds introduced here, and their absorption as well as ultrafast relaxation pathways.

Chapter 3

Absorption and Relaxation Pathways in Small Heteroaromatics

3.1 Introduction

This thesis is focused around the Jablonski diagram introduced in the Introduction, which is used as a tool describing the flow of energy from irradiation of the molecule to the creation of singlet oxygen through sensitisation. The natural starting point is to focus first on the absorption of light (**C** in Figure 3.1) and evaluate how computational techniques can aid the understanding of these processes. The chapters that follow this one will concentrate mainly on larger macrocyclic heteroaromatics, such as of *porphyrin*-family introduced in the introduction. This is due to the fact that all molecules that are in clinical use as photosensitisers in photodynamic therapy today are macrocycles of this type. [9, 15, 140, 141] A lot can however be learned from studying smaller heteroaromatics, such as indole or pyrrole (Figure 1.1). In fact, as will become clear in this chapter, these compounds have a rich and interesting photochemistry and take part in processes of high importance in their own right.

As mentioned in the introduction heteroaromatic compounds are well know strong absorbers of UV and visible light, and they are also very common building blocks in biology in general. Natures preferred form of storing the genetic code of living beings, nucleic acid bases (Figure 3.2), are important examples but heteroaromatics are also found in amino acid side chains as well as enzyme co-factors. [142, 143] Crucially they

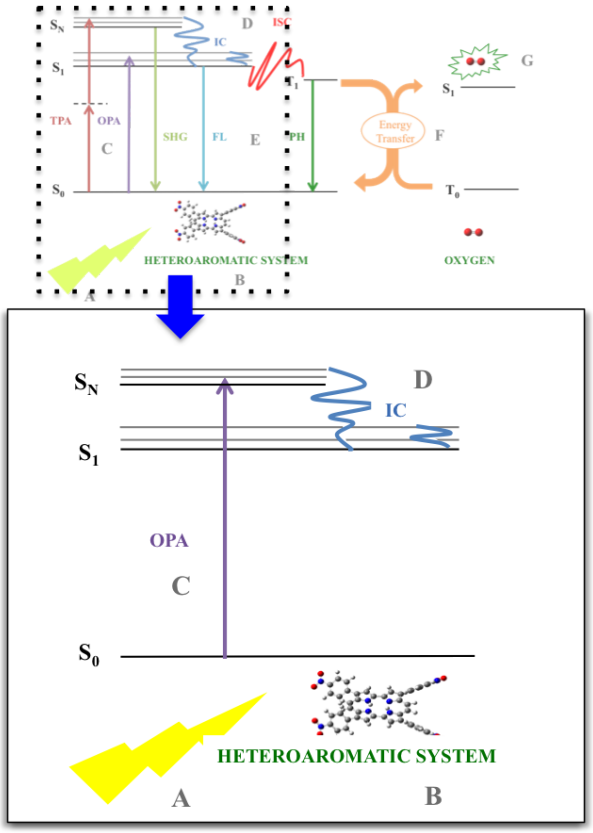

Figure 3.1: The Jablonski diagram for the photosensitisation pathway of PDT that this thesis is centre red on, with the relevant section and processes highlighted. Heteroaromatics have interesting absorption (**C**) and relaxation processes (**D**), which will be the topic of this chapter.

are also present in pigments designed to protect living organisms from the damaging effects of UV light, such as eumelenine (Figure 3.2).[144, 145] The reason for their presence in pigments lies in the fact that, despite their strong absorption in the UV-visible region, these heteroaromatics have very low fluorescence quantum yields in general. This means that the absorbing molecular system spends very little time in its excited state manifold.[6, 8] When the system is in a biological environment a low quantum yield is good news as an excited state is likely to take part in destructive chemical reactions. Photo-stability is clearly a very valuable characteristic and a short-lived excited state rationalises the use of heteroaromatics in UV-protecting pigments as well as the chosen building block for the precious genetic code. In order to provide insight into the photochemistry of these types of compounds excited state relaxation processes (**D** in Figure 3.1) clearly needs to be investigated in addition to absorption characteristics. As the relaxation is happening on such a fast time scale, making experimental analysis very challenging, an input from computational chemists can be crucial.

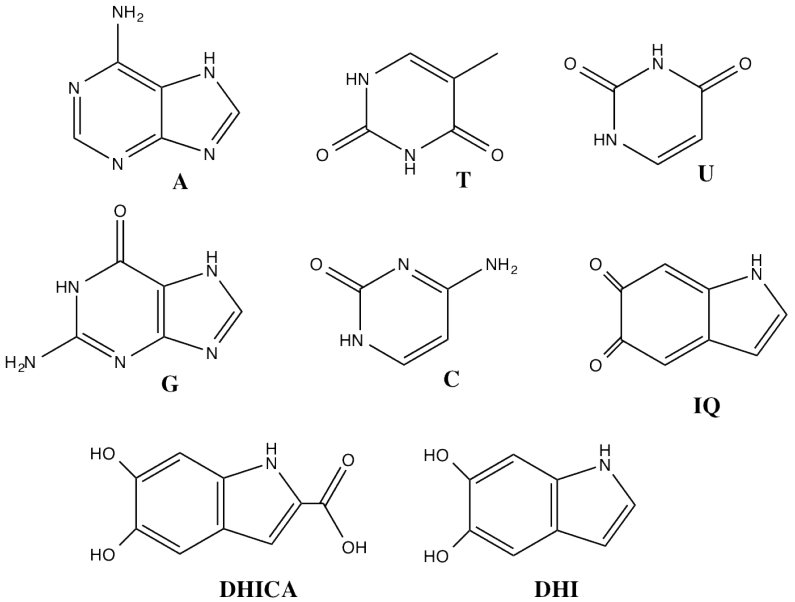

Figure 3.2: Nucleic acid bases Adenine (**A**), Thymine (**T**), Guanine (**G**), Cytosine (**C**) and Uracil (**U**). The three main components of the polymer eumelanine (the most common form of melanin in the human body) are 5,6-dihydroxyindole-2carboxylic acid (**DHICA**), 5,6-dihydroxyindole (**DHI**) and indolequinone (**IQ**)

The work presented in this chapter is all driven by the need for a deeper understanding of the excited states available to these small heteroaromatic molecular structures as well as insights into the dynamics that control their very fast relaxation pathways back to the ground state. Recent advances in the development of very fast laser pulses means that there is an experimental set up available to investigate processes that are as fast as the *ultrafast* relaxation of excited heteroaromatic chromophores. One procedure that has had a rapid rise in popularity, due to its ability to follow the evolution of an excited state, is a so-called *pump-probe* experiment.[65, 146–148] This technique has been been designed so that the molecule is pumped (i.e. excited) with a laser of a set wavelength and then probed using a number of different wavelengths, after a varying time delay (Δt is typically in the order of 10s of fs).[149] This generates a time-resolved photoelectron (TRPE) spectrum that can map the decay of specific states. In combination with computational calculations, these experiments can contribute to the understanding of the behaviour of biologically relevant heteroaromatic chromophores.

Powerful computational methods, using response theory as well as multi reference electronic structure techniques, such as CASSCF, introduced in the Theory section of this thesis, can now be used to investigate both absorption and relaxation characteristics of molecules the size of the systems introduced in Figure 3.2. Especially useful in this regard is the capability of modern computational algorithms to locate minimum energy crossing points along conical intersection seams, and investigating the local topology of the potential energy surface.[104, 107, 150, 151] Even though such calculations are challenging,[152] the output is crucial in helping the interpretation of the TRPE output.

The work discussed in this chapter involves detailed collaboration with experimental groups specialising in time-resolved photoelectron spectra. Experimental studies were carried out by the groups of Dr David Townsend at Heriot Watt University (indole and 5-hydroxyindole) and Dr Vasilios Stavros at Warwick University (imidazole and its methylated derivatives). The relevant experimental data collected by these groups is referenced below as appropriate.

3.2 The excited states of indole and 5-hydroxyindole

When the components of the eumelanine polymer presented in Figure 3.2, which is the main form of melanin pigment in the human body, is looked at more closely, it becomes clear that they share a common motif; the *indole* structure (Figure 3.3). Indole could clearly provide a good first approximation for a study into the absorption and relaxation processes of eumelanine. As both **DHICA** and **DHI** (Figure 3.2) also have a hydroxyl group in the 5-position, an investigation of indole compared with 5-hydroxyindole could shed light into the role of this hydroxyl group in the melanin system.

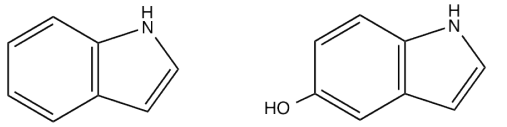

Figure 3.3: Indole and 5-hydroxyindole are good starting motives when investigating the excited state dynamics of the components of eumelanine

The excited states of indole are already well characterised and experiment made in the region of 220 - 285 nm have identified two $\pi\pi^*$ states of A' symmetry, These are traditionally described as being of either ^1L_a or ^1L_b-character.[117], as introduced in the Theoretical Background section. Both the ^1L_a and ^1L_b states are short lived, as can be seen from the lack of vibrational structure in absorption spectra from previous experiments.[153, 154] The short lifetime of the ^1L_a state has been suggested to be due to the fact that the minimum possible being close to a barrier-less path to a conical intersection to the ^1L_b state. There is also evidence of a vibronic band lying very close to the ^1L_b minimum with a curiously short life time, caused by coupling to an additional dissociative electronic state. Put together, these facts all indicate that the presence of an optically dark $\pi\sigma^*$ state. A $\pi\sigma^*$ state is dissociative along the coordinate aligned with the anti-bonding σ^* orbital between the H atom and the heteroatom, here N.

Dissociative states of $\pi\sigma^*$ character in heteroaromatic molecular systems have been under a lot of investigations, theoretical as well as experimental, in recent years

and are now recognised as a very common feature controlling excited state relaxation dynamics of heteroaromatics.[155–157] In indole the $\pi\sigma^*$ state is of A'' symmetry with significant Rydberg character. Sobolewski and Domcke have carried out extensive calculations on indole, and suggest that the $\pi\pi^*$ states couple with the $\pi\sigma^*$ along the N-H stretching coordinate.[158] They also found a conical intersection connecting the $\pi\sigma^*$ state with the ground state at longer N-H bond extensions. The latter provides a fast and efficient route to remove excess UV energy non-radiatively.

This collaborative section evaluates the role of the $\pi\sigma^*$ state in the relaxation dynamics of the ^1L_a state of indole and 5-hydroxyindole, estimating whether this state plays a role in its very fast decay path, and the effect of 5-hydroxylation on these dynamics. The tools used were TRPE spectroscopy in conjunction with high level CC response theory and multi-reference computational calculations.

3.2.1 Optimised Geometries

In order to evaluate accurate excited states, and their properties, of indole and 5-hydroxyindole the molecules were first optimised on their ground state potential energy surface using DFT. For organic molecules that have a well defined ground state determinant (i.e. no apparent static correlation issues) DFT is an advantageous method for optimisation of molecules of this size.[159] This is especially true when using the B3LYP hybrid functional, as introduced in the Theory section of this thesis, which has become the go-to functional for ground state potentials of organic systems. At each B3LYP/aug-cc-pVDZ ground state stationary point found analytical hessians were computed to evaluate each point as a minimum. Structures are presented in Figure 3.4

Both indole and 5-hydroxyindole are planar aromatic systems, with the N-H bond pointing orthogonally out from the π-system, of which the nitrogen lone pair takes part. The 5-hydroxyl substituent have minima where the O-H bond is in the plane of the π system. All aromatic bonds are kept within 0.01 Å upon hydroxylation, indicating that the functionality has little effect on the aromaticity of the π-system in the ground state.

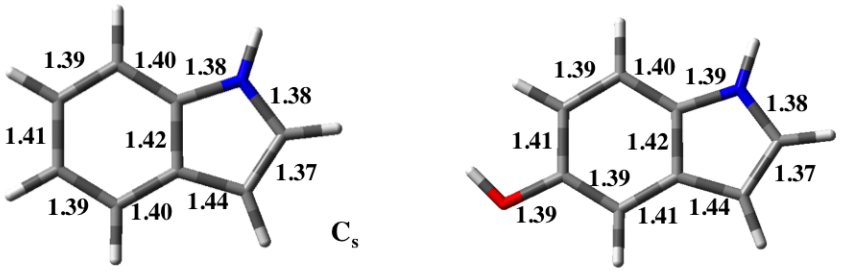

indole **5-hydroxyindole**

Figure 3.4: Optimised ground state minimum geometries of the indole and 5-hydroxyindole molecular structures, with bond lengths reported in Ångström.

3.2.2 Vertical UV absorption spectra

Coupled Cluster and DFT with its linear response (LR) was used to calculate both excitation energies and oscillator strengths. In this work the CC expansion was truncated at the CCSD level, meaning the effect of both single and double excitations on the ground state were included. The CCDR(3) method was also used to investigate the effect of triple excitations by adding a non-iterative correction in order to make excitation energies correct to 3rd order in the fluctuation potential.

The vertical states and their oscillator strengths for indole and 5-hydroxyindole were calculated at the TD-DFT, LR-CCSD and CCDR(3) levels of theory, using the Gaussian[160] and Dalton[161] suites. An aug-cc-pVDZ basis set was used as considered necessary in order to capture states with large Rydberg-type character, such as the $\pi\sigma^*$ state of indole. The CC and DFT response results were in good agreement with each other, and the CC set of absorption energies and oscillator strengths are presented in Table 3.1 Both state ordering and relative state ordering are agreeing well with previous calculations [162, 163].

For each excited state calculated, the orbitals involved in the transitions were plotted along with their response eigenvector coefficients, ${}^{R}c_i$, in Figure 3.13. The coefficients indicate the importance of the pictured transition in the right hand eigenvector of the state.[124] These orbitals help to show the general character of each state, and also aid the interpretation of the experimental output from the TRPE experiment as discussed in the following section. Here it is for example clear that the

Table 3.1: Resulting optical parameters for indole and 5-hydroxyindole at the linear response CCSD and CC(3) levels of theory, using the aug-cc-pVDZ basis set

	Indole			5-hydroxyindole		
State	CCSD	CCR(3)	f	CCSD	CCR(3)	f
$^1A'(^1L_b)$	4.823	4.762	0.0280	4.539	4.458	0.0636
$^1A'(^1L_a)$	5.241	5.117	0.1018	5.204	5.087	0.1223
$^1A''(^1\pi\sigma^*_{NH})$	5.046	5.017	0.0022	4.945	4.930	0.0000
$^1A''(^1\pi\sigma^*_{OH})$	...	...	...	5.063	5.045	0.0003

$^1\pi\sigma^*$ valence states are highly mixed with a diffuse state of Rydberg-type.

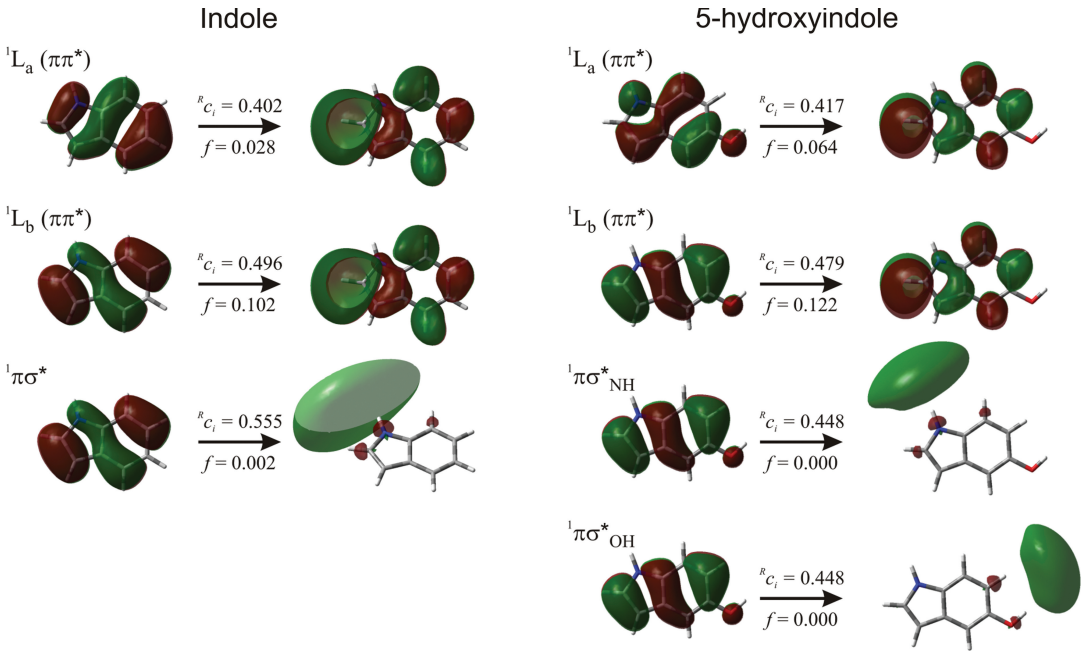

Figure 3.5: Orbitals involved in the transition to the ^1L_a, ^1L_b and $^1\pi\sigma^*$ states of indole and 5-hydroxyindole. Their their associated LR-CCSD amplitudes, ^Rc_i, and oscillator strengths, f, are also indicated

In Figure 3.6 the experimental gas-phase UV absorption spectra for both indole (dashed line) and 5-hydroxyindole (solid line) is presented. There is a clear agreement between experiment and theory in the effect of hydroxylation. Whilst the $^1\pi\sigma^*_{NH}$ and ^1L_a state stay in a relatively similar position energetically upon hydroxylation, the

^1L_b state is shifted by more than 0.3 eV in the calculated spectrum. Looking at the experimental data the broad peaks that correspond to the ^1L_a state, between 220 nm and 280 nm, are both in the same position despite hydroxylation. The ^1L_b absorption on the other hand is both red-shifted, as predicted in the calculations, as well as broadened. It is worth to note here that the ^1L_b state origin has been shown previously to be at 283.8 nm for indole[164–166] and 303.9 nm for 5-hydroxyindole[163, 167]. The red shift is clearly much larger in the experiments presented here. The fact that the absorption cell used in the experiment was at a high temperature, creating hot-bands during the measurement, explains this effect.

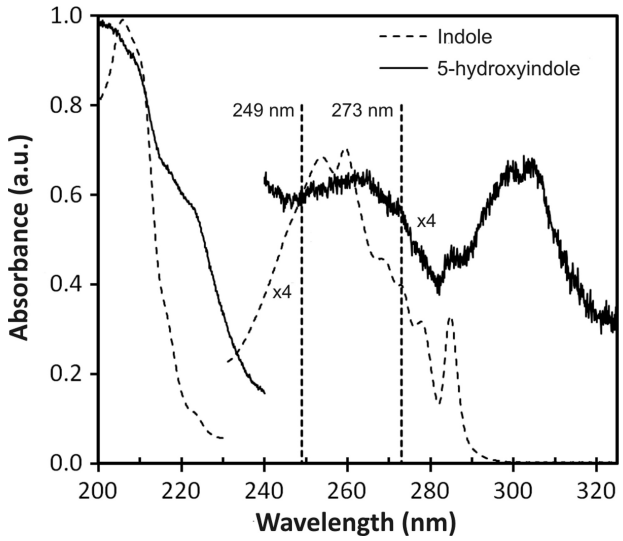

Figure 3.6: Experimental UV absorption spectrum for indole (dashed line) and 5-hydroxyindole (solid line) in the gas phase. The two excitation wavelengths for the pump-probe experiment (249 nm and 273 nm) are also indicated. This figure is reproduced from [168].

3.2.3 Excited state relaxation dynamics

In order to probe the landscape of the excited states of indole and 5-hydroxyindole and help in the interpretation of the experimental pump-probe outputs, rigid scans were run along important bond dissociation coordinates. Scans such as these illustrate cut-outs of the potential energy surfaces along coordinates that are of significance. Here

both the N-H bonds and the O-H bond were probed, in order to estimate the position of the $^1\pi\sigma^*$ states as well as any barriers separating the Franck-Condon region from reaction channels along this coordinate. The ground state as well as the ^1L_a, ^1L_b and $^1\pi\sigma^*$ states were all investigated along the N-H coordinate for indole and along the N-H and O-H coordinate for 5-hydroxyindole using CCSD response theory. Figure 3.7 shows the resulting plots that will be used as a guide to help interpret the output from the TRPE experiment

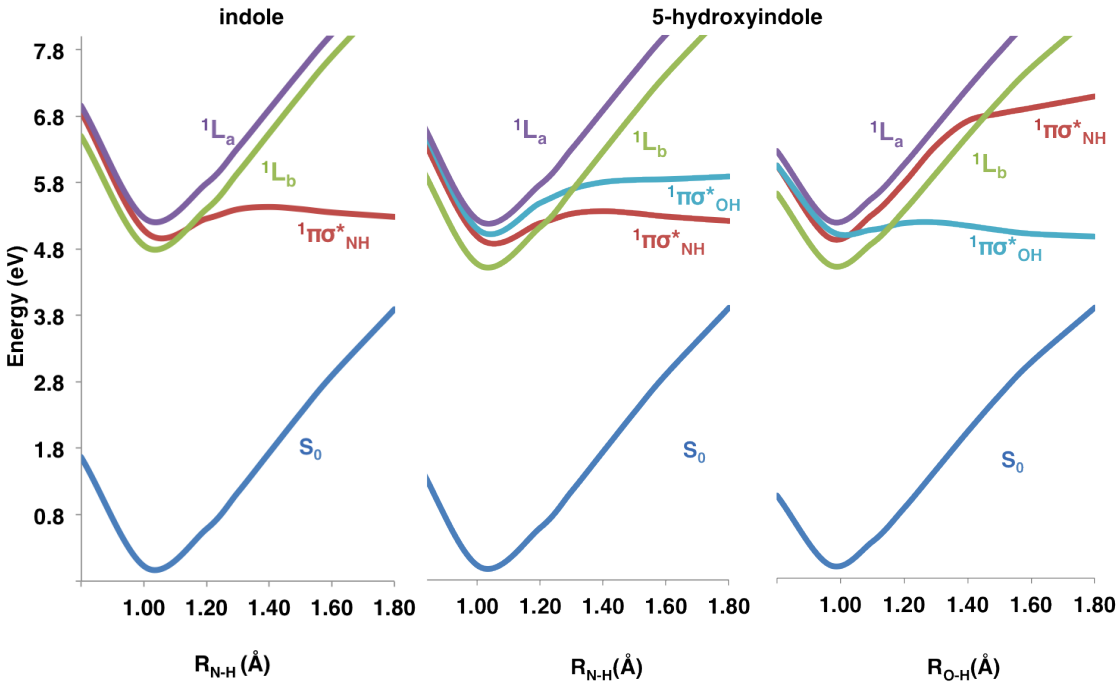

Figure 3.7: Potential energy plots along the N-H coordinate for indole and along the N-H and O-H coordinates for 5-hydroxyindole

The pump-probe experiment was carried out by members the Townsend research group at Heriot Watt University and involved two excitation wavelengths, 249 and 273 nm respectively for indole and 5-hydroxyindole. Indole was then probed at 300 nm whilst 5-hydroxyindole was probed at 320 nm. Combined, these values are larger than the vertical ionisation energies for both molecules, which are 7.90 eV (157 nm) for indole and 7.72 eV (160 nm) for 5-hydroxyindole. The pump-probe delay was varied within a 50 ps experimental window.

The output from the TRPE experiments result in the estimation of time delay constants, τ. These essentially indicate mean life-time associated with the different processes that are taking place. In Figure 3.8 the time constants for indole and 5-hydroxyindole, excited at 249 nm (**(a)** and **(c)**) and 273 nm (**(b)** and **(d)**), are presented. These constants, and their spectra, were determined using a standard fitting procedure as described in Ref [169]. The fitted relative amplitudes of the time constants are presented as a function of the electron kinetic energy, which results in a set of decay associated spectra, DAS. Even though the time constants themselves have a numerical uncertainty of $\pm 20\%$, the advantage of using TRPE lies in the comparison of the *relative* amplitudes of the time constants in the DAS with each other. This provides a way to resolve processes which occur on similar timescales from each other, which is very useful as it means the states, and their dynamics, can be evaluated individually. The three components of the decay process determined from this data set were τ_1<100 fs and $\tau_2 = 0.7$ - 1.4 ps as well as τ_3, which represent an extremely long-lived signal.

Excitation of indole at 249 nm wavelength has been shown previously to populate the ^1L_a state exclusively.[170–172] In the region of 0.6 to 1.0 eV in the DAS of indole, (excited at 249 nm **(a)** in Figure 3.8), there is a large positive amplitude for τ_1 that corresponds to the decay of the initial ^1L_a state. Looking at the 0.1 - 0.6 eV region for the same time constant there is an onset of a negative amplitude signal, indicating population of a new state. Below 0.25 eV the signal has good overlap with the τ_3 time constant which originates from the ^1L_b state. The reason this time constant can be associated with the ^1L_b state is clear from earlier theoretical work[155, 158, 162] as well as the potential energy profiles in Figure 3.7. As indicated in the indole plot, the ^1L_a is strongly bound along the N-H coordinate, meaning that decay is not likely to occur through N-H bond fission as previously suggested.[173] In the 0.25 - 0.6 eV energy region of τ_1 the signal does not mach τ_3, but instead overlaps in both shape and amplitude with the 0.7 - 1.4 ps time constant, τ_2. The signature is suggested to correspond to the $^1\pi\sigma^*$ state, as it has been implicated in previous calculations and experiments.[155, 174] It is also worth to note that this signature has no initial population, but competes with τ_3 as a relaxation pathway for the initially populated ^1L_a state. At 0.7 ps the lifetime of the $^1\pi\sigma^*$ state is relatively long. But a look at the energy profiles along the N-H coordinate in Figure 3.7 seems to indicate that the

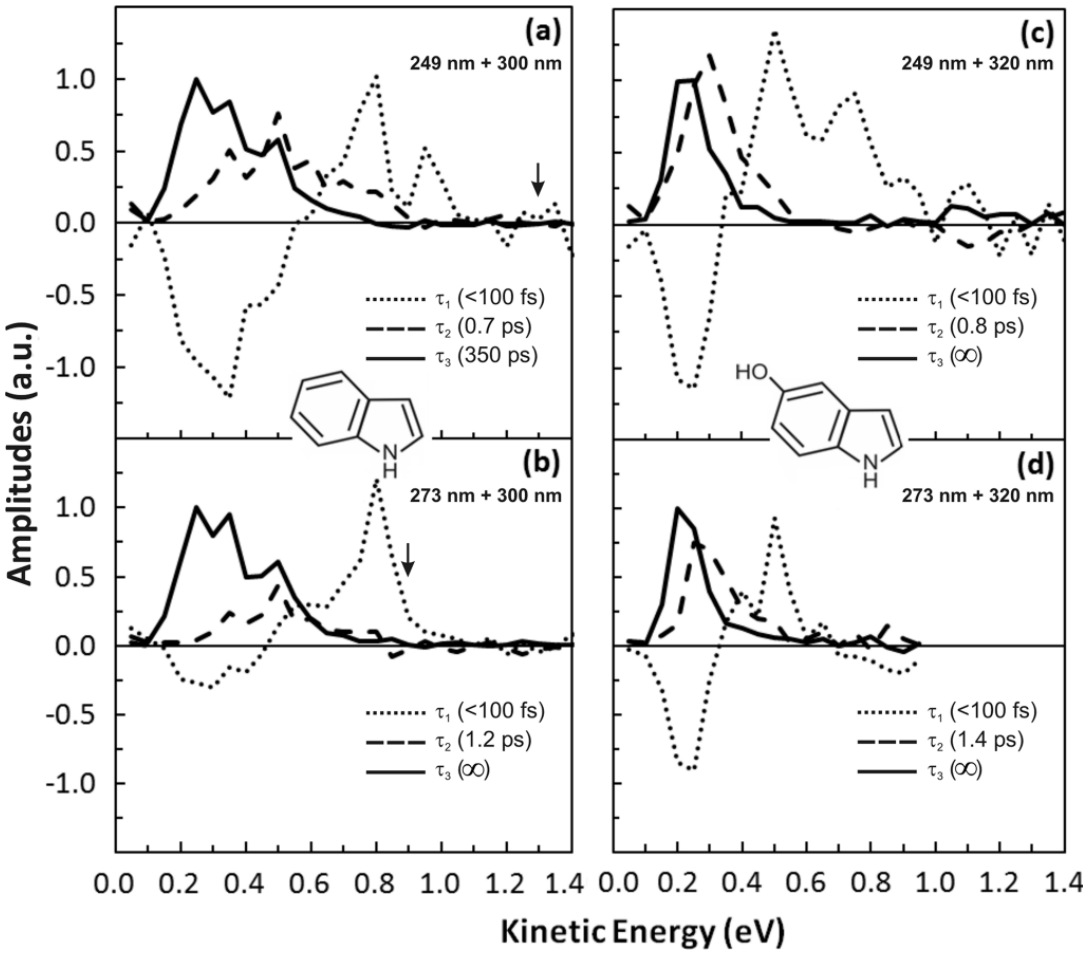

Figure 3.8: Decay associated spectra (DAS) for indole, (a) and (b), and 5-hydroxyindole (c) and (d). The time constants are all fitted to each other, where the maximum amplitude of τ_3 is set to 1 and the other amplitudes are scaled relative to this. Reproduced from [168].

crossing takes place in the vicinity of the small barrier at 1.35 Å, which explains the long-lived nature of the state.

The DAS of indole excited at 273 nm shows very similar profiles to the 249 nm excited signatures, with initial population into the ^1L_a state, followed by a competing relaxation into either the ^1L_b or the $^1\pi\sigma^*$ state, all at the same electron kinetic energies. Curiously, the time constant for the $^1\pi\sigma^*$ state, τ_2, is significantly longer than at the higher energy excitation (1.2 ps vs. 0.7 ps). As the excitation energy is lower than before the $^1\pi\sigma^*$ state is unlikely to be able to cross the barrier in order to access the decay channel to the S_0 ground state (at the elongated N-H bond). A different vibrational mode must therefore be involved in this decay. We were however unable to locate such a crossing and it remains an open question.

So, as a summary, the experiments at 249 nm and 273 nm excitation wavelength suggests that the dynamics of indole, after excitation into the ^1L_a state, is dominated by rapid relaxation through non-adiabatic coupling to both the ^1L_b state and the optically dark $^1\pi\sigma^*$ state.

The location and nature of these crossing points were then investigated using CASSCF calculations, as neither DFT nor CC response methods are suitable for the construction of qualitatively correct wave functions in areas of non-adiabatic coupling between ground and excited states (as in the case of the S_0 and $^1\pi\sigma^*$ state crossing). The active space was constructed of 12 electrons in 11 orbitals, and included 6 π orbitals as well as four π^* and one σ^*, to capture the character of the states of interest. Two issues are important to point out before looking into the CASSCF results. First; the ordering of the first $^1\pi\pi^*$ states, corresponding to the ^1L_a and ^1L_b states, is highly sensitive to dynamical correlation. As CASSCF only incorporates dynamical correlation between the electrons included in the active space care must be taken when evaluating energetics of the states. Second; as soon as the geometries start to distort, in areas of the excited state surfaces removed from the Franck-Condon region, the labels ^1L_a and ^1L_b lose their actual meaning. Conical intersection searches were carried out for crossings of the $^1\pi\pi^*$ states, the $^1\pi\pi^*$ / $^1\pi\sigma^*$ states and the $^1\pi\sigma^*$ / ground (S_0) state, using a 6-31+G(d) basis. Minimum energy conical intersections were found along the seam of intersection between all three pairs of states, and their branching space vectors, the gradient difference (GD) and derivative coupling (DC) vectors, are illustrated in Figure 3.9.

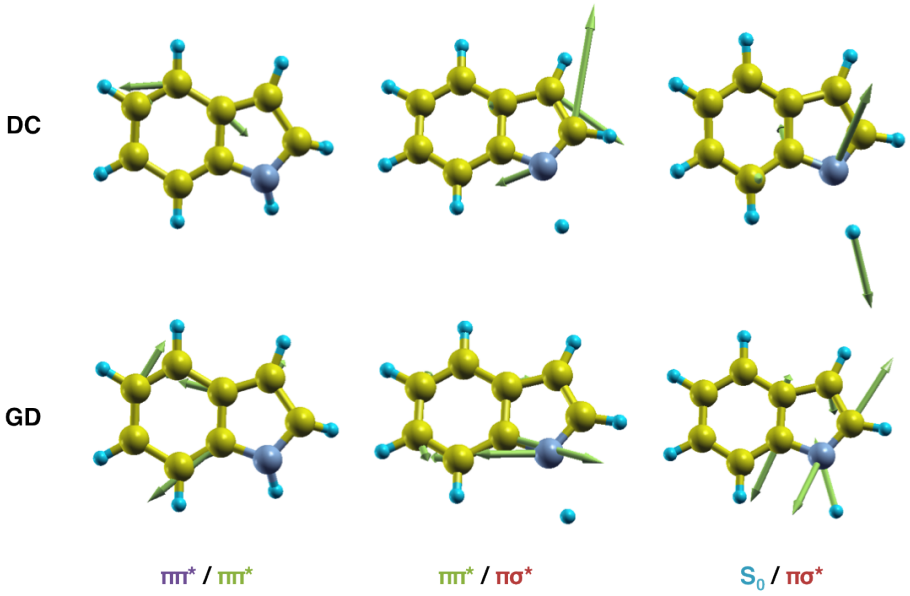

Figure 3.9: Derivative coupling (DC) and gradient difference (GD) vectors for each crossing point in the indole CASSCF calculation.

The crossing between the two $^1\pi\pi^*$ states does not occur along the N-H dissociation coordinate, but involves out-of-plane puckering by the N atom as well as N-C_2 bond stretching. This active space is similar to previous theoretical work.[154] As expected from previous work on $^1\pi\sigma^*$ states the crossing between the $^1\pi\sigma^*$ and the ground state is found at an elongated N-H bond, at 1.8 Å.[155, 158, 162] The $^1\pi\pi^*$ / $^1\pi\sigma^*$ crossing is located at a 1.2 Å N-H bond distance and involves in-plane movement in the N-C_2 bond as well as bond contraction between the N and the ring-fused C atom.

With regards to the effect of 5-hydroxylation on the relaxation dynamics of indole, the DAS signatures in Figure 3.8 at 249 nm (**(c)**) and 273 nm (**(c)**) it is clear that all time constant amplitudes are found at the same kinetic energies as in indole. The relative amplitudes also show that there are no competing pathways involved that could be due to coupling to any new states. The OH $^1\pi\sigma^*$ state does not interact with the states that were initially populated. These results can be rationalised when looking at the orbitals involved in the transitions (some of which are presented in Figure 3.13), as it becomes evident that the O-H anti-bonding set is a spectator in

the description of these states. The core indole moiety can therefore be postulated to be the crucial component that controls the excited state dynamics of the eumelanine complex.

3.3 The excited states of imidazole and its methylated derivatives

The $^1\pi\sigma^*$ state, as introduced in the previous section on indole, has been the topic of many studies, both theoretical and experimental, in recent years. The reason for this interest is the realisation that this state might be the trigger for the ultrafast decay that control the excited state dynamics of heteroaromatic compounds, and thereby contributing to the photo stability of the bimolecular building blocks that incorporate the heteroaromatic motif. [155–157, 175]

One interesting viewpoint on this state and its role in excited state dynamics is the efficiency by which it couples to the ground, S_0, state and to nearby $^1\pi\pi^*$ states. An evaluation of the coupling efficiency as a function of molecular structure could not only contribute to the fundamental understanding of the dynamics of these states, but also shed new light into how structure can control excited state dynamics of this important set of bimolecular building blocks.

Using a pump-probe set-up in combination with a velocity map imaging (VMI) device is one way of targeting the dynamics of the $^1\pi\sigma^*$ state.[176, 177] The incorporation of the VMI component stems from a set up that involves excitation of the system to induce photo fragmentation along a dissociative coordinate such as that of a $^1\pi\sigma^*$ state. The fragments produced by the photo fragmentation are accelerated using electrostatic lenses towards a detector that will register not only a signal that is dependent on time but also on kinetic energy. As a $^1\pi\sigma^*$ state is dissociative in character along the X-H bond (where X is any heteroatom) a measurement of the resulting H^+ ions and their kinetic energy can give an indication on the relaxation dynamics that were involved in the creation of the fragment. The general idea is that efficient coupling between the $^1\pi\sigma^*$ and the S_0 state leads to a molecule in a vibrationally hot S_0 state. Any H-atom dissociation then happens through statistical unimolecular decay, leading to H^+ ions of comparatively LOW kinetic energy. On

the other hand, if the coupling between the states is less efficient, the H-atom will dissociate directly from the $^1\pi\sigma^*$ state, generating H^+ ions of HIGH kinetic energy. Theoretical calculations as to the actual position of the states involved in the specific molecular system will contribute to the understanding of the pump-probe VMI experiments.

This study set out to investigate the dynamics of the core building blocks of the genetic material. Realising that both adenine and guanine (**(A)** and **(G)** in Figure 3.2) contain an imidazole component provides a starting point. This molecule is of an ideal size to investigate structure/excited state dynamics relationships. Previous calculations on imidazole by Barbatti *et al.* [178] has shown that the crossing between the $2^1A'$ ($^1\pi\pi^*$) and the $1^1A''$ ($^1\pi\sigma^*$) in imidazole is mediated by motion out of the plane of the aromatic system. We therefore set out to investigate the effect on the excited state dynamics of imidazole as a function of methylation of the ring. The systems are pictured in Figure 3.10. As more bulky groups are added the access to the out-of-plane modes are expected to be impaired, and so the efficiency of the $^1\pi\pi^*/^1\pi\sigma^*$ coupling can be evaluated at the same time as the $^1\pi\sigma^*/S_0$ dynamics.

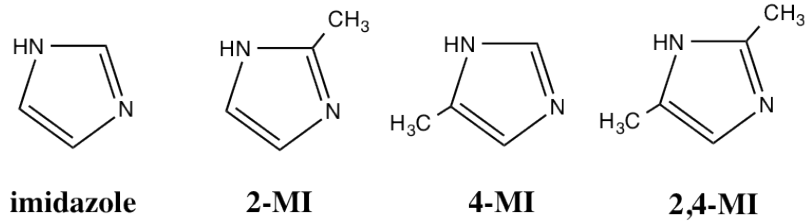

Figure 3.10: The series of methylated imidazole structures investigated here; imidazole, 2-methylimidazole (2-MI), 4-imidazole (4-MI) and 2,4-dimethylimidazole(2,4-MI)

3.3.1 Optimised Geometries

The series of imidazole and its methylated derivatives were first optimised on their ground state potential energy surface using DFT with the B3LYP functional and the 6-31G* set of basis functions. Analytical Hessians were estimated at each stationary point found, in order to confirm minimum energy geometries. The optimised struc-

Table 3.2: High kinetic energy time constants, τ_H, and low kinetic energy time constants, τ_L, imidazole, 2-MI, 4-MI and 2,4-MI

	Time constants / fs	
Molecules	τ_H	τ_L
imidazole	78 ± 37	163 ± 50
2-methylimidazole	131 ± 16	305 ± 57
4-methylimidazole	185 ± 37	334 ± 59
2,4-methyl imidazole	139 ± 56	250 ± 105

tures are presented in Figure 3.11. The effect of methylation on the ground state geometry is minimal, and all aromatic π-bonds stay within 0.01 Å.

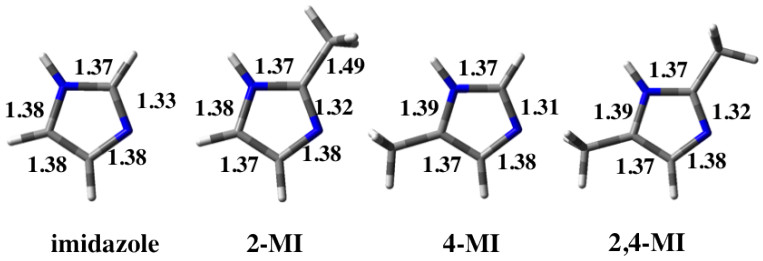

Figure 3.11: Optimised bond lengths (Å) of the ground state minimum geometries of the imidazole series investigated here.

3.3.2 Time resolved H^+ signals

The pump-probe experiment was used together with VMI techniques and carried out by members of the Stavros research group at Warwick University. They result in a spectra of H^+ signal intensity as a function of the time delay, as illustrated for unmethylated imidazole in Figure 3.12. The pump wavelength used was 200 nm whilst the probe wavelength was 243.1 nm. The data in the figure is fitted using a standard fitting procedure described in ref. [179]

For each energy component a time constant can be deduced: τ_H for high kinetic energy H^+ signals and τ_L for low kinetic energy signals. Time constants for imidazole, 2-MI, 4-MI and 2,4-MI are presented in Table 3.2.

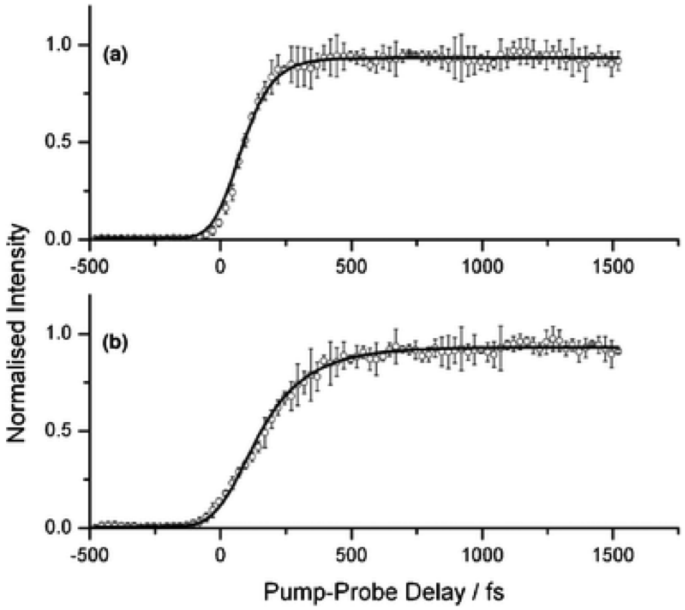

Figure 3.12: Results from the pump-probe experiment (excited at 200 and 243.1 nm respectively). High energy components for the imidazole molecule are shown in (a) and low energy H^+ signals in (b), as a function of the pump/probe delay. These are used to estimate separate time constants, τ, for both components. Reproduced from [175].

Absorption at 200 nm of imidazole to the $2^1A'$ state, followed by relaxation through internal conversion to the $1^1A''$ state and subsequent dissociation happens with a time constant of 78 $\pm$ 37 fs. As this is the high kinetic energy time constant it is a result of dissociation along the $^1\pi\sigma^*$ state. This suggests that build up in the $^1\pi\sigma^*$ is very rapid, meaning that the distortions of the ring to facilitate the $2^1A'$ $1^1A''$ coupling is very efficient. Even though this strongly suggest that the $^1\pi\sigma^*$ state actively participate in this conversion, the fact is that only the H-dissociation mode is investigated here. That means that the dominance of this or other modes, such as ring-opening reported by theoretical work, can not be ruled out.[178]

Considering the low energy signal for imidazole, the time constant is 163 $\pm$ 50 fs. It was postulated in the introductory section of this study that the slow H^+ atoms could result from unimolecular decay, caused by highly vibrationally excited modes, on the S_0 surface. However, the general time frame for statistical decay is in the order of ns.[180] Clearly these H-atoms originates from other processes. Multiphoton processes, such as further absorptions of pump photons by the parent, has been seen in previous work and could be a likely candidate.[181]

Methylation effects on the imidazole transient signals is also summarised in Table 3.2. Both the high and low kinetic energy time constant components are longer in 2-MI, 4-MI and 2,4-MI compared to the imidazole parent system. As theory has postulated ring distortions to be responsible for the coupling of the $2^1A'$ and the $1^1A''$ ($^1\pi\sigma^*$) state the addition of bulky methyl groups could hinder this motion. This would clearly explain the high kinetic energy component lengthening. For the low energy component however, as the origin of this signal it not definitely known, it is not straight forward to draw conclusions as to its time constant increasing.

One theory as to the increased time constants could be the increased densities of vibrational states at the excitation frequency used in this experiment The more vibrational modes that gets excited at 200 nm, the more the system can sample the space orthogonal to the ones that facilitate coupling. This leads to increased possibilities of sampling these modes, which do not couple the $2^1A'$ and $1^1A''$ surfaces, meaning that the system spends more time on the $2^1A'$ state, leading to longer time constant for both high and low kinetic energy H-atom signals.

In order to investigate whether the increase in time constants upon methylation of imidazole is caused by an increase in vibrational modes, computations of the vertical

Table 3.3: Vertical Excitation energies (ΔE) for imidazole and its methylated derivatives for the $2^1A' \leftarrow X^1A'$ transition. The experimental values are extracted from the UV absorption spectrum in Figure 3.3

ΔE for the $2^1A' \leftarrow X^1A'$ transition /eV				
Molecules	DFT	CCSD	CCSDR(3)	Expt.
imidazole	6.16	6.55	6.44	∼5.55
2-methylimidazole	5.95	6.58	6.51	∼5.50
4-methylimidazole	5.87	6.30	6.20	∼5.45
2,4-methyl imidazole	5.69	6.23	6.19	∼5.35

electronic states available were carried out. The expectation would be that the energy difference between the ($2^1A'$) excited state relative to the ground state (X^1A') would be smaller for 2-MI, 4-MI and 2,4-MI when comparing to imidazole.

3.3.3 Vertical UV absorption spectra

Excitation energies were calculated using CC and DFT with their linear response for the $2^1A'$ ($^1\pi\pi^*$) state of all methylated imidazole derivatives. For the CC calculations, the CCSD method was used in conjunction with the aug-cc-pVTZ basis set and also CCSDR(3) with the aug-cc-pVDZ basis using the Dalton 2.0 code.[161] For the TD-DFT calculations, the B3LYP functional was used with the aug-cc-pVTZ set of basis functions, using the Gaussian software suite.[160] The energy differences of the states are presented in Table 3.3

These calculations for imidazole gives similar energies as previous theoretical work.[182] The coupled cluster calculations are all in agreement with the DFT calculations with respect to the magnitude of the energies. The DFT results are however more in agreement with the experimental spectra presented in Figure 3.3 when it comes to the effect of methylation trend, and are also essentially converged with respect to basis set.

The DFT results indicate that methylation of the imidazole system lowers the energy of the $2^1A'$ state, increasing the density of states accessible at 200 nm. This supports the observed increase in time constants for the H-atom transient signals for both 2-MI and 4-MI in Table 3.2. The 2,4-MI signals are however curious in the fact

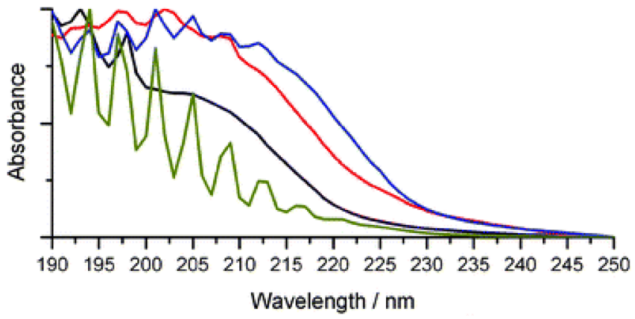

Figure 3.13: UV absorption spectra of imidazole (black), 2-MI (red), 4-MI (blue and 2,4-DMI (green), in the vapour phase. Reproduced from [175]

that they are *faster* than the 2-MI and 4-MI signals at low kinetic energy, and faster than 4-MI at high kinetic energy, despite being more substituted with bulky groups. It does indicate that the $2^1A'$ potential energy surface for 2,4-MI have a topology that allows for even more efficient coupling of the $2^1A'$ and $1^1A''$ states.

3.4 Conclusion

Time resolved pump-probe experiments were combined with high level response theory and multi-reference calculations in order to investigate the excited states of the core component of the eumelanine pigment, using indole and 5-hydroxyindole, and the adenine nucleic acid, using the imidazole molecule.

The non-adiabatic dynamics of indole and 5-hydroxyindole are both dominated by initial ultrafast (<100 fs) relaxation dynamics from the prepared ^1L_a state. A $^1\pi\sigma^*$ state as well as the ^1L_b state both provide relaxation channels for this decay. The similarity of the dynamics with or without 5-hydroxylation suggests that the role of the OH-group is negligible, and indicates that the indole moiety, and the N-H $^1\pi\sigma^*$ state, is very important in controlling the dynamics of the eumelanine pigment and its photostability.

Imidazole can be used as an approximation of the adenine nucleic acid base, and incorporating methylated derivatives show that the relaxation dynamics from the $2^1A'$ state, via the $^1\pi\sigma^*$ state to subsequent dissociation, is a very complex problem.

Whilst the relaxation and dissociation resulting in high kinetic energy H-atoms in imidazole happens with a 78 $\pm$ 37 fs time delay the low kinetic energy H-atoms are produced at 163 $\pm$ 50 fs. This is too fast to be attributed to unimolecular decay and is more likely caused by multi photon absorption processes. Methylation increases the time signals as a result of both hindering of ring distortions as well as the increase of vibrational modes accessible to the systems.

In small heterocyclic aromatic molecules the excited state dynamics is clearly dominated by the presence of so-called $^1\pi\sigma^*$ states in the examples looked at in this chapter. Computational studies in combination with pump-probe experiments means that these types of states can be investigated intimately, which can lead to conclusions with regards to the participation of these types of states in the dynamics of important bimolecular systems such as melanin pigments or nucleic acids.

Chapter 4

Linear and Non-Linear Absorption in Substituted Porphycenes

4.1 Introduction

A molecular structure related to the porphyrin core is the *porphycene* (**Pc**) compound, a reduced porphyrin isomer introduced in the Theoretical Background section. The **Pc** core structure has been shown to have a maximum absorption at slightly longer wavelengths than porphyrins (around 633 nm) due to lower molecular symmetry and has potential as a promising candidate for PDT for a number of reasons. Not only does in-vitro studies show a modest singlet oxygen quantum yield, **Pc** and its derivatives also show selective uptake in membrane related organelles, such as the mitochondria.[183, 184] As organelles of these types are crucial for cell function, application of radiation lead to very efficient apoptosis (cell suicide) of the cells targeted by the photosensitiser. From a photocheimists point of view however, the main advantage of porphycene over porphyrin however lies in the application of TPA PDT.

The **Pc** macrocycle was the first porphyrin isomer to be synthesised, in the late 1960, and theoretical, as well as experimental, results show that the **Pc** system has a very strong TPA compared to porphyrin analogues in the same spectral region.[185, 186] As such it is a promising molecular starting point for a study into the effects of systematic structural variations on its TPA spectra[114, 183, 187, 188].

For the simultaneous absorption of two photons, the transition moment tensor $M_{\alpha\beta}$ for the TPA is determined from the quadratic response term, as introduced in the Theoretical Background chapter. The actual TPA transition strength, δ^{TPA}, is then estimated as a rotationally averaged quantity:

$$\delta = F\delta^F + G\delta^G + H\delta^H \tag{4.1}$$

$$\delta^F = \frac{1}{30}\sum_{\alpha,\beta} M_{\alpha,\alpha}M^*_{\beta,\beta}$$

$$\delta^G = \frac{1}{30}\sum_{\alpha,\beta} M_{\alpha,\beta}M^*_{\alpha,\beta}$$

$$\delta^F = \frac{1}{30}\sum_{\alpha,\beta} M_{\alpha,\beta}M^*_{\beta,\alpha}$$

The values F, G and H depend on the polarisation of the incident photons and the conditions applied in this work was linear polarisation, where $F = G = H = 2$.

In the study presented in this chapter we have chosen to investigate the TPA qualities of the **Pc** macrocycle, and specifically how these vary with molecular structure. As electron acceptor- or donor-groups, attached with and without an extended π-bridge, have been demonstrated previously to increase the TPA transition strength the derivatives here were designed with *2,7,12,17–nitrophenyl* substituents as strong electron acceptors (**PcPN**) and *2,7,12,17–dimethylamine* substituents as strong electron donors (**PcDMA**). A phenyl-bridge was chosen to extend the π-system and promote charge transfer through the structure. We also investigated the effects of the coordination of the macrocycle to a Zn and Pd metal centre. The addition of Zn has shown to be beneficial in OPA PDT using the phthalocyanine photosensitiser, both in improving its OPA absorption as well as the facilitation of greater cellular uptake. Inclusion of Pd was chosen both due to its common usage in numerous experimental assays for the study of O_2 phosphorescence, as well as a starting point for future studies into its effects on internal pathways such as ISC in the photosensitiser. The **Pc** derivatives were designed as illustrated in Figure 4.1 and Table4.1, and selected to highlight how a systematic change in molecular structure ultimately affects the TPA transition strength.

This work focuses on the δ^{TPA} as calculated using the quadratic response of

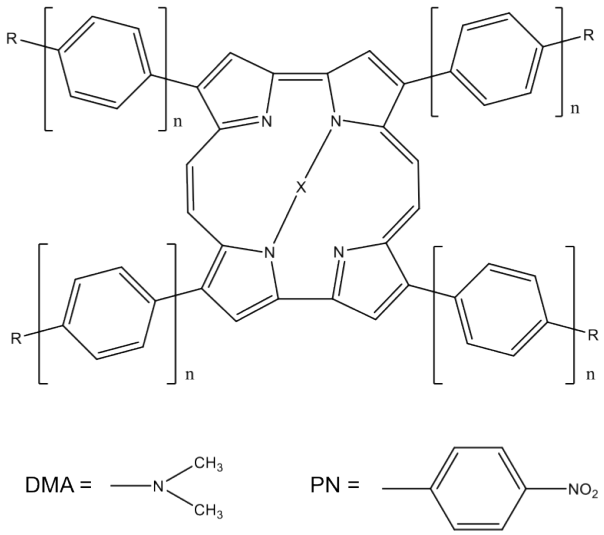

Figure 4.1: This figure illustrates the substitution pattern used for the porphycene derivatives investigated in this study. The full list of derivatives are found in Table 4.1

Table 4.1: Porphycene derivatives investigated in this study. "R", "n" and "X" refer to electron donor/acceptor groups, degree of conjugation and macrocyclic core respectively, as illustrated in Figure 4.1.

Compound	R	n	X
PcPN	PN	0	2H
PcCPN	PN	1	2H
ZnPcPN	PN	0	Zn
ZnPcCPN	PN	1	Zn
PdPcPN	PN	0	Pd
PdPcCPN	PN	1	Pd
PcDMN	DMN	0	2H
PcCDMN	DMN	1	2H
ZnPcDMN	DMN	0	Zn
ZnPcCDMN	DMN	1	Zn
PdPcDMN	DMN	0	Pd
PdPcCDMN	DMN	1	Pd

a DFT reference. This method is also ideal for optimisation of the geometries of **Pc** - type molecules as it scales favourably with the size of the system, making accurate geometries possible for large structures. The basic Hartree-Fock method is also well known to fail to accurately describe the aromaticity pattern of these systems, unless coupled with computationally expensive correlation methods.[189, 190] These advantages of DFT are combined with photochemical properties through the use of time-dependent DFT, where the linear and quadratic response functions gives OPA and TPA information respectively.[43, 44, 111, 121, 122] The applicability of the chosen structures as photosensitiser agents for use in a biological environment was further investigated by calculations of the OPA spectra with the systems immersed in a polarisable continuum solvent, using the PCM method. This method has been shown to be successful in combination with linear response DFT for reproducing optical spectra of porphyrins in solution. [191, 192]

4.2 Computational Details

The ground state geometries of each molecular system were optimised using the hybrid B3LYP exchange- correlation functional with the 6-31G* Pople-type basis set on all light atoms. For the metal atoms a relativistic Stuttgart/Dresden (SDD) pseudo potential was applied for the core electrons and the corresponding basis set for the valence electrons[73, 193, 194]. Analytical Hessian calculations were performed to confirm the nature of the stationary point.

At each confirmed ground state optimised geometry one- and two-photon absorption spectra were computed using linear response and quadratic response. All geometry optimisations and OPA linear response calculations were computed using Gaussian 09,[160] whilst TPA quadratic response theory calculations were performed using a local version of the Dalton 2.0 program[161].

The linear response calculations were carried out with the Coulomb-Attenuated version of the Becke three-parameter hybrid B3LYP functional, CAM-B3LYP[93]. The CAM-B3LYP functional was also employed in the quadratic response calculations.

When considering calculations of molecular properties the nature of the perturbation needs to be considered when choosing a basis set and, as the absorption of radiation depends on the polarisability of the electron cloud, polarisation functions

are considered important. However, the importance of diffuse functions is expected to diminish as the number of basis functions are increased. In order to see how well this statement applied in our case and to get a suitable reference for our calculations we chose the relatively simple 6-31G* as the basis set on the light atoms for a linear response calculation on the **Pc** core and compared with a basis that includes diffuse functions. As can be seen from table 4.2 the 6-31G* basis reproduces state ordering, energies and oscillator strengths results from the diffuse function basis, up to 240nm, and hence describes well the important Soret- and Q-regions of porphyrins. 6-31G* functions were therefore used for all light atoms as it was expected to provide a suitable balance between computational cost and accuracy.

In order to assist in the interpretation of the excited states data, a NTO representation was calculated for each excited state of interest from the linear calculations. Solvent interactions were estimated using the PCM, in which the calculation is carried out within a cavity surrounded by a reaction field from the solvent. The solvent was specified as water using the standard dielectric constants of Gaussian09 and non-equilibrium solvation was used in order to avoid the solvent adjusting to the excited state geometry. The solvatochromic effects determined leads to information regarding shifts in the absorption bands, in both OPA and TPA, but the effect on intensity profiles is determined only for OPA. The calculation including solvent effects on TPA is not determined here, although the methods exist [195–197].

4.3 Results and Discussion

4.3.1 Geometry Optimisations

The compounds included in this study all have substituents with a limited number of rotational degrees of freedom. In order to inspect the effect of various rotomers an investigation was carried out on one of the selected compounds. A model system, **PcPN**, was manipulated by varying the starting dihedral angles between the plane of the macrocyclic core and the plane of the substituents, as described in Figure 4.2 and Table 4.3. The ground state energy differences between the various rotomer conformations were found to be very small. Each rotomer was subsequently investigated for OPA and TPA and the differences in the investigated spectra were also found to

Table 4.2: Resulting OPA spectrum from a basis set comparison on the **Pc** core.

6-31G*			
wavelength (nm)	energy (eV)	oscillator strength	symmetry
575	2.195	0.1562	^1B_u
541	2.319	0.2392	^1B_u
359	3.54	0.0000	^1A_g
354	3.574	0.0136	^1B_u
312	3.998	0.7685	^1B_u
306	4.075	0.7302	^1B_u
299	4.179	0.0000	^1A_g
297	4.208	0.0000	^1B_g
290	4.331	0.0000	^1A_u
286	4.391	0.5506	^1B_u
265	4.723	0.0000	^1A_g
248	5.032	0.0000	^1A_g
238	5.249	0.0000	^1A_g
aug-cc-pVDZ			
wavelength (nm)	energy (eV)	oscillator strength	symmetry
583	2.125	0.1489	^1B_u
553	2.238	0.2271	^1B_u
358	3.456	0.0000	^1A_g
356	3.474	0.0340	^1B_u
320	3.865	0.7760	^1B_u
314	3.946	0.9129	^1B_u
301	4.116	0.0000	^1A_g
296	4.181	0.0000	^1B_g
289	4.284	0.0000	^1A_u
287	4.309	0.3634	^1B_u
268	4.618	0.0000	^1A_g
252	4.901	0.0000	^1A_g
242	5.110	0.0000	^1A_g

Table 4.3: Geometrical rotational parameters illustrating the results of the rotamer investigation. Angles are specified in Figure 4.2

Compound	Starting Angles				Optimised Angles				δ^{TPA} E
	a	b	c	d	a	b	c	d	
PcPN-1	90	90	90	90	137	42	45	136	0
PcPN-2	135	135	45	135	134	137	44	138	7×10^{-5}
PcPN-3	45	45	135	135	44	45	134	137	2×10^{-4}
PcPN-4	135	45	135	135	135	44	134	137	7×10^{-5}

be very small, and the molecules studied were a combination of all conformers.

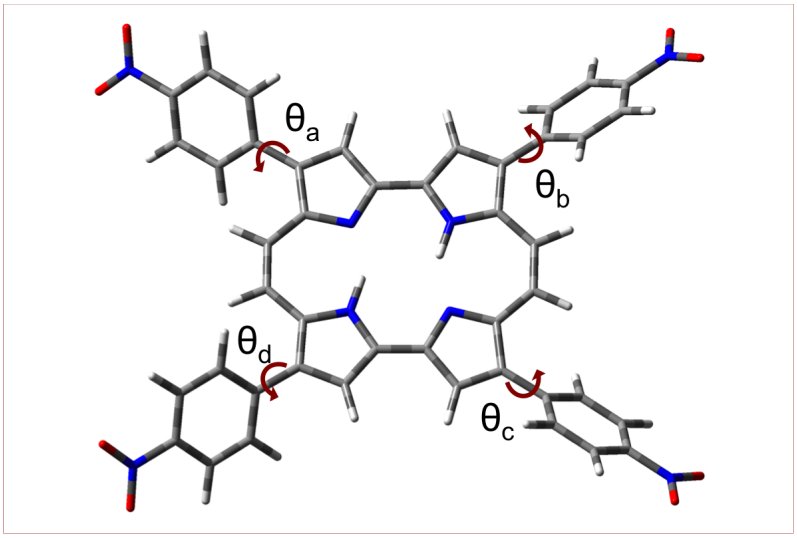

Figure 4.2: Ground state rotomers of one **Pc** derivative were investigated. Full data from the optimisation results are found in Table 4.3

Key parameters of the geometry optimisation of all molecules are presented in Figure 4.3 as well as Table 4.4. The minimum energy geometry that was found for the free porphycene macrocycle is completely flat and of C_{2h} symmetry. In the lowest energy geometries of the further systems on the other hand, a twist can be seen in the porphycene centre leaving it non-planar. The out of plane twist is not very profound in the cases where the macrocycle is coordinated to a metal, although it is still evident. The non-planarity does not effect the symmetries of the systems, and they transform according to the elements of their respective point groups (Figure 4.4).

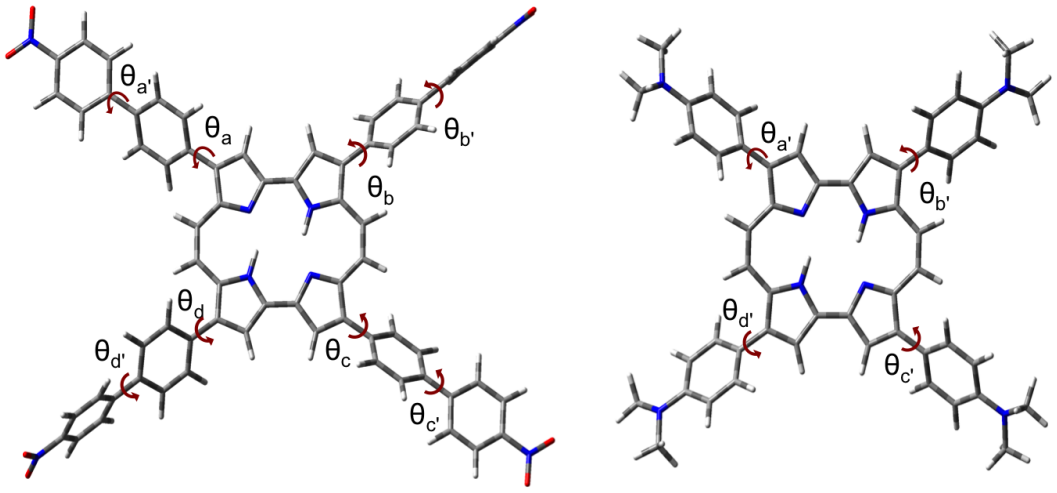

Figure 4.3: **PcCPN** and **PcCDMN** with angles indicated to demonstrate selected geometrical parameters of the chromophores in this study. Parameter data is presented in Table 4.4

Table 4.4: Data for the geometrical parameters introduced in Figure 4.3

Compound	Angles								Point Group
	a	b	c	d	a'	b'	c'	d'	
Pc									D_{2h}
PcPN	46	43	46	43					C_2
PcCPN	45	44	45	44	37	-36	37	-36	C_2
ZnPcPN	46	45	136	44					C_1
ZnPcCPN	46	44	46	44	36	37	-36	-36	C_3
PdPcPN	47	45	136	44					C_1
PdPcCPN	47	45	47	45	37	37	37	37	D_2
PcDMA									C_1
PcCDMA					42	40	42	40	C_2
ZnPcDMA									C_1
ZnPcCDMA					42	42	42	42	D_2
PdPcDMA									C_1
PdPcCDMA					43	43	43	43	D_2

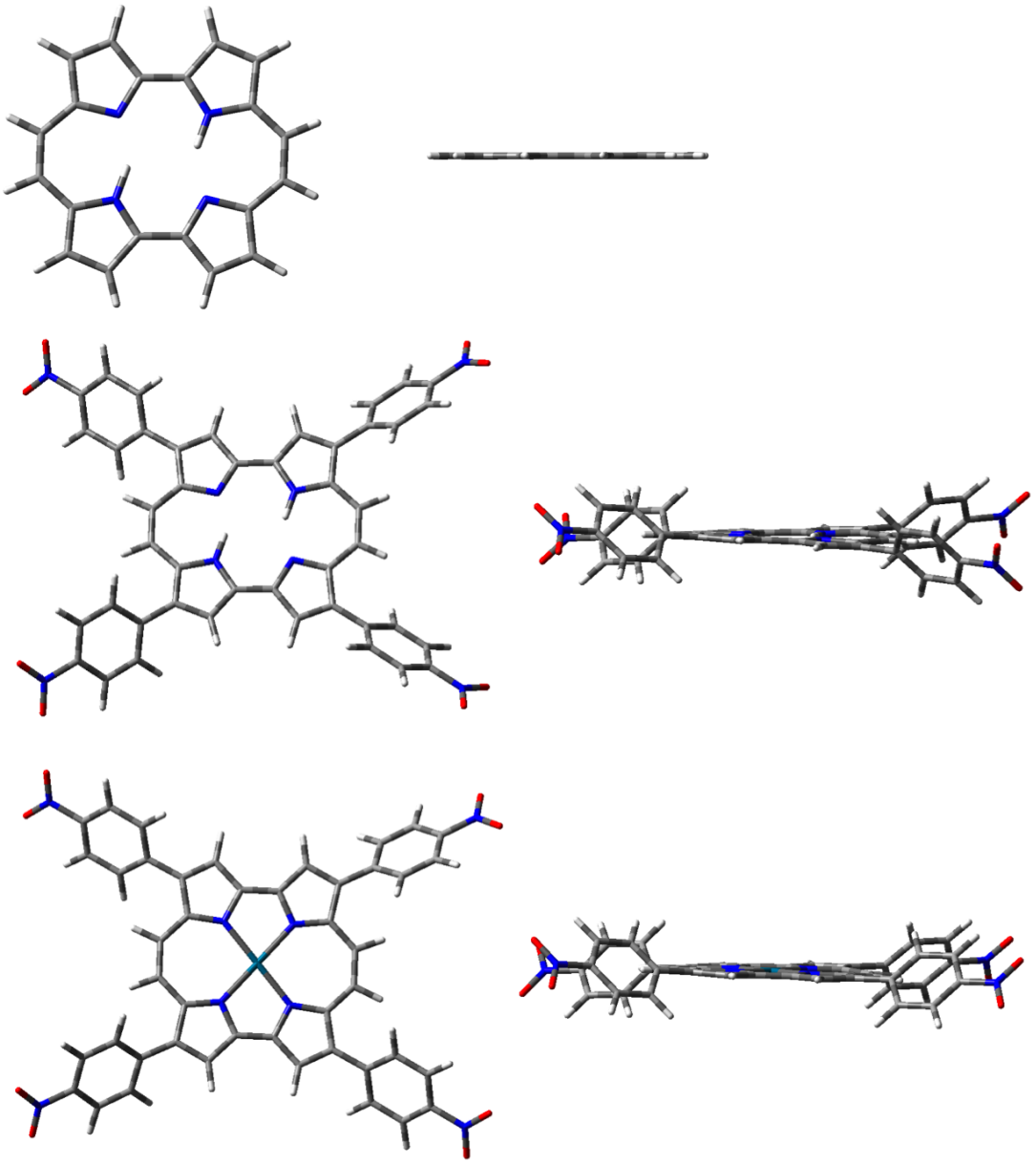

Figure 4.4: Optimised geometries of **Pc, PcPN and PdPcPN. Whilst the core Pc free base is flat, the substituted derivatives all have a twist in the core macrocyclic moiety.**

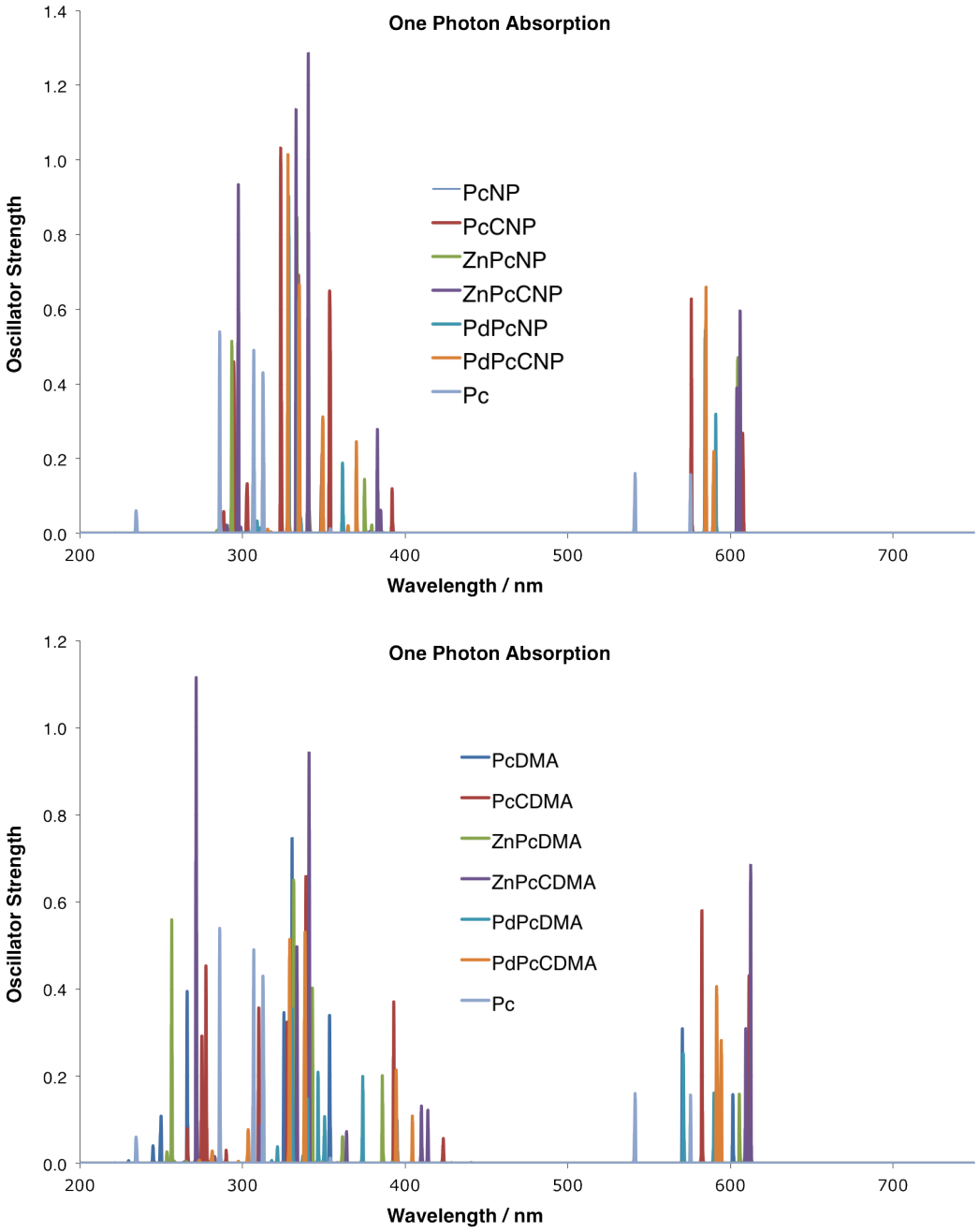

Figure 4.5: One Photon Absorption results for **Pc**, as a free base or chelated to **Zn** or **Pd**, and its various nitrophenyl (**PN**) and dimethylamine (**DMA**) derivatives

4.3.2 One-Photon Absorption

The OPA transitions, from the linear response CAM-B3LYP/6-31G*,SDD computation, were calculated for the first 20 excited states of the optimised geometries on the ground state potential energy surface for each system. The resulting spectra for the free base **Pc** macrocycle and the various derivatives are displayed in Figure 4.5. It is evident that nearly all the compounds display the two classic dominant regions of absorption, the Soret- band at 300 - 400 nm and the Q-band at 550 - 650 nm. These regions of absorptions are expected from the GFO model. As introduced earlier on in this thesis, the relative intensity of these two bands in **Pc**, and the reason they differ from porphyrin, is due to the non-degeneracies of the LUMO and LUMO+1 frontier orbitals. It can be seen here that the intensities of the Soret- and Q-bands are relatively similar in **Pc** as well as the **Pc** derivatives. This indicates a deviation from degeneracy of the LUMO orbitals, as expected, in the traditional, wavefunction-based, orbital picture. In DFT however the evaluation of the Kohn-Sham orbitals are not necessarily trivial and in order to further analyse the nature of the transitions the NTOs of a selection of compounds were calculated and plotted (Figure 4.6).

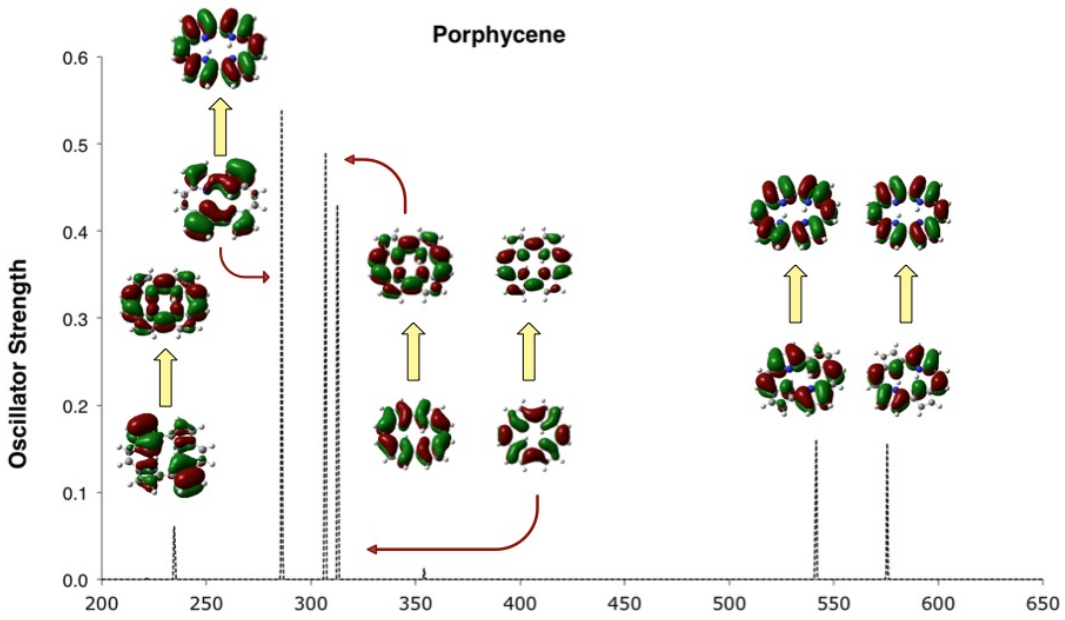

Figure 4.6: NTO representation of the transitions of free base **Pc**.

In the **Pc** core it is seen that the transitions in the Q- and Soret bands are mainly a result of electron density redistribution within the core aromatic structure, in accordance with the GFO model. However, a significant contribution can be seen from a transition from an orbital that can mainly be described as the HOMO+2 frontier orbital in one of the transitions in the Soret-band (in the region of 300 nm in Figure 4.6). Bands involving transitions like these are commonly known as N-Type bands, in general porphyrin photochemistry. N-type states are due to absorptions involving orbitals with significant density on the pyrrole moieties only, rather than evenly distributed over the full π-system as in the Gouterman set. Transitions of these types are commonly seen in wavefunction methods, such as Coupled Cluster [61, 63, 198], as well as in TD-DFT calculations [43, 199] but normally in the higher energy regions above the Soret-transitions. These findings correspond well to weak absorptions that can be seen as a shoulder of the N-band in the experimental spectra [112, 200]. Even though some TD-DFT functionals behave well in the position of the N-states, they have also been seen to be incorrectly included in the Soret-region, and been suggested to be responsible for TD-DFT results that reflect the experimental shape and intensity of the Soret-band [199]. Considering the computational challenges involved in describing a system the size of *Pc* correctly and the lack of experimental resolution in the high energy region of the absorption spectra, the correct assignment of the states involved is still a non-trivial task and the determination of the role of N-type states in the qualitative description of the excited states of porphyrin-type compounds in general is challenging. The introduction of long-range corrected DFT functionals for use in TD-DFT further complicates matters. As these functionals are designed to better describe charge transfer states, such as N-type states where charge density is localised on the pyrrole moieties of the macrocycle instead of the full π-system, they tend to lead to a stabilisation of these states meaning that they are commonly found in between the Q- and the Soret-bands. The presence of N-type transitions has lead to suggestions that the GFO model might not be entirely suitable for the **Pc** core and its derivatives, and further investigations into the applicability of this model is being carried out in our group as well as others[115].

The OPA transitions in the substituted **Pc** derivatives were also analysed using their NTOs and examples of the plotted orbitals for an acceptor (**PcPN**) and donor complex (**PcCDMN**) are shown in Figure 4.7. It is clear that the absorption in

the Soret- and Q-regions are mainly caused by transitions within the core aromatic structure with added N-type bands, as in **Pc**. There is however also evidence of charge transfer through the conjugated phenyl moiety to and from the electron accepting and donating substituents respectively, at short wavelengths and also in the mid-wavelength region (at 280 nm and 380 nm respectively, for both for **PcNP** and **PcCDMN**).

For the species that contain a metal centre, the same transition densities can be seen as for the transitions of the previously investigated structures in the Q-region and in the Soret-region. There is also contribution from absorption from two degenerate d-orbitals on the metal as well as from the substituents at high energy transitions into the Soret-region. This points to a further break down of the GFO model that becomes evident from the relative weakening in the intensity of the Soret-band for these derivatives. It is important to highlight at this stage that the nature of TD-DFT using response theory (where the propagator is truncated at the level that it only include *single* excitations) means that high energy transitions are likely to have contributions of higher order excitations, and therefore not be well described.

4.3.3 Two-Photon Absorption

The TPA spectra from the quadratic response CAM-B3LYP/6-31G*,SDD calculations, were simulated for 10 excited states of each irreducible representation of the point group that the optimised structures belongs to. It is important to note that the wavelength of absorption presented is the total for the two-photon process, i.e. the results presented is the resonant absorption of two photons of equal wavelength.

The spectra all show a clear main absorption into the Soret-region, at 200 - 400 nm, and very small absorption into the Q-band. The effect of the substitution of the macrocycle is seen as a red shift in the TPA maximum in all the structures investigated, compared to the free **Pc** macrocycle (Figure 4.8 and Figure 4.9). Addition of an electron-withdrawing or donating substituent leads to an absorption maximum in the region of 250 - 300 nm, which corresponds to a wavelength of incident light of 500 - 600 nm. This wavelength is approaching the optical window of tissue penetration, at 650 - 1300 nm, which is an encouraging result for applications in a biological environment. The chelation of the base to a Zn metal leads to an even larger red-shift

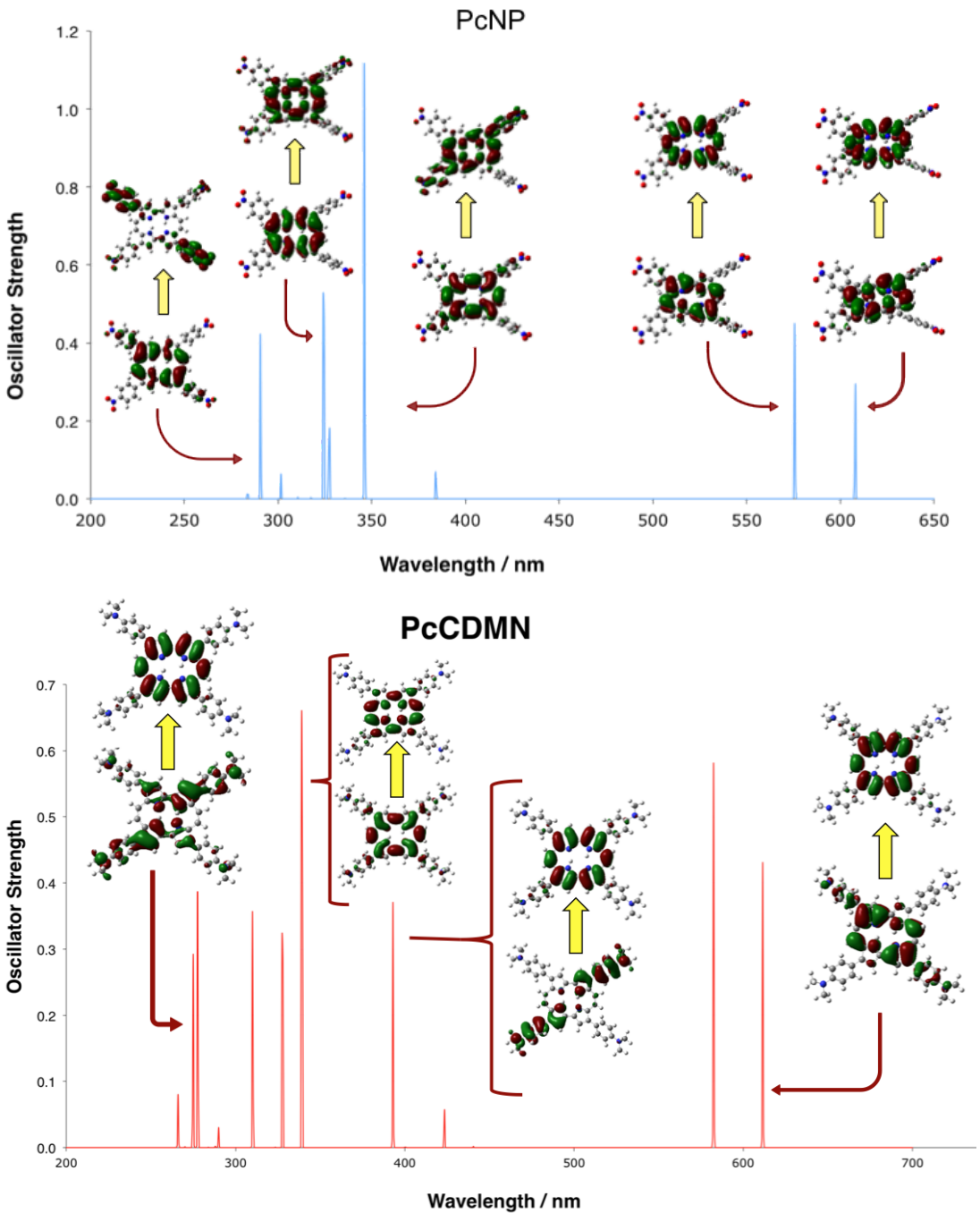

Figure 4.7: NTO representation of the transitions of **PcNP** and **PcCDMN.**

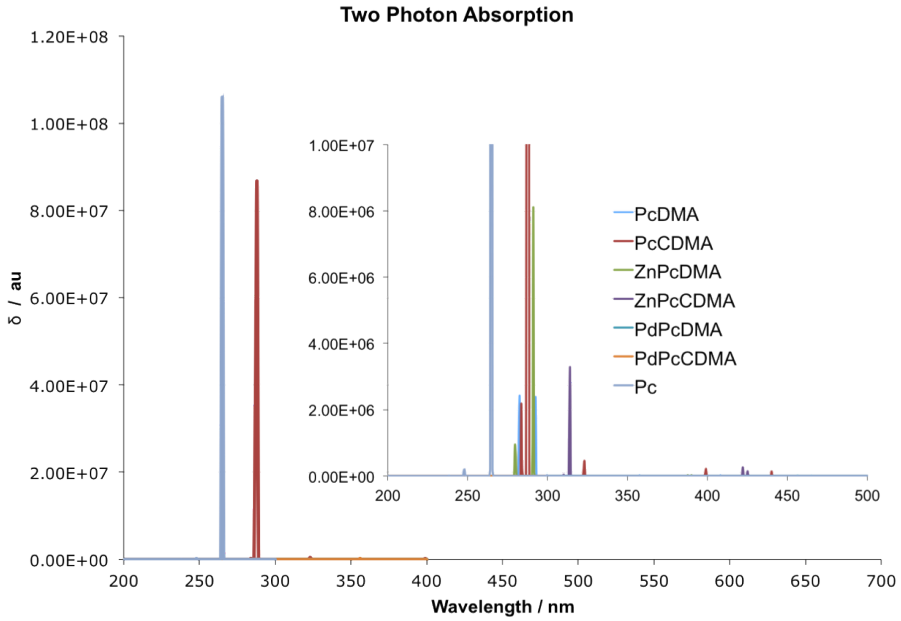

Figure 4.8: Two Photon Absorption results for **Pc**, as a free base as well as chelated to **Zn** and **Pd** with **DMA** derivatives

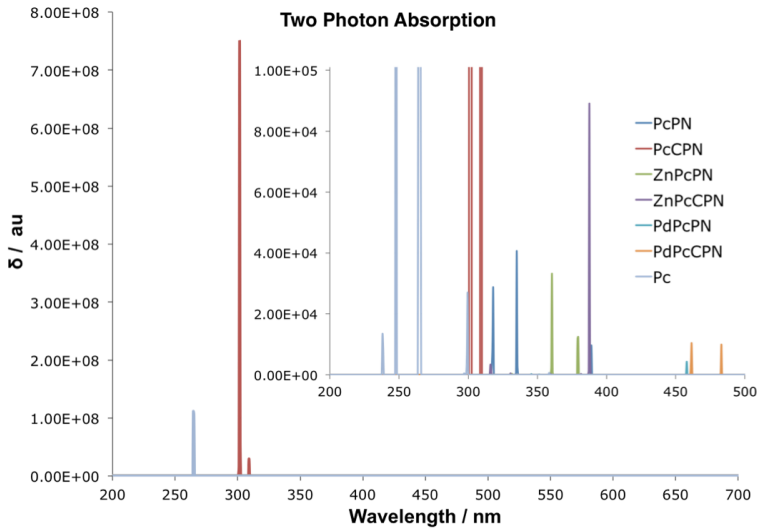

Figure 4.9: Two Photon Absorption results for **Pc**, as a free base as well as chelated to **Zn** and **Pd** with **PN** derivatives

with an absorption maximum at 370 - 390 nm. As the corresponding operating wavelength then would approach 740 - 780 nm these molecules absorbs well within the

range of the optical window. With Pd coordinated to the centre of the ring the absorption maximum is further red-shifted, 350-450 nm, corresponding to an operating wavelength of up to 900 nm. This wavelength is in an even more preferable position in the tissue penetration window as the absorption due to various chromophores is approaching an absolute minimum at this point. For the application of the compounds as photosensitisers for future use in PDT, the wavelength of maximum absorption is indeed crucial, but an optimal photosensitiser must also have a high TPA transition strength in the relevant region.

The TPA transition strength, δ^{TPA}, in the investigated compounds is improved by addition of electron-withdrawing groups compared to the free **Pc** molecule. However, the increase is only evident when substituents are separated from the macrocyclic structure by a π-bridge that extends the conjugation of the system. The reason for the effect of the addition of substituents in this manner is the increased transition dipole moment. The very large transition strength of the TPA of the **Pc** free base macrocycle, as well as for **PcCPN** and **PcCDMA**, when comparing to the alternative molecular structures, can be explained in terms of one-photon *resonance enhancement* of the transition. The phenomenon of resonance enhancement is best illustrated by consideration of the sum-over-states expression introduced in Equation 2.71 in the Theoretical Background chapter introducing TPA for PDT. The magnitude of $M_{\alpha\beta}$ depends on the difference of the k-th state and the frequency of the total excitation through the denominator in the expression, $(\omega_k - \omega)$, which will approach zero if the frequency of the incident light approaches the frequency difference between the intermediate and the ground state. Since the intermediate state is a linear combination of all real eigenstates of the system, a TPA transition that proceeds through an intermediate state that can be described mainly in terms of a real state will be significantly enhanced. An allowed OPA Q-transition accidentally degenerate at half the Soret-transition energy will therefore greatly enhance the TPA transition into the Soret-band. The effect of resonance enhancement is clearly seen in the case of the free **Pc** macrocycle as well as **PcCPN** and **PcCDMA**, but also, to a lesser extent, in the Zn-chelated compounds, as displayed in Table6.3. The values of the δ^{TPA} at wavelengths that are near or at resonance can not be determined explicitly, as evident from Equation2.71, using the method described here but is useful in the interpreting of general trends in the TPA spectra. The wavelengths of maximum TPA in the

Soret-region for these systems are very nearly in resonance with an allowed OPA in the Q-region, which leads to the conclusion that the δ^{TPA} in the Soret-region should be very large. This is not the case for any of the other systems, which rationalises the comparably low TPA transition strengths for these species. Resonance enhancement also rationalises why there are only very weak TPA transitions to be seen in the Q-region for any of the investigated photosensitisers, as there is no allowed one-photon transition near half the wavelength value of this region. It is worth to note that the values of the δ^{TPA} at wavelengths that are near or at resonance can not be determined explicitly using the method described here, as they require the use of damped response functions. [111, 201, 202] At resonance enhanced TPA transitions it is also expected that vibronic contributions plays a non-neglible role, which leads to so called intensity stealing by otherwise forbidden signals in the symmetric molecules and also potentially accesses purely vibrational channels which distorts and shifts the absorption peak.[203–205] Nevertheless, it is important to note that non-dampened response theory is very useful in the interpreting general trends in the TPA spectra upon varying the electronic structure. The effect of large structural changes like these on the TPA transition strength, especially as a cause of resonance enhancement, is also supported by experimental studies. This highlights the fact that a theoretical input could be crucial in studies such as these, where the photosensitisers are challenging synthetic targets, as well as studies where new structure-TPA relationships are being investigated. Examples of the latter are the investigation into the effect of the substitution of core heteroatoms in a macrocycle on the TPA transition strength, as well studies into the effect of donor and acceptor substitution patterns, which are the topics of the subsequent chapters in this thesis.

4.3.4 Solvation Effects

The effect of a solvent on the OPA spectra was calculated using the PCM to simulate water surroundings, on PCM optimised geometries using the Gaussian09 standard static and optical dielectric constants of 78.36 and 1.78 respectively. In the resulting absorption spectra, for the OPA transitions, two general trends can be seen in terms of the oscillator strength of the transition. For the compounds with a phenyl moiety, extending the conjugation of the chromophore, the main transition into the Soret-

Table 4.5: Wavelengths (nm) of maximum TPA and OPA for the various species in the Q and Soret-region. Marked in bold are the transition wavelengths that are in near-resonance.

	OPA Maxima		TPA Maxima
	Soret	Q	Soret
Pc	320	**530**	**265**
PcPN	345	575	300
PcCPN	360	**580**	**300**
ZnPcPN	340	595	365
ZnPcCPN	360	600	390
PdPcPN	355	585	465
PdPcCPN	370	585	470
PcDMA	330	570	282
PcCDMA	339	**582**	**287**
ZnPcDMA	331	592	290
ZnPcCDMA	340	**612**	**313**
PdPcDMA	330	571	456
PdPcCDMA	338	591	482

band is significantly enhanced, as demonstrated in 4.10. This is also the case in compounds chelated to a Pd metal centre. Enhanced absorption points to the fact that the solvent has a positive effect on the difference in dipole moment between the ground and the Soret-state in going from the gas- to the solution-phase, and has been demonstrated for porphyrins in previous PCM studies[206].

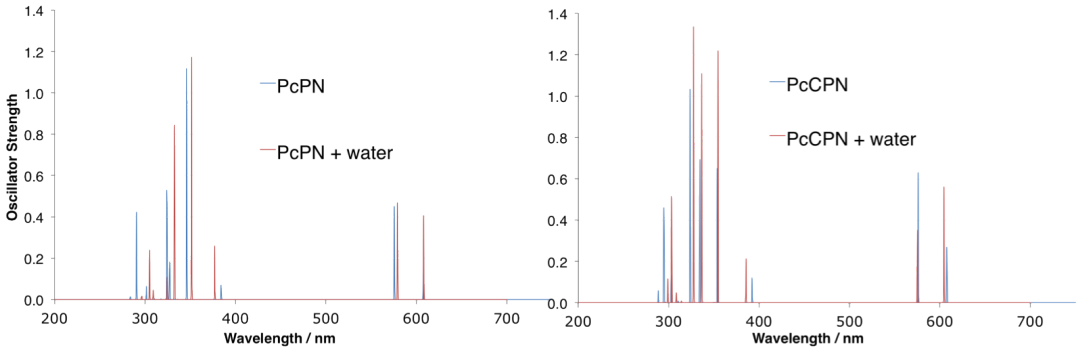

Figure 4.10: OPA results with and without water surroundings for **PcPN** and **PcCPN**.

The analysis of the solvatochromic shifts show only a very slight change in the

bands for all chromophores, which does not impact the OPA transitions to a very large degree. However, it is important to keep in mind that these small solvatochromic shifts in the states are also valid for the TPA transitions. This is pertinent in that only a small shift in the position of the Q-band can have a very large impact on the TPA into the Soret-band, through a resonance enhanced transition.

4.4 Conclusion

This chapter introduced the use of linear and quadratic density functional response theory to display the effects of structure on OPA and TPA characteristics in substituted **Pc** photosensitisers. From the linear response results the expected spectral pattern could be seen in two clear Soret and Q-bands in the absorption spectra for all the investigated **Pc** derivatives. These bands are well characterised for the free base porphyrin, using the classic Gouterman model. Analysis of the NTO's of these bands for the **Pc** systems investigated here however, suggest that this classic four-orbital model might not give a complete picture of the transitions in **Pc**. Specifically the model does not fully account for the inclusion of N-type transitions in the Soret-band. The trend seen in the structural effect on OPA and TPA follow the expected trend from previous experimental work on porphyrin. Both the OPA and TPA results also demonstrate that the **Pc** macrocycle has a range of promising attributes for use as an agent in photodynamic therapy as both one- and two-photon activated photosensitiser. In particular, the use of TPA to tune the maximum wavelength of absorption to within the optical window of tissue penetration is predicted to be very fruitful for this series of **Pc** derivatives, especially upon coordination to a Zn or Pd metal centre. A very large increase in TPA transition strength was displayed for derivatives bearing electron withdrawing or donating substituents where the chromophore was extended in order to facilitate large charge transfer during the transition. The phenomenon of resonance enhancement plays a significant role in contributing to the very large TPA transition strength values that could be seen. Future research into TPA PDT should aim at the development of structures that exhibits strong resonance enhancement as well as an absorption maximum within the optical window of tissue penetration. The solvent effects demonstrated using the PCM on the OPA transitions are small, but needs to be taken into account, as very small effects on the OPA spectra can still

afford very large changes in the TPA spectra.

The theoretical data presented here indicates that there is a large amount of information to be gained on the photochemical behaviour of relatively large chromophores from computations. These results can then be used as foundations for future experimental research and a theoretical input has the potential to greatly drive the development of photosensitiser agents.

Chapter 5

The effect of Substitution Pattern on Linear and Non-Linear Absorption in Macrocycles

5.1 Introduction

As we have seen in this thesis, an investigation of the TPA wavelength in a macrocyclic chromophore can lead to various benefits for a number of applications, most notably PDT. However, non-linear optics are also of huge importance in biological imaging.[15, 207, 208] One example of non-linear optical imaging is SHG imaging, first observed by Franken *et al.* in 1961.[209] Whilst TPA occurs via an intermediate state to an available excited state, SHG does not rely on an excited state being formed and is commonly viewed as a *scattering* process, as described in Figure 5.1. With regards to the use of these techniques in biological imaging, such as multi-photon microscopy, an SHG signal that is scattered instantaneously is preferred over a signal generated by TPA followed by fluorescence. Apart from providing light that retains phase and polarisation after interaction with the sample, SHG also avoids the creation of states that could lead to possibly harmful photochemistry.

Overall SHG efficiency is related to the molecular first hyperpolarisability, β, through the second order susceptibility, $\chi^{(2)}$, of the material along the Z-axis of

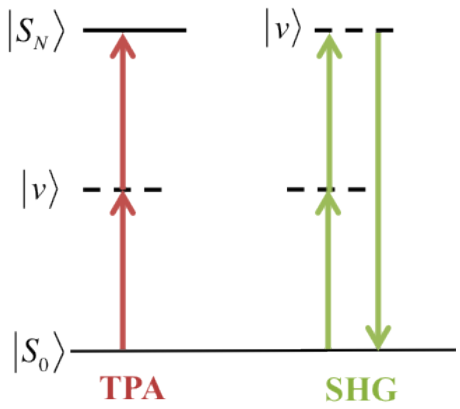

Figure 5.1: The real singlet (S, solid) and intermediate (v,dashed) states for transitions in typical systems that are TPA and/or SHG active

the laboratory frame;

$$\chi^{(2)}_{zzz} = Nf\beta_{zzz}\langle cos^3\alpha\rangle \tag{5.1}$$

where the N is the number density of absorbers in the material, f is the local field factor accounting for the orientation of the incoming laser light and $\langle\ cos^3\ \alpha\ \rangle$ takes into account the orientation of the absorbers with respect to the lab frame.[208] Even though the susceptibility is in general reported as a rotationally averaged quantity, the diagonal z-component is described to dominate in the expression above. This is due to the fact that, as with TPA discussed in the previous section, the chromophores with large non-linear optical effects often have CT transitions. As SHG systems are often chosen to have their CT direction along a specific coordinate of the system (z), the β_{zzz} component then dominates the effect.

There are numerous approximations available for the calculation of hyperpolarisabilities. Apart from the response method, introduced in the Theoretical Background of this thesis, a sum-over-state (SOS) approach is also common. Unlike the former, which implicitly includes a summation over *all* states, the latter needs to be truncated to include only a couple of excited states. In this chapter we applied the three-state approximation (TSA) to the SOS method:

$$\beta^{TSA}_{ZZZ,0} = \frac{3\Delta\mu_{01}(\mu_{01})^2}{(\Delta E_{01})^2} + \frac{3\Delta\mu_{02}(\mu_{02})^2}{(\Delta E_{02})^2} + \frac{6\mu_{01}\mu_{12}\mu_{02}}{(\Delta E_{01})(\Delta E_{02})} \tag{5.2}$$

The first two terms in the sum are the diagonal contributions to the hyperpolarisability from the first and second excited states and the third term is the interaction component from the interactions of these two states with the ground state. The benefit of the TSA is that, if these three states are involved in increasing the β, then the molecular structures involved can be investigated in more detail.

In 2013, the Anderson group at Oxford University published findings that indicated that systems based on **P** with *only* an electron donating substituent, a "push-no-pull" system, in fact exhibited as large SHG as conventional "push-pull" systems with the same conjugating bridge length.[207] These findings suggests that an acceptor group could in fact be unnecessary when maximising higher order hyperpolarisabilities, meaning the design of SHG, as well as potentially TPA, active compounds could be much simplified. The reason for this effect was suggested to be the electron deficiency of the macrocycle, leading to it taking on the role of an efficient electron acceptor, without the need for addition of a specific electron withdrawing group.

In this chapter we present the study of a set of "push-no-pull" systems using DFT computations, in order to shed light on the optical behaviour of these systems as a function of electron-push or -pull strength. A set of substituents were chosen for **P** and **Pc** macrocycles that reflect a range of electron absorption and withdrawing strengths, as indicated in Figure 5.2. These substituents were then systematically attached to the core macrocycles in order to create a set of conventional "push-pull" compounds, "push-no-pull" systems and also a set of "no-push-pull" chromophores. The linear and quadratic response functions of the DFT electronic structures were then used to evaluate the full UV-vis absorption spectra, the TPA spectra at the same range and the SHG capabilities at wavelengths pertinent to biological imaging. The results presented here give a qualitative picture of the evolution of the non-linear optical properties as a function of the electron withdrawing/donating nature of the substituents.

5.2 Computational Methods

In this chapter, the geometries and the optical properties were evaluated using DFT and TD-DFT respectively. A CAM-B3LYP/6-31g(d,p) level of theory was used throughout.[130, 131] Optimisations and linear response functions were calculated us-

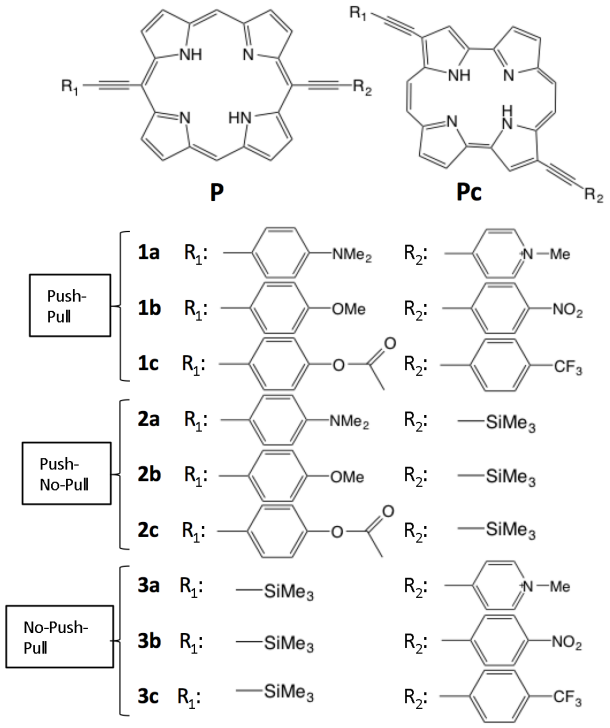

Figure 5.2: A figure describing the set of substituents investigated in this study for **P** and **Pc**. The electron-pulling/-pushing strengths increases as we go from a to c, and the trimethyl-silane substituent is representing neither electron-push nor -pull.

ing Gaussian09[210] and the quadratic response functions were determined in Dalton2013.[211] The excitation energies (ΔE_{0n}) and the differences in the dipole moments ($\Delta\mu_{0n}$ between the ground and state n) were calculated using the linear response, whilst transition dipole moments (μ_{nm}, between states n and m) were determined from the second residue of the quadratic response.

5.3 Results

5.3.1 Geometry Optimisations

All **P** and **Pc** derivatives were optimised to stationary points on their ground state potential energy surfaces using the CAM-B3LYP functional[130] and the 6-31G(d,p) basis set of the Pople family[73], without imposing any symmetry constraints.

5.3.2 Linear Response

The simulated UV-vis spectra for the first 20 excited states of one selected push-pull (set 1, as introduced in Figure 5.2), push-no-pull (set 2, Figure 5.2) and no-push-pull (set 3, Figure 5.2) of **P** and **Pc** are presented in Figure 5.3. For the **P** derivatives, this specific set reflects the work of the Anderson group who introduced the concept of push-no-pull chromophores for SHG applications. The experimental data is compared to the results obtained here for the first low energy states in the Q-band in Table 5.1. Any alkyl chains present in the experimental structural motives were replaced with methyl groups in order simplify the calculations without affecting the absorption charactersitics.

Reproducing the experimental results, the Q-band absorption maxima for the push-no-pull and the no-push-pull chromophores are seen to be red-shifted compared to the push-pull systems. The computations do not however reflect neither the degree of shift nor the relative oscillator strengths observed. In the experiment the push-no-pull absorptions in the Q-region was red-shifted further, and had larger oscillator strengths than the no-push-pull system, but the computations predict the opposite effect. The **Pc** series in Figure 5.3 follow the same trend as the **P** series, but has stronger absorption peaks in the Q-region. This is a common effect seen when comparing to

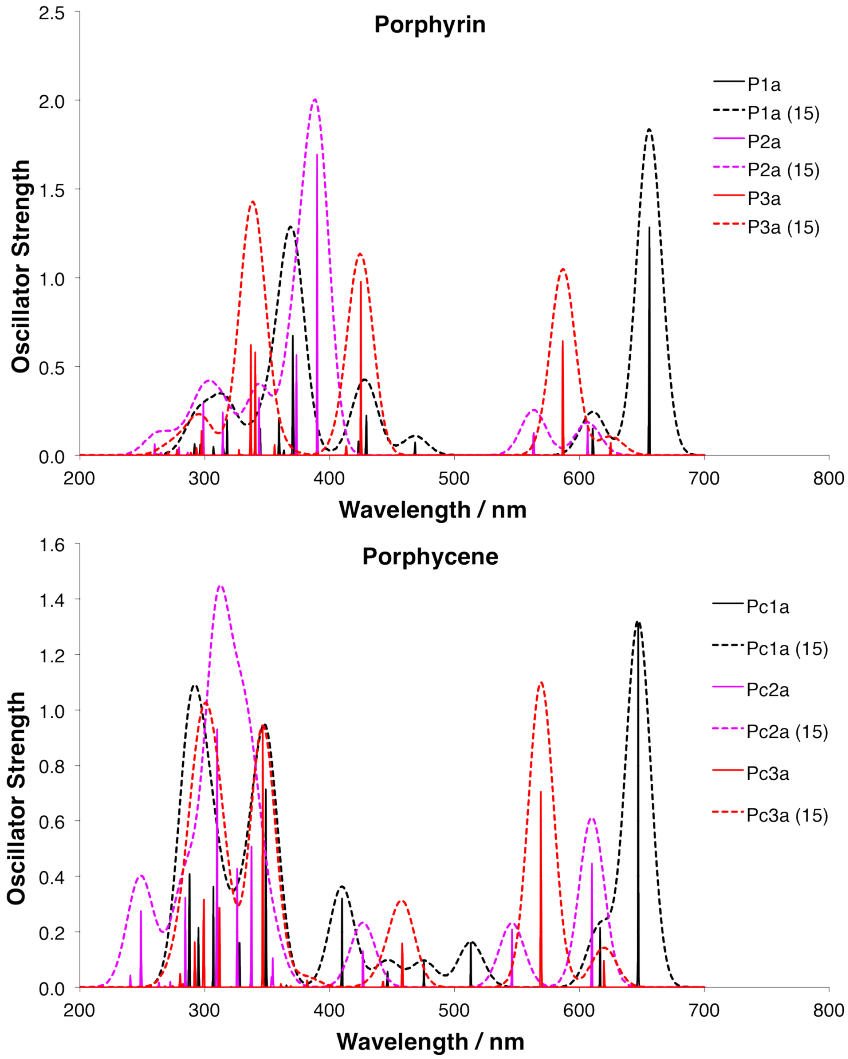

Figure 5.3: UV-Vis absorption spectra simulated using TD-CAM-B3LYP//6-31G(d,p) for the first 20 excited states, for **P** and **Pc**. Push-pull (**P1a** and **Pc1a**, black), push-no-pull (**P2a** and **Pc2a**, pink) and no-push-pull (**P3a** and **Pc3a**, red). Dashed lines indicate gaussian broadening functions being used ($\sigma = 15nm$).

Table 5.1: Resulting optical parameters for **P** and **Pc** with electron pushing and pulling substituents.

Molecule	State	λ (nm)	f	λ_{exp} (nm)	f_{exp}
P1a	S_1	656	1.84	707	0.25
	S_2	610	0.25	627	0.31
P1a-DMF	S_1	629	1.33		
	S_2	582	0.12		
P2a	S_1	606	0.19	689	0.12
	S_2	563	0.25	609	0.33
P2a-DMF	S_1	617	0.45		
	S_2	571	0.25		
P3a	S_1	625	0.10	671	0.05
	S_2	587	1.05	590	0.18
P3a-DMF	S_1	604	0.38		
	S_2	571	0.35		
Pc1a	S_1	656	1.84		
	S_2	610	0.25		
Pc2a	S_1	606	0.19		
	S_2	563	0.25		
Pc3a	S_1	625	0.10		
	S_2	587	1.05		

Table 5.2: Resulting absorptions and oscillator strengths for the first two excited states of **P1a**, **P2a** and **P3a** using a range of functionals. Wavelenths are in nm.

	CAM-B3LYP		M06-2X		B3LYP		PBE0	
P1a	656	1.84	668	1.98	826	1.26	787	1.43
	610	0.25	606	0.13	702	1.26	673	0.03
P2a	606	1.33	588	0.22	613	0.41	600	0.42
	563	0.12	545	0.30	588	0.27	573	0.26
P3a	624	0.10	617	0.10	725	0.04	691	0.04
	587	1.11	583	1.14	633	1.04	616	1.09

P type chromophores and is due to the non-symmetric centre core macrocycle.

The most likely reasons for such a large disparity with respect to experiment are unsuitable functional/basis set combination and/or absence of solvent effects. A functional test was therefore set up for the **P1a** to **P3a** series, using as alternative long-range corrected functionals - M06-2X[95] - as well as two hybrid functionals without a correction - PBE0[212] and B3LYP[93]. Table 5.2 show that all functionals reproduce the same pattern, meaning that the reordering of the calculated states compared to the experimental states is not a functional effect. In the case of the B3LYP functional the states are also very poorly described and the lack of long-range correction to the behaviour of the exchange is clearly crucial for charge transfer states such as the ones involved in push-pull-type chromophores.

In order to investigate the solvent effect the same series (**P1a** to **P3a**) was also computed using the PCM. This does not take into account any specific solvent interactions but rather calculates the effect of the system located in a cavity of solvent specified by its dielectric constants. The Gaussian09 standard dielectric constants for DMF was used with the non-eqiuilibrium solvent model in order to avoid the the solvent cavity adjusting to the excited state geometry. As presented in Table 5.1, the addition of a solvent environment continuum around the system leads to a linear absorption spectra that reproduces the experimental trend in the shifts and relative intensities of the Q-band well. For reproducing accurate experimental absorption spectra using linear response DFT, solvent effects are therefore recommended. The solvatochromic effects determined leads to information regarding shifts in the absorption bands, in both OPA and TPA, but the effect on intensity profiles is determined only for OPA. The calculation including solvent effects on TPA is not determined

here, although the methods exist [132, 196, 197].

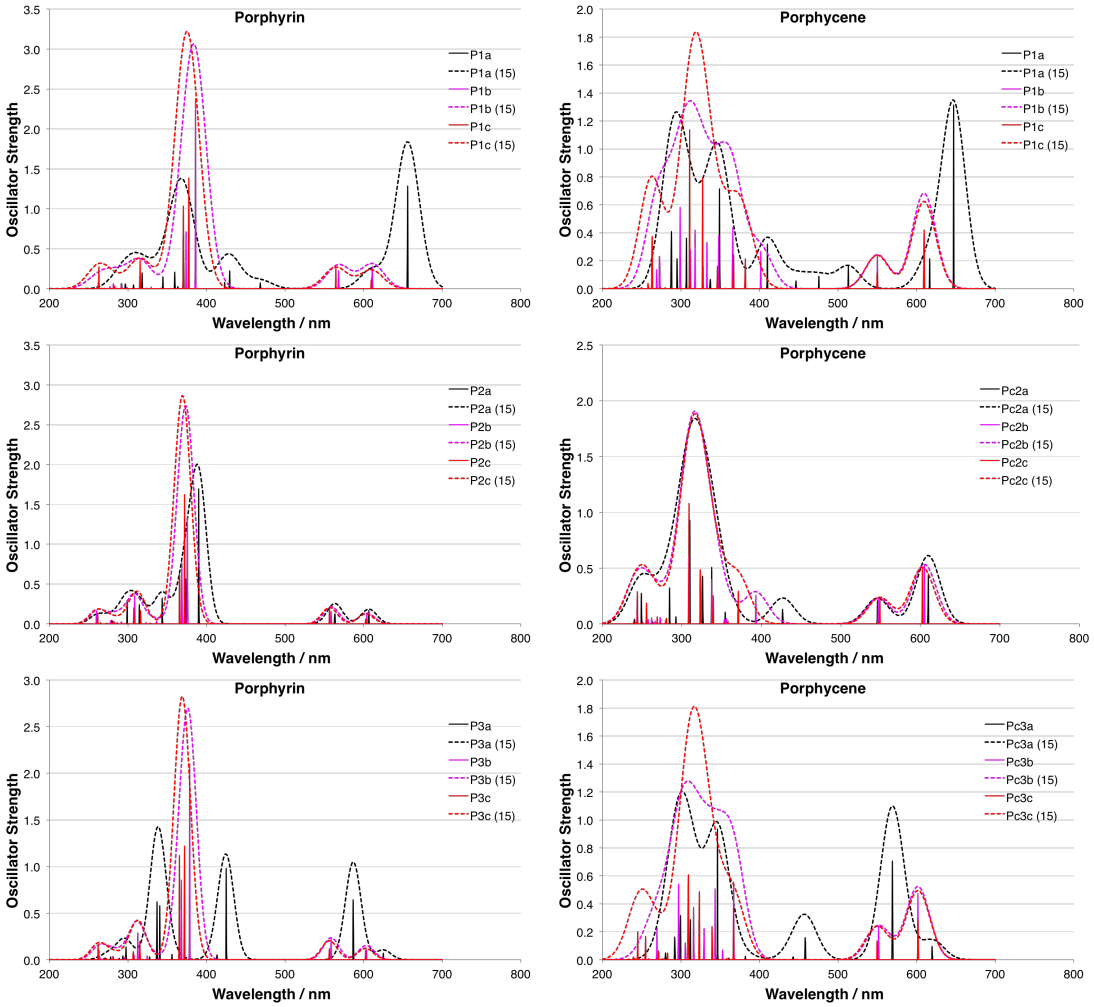

Figure 5.4: Each series represent sets of push-pull (series 1), push-no-pull (series 2) and no-pushpull (series 3) with substituent with varying electron withdrawing/pulling and donating/pushing effects. Dashed lines indicate gaussian broadening functions being used ($\sigma = 15nm$).

In Figure 5.4 the complete set of **P** and **Pc** derivatives are presented, plotted with gaussian functions with 15 nm broadening, as well as in the form of the actual calculated transitions in stick format. The effect of increasing the push/pull strength of the substituent is generally very small, with oscillator strengths and absorption wavelengths in the Q-band staying within $\leq$ 0.1 a.u. and $\leq$ 5 nm respectively. This is true across all three series, with the notable exception of the very strongly electron

Table 5.3: Absorption wavelengths for the TPA of the **P** series with signals that have a *real* state near half the wavelength of the transition, indicating resonance enhancement

	OPA (eV)	TPA (eV)	δ^{TPA}
P1a	1.89	**3.75**	4.7 $\times 10^6$
P2a	2.04	**4.15**	4.8 $\times 10^8$
P3a	1.98	3.79	1.0 $\times 10^4$

pulling methylpyridinium substituent (**P1a**, **Pc1a**, **P3a** and **Pc3a**).

5.3.3 Quadratic Response

5.3.3.1 TPA

The TPA transition strength for **P** and **Pc** with substituents with varying electron pushing and pulling ability (the **1-3a** sets for **P** and **Pc**) is presented in Figure 5.5, as a function the excitation energy. As expected from the consideration of OPA resonance enhancement of the TPA signal (as discussed in the previous chapter for substituted **Pc**), the strongest transitions is away from the Q-region of the spectra. Only the Soret- region is therefore presented. Resonance enhancement also makes it problematic to compare absolute TPA transition strength values, and therefore it is common to only compare *relative* TPA transition strength when using non-damped quadratic response theory. For the **P** series, the push-pull and push-no-pull substitution patterns both yield large TPA signals, whilst the no-push-pull system has little or no absorption in this region. This seems to reflect the hypothesis for these compounds, in that an electron donating substituent is more important than an electron withdrawing one for the non-linear optical effects. Investigating the signals in detail, with specific attention to the possibility of resonance enhancement, shows that the position of the states needs to be considered, as a result of the donor type. In Table 5.3 the maximum TPA transitions are presented, next to the first excites state of the **P1-3a** series. In the case where there is suspected OPA resonance enhancement of the signal, the excitation energy is highlighted in bold. This indicates that resonance enhancement is crucial for the observed increase.

Looking at the general effect of the strength of the electron push/pull substituent, it seems that the presence of the nitrophenyl withdrawing group shows a large TPA

transition strength in **P1b** and **P3b**. Contrary to the OPA case, the transition strength is more affected by the nature of the substituent, and its effect on the position of the states, rather than its electron withdrawing capabilities per se.

Due to resonance enhancement Pc is expected to have a larger TPA over all due to the favourable position of the Q-band in the OPA spectra. This is reflected here for the whole series (apart from **Pc1c**, which does not have complete data at the moment of writing). Unlike the **P** case, the TPA trend here seems to disagree with the hypothesis that the electron push/pull substitution pattern does affect the transition strength. When investigating the effect of push/pull strength on the TPA spectra in Figure 5.6, it is also evident that the substitution type has a large effect on the strength of the signal. It is however inverted compared to expected, with increasing δ^{TPA} for decreasing push/pull strength.

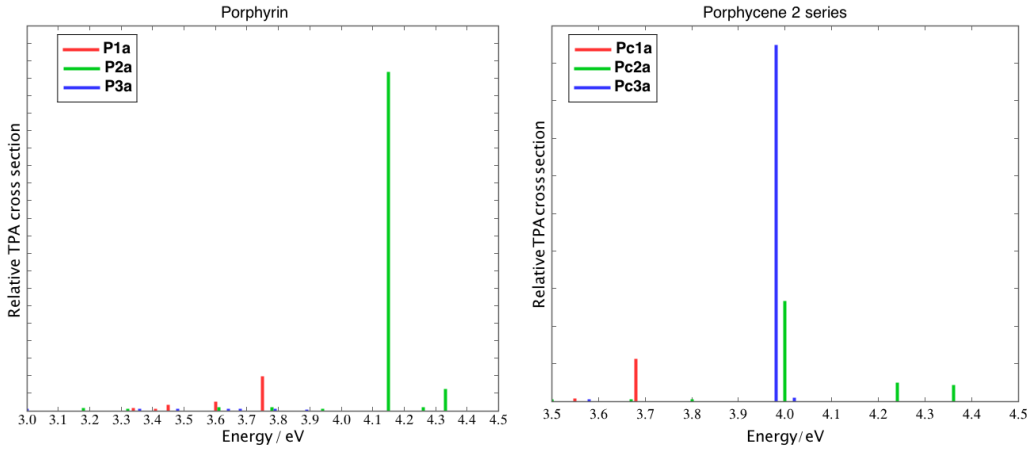

Figure 5.5: TPA transition strengths are displayed as a function of the energies of the states for the Soret-band energy region. Push-pull is displayed in red, push-no-pull in green and no-push-pull in blue.

5.3.3.2 SHG and static hyperpolarisabilities.

As the creation of a SHG photon, contrary to a TPA, is commonly considered to be a scattering process, it is interesting to see the effect of the substitution pattern in the case of both the static and dynamical hyperpolarisabilities. First, the SHG response was determined using response theory, both for the static, $\beta_{zzz,0}$, and the dynamical, β_{zzz}, case, as illustrated in Table 5.4. For the dynamic situation, the evaluation was

Table 5.4: Hyperpolarisabilities for the **P** series (a.u.)

Property	P1a	P1b	P1c
$\beta_{zzz,0}$	206892.11	37204.07	9557.05
$\beta_{zzz,800}$	892081.45	1102190.00	146515.12
Property	P2a	P2b	P2c
$\beta_{zzz,0}$	26062.43	11130.94	1317.22
$\beta_{zzz,800}$	1320180.00	190200.14	30247.25
Property	P3a	P3b	P2c
$\beta_{zzz,0}$	52902.65	16886.17	3156.42
$\beta_{zzz,800}$	687495.80	294592.37	16443.33

carried out at 800 nm, as this is a common SHG imaging wavelength to use with current instrumentation. To illustrate the point better, the results were also plotted in Figure 5.7. In these results there is clear evidence of the effect of the substitution pattern on the *dynamical* β. Just as in the work by the Anderson group, the push-no-pull systems show a striking increase in the β_{zzz}. As this is the component that normally dominates the SHG signal, these are promising results. The effect of the transition strength, introduced in Figure 5.8, is as predicted across the series, with a decline in both $\beta_{zzz,0}$ and β_{zzz} as the strength increases, apart from in the case of the nitrophenyl, where the effect is more pronounced, just as in the TPA study.

In response theory methods the results are obtained without the need for evaluating the sum-over-state expression explicitly. This implicit all-state approach does have some drawbacks, such as the artificial strengthening of the signal to too large a degree in resonance enhanced TPA. One further point is that the method does not shed light on the specific components that are involved in the property. In order to attempt to pinpoint a structure-β relationship, the static hyperpolarisability was also determined using a TSA.

The static results from the TSA are presented in Table 5.5, and the data for the specific components used are listed in Table 5.6. Both methods produce a $\beta_{zzz,0}$ response that is largest in the case of a traditional push-pull set up. The TSA approach seems to also reproduce the pattern that the push-no-pull system has the smallest static component of the three. As the data is available for each of the components that make up the $\beta^{TSA}_{zzz,0}$ it is straight forward to conclude that the combination of a large transition dipole moment to either of the states used in the description is crucial

Table 5.5:

Property	P1a	P2a	P3a
$\beta_{zzz,0}$	206892.11	26079.20	52891.20
$\beta^{TSA}_{zzz,0}$	563647.71	76305.12	286624.18

Table 5.6: The static and dynamic βs decrease with decreasing substituent push/pull strength, apart from in the case of the nitrophenyl derivative (**P1b**)

TSA component	P1a	P2a	P3a
$\delta\mu_{01}$	-3.38393468	0.15900722	2.19557816
$\delta\mu_{02}$	-1.4054418	0.49227833	0.28569911
μ_{01}	-6.2880701	1.9184143	0.93780315
μ_{02}	-2.029375	1.9723327	-4.4985528
μ_{12}	-0.16744863	0.11085215	-0.35791829
δE_{01}	6.95E-02	7.51E-02	7.29E-02
δE_{02}	7.46E-02	8.09E-02	7.76E-02

for a large response. The use of NTOs to visualise the transitions is also useful, and the orbitals for the specific transitions are introduced in Figure 5.9, and highlight the important CT transitions.

5.4 Conclusion

The OPA results that were calculated in this chapter indicates that it is important to include solvents for response calculations, if the results are to be compared with experimental data. As the solvent affects the position of the states, it would also be a good continuation of this work to run TPA calculations in solvent too. This is due to the fact that TPA strength is very dependent on the positioning of the states, relative to each other. The exciting case of properties that depend on scattering processes, such as the dynamical β_{zzz}, seems to be that they do not conform to traditional argument when it comes to their enhancement. In the case of absorption involving an existing state however, an increase in the transition moment *as well as* the relative position of any intermediate states, plays a crucial role. But for the scattering dynamics, there seems to be no effect of the latter. Porphyrin, and its reduced isomer porphycene, are both macrocycles that seem to be able to act as an electron acceptor in their own right. This means that the addition of an electron

pulling substituent might not be needed for the synthetic development of imaging dyes for SHG, leading to a much simplified process.

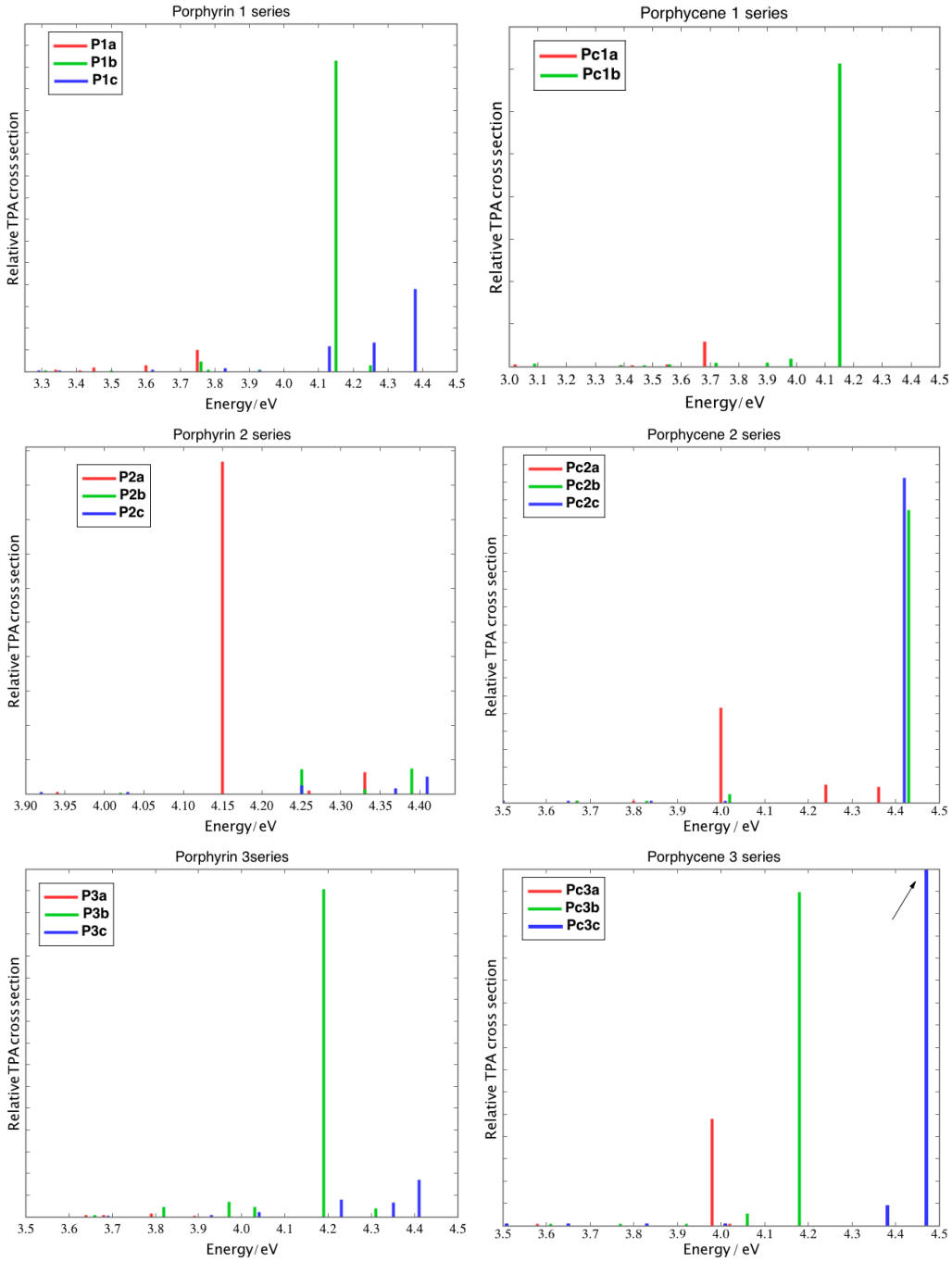

Figure 5.6: TPA transition strengths are displayed as a function of the energies of the states for the Soret-band energy region. The electron push/pull strength is decreasing in the order from red to green to blue. Note the arrow in the Porphycene 3 series, which indicates a very large TPA transition strength, out of range.

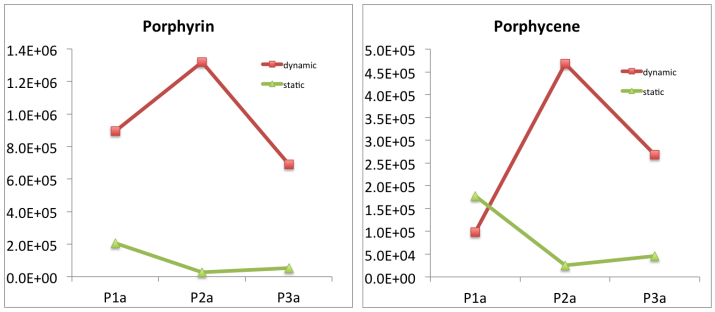

Figure 5.7: Hyperpolarisabilities (dynamic in red and static in green) of both the **P** and **Pc** set going from push-pull, push-no-pul to no-push-pull.

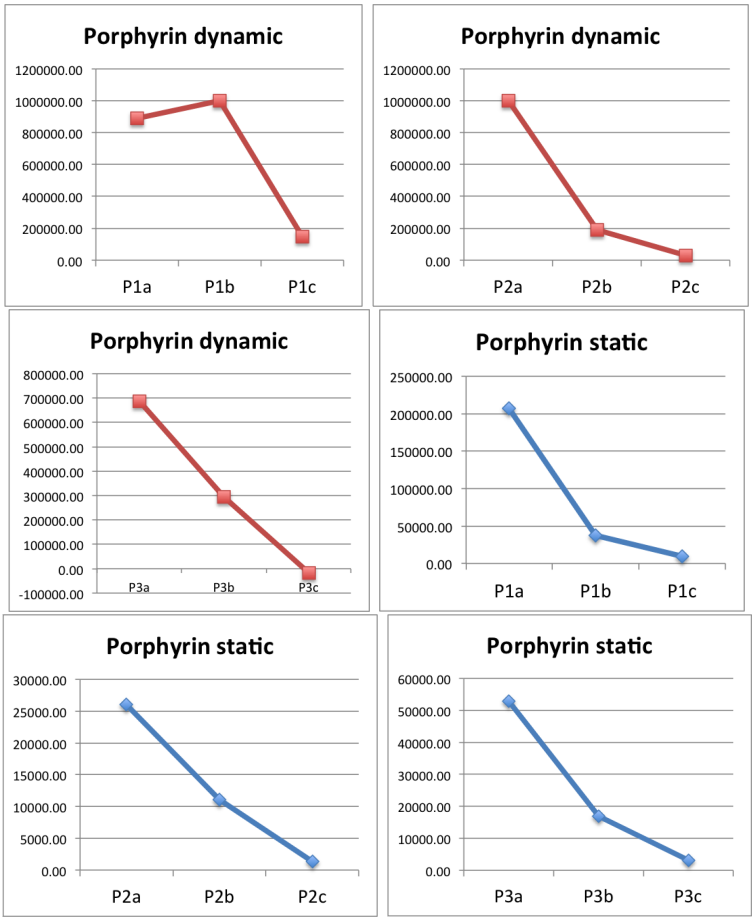

Figure 5.8:

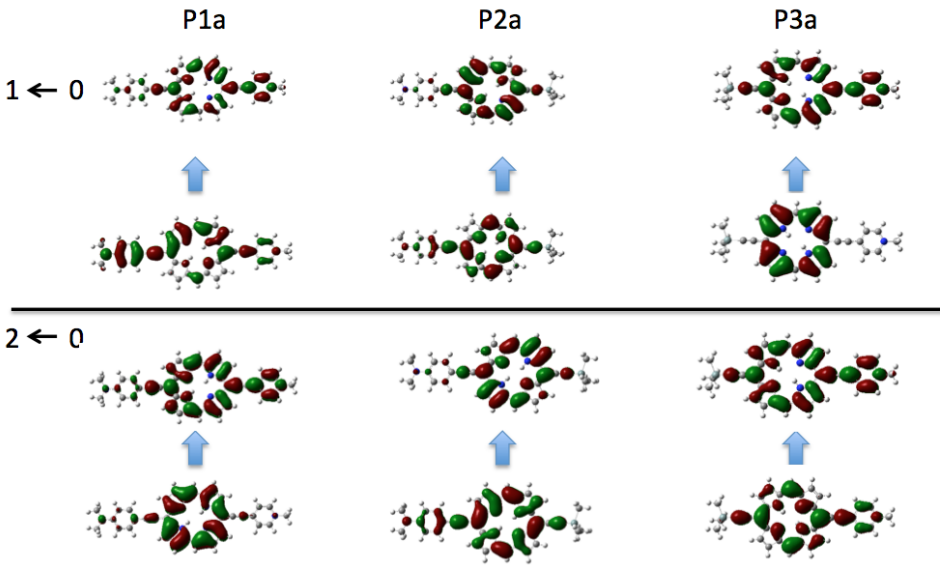

Figure 5.9: Natural transition orbitals for the first two states in the P1-3a series

Chapter 6

The effect of the electronic structure on the linear and non-linear absorptions in porphyrins

6.1 Introduction

Even though porphyrins have been investigated for decades, modern synthetic chemists continue to expand and investigate the structural changes that can be made to a porphyrin - type system. From the viewpoint of the photochemist it is interesting to see the changes to the absorption characteristics these modifications have, in order to possibly pinpoint new photosensitiser agents for PDT.

The first constitutional isomer of the core porphyrin (**P**) system to be presented was the Porphycene (**Pc**) macrocycle, already introduced in the previous two chapters, and since then related varieties such as Hemiporphycene (**HPc**) and Corrphycene (**CPc**) have also been developed (Figure 6.1).[185, 213] These structural isomers have similar properties to the parent **P** in terms of structure and coordination, and have been shown to have porphyrin-like OPA spectra with variations only in the intensity profiles, caused by change in the symmetries of the species, rather than absorption wavelength.[115] As early as the 1940's it was realised that a structural isomer did not need all its Nitrogen atoms pointing into the centre of the core macrocycle, but could experience confusion of the pyrrole unit, and keep its stability.[214] It was not until

1994 that the first of the confused porphyrin isomers were actually synthesised, with N-confused porphyrin (**NCP**) being reported independently by two groups.[215, 216] Due to the change in conjugation pathway in the molecule, confused porphyrins have properties that varies from the parent **P**, in physical, structural and coordination properties. Examples are their multivalent character as a metal ligand, fusion properties in aggregates, and a red-shift seen in OPA measurements.[217] Further work also showed the doubly-confused (**N_2CP**) to be relatively stable.[218] Research into new and more efficient synthetic routes continues to lead to the discoveries of novel **P** isomers, the latest being the Neo-confused porphyrin (**NeoCP**). These have one pyrrole unit oriented so that its N atom is fused to carbon in a position known as the *meso*-position of the macrocycle (Figure 6.1).[219] The preliminary investigation into the photochemical properties of this latest structural isomer show a porphyrin-like linear absorption pattern.

One alternative approach for structural change in porphyrin-type systems is to attempt to alter the electronic structure of the macrocyclic core though atom substitution. Changing one nitrogen atom in the porphyrin core to a heavier sulphur or selenium atom has been shown facilitate larger spin-orbit coupling, which is advantageous for PDT, but have only a slight shift in the absorption maximum to longer wavelengths (to 665 nm). Substitution of a further N atom with S or Se moves the absorption maximum to longer wavelengths, but shows a negative effect in the generation of singlet oxygen. Even though the singlet oxygen generation is decreased in the structures where two core heteroatoms have been substituted, they have been proven to be more effective than meso-substituted pure porphyrin cores in in vivo studies.[140, 220] A change of the central atom to a group 16 atom has also been shown to change the compound ability to chelate to a metal, which has been suggested to improve the availabilty for bio-applications.[220]

The avenue for the use of core-substituted macrocycles for TPA PDT is still in its early stages of investigation, but does show some promise. Small changes in the electronic structure of extended, and bridging, porphyrins through the substitution of nitrogen atoms for oxygen atoms in the pyrrole-units of the macrocycle had a minor effect the OPA signature, whilst it afforded a very large change in the TPA spectra. [221, 222] As this can provide a powerful mechanism, where the TPA can be improved without large structural additions, we set out to systematically investigate

the **P** macrocycle and its reduced and isoelectronic isomers and their OPA and TPA properties.

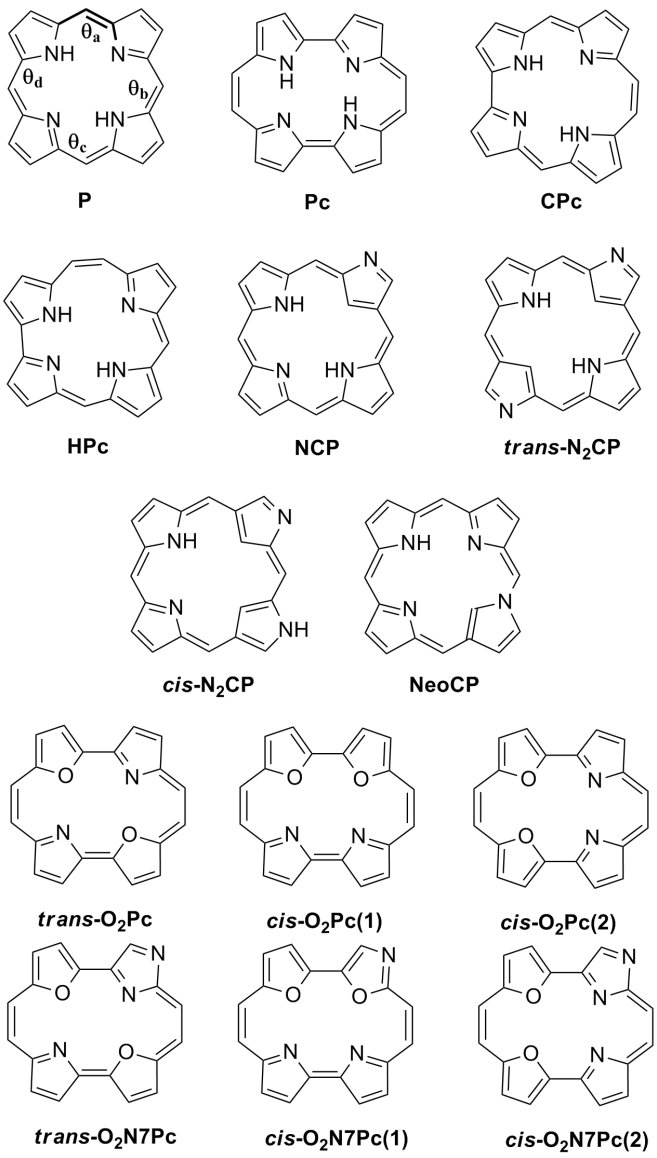

Figure 6.1: The structural electronic isomers investigated herein. The dihedral angles referred to in geometry discussion is highlighted in **P** (spanning from C in the meso–position to N on the subsequent pyrrole unit, as per the bold bonds in θ_a).

In this study, absorption calculations were carried out for **P**, **Pc**, **HPc**, **CPc**, **NCP**, **N_2CP** and **NeoCP**, to provide an overview of constitutional porphyrin isomers and

their OPA and TPA properties. In order to get a deeper understanding of how δ^{TPA} is effected by the electronic structure of the core, we also a series of dioxa-porphycenes together with a set of dioxa-porphycenes with a N atom in its confused position, according to Figure 6.1.

Several experimental and theoretical investigations have been carried out on the TPA qualities of **P** as well as **Pc**, and the latter shows exceptional promise as a TPA PDT sensitiser due to its exceptionally large δ^{TPA} compared to the **P** core.[114–116] The δ^{TPA} of **NCP** have also been investigated experimentally, and show similar properties to the **P** core.[223] As far as we are aware neither **HPc**, **CPc** nor **NeoCP** have been reviewed for their TPA properties.

6.2 Computational Methods

The ground state geometries of each molecular system were optimised and analytical Hessian calculations were preformed to confirm the nature of each stationary point on the potential energy surface.

At each confirmed ground state optimised geometry vertical one- and two-photon absorption spectra were computed using linear response and quadratic response DFT respectively. All geometry optimisations and OPA linear response calculations were computed using Gaussian 09,[160] whilst TPA quadratic response theory calculations were performed using a local version of the Dalton 2.0 program.[161] The robust CAM-B3LYP functional, with the 6-31G** Pople-type basis set on all atoms, were used throughout and, in order to analyse the nature of the electronic transitions in detail NTOs were calculated for each transition.[139]

6.3 Results and Discussion

6.3.1 Reduced Porphyrin Isomers.

All four N-sites in the **P** parent are possible binding sites of the two inner hydrogen atoms and even though the *cis*-isomers, with hydrogens on adjacent N-sites, in general are less stable they are known to take part in the step-wise N-H tautomerism observed in **P**.[224–226] It was therefore considered pertinent to include all possible

cis-isomers of the reduced isomers investigated here, and analyse their optical response. The optimisation results of the reduced porphyrin isomers, with their pyrrolic hydrogen atoms in the *cis* as well as *trans*-position, all resulted in a planar series of systems, apart from *cis*-**Pc-2** (Figure 6.2 and Figure 6.3). *Cis*-**Pc-2** did not suggest itself to be stable as a free base, and theoretical and experimental work suggests that there is in fact a crossing point between the *cis* and *trans* surfaces along the tautomerisation path, rendering this isomer unacessable for the unsubstituted free base [227]. No optical response was therefore calculated for this isomer. The overall results confirm previous theoretical, as well as experimental, studies of these compounds [190, 228, 229]. Table 6.1 describes the relative energies and symmetries, which can be rationalised by the consideration of angle strain as well as hydrogen bonding stabilising factors.

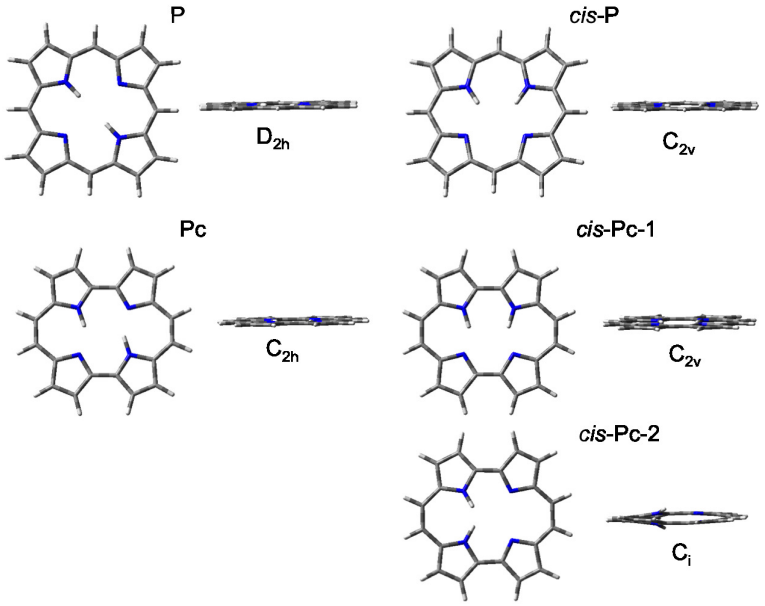

Figure 6.2: The optimised geometries of **P** and **Pc**, and their respective *cis* and *trans*-isomers, from which the absorption qualities were calculated.

The smaller rectangular cavity of **Pc** contributes to favourable hydrogen bonding interactions, making it the most stable isomer investigated. For the two isomers with trapezoidal cavity hydrogen bonding stabilises **HPc** to a larger extent than **CPc**, counteracting angle strain, rendering the latter the least stable of the reduced set of isomers. These steric strains are not enough to take the $(4n+2)\pi$-electron struc-

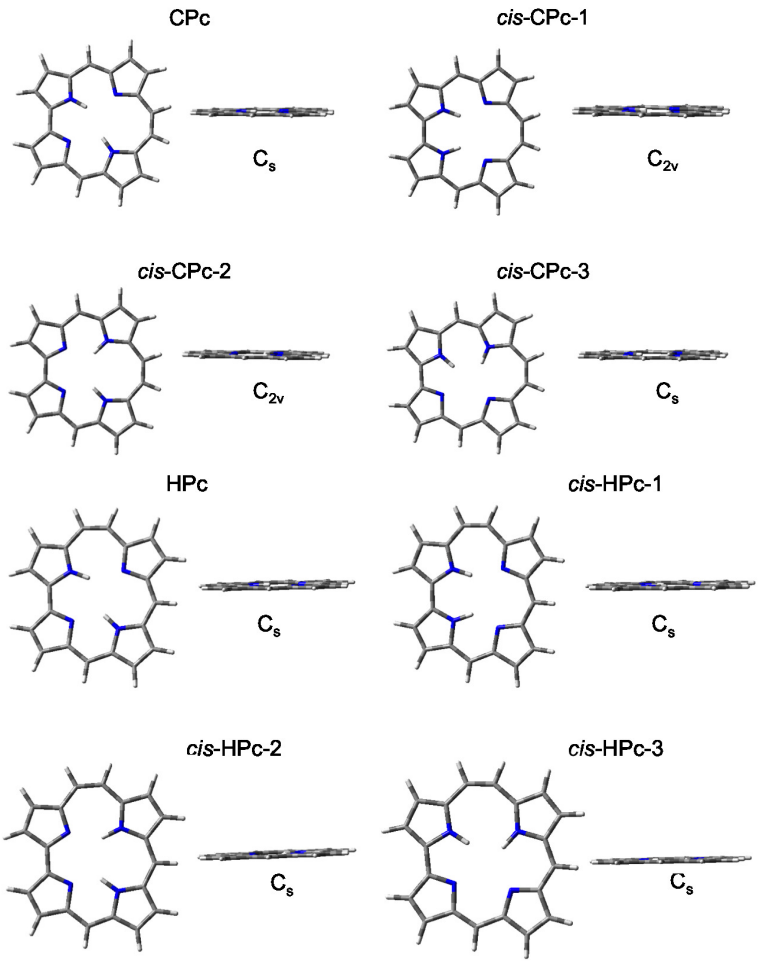

Figure 6.3: **CPc** and **HPc** isomer optimised geometries. These were used to calculate vertical OPA and TPA transitions.

tures out of planarity, and thereby break the aromaticity. The energies of the more symmetrical of the *cis*-isomers of **CPc** suggest that they are stable, and indeed rapid tautomerisation of the central hydrogen atoms has been shown experimentally[213].

The simulated spectra of the set of reduced porphyrin isomers show two dominant regions of absorption for the series, one in the 200–350 nm region and one at 470–570 nm as seen in Figure 6.4 and Table 6.2. These two regions have been characterised extensively for the prophyrin family over the years, and in fact no other compound have probably been analysed in terms of its UV–visible spectrum more than the **P** free base.

Table 6.1: Optimised parameters of the series of reduced porphyrin isomers. The relative energies (kJ/mol) of the *trans*-isomers are with respect to the **P** parent macrocycle, whilst the relative energies of the *cis*-isomers are with respect to their respective stable *trans*-conformer

Compound	Point Group	Energy (a.u.)	Δ E (kJ/mol)
P	D_{2h}	-989.0240	0
cis-**P**	D_{2h}	-989.0105	34.11
Pc	C_{2h}	-989.0254	-3.54
cis-**Pc-1**	C_{2v}	-989.0223	8.14
cis-**Pc-2**	C_i	-988.9784	123.40
CPc	C_s	-989.0062	46.74
cis-**CPc-1**	C_{2v}	-988.9977	21.47
cis-**CPc-2**	C_{2v}	-988.9966	24.25
cis-**CPc-3**	C_s	-988.9775	72.51
HPc	C_s	-989.0180	15.58
cis-**HPc-1**	C_s	-989.0108	18.19
cis-**HPc-2**	C_s	-989.0078	25.77
cis-**HPc-3**	C_s	-988.9854	64.17

In the **P** macrocycle the GFO model predicts a cancellation of transition moments into the Q-region and a complementary strengthening of transition moments into the Soret-region, which is reproduced here. There are plenty of theoretical results which support the use of the GFO model for the assignment of the transitions into these regions in **P**.[44] When it comes to the reduced **Pc** and **HPc** derivatives however, there is a clear strengthening of the Q- relative to the Soret-region. This is a well known phenomenon and results from the two LUMO-orbitals no longer being near degenerate. The relative location of the states in the Q-region will be important when discussing the TPA absorption pattern (*vide infra*).

The optical responses of the *cis*-isomers of the reduced isomers follow the same trends, with clear Soret– and Q–bands, as their *trans*-isomers, including the relative strengthenings of the Q–bands in **Pc** and **HPc** (Table 6.2). *cis*-**CPc-3** experiences strengthening of the transition in the Q–region, contrary to what was found in the parent *trans*-isomer, similar to the case of **Pc**.

In the **Pc** and **HPc** derivatives the NTOs that describe the transitions making up the Q-band show absorption from the HOMO and HOMO-1 orbitals exclusively into one of the LUMO pair, in accordance with the GFO model. In the Soret–region

Table 6.2: Overview of the wavelengths (λ) and oscillator strengths (f) for key transitions from the linear response of reduced **P**–isomers

	Absorption			
Compound	Q-region		Soret-region	
	λ (nm)	f	λ (nm)	f
P	559	0.0021	345	0.8416
	507	0.0015	333	1.1671
cis-**P**	552	0.0002	346	0.7953
	516	0.0061	339	0.8892
Pc	564	0.1578	310	0.7557
	534	0.2343	304	0.7721
cis-**Pc-1**	557	0.1835	309	0.6951
	533	0.1979	300	0.9271
CPc	497	0.0003	348	0.5164
	463	0.0028	340	1.1576
cis-**CPc-1**	494	0.0035	338	0.5945
	470	0.0683	336	1.0433
cis-**CPc-2**	496	0.0001	349	0.4497
	476	0.0325	343	0.9356
cis-**CPc-3**	548	0.0121	356	0.3191
	503	0.1318	342	0.8802
HPc	491	0.0899	337	0.4450
	486	0.0380	336	0.6407
cis-**HPc-1**	521	0.1432	334	0.2599
	478	0.0383	330	0.5922
cis-**HPc-2**	538	0.0229	344	0.5115
	521	0.0647	333	0.6249
cis-**HPc-3**	514	0.1454	332	0.4894
	477	0.0619	318	0.5610
			304	0.7344

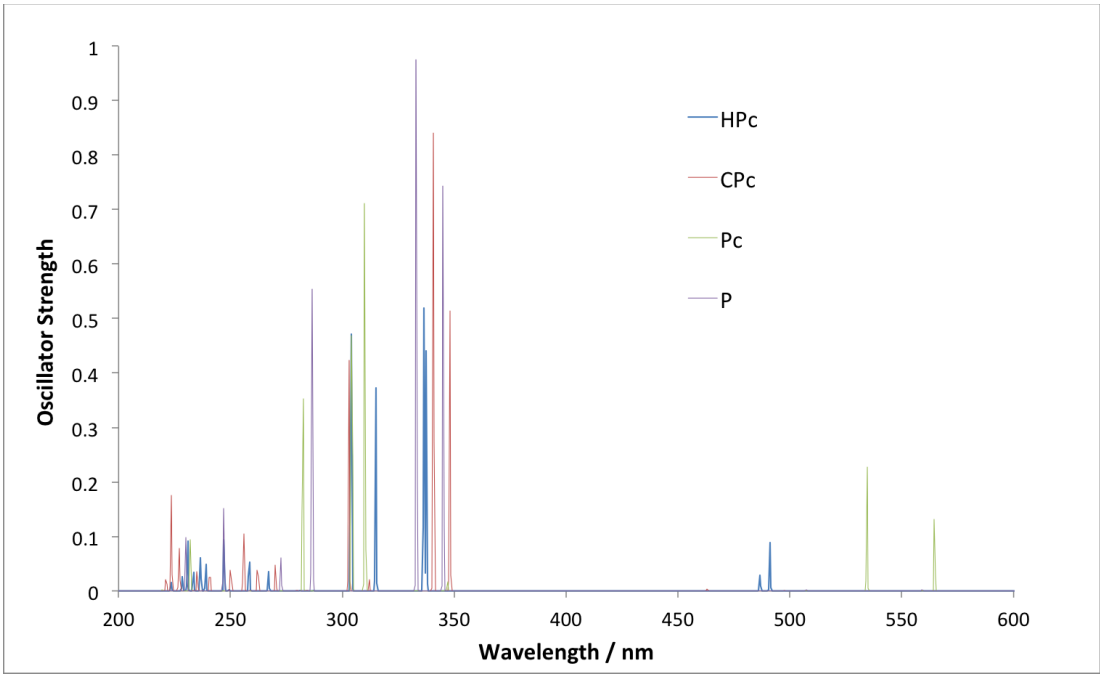

Figure 6.4: Simulated OPA spectra for a selection of the reduced porphyrin isomers, as well as the parent porphyrin (**P**), all showing main absorption into the 300–350 nm Soret-region. The absorption into the longer wavelength (470–570 nm) Q-region is present for all but strongest for **Pc** and **HPc**.

however, **HPc** show more than the two transitions that are expected above 300 nm, if the GFO model is used. Analysis of the NTOs confirms that the region consists of transitions amongst N-type orbitals (see at 315 nm in Figure 6.5). For **Pc**, a significant contribution can also be seen at higher energy than the Soret-region from transitions from an orbital that mainly can be described as the HOMO-2 frontier orbital.

The TPA spectra all show a clear main absorption into the Soret-region, at 200 - 300 nm, and very small absorption into the Q-region (Fig. 6.6 and Table 6.3). The effect on the absorption wavelength of the reduced isomers in comparison to the parent **P** is a blue shift with the wavelength of maximum absorption going from 285 nm for **P** to 264 nm for **Pc**, 246 nm for **HPc** and 226 nm for **CPc**. It is worth to note that these correspond to a wavelength of incoming light of twice that wavelength, in the area of 450 - 528 nm.

The δ^{TPA} for all reduced isomers is also presented in Table 6.3 and Figure 6.6 and

Table 6.3: Key transitions from the quadratic response calculations of the reduced **P**–isomers.

Compound	Absorption			
	Q-region		Soret-region	
	λ (nm)	δ^{TPA} (a.u.)	λ (nm)	δ^{TPA} (a.u.)
P	419	1.11×10^3	321	4.47×10^3
			285	4.51×10^6
cis-**P**	549	88.1	337	19.4
	515	54.8	309	42.0
Pc			299	3.42×10^4
			267	2.37×10^8
cis-**Pc-1**	554	3.11×10^2	279	3.55×10^6
	530	1.51×10^2	260	1.28×10^7
CPc	494	6.12×10^2	338	5.75×10^1
	461	2.03×10^3	261	1.43×10^2
cis-**CPc-1**	492	3.80×10^2	338	2.78×10^2
	466	2.41×10^3	309	4.35×10^3
cis-**CPc-2**	547	3.82×10^2	276	1.14×10^5
	502	1.45×10^3	255	3.55×10^5
cis-**CPc-3**	488	1.27×10^2	238	3.56×10^4
	466	2.01×10^3	231	1.66×10^6
HPc	488	6.04×10^2	246	1.40×10^7
	484	1.21×10^3	235	4.79×10^5
cis-**HPc-1**	519	6.40×10^2	260	3.49×10^7
	575	5.68×10^2	239	3.15×10^7
cis-**HPc-2**	535	4.12×10^2	263	2.15×10^5
	519	2.87×10^2	259	1.25×10^9
cis-**HPc-3**	513	1.27×10^3	259	4.34×10^6
	475	4.79×10^2	237	2.68×10^8

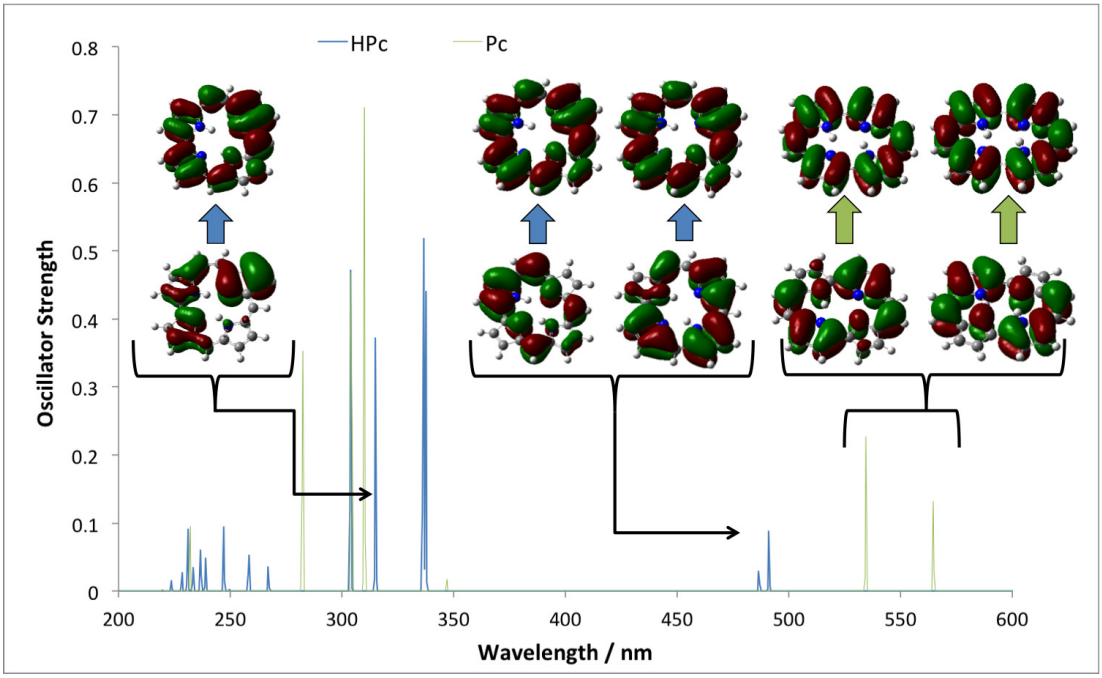

Figure 6.5: NTOs calculated for **Pc** and **HPc** show GFO transitions into the Q–region, whilst the Soret–region displays non-GFO transitions, which highlights that tis method needs to be expanded in order to fully describe relevant states for reduced isomers.

the main feature is the exceptionally large value that can be seen for **Pc**, compared to the parent **P**, an increase that is also evident in the *cis*-**HPc-2** isomer, as well as to some degree for *cis*-**CPc-3**. These three were the same set of compounds that were shown to have strong, non-cancelling, transition strengths in the Q-region of the OPA spectrum. The reason for the corresponding increases in δ^{TPA} is caused by one photon resonance enhancement of the two photon signal.[48] The effect of resonance enhancement is clearly seen in the case of the free **Pc** macrocycle as well as in *cis*-**HPc-2** and *cis*-**CPc-3**. The large difference in the TPA transition strength in compounds differing in only the position of the coordination of the core hydrogen shows how exceptionally subtle the effects can be, and how sensitive TPA properties are to the position of the various states and the possibility of resonance enhances transitions. Resonance enhancement also rationalises why there are only very weak TPA transitions to be seen in the *Q*-region for any of the investigated chromophores, as there is no allowed one-photon transition near half the wavelength value of this

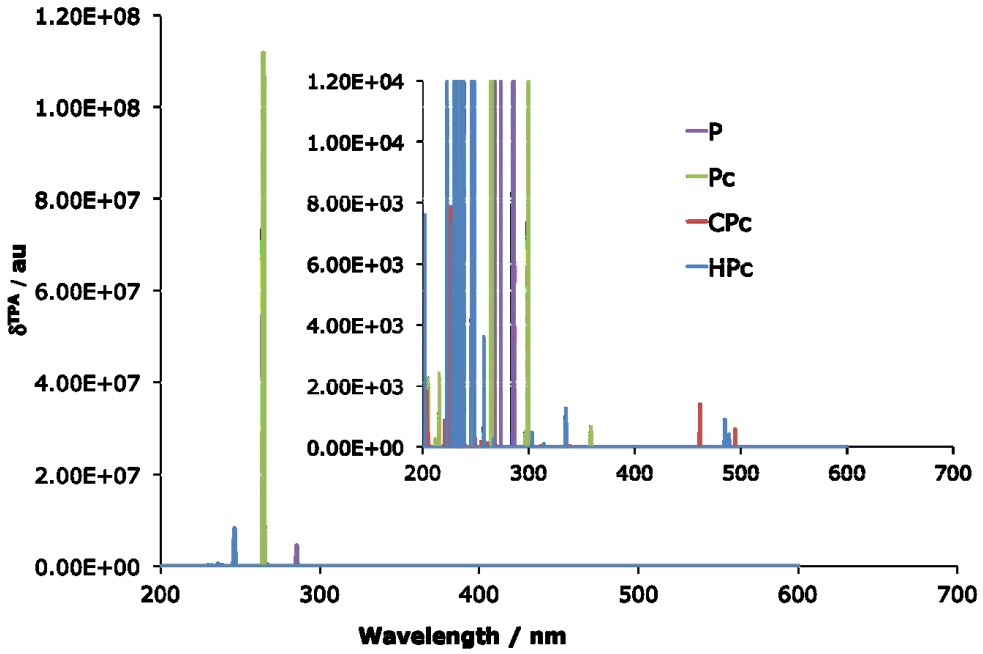

Figure 6.6: Simulated TPA spectra for reduced porphyrin isomers. Note the change in scale between the two versions. All isomers show absorption into the 200-350 nm Soret-region.

region.

6.3.2 Confused Porphyrin Isomers.

The resulting geometries of the confused porphyrin isomers are displayed in Figure 6.7 as well as 6.4.

The planar **NCP** structure optimised to a second order saddle point, with two imaginary vibrational frequencies. Both of these vibrations were related to the relief of steric crowding in the macrocyclic centre, by the out-of-plane movement of the confused pyrrole ring, with the methylene H in the centre of the ring bending out of the plane made by the remaining pyrrolic rings (θ_a in Table 6.4). Optimisation of the planar *trans*-**N_2CP** lead to a fourth order saddle point with the four vibrational modes also describing relief of the steric crowding in the centre. Optimisation along the four modes resulted in two minima, one belonging to the C_2 point group (*trans*-**N_2CP(1)** in Table 6.4) and one with 12.71 kJ/mol higher minimum energy and with

Table 6.4: Optimised parameters of the series of confused porphyrin isomers. The dihedral angle is described in Figure **??**.

Compound	**Optimised dihedral angles**				**Point Group**	**Δ E (kJ/mol)**
	θ_a	θ_b	θ_c	θ_d		
NCP	10.04	-1.78	0.00	-3.61	C_1	
trans-**N_2CP(1)**	-11.57	5.77	-11.57	5.77	C_2	0
trans-**N_2CP(2)**	10.12	4.66	-10.12	-4.66	C_i	12.71
cis-**N_2CP(1)**	-8.34	14.88	1.91	0.62	C_1	0
cis-**N_2CP(2)**	8.31	-14.87	-1.91	-0.62	C_1	2.31×10^{-4}
NeoCP	0.29	-2.64	0.14	0.52	C_1	

C_i symmetry (*trans*-**N_2CP(2)** in Table 6.4). The *cis*-**N_2CP** optimisation also yielded two geometries, both of C_1 symmetry (*cis*-**N_2CP(1)** and **(2)** in Table 6.4). It is evident from their relative energies and dihedral angle data in Table 6.4 that these are each other's inverts.

The OPA spectra for the N-confused isomers are displayed in Figure 6.8 and Table 6.5. The classic GFO-related transitions can be seen for these compounds as well as the reduced isomers, in a clear dominant region of absorption in the 200–370 nm Soret-region. The absorption into the Q-region is significantly weaker than in the classic case however, with only two clear transitions at 505 nm and 560 nm for **NeoCP** and *cis*-**N_2CP(2)** respectively. An NTO analysis of these compounds show the classic absorption amongst the Gouterman orbitals for all compounds, with the expected transitions amongst the GFOs in the Soret and Q-region. These are visualised in the **NeoCP** example in Figure 6.9 by transition **4** and **1**. There are also, however large contributions into the Soret-region by non-GFO transitions. Transition **8** show an orbital that can mainly be described as HOMO-2 to a GFO LUMO whilst transition **3** show main electron density in a LUMO+2 – like porphyrin orbital after the transition. This yet again highlights the fact that an orbital–based model must be used with caution when analysing spectra of electronic isomers of porphyrins.

The TPA spectrum for the confused set of porphyrins are shown in Table 6.6 as well as Figure 6.10, where the **P** signals have been added for comparison. As with the reduced isomers, one photon resonance arguments rationalises the fact that all compounds have little or no absorption into the Q-region, as there is no OPA signal near half of the TPA. Contrary to the reduced isomers, there is a negative effect on

Table 6.5: Key transitions from the OPA calculations of the confused set of isomers, in terms of their wavelengths (λ) and oscillator strengths (f).

Compound	Absorption			
	Q-region		Soret-region	
	λ (nm)	f	λ (nm)	f
NCP	597	0.0023	369	0.5473
	518	0.0014	349	0.9191
trans-**N_2CP(1)**	649	0.0176	372	0.6344
	535	0.0015	358	0.8573
trans-**N_2CP(2)**	658	0.0151	376	0.6236
	546	0.0027	366	0.7776
cis-**N_2CP(1)**	555	0.0583	353	0.6288
	440	0.0088	332	0.2940
cis-**N_2CP(2)**	555	0.0582	353	0.6920
	440	0.0088	332	0.2938
NeoCP	505	0.0548	340	0.4742
	456	0.0037	329	0.6805

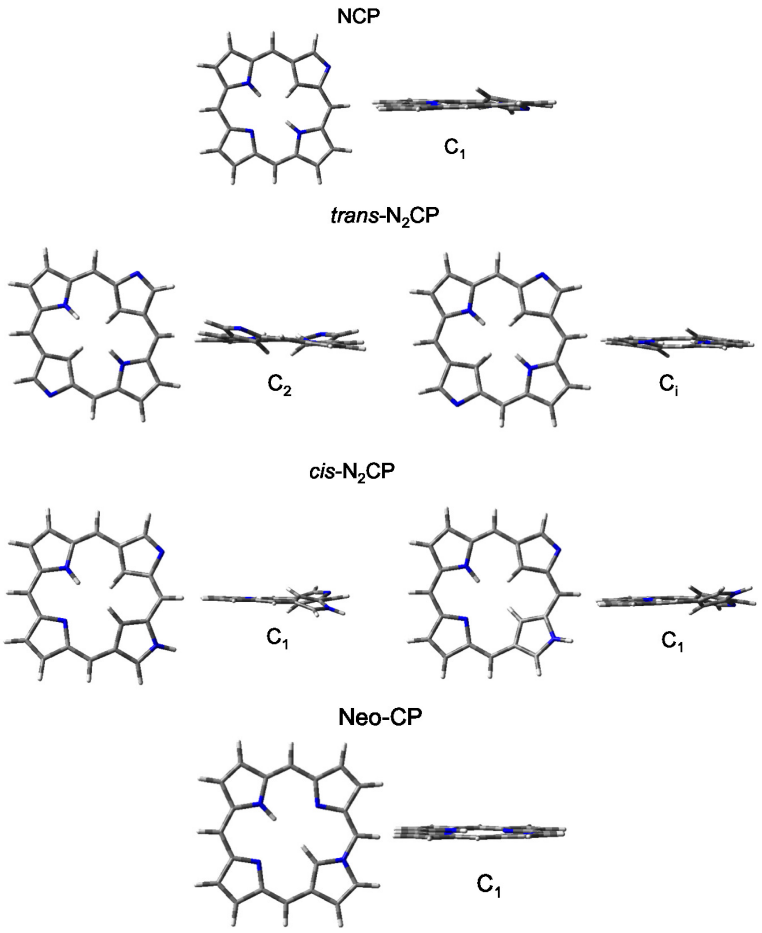

Figure 6.7: The optimised geometries of the confused series of porphyrin isomers

the δ^{TPA} in comparison with the parent **P**. Inspection of the OPA spectra would suggest that **NeoCP** and *cis*-**N_2CP(2)** have potential for resonance enhanced TPA into the Soret-region, as they both exhibit relatively strong OPA into the Q-region. This turns out to influence the TPA of those two species, which do have clear TPA peaks. However, when comparing with **P** it becomes evident that confusion does not benefit the over-all TPA qualities of the compound. It is worth noting here though, that this does not exclude the use of a confused porphyrin derivative in a biological solvent. The results presented here, suggests that the newly discovered **NeoCP** and the *cis*-**N_2CP(2)** are potential candidates. Indeed *cis*-**N_2CP**, and especially its Cu and Ag derivatives, have already been shown to be promising in the development of photosensitzers for use in OPA PDT, and could therefore potentially be probed for

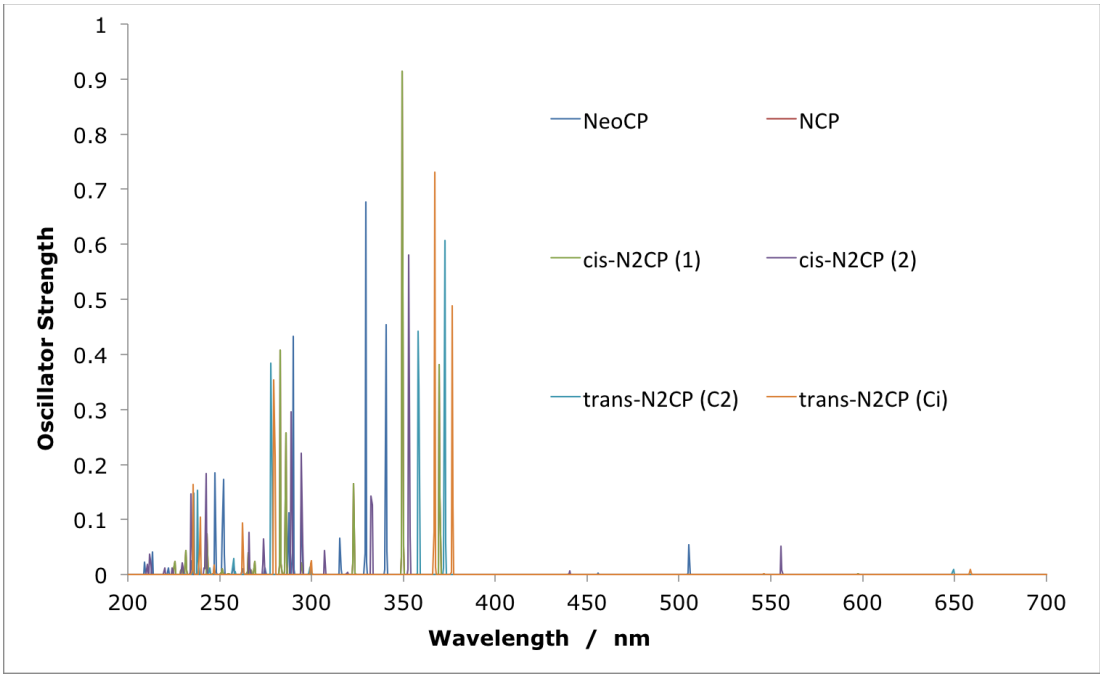

Figure 6.8: One-photon absorption transitions for the set of confused porphyrins. All show absorption into the Soret- and the Q-band

TPA PDT development.[217]

6.3.3 Dioxa-porphycene isomers.

Both the series of **O_2Pc** and **O_2N7Pc** optimised geometries are presented in Figure 6.11 and Figure 6.12, as well as in Table 6.7. The whole series optimised to planar geometries, with the trans-isomers being most stable (Note that *trans* here refers to the substitution site, as these do not have centre hydrogen atoms coordinated to the core).

In Figure 6.13 the OPA spectra of the **O_2Pc** derivatives are seen to display the classic GFO transitions, as expected for **Pc**. The transitions overlap each other to a large degree across the dioxa-substitution pattern. There is however a slight but clear split of the main transitions into the Q-region with respect to the **Pc** macrocycle, as indicated in Figure 6.13.

The OPA spectra for the **O_2N7Pc** set of structures is presented in Figure 6.14,

Table 6.6: A selection of key transitions from the TPA calculations of the confused set of isomers. Wavelengths (λ) and δ^{TPA}.

Compound	Absorption			
	Q-region		Soret-region	
	λ (nm)	δ^{TPA} (a.u.)	λ (nm)	δ^{TPA} (a.u.)
NCP	594	1.47×10^1	268	4.02×10^3
	517	3.61×10^1	253	1.27×10^2
trans-**N_2CP(1)**			285	1.57×10^3
			2.57	1.39×10^4
trans-**N_2CP(2)**			284	4.03×10^3
			256	1.41×10^4
cis-**N_2CP(1)**	554	1.89×10^2	288	2.77×10^4
	438	2.49×10^3	272	1.33×10^5
cis-**N_2CP(2)**	554	1.89×10^2	288	2.75×10^4
	438	2.49×10^3	272	1.38×10^5
NeoCP	500	2.32×10^2	249	3.51×10^6
	451	1.32×10^3	245	7.49×10^6

Table 6.7: Optimised parameters of the series of dioxa-porphycene isomers.

Compound	**Point Group**	**Energy (a.u.)**	**Δ E (kJ/mol)**
trans-**O_2Pc**	C_{2h}	-1029.20223202	0
cis-**O_2Pc(1)**	C_{2v}	-1029.19462111	19.98
cis-**O_2Pc(2)**	C_{2v}	-1029.19689738	14.00
trans-**O_2N7Pc**	C_s	-1045.24981542	0
cis-**O_2N7Pc(1)**	C_1	-1045.24028475	25.02
cis-**O_2N7Pc(2)**	C_1	-1045.24367034	16.13

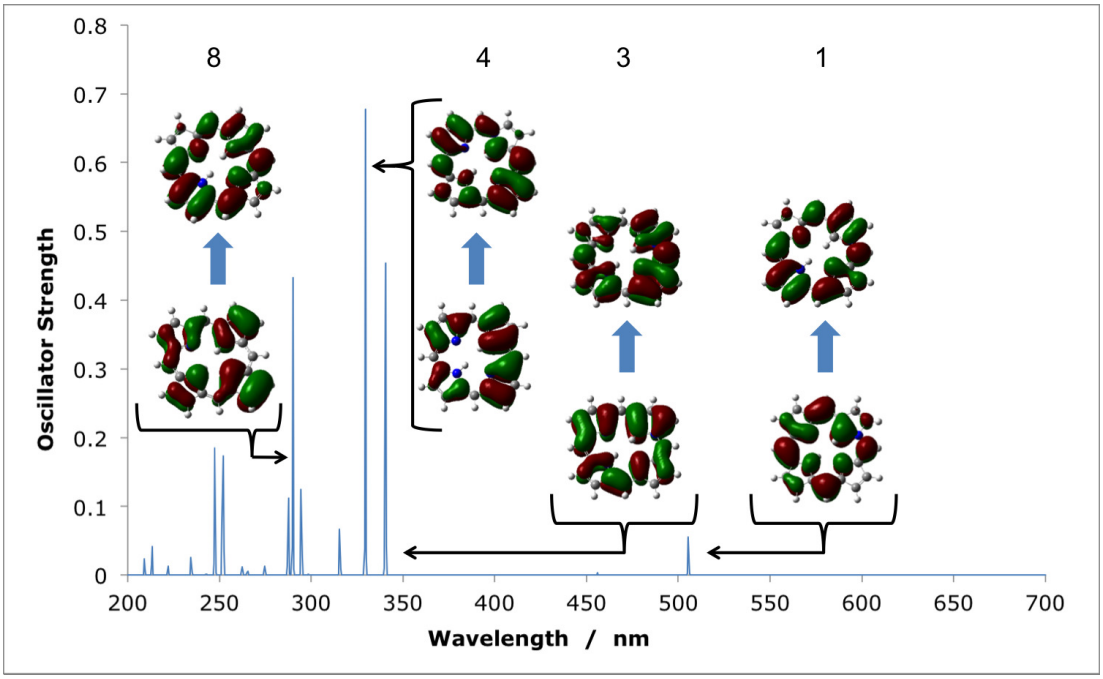

Figure 6.9: Key transitions in the absorption spectra of **NeoCP**, as visualised using NTOs. Transition number **8** clearly show a transition amongst non-Gouterman frontier orbitals

and show a pattern analogous to the $\mathbf{O_2Pc}$ derivatives. The absorption into both the Soret- and Q-transitions are reproduced, and again the main difference lies in the splitting pattern amongst the Q-region transitions in comparison to the **Pc** absorption signals.

The TPA spectra are presented in Figure 6.15 and Figure 6.16. Clearly the very small difference in the Q-region splitting seen in the OPA spectrum has an very large impact on the TPA qualities of the molecules, as shown previously in the reduced set of isomers. A small shift moves the OPA Q-transition to a region where a TPA exists at twice the wavelength which means an effective strengthening of the signal through resonance enhancement. A similar TPA pattern can be seen for the $\mathbf{O_2N7Pc}$ compounds, with a large δ^{TPA} for $\mathbf{O_2N7Pc(2)}$ in comparison to the other derivatives (Figure 6.16). Interestingly, the resonance effect is not nearly as pronounced for this series of compounds as for the $\mathbf{O_2Pc(2)}$ set. In Figure 6.17 the effect of resonance enhancement is presented in a purely state–based approach in which it can clearly be

Table 6.8: Selected OPA calculation results for the core–substituted porphyrins, in terms of their wavelengths (λ) and oscillator strengths (f).

Compound	Absorption			
	Q-region		Soret-region	
	λ (nm)	f	λ (nm)	f
trans-**O_2Pc**	619	0.0900	317	0.9271
	528	0.2414	303	1.3285
cis-**O_2Pc(1)**	570	0.0972	317	0.9901
	514	0.1488	311	1.0832
cis-**O_2Pc(2)**	569	0.1006	321	1.0384
	512	0.1525	605	1.1899
trans-**O_2N7Pc**	624	0.1087	316	0.8603
	529	0.2353	294	1.0586
cis-**O_2N7Pc(1)**	558	0.1276	312	0.9819
	500	0.1348	308	0.9810
cis-**O_2N7Pc(2)**	580	0.1100	321	0.9903
	512	0.1647	297	0.8788

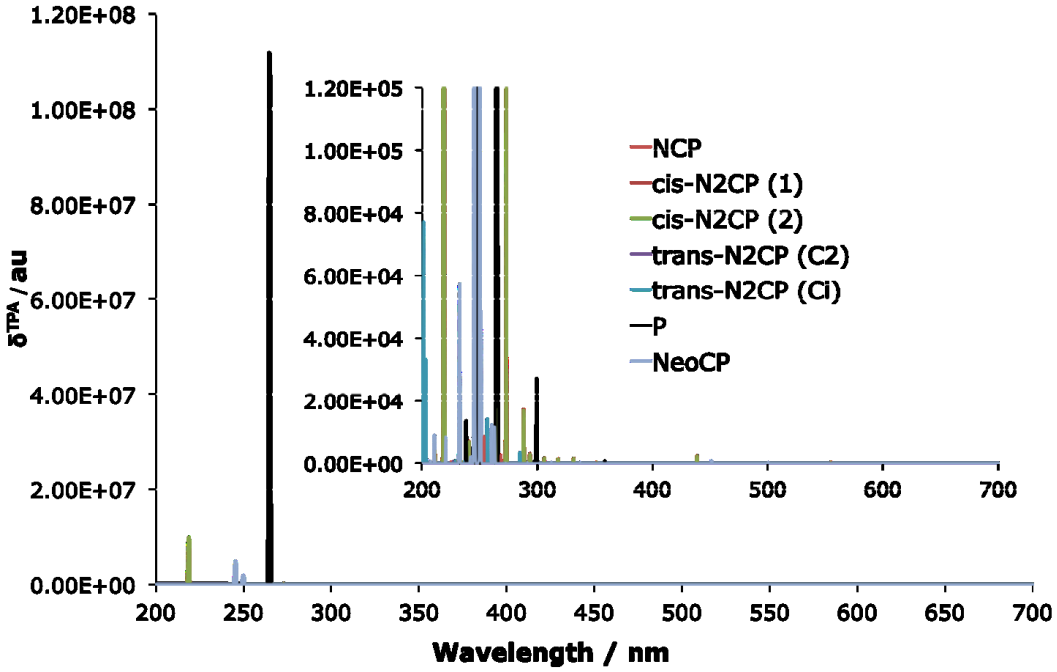

Figure 6.10: TPA spectra for the confused isomers, with **P** added as a reference. Confusion have negative impact on the δ^{TPA} in comparison with the porphyrin parent

seen to be an effect of the position of a Q-region transition at near half the wavelength of the TPA transition.

6.4 Conclusion

In this chapter linear and quadratic density functional response theory was used to systematically study the effects of the core electronic structure of porphyrin isomers on their OPA and TPA characteristics. The OPA spectra reproduced the well known Gouterman pattern of absorption signals in the Soret- and Q-regions across the series of compounds. However, the use of natural transition orbitals to investigate the nature of the transition pointed to the fact that the Gouterman orbital picture might not be sufficient to describe these transitions fully. The GFO model was developed for the **P** macrocycle and was derived based on the degeneracy of the two LUMO orbitals. This degeneracy is successively being broken in derivative compounds and

Table 6.9: A selection of key transitions from the TPA calculations on the core–substituted porphyrins. Wavelengths (λ) and transition strengths (δ^{TPA}).

Compound	Absorption			
	Q-region		Soret-region	
	λ (nm)	f	λ (nm)	f
trans-**O_2Pc**	618	8.77×10^{-7}	269	4.34×10^{7}
	526	6.60×10^{-8}	235	1.04×10^{6}
cis-**O_2Pc(1)**	569	1.72×10^{3}	265	3.48×10^{5}
	513	4.06×10^{2}	249	2.32×10^{5}
cis-**O_2Pc(2)**	567	2.17×10^{3}	255	1.07×10^{11}
	510	4.59×10^{2}	254	6.28×10^{2}
trans-**O_2N7Pc**	621	3.19×10^{0}	268	1.50×10^{8}
	528	3.26×10^{1}	246	1.25×10^{5}
cis-**O_2N7Pc(1)**	556	2.44×10^{3}	247	3.66×10^{7}
	498	4.00×10^{2}	238	9.17×10^{5}
cis-**O_2N7Pc(2)**	577	2.07×10^{3}	297	2.27×10^{6}
	510	5.73×10^{2}	252	5.81×10^{8}

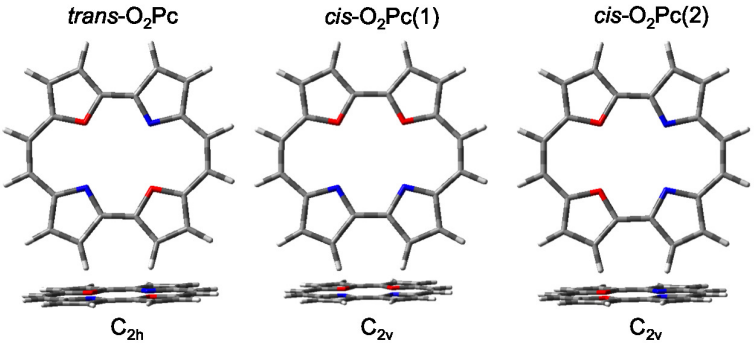

Figure 6.11: The optimised geometries of the dioxa-porphycene series

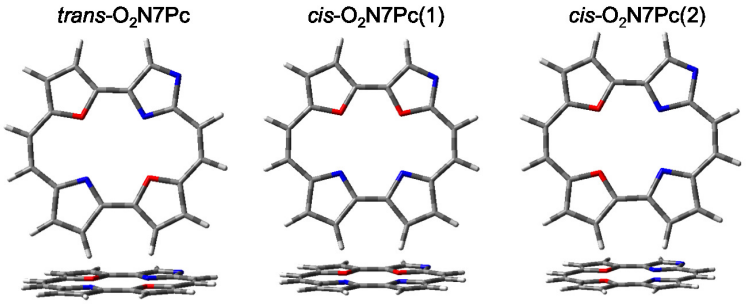

Figure 6.12: The optimised geometries of the dioxa-porphycene series, bearing a Nitrogen atom in the confused 7-position of the **Pc** macrocycle

although the GFO model accurately describes some trends (such as the Q–transition strengthening in **Pc** relative to **P**) it also fails to account for some key transitions (such as the Soret–region contributions in **NeoCP**). There is therefore a need to also look specifically into the location of the states if one wants to rationalise the full absorption pattern in porphyrin isomers. Interestingly, it was shown that the TPA pattern was very much more sensitive to the changes in the electronic structure than previously expected. Confusion of the N-atoms in the porphyrin macrocycle did little to improve the TPA qualities whilst substitution of the pyrrolic Nitrogen atoms by Oxygens, as well as changing the Hydrogen coordination of the core, could lead to an incredible increase in the TPA transition strength. These large changes in the TPA spectra were not reproduced in the OPA spectra, where only small changes were seen. However, these small changes were sufficient to move the OPA signal to a region where it could contribute to one-photon resonance enhancement of the TPA signal, and thereby

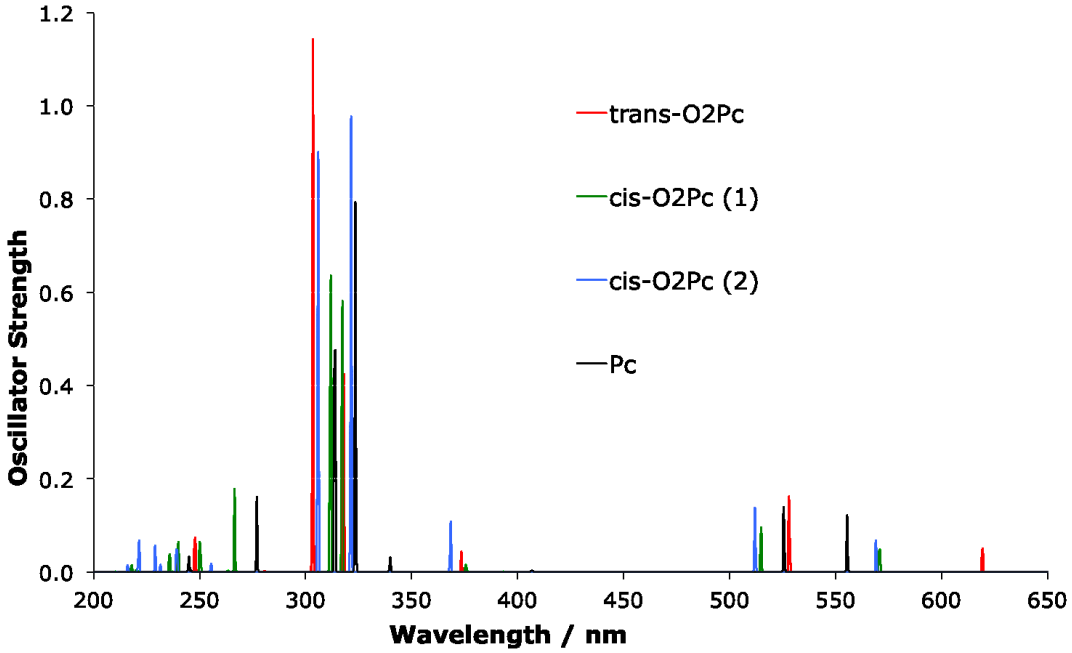

Figure 6.13: Simulated spectra for OPA in dioxa-porphycene derivatives

making the effect on the TPA more significant. This subtlety in the non-linear TPA means that a change in the core electronic structure of compounds is a potentially very powerful avenue, by which the TPA qualities of porphyrinic compounds can be fine tuned, without the need for large structural changes to the extremities of the macrocycle. This also highlights the importance of computational techniques for use in structure-reactivity relationship studies, as a large number of compounds can be probed and unexpected absorption qualities such as the ones presented here can be identified.

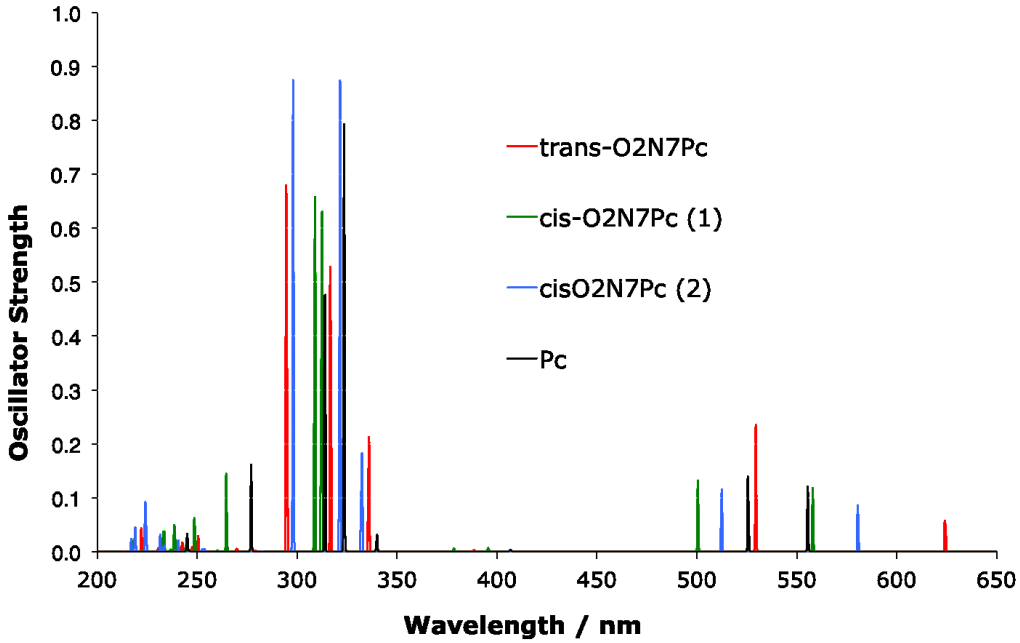

Figure 6.14: The absorption spectrum for dioxa-porphycenes with added an added nitrogen atom in the confused 7-position of the **Pc** core

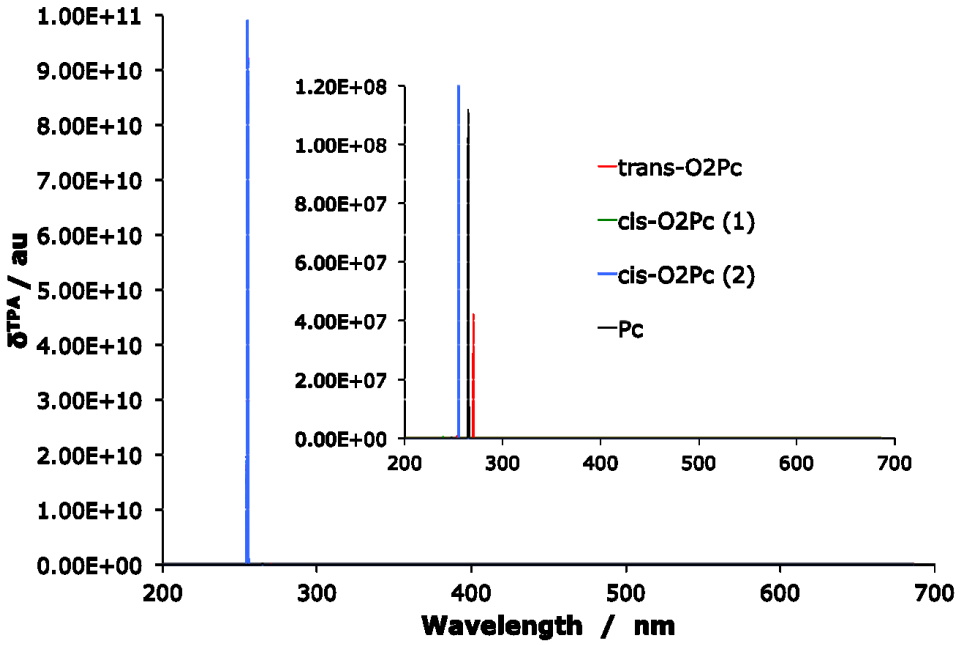

Figure 6.15: The two-photon absorption spectrum for dioxa-porphycenes as well as the **Pc** core for comparison. The signal for the $\mathbf{O_2Pc(2)}$ is several orders of magnitude larger than the related derivatives.

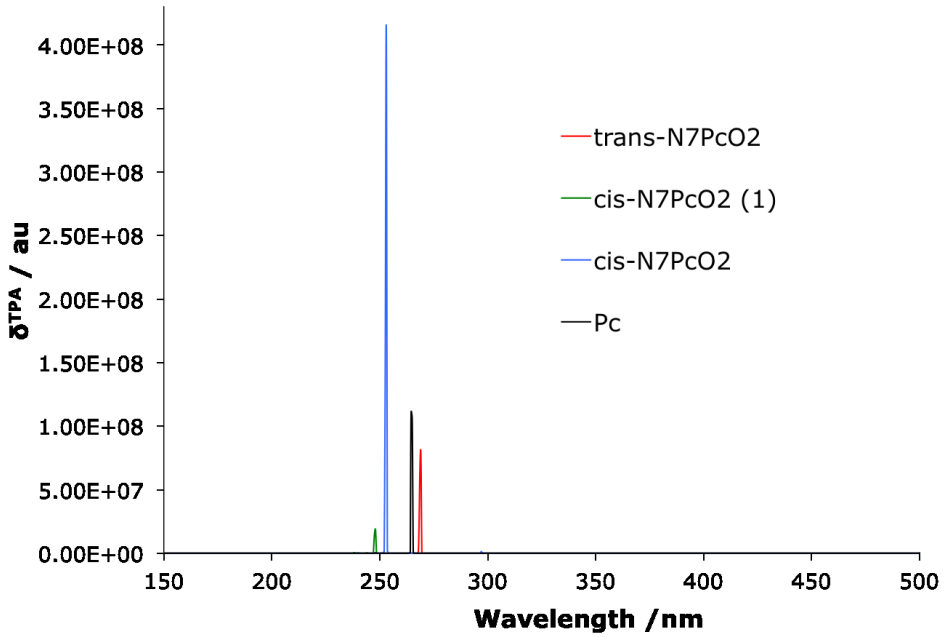

Figure 6.16: The two-photon absorption spectrum for dioxa-porphycenes with confused Nitrogen as well as the **Pc** core for comparison.

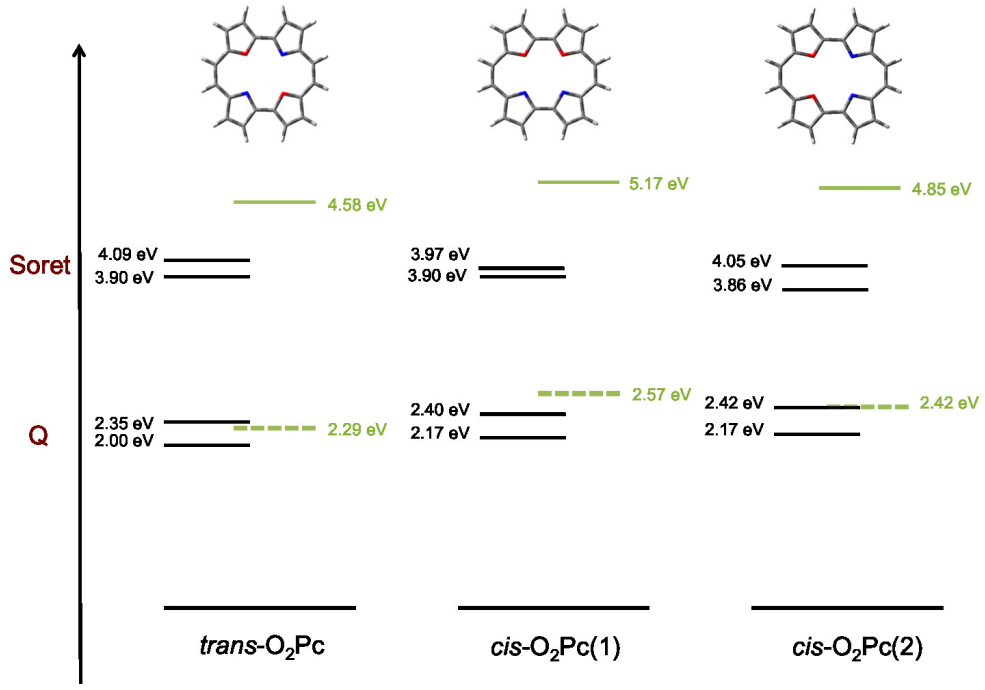

Figure 6.17: This absorption scheme illustrates the concept of resonance enhancement in the series of $\mathbf{O_2Pc}$ derivatives. Black horizontal lines are states available for OPA, clearly forming the Soret- and the Q-regions. Green lines are the dominant TPA transition, with the dashed line representing the virtual state. When the latter state can be represented in terms of a real state, resonance is expected to affect the TPA signal by greatly enhancing it.

Chapter 7

Absorption in Aggregated Porphyrins

7.1 Introduction

After looking into the specific absorption characteristics of single molecules in the gas phase, the next step is to concentrate on the situation when a number of chromophores are non-covalently bound to each other, and forming aggregates. The theoretical interpretation of non-covalently bound aggregates of molecular systems, and especially their spectroscopy, has been a topic of interest for decades and includes seminal contributions such as Frenkel's molecular exciton concept for the analysis of band spectral shapes in molecular crystals in the 1930s [230, 231], and Kasha's exciton coupling papers from the early 1960s [232]. The latter describe the splitting of excited states, when going from one chromophore to a pair of interacting chromophores, in terms of the coupling of simple transition dipoles. This theoretical framework has since been used as a successful analysis tool for the spectroscopy of systems ranging from crystals to simple dimers. As the field of quantum chemistry developed, with considerable increases in efficiency of computer algorithms as well as hardware, so did the accuracy of the theoretical interpretation of the spectroscopic properties of non-covalently bound molecular systems, using wavefunction based methods [233–238] as well as density functional theory (DFT)[100, 239–241]. DFT is especially interesting as its favourable scaling lends itself to the theoretical description of comparably large

molecular systems. This opens up the topic to include systems that are of interest in highly topical applications such agents for PDT.

The investigations into the spectroscopy of aggregates using computational methods introduce a whole new set of considerations, compared to ground state studies. Some characteristics are better described than others, and the development of DFT functionals capable of describing weak non-covalent interactions as well the development of functionals that are suitable for excited states has only fairly recently begun to appear [99, 241, 242].

There is great interest in reproducing aggregation in macrocycles such as **P** and **Pc** and predicting changes in their photophysical characteristics upon complexation. This is true not only from a point of view of topical applications such as photosynthesis, where the efficiency of light harvesting supramolecular structures depends on the aggregation of the chromophores, but also in development of PDT, where aggregation is common in solutions of the chromophores used as photosensitisers in vivo[140, 243]. Even though aggregation of chromophores tend to broaden the absorption spectrum, making more wavelengths available for various applications use, it may also enhance the excited state decay rate.[244] As the latter competes with the photosensitisation pathway in PDT it is a very important loss process to understand. In nature on the other hand, photosynthetic light-harvesting complexes, based on the porphyrin core structure, depend heavily on this aggregation to broaden their absorption capabilities. A computational investigation into the aggregation characteristics of porphyrin-type macrocycles is therefore of large interest in the development of efficient photosensitisers, attempting to exploit the broadening of the absorption spectra whilst at the same time avoid the excited state decay[243, 245, 246]. As the field of computational chemistry matures to the task of investigating the spectroscopy of large aggregated structures there are great potential insights to be gained.

This chapter will report on the results from a study set out to investigate the effect of aggregation on the spectroscopic properties of dimers of **P** and **Pc** Figure 7.1. The aggregates investigated are characterised as being of J- or H-type geometries, as described in Figure 7.1. This terminology was first developed by Jelley and Sheibe through their work on aggregation in cyanine dyes [247]. The inclusion of T-shaped dimers in this study was motivated by previous porphyrin studies as well as work on the benzene dimer. As the latter can be regarded as the benchmark when it comes

to wavefunction studies on aggregated chromophores[238, 248, 249], it is of great interest to evaluate the spectroscopic properties of this conformer, as well as the traditional H- and J-type aggregates.

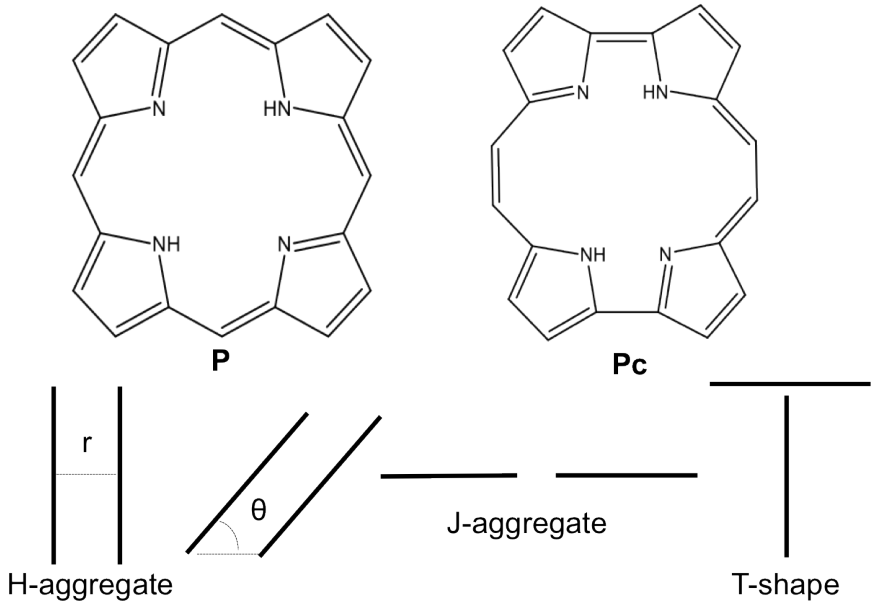

Figure 7.1: The aggregation in porpyrin **(P)** and porphycene **(Pc)** dimers, separated by r, can be classified as being of J-type (head-to-tail orientation, $0^\circ < \theta < 54.7^\circ$) or H-type (face-to-face orientation, $54.7^\circ < \theta < 90^\circ$) The nomenclature of the aggregation designations are from the early studies on aggregation in cyanine dyes by Jelley and Scheibe [247]. The T-shaped orientation was also included in this study.

7.2 Computational Methods

The nature of the interaction between stacked non-polar π-systems means a good treatment of dispersion effects is essential for a correct description of the geometry and binding energy. As this interaction is dependent on the correlated instantaneous fluctuations in the electron cloud of one region (and how it responds to the fluctuations of the electron cloud of another region) it is poorly described using a mean field approach. Despite the fact that DFT in general includes approximate electron correlation effects, most functionals fail to describe dispersion interactions quantitatively, due to their local nature failing to account for the r^{-6} dependence in the disper-

sion expression, $C_6 r^{-6}$ [250, 251]. Even though a rigorous non-empirical evaluation of the interaction would be the most desirable option, it will fast become computationally challenging, thereby ruining the advantageous DFT scaling and hence be computationally unfeasible for systems the size of porphyrin-aggregates. Alternative approaches include the use of an existing empirical potential from a well resolved system, such as a rare gas, to tailor the functional itself [252]. The results from these functional adjustments are however limited by their transferability to more general systems. As mentioned in the Theoretical Background section, a more successful approach has been the practice of adding a correction term to the existing DFT mean-field energy, as in Equation 7.1:

$$E_{Total} = E_{DFT} + E_{disp} \tag{7.1}$$

The representation of the correction term E_{disp} varies, but is of the general form

$$E_{disp} = -\sum_{n}\sum_{i>j} f_{damp,n}(r_{ij})\frac{C_{n,ij}}{r_{ij}^{n}} \tag{7.2}$$

where i and j denotes a pair of interacting atoms, and $C_{n,ij}$ and $f_{damp,n}$their dispersion coefficient and dampening function respectively, both of order n.

An added description of the dispersion energy of this type has been shown to describe the correct binding energy for a large range of weakly bound complexes, including large stacked systems with π-interactions[97–100].

In order to avoid the incorrect description of bonds below common Van der Waals distances the addition of a dampening function with fast decay at small r is crucial. The dampening scheme of Grimme's successful B97-D functional series [101], fulfil this requirement and is of the form:

$$f_{damp}(r) = \frac{1}{1+\exp(-\alpha(\frac{r}{r_0-1}))} \tag{7.3}$$

where r_0 is the sum of the Van der Walls radii and the α parameter controls the strength of the correction.

As a reasonable expectation in a study such as this is to see bands involving so-called exciton bands, where charge density is being transferred from one monomer of the aggregate to the other, the use of a LC functional is crucial.[253] With the impor-

tance of dispersion as well as long-range correction in mind Chai and Head-Gordon added empirical dispersion terms to their own fully optimised LC exchange-correction functional, denoted ωB97XD [242, 254]. They followed Grimme's dispersion format, apart from the use of their own dampening function of the form

$$f_{damp}(r) = \frac{1}{1+\exp(-\alpha(\frac{r}{r_0})^{-12})} \tag{7.4}$$

As the polarisabilities used in the construction of the dispersion coefficient are based on values for the ground, rather than the excited state, the behaviour of dispersion functionals in linear response TD-DFT calculations of excitation energies are not easily predicted. However, as the excited states of the aggregates are expected to be delocalised to a large degree across the complex, the importance of a functional that can deal with CT excitations is expected to outweigh the need for accurate dispersion treatment of the few electrons that will be excited. Indeed, in tests of the ωB97XD functional, where vertical CT excitation energies were investigated, the resulting excitation energies were qualitatively correct, as compared to high-level SAC-CI results, compared to the poorer results seen in the B97-D excitations [254]. It is worth to point out, however, that investigations into excimer (excited dimer) formation using TD-DFT, which require full excited state optimisations, showed that, even though LC was crucial for a correct description, empirical dispersion effects did also prove vital for the correct bound behaviour of the excimers [241]. There has been developments in the dispersion functional methodologies, such as retrieving polarisability data from TD-DFT rather than using empirical data, in the D3 scheme by Grimme [255]. The improvements in terms of binding energies for large macrocyclic dimers, such as porphyrin, has however been shown to be minor. Both the -D and the -D3 approach give porphyrin binding energy results in the order of 20kcal/mol. The form of the dispersion dampening terms have also been improved further to give more accurate descriptions, for example the recent D3 improvement scheme developed by Grimme that adds a Becke-Johnson dampening function. [255] However, benchmark studies highlight that the improvement is minor as the mathematical forms of the dampening function is varied [255]. Further, the DFT-D approach for the benzene dimer, generally considered the prototype for benchmarking $\pi-\pi$ interactions, has been shown to give results with a precision similar to CCSD(T) results [249, 256–

258]. All our ground state characterisations were therefore carried out with the B97-D functional in combination with an Ahlrichs-type basis set of TZVP quality [74]. The Ahlrichs series of basis sets have been used extensively for DFT energy and gradient calculations and is preferred over for example Dunning's basis sets, as the latter is fitted to wavefunction results [259]. All reported energies are corrected for Basis Set Superposition Error (BSSE) using the counterpoise corrected method.[260] It is worth noting however that the correction were in the order of 0.003 Hartrees. This is due to the use of a basis set of triple zeta quality on a system as large as a porphyrin aggregate, which is expected to diminish the BSSE [99].

Our vertical excitations are determined using linear response DFT. A small benchmark set for the porphyrin monomer was prepared to evaluate the behaviour of B97-D and ω-B97XD, as well as the the long range corrected CAM-B3LYP [130] and PBE0[212] functionals. All computations were carried out using Gaussian09. [160]

7.3 Results and discussion

7.3.1 Optimised Aggregates

Full ground state optimisations of the aggregates were started with the monomers at various geometries ranging from H- to J-type aggregation; face-to-face (**P-H**,**Pc-H**), head-to-tail (**P-J**,**Pc-J**), slipped co-facial (**P-ScF**,**Pc-ScF**) and T-shaped starting geometries (**P-T(A)**, **P-T(B)**, **Pc-T(A)**,**Pc-T(B)**, **Pc-T(C)**, **Pc-T(D)**) as per Figure 7.2. For the J- and H-type geometries the parallel as well as the H-tautomer arrangement of the pyrrolic hydrogen was probed (equivalent of a 90° interplanar rotation in porphyrin), as both porphyrin and porphycene have rapid pyrrolic H-tautomer interconversion at room temperature [227, 261]. Each stationary point was characterised using analytical Hessians. The parameters in focus of this optimisation investigation were the interplanar distance, r, set to $3.30\mathring{A}$ in the first instance (for H- and slipped-co-facial aggregates), the aggregation angle θ (ranging from 90° to 0° via 56°) and, orthogonal to that angle, the off centre slipping angle $\theta_\perp$ (set at 90° for all aggregates), as described in Figure 7.2.

Starting the optimisation at a strict face-to-face H-type geometry, with θ at 90°, $\theta_\perp$ at 90°, and $3.7\mathring{A}$ interplanar distance, the porphyrin aggregates converges to a

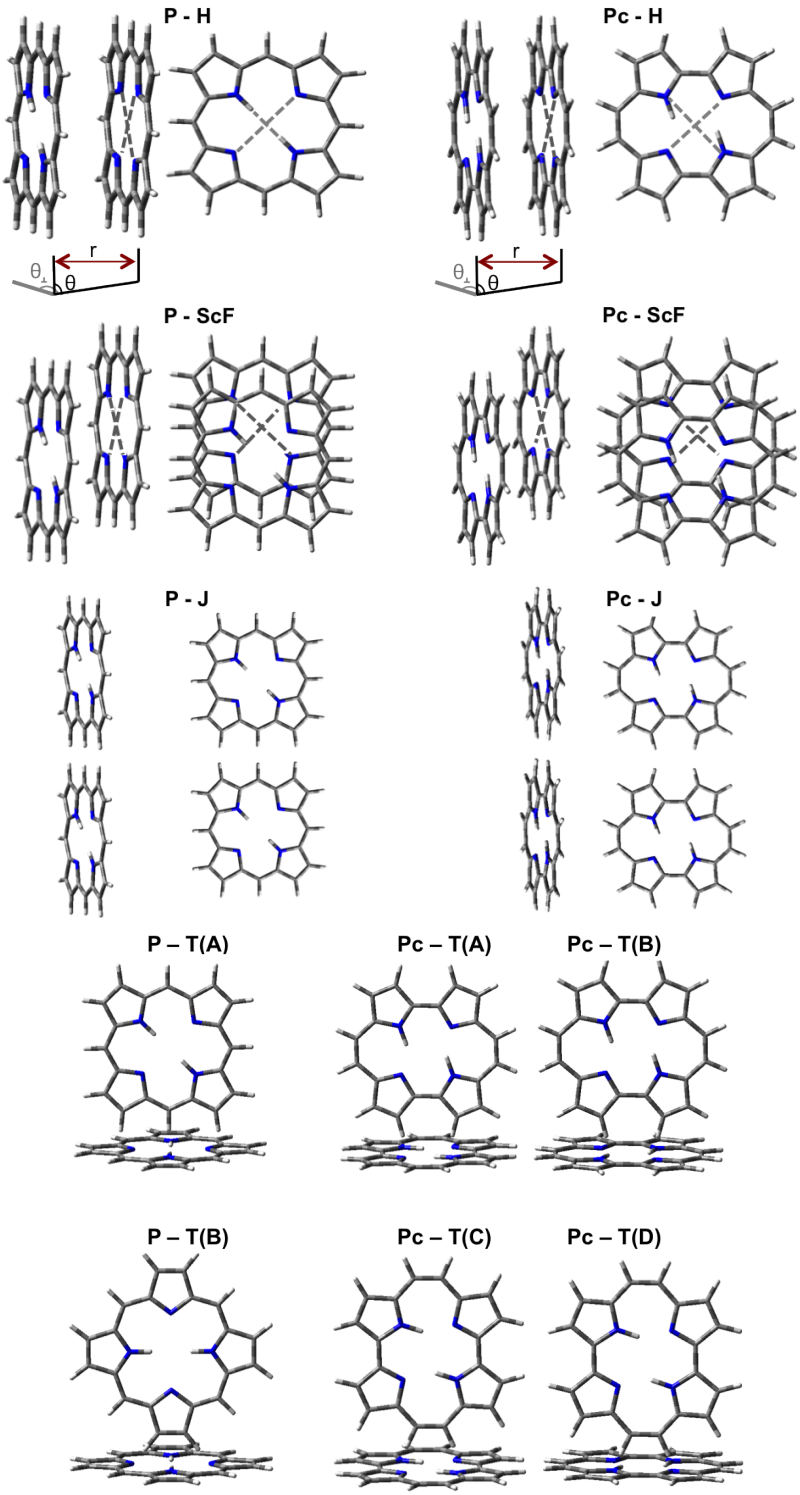

Figure 7.2: Starting geometry for the aggregates, ranging from H to J-type aggregation, as well as T-shaped geometries. The dashed lines refer to the sites of H-tautomerisation and the aggregation angle θ and $\theta_{\perp}$, orthogonal to the aggregation coordinate, are indicated.

minimum energy stationary point at a slightly slipped cofacial geometry for both hydrogen-tautomers, as per Table 7.1. These minima are in the order of 6 kcal / mol below the energies of the starting geometries, and suggests a very shallown nature of the potential energy surface in this region. The non-parallel hydrogen-tautomer geometry converges to a minimum where the orthogonal slip angle is more pronounced, reaching a value of $\theta_{\perp} = 99.79$. This tautomer also yields a marginally lower minimum (Δ E =1 kcal/mol) than the version with parallel hydrogens, with a very slight increase in binding energy due to increase in electrostatic attractive forces. These results are in good agreement with previous investigations of the porphyrin aggregation surface by Muck-Lichtenfeld and Grimme [248]. Unlike the slipping modes seen in porphyrin, the porphycene H-type starting geometries ($\theta = 90^{\circ}$, $\theta_{\perp} = 90^{\circ}$, r= $3.7\mathring{A}$), with and without hydrogen tautomerisation, converges to a first order critical point, with one very small imaginary frequency (in the order of $-3cm^{-1}$), in the direction of rotation between the macrocyclic planes of equal and opposite directions. Exploring the surface in the direction of the twist coordinate resulted in a minimum energy aggregate as per Table 7.1, where the two planes are rotated with respect to eachother by 20° .

As in the H-aggregate, the slipped co-facial starting geometry of porphyrin ($\theta = 56.7^{\circ}$, $\theta_{\perp} = 90^{\circ}$, r= $3.26\mathring{A}$) is a critical point on the potential energy surface for both tautomers. The imaginary frequency modes are along the slipping coordinate orthogonal to the starting slipping direction, $\theta_{\perp}$. Probing the surface along this mode yield minima as described in Table 7.1. These minima are of identical binding energy to the porphyrin minimum found from the H-type aggregate starting point but in the opposite direction along the $\theta_{\perp}$ mode. This suggests a 'sombrero-hat'- type potential energy surface for porphyrin, which has been proposed earlier [248]. The porphycene slipped co-facial optimisation with alternating tautomers is also a critical point of first order. The modes with negative frequency are along $\theta_{\perp}$ and probing the surfaces along this coordinate yields a minimum geometry, which also incorporates a twist in the direction of rotation between the two porphycene planes, of 18°. As in porphyrin, the hydrogen-tautomer arrangement yields a marginally lower energy minimum.

With a J-type aggregation setup, the porphyrin optimisation proceeds by slipping the structure towards a slipped-cofacial geometry, optimising the electrostatic interactions between the two planes. A minimum energy structure is reached at an angle

of $\theta = 68^{\circ}$, $\theta_{\perp} = 72^{\circ}$ and an interplanar distance at $r = 3.22\mathring{A}$. The J-type geometry in porphycene also follows the same path as the porphyrin analogue and optimises along the aggregation coordinate towards a H-aggregate with $\theta = 74^{\circ}$ and $\theta_{\perp} = 69^{\circ}$.

None of the porphyrin T-shaped aggregates are a minima on the B97-D/TZVP potential, but higher order saddle points. As in the case of the J-type set-up, the optimisation leads to a slipped co-facial structure analogous to the other starting geometries, as presented in Table 7.1. The T-shaped aggregate of benzene, as has been shown in benchmark calculations, is nearly iso-energetic to the slipped co-facial conformer at this level of theory, and is in fact favoured at high temperatures due to is higher flexibility [249, 257]. This is not the case in porphyrin, and the large surface area of the macrocyclic plane, and hence the increased dispersion stabilisation in a co-facial arrangement, contributes to the stabilisation in the aggregates.

Porphycene T-shaped geometries **A**, **B** , **C** and **D** follows the same trend as the porphyrin examples and optimises to a minimum with a slipped co-facial geometry. Depending on the starting conformation, the slipping takes place towards closest co-facial alignment, leading to a set of minima with various rotations between the macrocyclic planes, as described in Table 7.1.

The overall potential energy surface in the ground state of porphyrin and porphycene upon aggregation are both very similar in character; with very shallow minima. Especially for porphyrin the optimised geometries presented here are well known and highlights the success of the empirically corrected dispersion functional of the type used here. [262] A quick optimisation run on the lowest energy porphyrin minimum (**P-ScF**$_{taut}$) with a non-dispersion-corrected functional, here B3LYP with the same basis set, does not return an aggregate that is bound, but reaches a non-bound stationary point at $r = 4.4$ Å, $\theta = 132^{\circ}$ and $\theta_{\perp} = 130^{\circ}$. Overall, these results can be rationalised by the well known interplay between long range dispersion interactions and short range Pauli exchange repulsion and electrostatic interactions - which are considered the dominant terms in $\pi - \pi$ stacking interactions [263]. If the binding had been down to dispersion forces only, a maximum $\pi - \pi$ overlap would have been expected. Instead, the gas phase aggregates prefers the offset structure which promotes maximum $\pi - \sigma$ attraction whilst minimising any repulsion. The aggregation behaviour of porphycene, whilst not having been in focus of any theoretical studies known to the authors, follows the same trend as the porphyrin macrocycle but, due

Table 7.1: Optimised energy data for the aggregates calculated at the B97-D//TZVP level of theory, with counterpoise correction. a; Interplanar distances and slipping and rotation angles given in Å, and $degrees$, respectively. Total binding energy and the dispersion contribution to the binding is also given (in $kcal/mol$).

Optimised Aggregates							
	Geometrical Parameters[a]				E_{abs} (Ha)	E_{bind}	E_{Disp}
	r	θ	$\theta_{\perp}$	rotation			
P-H	3.36	64	79		-1978.2908	17.66	38.45
P-H$_{taut}$	3.29	65	99		-1978.2920	18.42	40.28
P-ScF	3.31	73	107		-1978.2911	17.86	40.08
P-ScF$_{taut}$	3.29	68	71		-1978.2920	18.41	40.32
P-J	3.31	72	108		-1978.2919	18.34	39.92
P-T(A)	3.30	68	70		-1978.2919	18.34	39.91
P-T(B)	3.32	73	107		-1978.2920	18.40	40.30
Pc-H	3.32	74	70	21	-1978.2981	18.84	43.69
Pc-H$_{taut}$	3.30	64	109		-1978.2983	18.92	43.97
Pc-ScF	3.27	74	69		-1978.2980	18.78	43.60
Pc-ScF$_{taut}$	3.31	63	109	18	-1978.3021	21.34	43.97
Pc-J	3.32	74	69		-1978.2982	18.86	43.60
Pc-T(A)	3.30	72	89	60	-1978.2970	18.14	42.42
Pc-T(B)	3.35	79	67	37	-1978.2979	18.67	43.07
Pc-T(C)	3.38	64	109	55	-1978.2982	18.93	43.97
Pc-T(D)	3.31	64	67	53	-1978.2978	18.64	43.68

the elongation of the over all $\pi-$ system compared to porphyrin, has available close lying minima that requires the two porphycenes to rotate relative to each other to maximise the attractive electrostatic forces.

7.3.2 Vertical Excitations

The state ordering of the lowest singlet excited states of porphyrin is well known and has been investigated extensively using experiments as well as high-level wavefunction methods. In order to evaluate the most suitable functional for the calculation of vertical states a small benchmark calculation was therefore set up, using the porphyrin free base, where each functional was compared with experimental porphyrin spectra as well as excitation data from EOM-CCSD and RASSCF/RASPT2 calculations. A number of basis sets were also investigated (see Appendix 1). Overall the state

ordering as well as state character was well represented with CAM-B3LYP as well as the ωB97XD functional, both of which are of the long-range corrected variety. Especially the latter produced results where N-type states were placed in the correct energy region. Addition of polarisation functions on all atoms did little to affect the result.

Even though the EOM-CCSD and RASSCF/RASPT2 methods would be ideal to utilise for accurate excitations in the aggregates, as they have for the monomers, such calculations would not be computationally feasible. The EOM-CCSD scales as conventional CCSD (N^6) and the limited number of active electrons and the orbitals that can be selected in the RAS space in the RASSCF/RASPT2 setup means excimer type excitations, involving essentially the full $\pi-$space, would fail to be accurately reproduced. The use of TD-DFT hence still remains the only accessible option with respect to balancing computational accuracy and cost for aggregates of chromophores the size of porphyrins.

The absorption characteristics of aggregated chromophores are often described in terms of the simple theoretical model for exciton transitions devised by Kasha et al. [232]. In this model the blue- or red-shift seen in the absorption spectra upon aggregation is accounted for by means of a quasi-classical vector model where transition dipole moments in the dimers couple and thereby perturb the electronic states, as illustrated in Figure 7.3.This interaction between transition moments leads to delocalisation of the excitation over the aggregate, meaning that an energy lowering takes place as the excited state of one monomer interacts with the ground state of the other. The splitting of the states caused by coupling of dipoles in monomer 1 and monomer 2, in the point-dipole approximation, are of the form:

$$\Delta E_{splitting} = \frac{2|M|^2}{R_{1,2}^3}(1+3cos^2\theta) \tag{7.5}$$

where the splitting in the monomer states upon aggregation, $\Delta E_{splitting}$ is derived using the angle between the dipoles, θ, and the transition dipole moment, M. As the splitting is dependent on the transition moment of the transition in the monomer, splitting is only expected to be observed for the states with appreciable oscillator strengths. It is seen that the stabilisation caused by the splitting decays with a R^{-3} dependency and hence slower than dispersion stabilisation (R^{-6}). This stabilisation

can lead to the formation of species that are only stable in the excited states, so called excimers. Kasha's model has been used in the definition of characterisation of aggregation type, where the flip from J- to H-type aggregation is seen where the exciton splitting is zero, at $\theta = 54.7^\circ$ ($=$ arc cos $1/\sqrt{3}$).

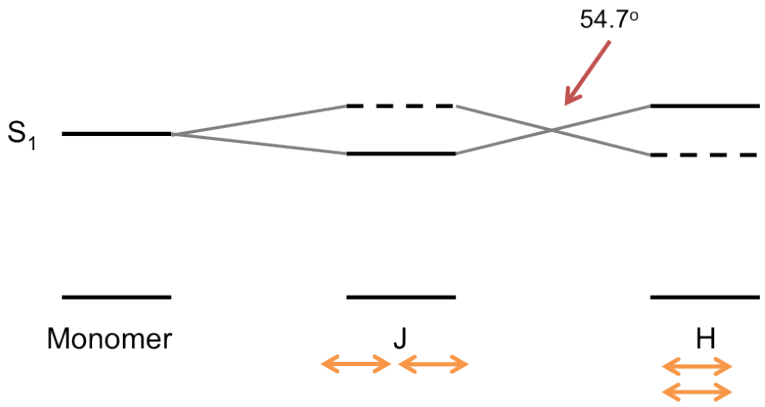

Figure 7.3: The splitting pattern in the first excited state in Kashas excitonic coupling scheme. Dashed line indicates dipole-forbidden state.

This model has been used successfully in spectral analysis of various aggregated chromophores for decades, including for porphyrin aggregates and their characterisation as J- or H-type [262, 264–270]. If, for example, there is a breakdown of the point-dipole approximation, however, it has been suggested to be potentially misleading [243]. This is especially a concern in porphyrins, due to the non-trivial absorption spectra of these systems, where standard absorption bands, such as the first excited state in the porphyrin monomer, in the so-called Q-band in the visible region, have orthogonal transition dipoles (*vide infra*). This implies that blue- as well as red-shifts could theoretically be seen in the *same* dimer structure, complicating the assignment of aggregation type. In addition, the presence of orthogonal H-bands in supposedly J-aggregated samples in condensed phase also leads to difficulties in the interpretation of the spectra [9, 271].

7.3.2.1 Slipping Excitations

In order to aid the non-trivial characterisation of porphyrin aggregates and their spectroscopy we set out to evaluate an absorption scheme for the porphyrin and por-

phycene aggregates as the slipping angle, θ, evolves from J- to H-type aggregation with the interplanar distance set to $3.30\mathring{A}$ and $\theta_{\perp} = 90^{\circ}$ and investigate the TD-DFT results. The analysis was carried out both with Kasha's model as well as a thorough characterisations of each state, using natural transition orbitals (NTOs). NTOs are created through unitary transformations of the set of canonical Kohn-Sham orbitals, virtual as well as occupied, generating a set that describes a particular particle-hole excitation [139]. Each excitation has an associate eigenvalue, λ, which indicates its importance in the overall transition, giving a tool for evaluating the character of a transition, which greatly aids the qualitative understanding of transitions available in porphyrin-type aggregates. A a better understanding of the relationship between aggregation formation and the electronic absorption characteristics of chromophores such as the ones investigated here would further the goal of their use in photovoltaics and photodynamic therapy as well as energy conversion devices. A concise aggregation-absorption scheme also has the potential be useful in the developments as a motivation tool for rational design of such materials using controlled processes such as self-assembly, sol-gel film formation or Langmuir-Blodgett techniques[272–274], as well as through the introduction of added side groups [267, 275].

Figure 7.4 shows the absolute ground state energies, given in eV for the set of functionals investigated here, for a slipping angle between 0° and 90° (using the 0° energy as reference) , and highlights the importance of the use of dispersion for ground state energies in π-aggregates. The CAM-B3LYP, PBE0 and ωB97XD functionals are all of the type that includes various fractions of exact exchange from Hartree Fock. This has been shown to be especially important for charge transfer states, which will be required for excitation studies. The latter also has the added benefit of an empirical dispersion correction, something that is shown here to be crucial in reproducing the ground state stability of the aggregates. The ωB97XD functional in fact reproduces the pattern expected to be seen for porphyrin aggregation, namely the stabilisation of the dimer along the aggregation coordinate, as does the B97-D functional. It is seen that (in the absence of relaxation along the $\theta_{\perp}$ coordinate, as presented in the Optimisation Section) the minimum energy lies around a 60° slipping angle, which reflects the expected maximum of electrostatic attractive forces and dispersion interactions. A functional without dispersion captures the electrostatic attractions at moderate angles, but as the repulsive forces come into play, as the overlap of the

π-systems increase, a lack of dispersion interactions fails to reproduce the aggregation stabilisation. This serves as a reminder of the interplay between dispersion forces and the electrostatic repulsion and attraction in complexes such as these (*vide supra*).

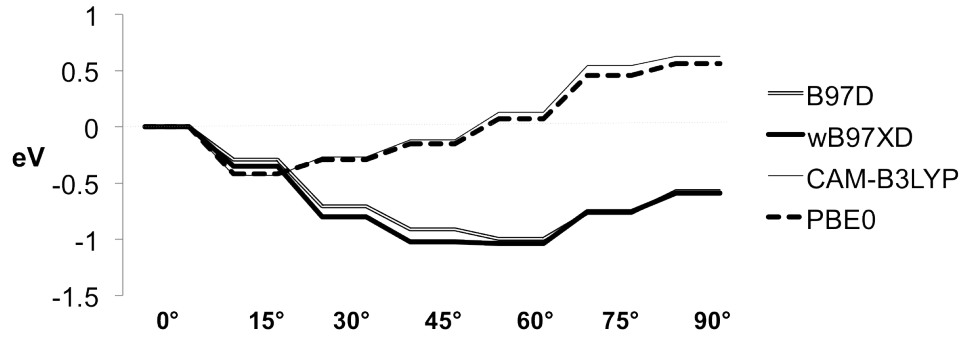

Figure 7.4: The absolute single point energies of a porphyrin aggregate as the slipping angle varies from 0° to 90° and the interplanar distance is set to 3.30 Å. The 0° energy is used as reference.

The vertical singlet states of the porphyrin aggregate, and their evolvement as the aggregation angle is varied, was calculated at the TD-wB97XD//TZVP level, and is presented in tabular form in Table 7.2.

The vertical singlet states of the porphycene aggregate, and their evolvement as the aggregation angle is varied, was also calculated at the TD-wB97XD//TZVP level, and is presented in tabular form in Table 7.3.

Across the slipping angle coordinate in porphyrin and porphycene the state-ordering in the lower energy region is well described in terms of Kasha's model. Even though the transition moments of the monomeric units do not lie parallel to the aggregation coordinates, the Q-type states are split into an orbital allowed and forbidden component and ordered as per Figure 7.3. As the porphyrins couple in a J-type fashion the first excited Q-type state at 2.17 eV is blue shifted to 2.09 eV, and the corresponding forbidden state is seen at 2.10 eV. The use of NTO's to characterise a state as being of the correct type is vital, as each state is described in terms of a complicated mix of excitation and de-excitation amplitudes and clear Gouterman type orbitals are difficult to assign. As the symmetry is lowered upon aggregation, symmetry labels also become less useful. As seen in Figure 7.5 the 'electron-hole pair' described by the NTO's, together with their eigenvalue, indicating their importance in

Table 7.2: Excited state analysis as the porphyrin slipping angle θ varies from 0° to 90°, as calculated at the TD-ωB97XD//TZVP level of theory.

Porphyrin Monomer			0°			15°			30°		
E (eV)	f	State	E (eV)	f	State	E (eV)	f	State	E (eV)	f	State
2.17	0.0014	Q $^1B_{3u}$	2.09	0.0005	Q ^1B_u	2.10	0.0009	Q ^1A_u	2.09	0.0010	Q ^1A_u
2.39	0.0010	Q $^1B_{2u}$	2.10	0.0000	^1A_g	2.10	0.0000	^1A_g	2.09	0.0000	^1A_g
3.58	0.9142	B(N) $^1B_{3u}$	2.33	0.0002	Q ^1B_u	2.34	0.0005	Q ^1A_u	2.30	0.0035	Q ^1A_u
3.69	1.2073	B $^1B_{2u}$	2.33	0.0000	^1A_g	2.33	0.0000	^1A_g	2.32	0.0000	^1A_g
3.97	0.0000	$^1B_{3g}$	3.43	2.4719	N ^1B_u	3.48	1.9500	N ^1A_u	3.28	0.0000	^1A_g
4.34	0.5100	$^1B_{3u}$	3.45	0.0000	^1A_g	3.49	0.0000	^1A_g	3.45	1.2900	N ^1A_u
4.48	0.0000	^1A_g	3.62	2.0854	N ^1B_u	3.61	2.3000	B ^1A_u	3.43	0.0000	^1A_g
4.52	0.0000	$^1B_{2g}$	3.65	0.0000	^1A_g	3.63	0.0000	^1A_g	3.45	0.2252	B ^1A_u
4.53	0.0000	^1A_u	3.65	0.0000	^1A_g	3.85	0.0000	^1A_g	3.48	0.2909	B ^1A_u
	45°			60°			75°			90°	
E (eV)	f	State	E (eV)	f	State	E (eV)	f	State	E (eV)	f	State
2.00	0.0000	^1A_g	1.99	0.0000	^1A_g	1.68	0.0000	^1A_g	1.44	0.0000	$^1B_{1u}$
2.05	0.0002	Q ^1A_u	2.05	0.0002	Q ^1A_u	1.82	0.0000	^1A_g	1.59	0.0000	$^1B_{1u}$
2.19	0.0000	^1A_g	2.21	0.0000	^1A_g	2.08	0.0010	Q ^1A_u	2.07	0.0000	$^1B_{1u}$
2.30	0.0005	Q ^1A_u	2.27	0.0041	Q ^1A_u	2.28	0.0000	^1A_g	2.09	0.0000	$^1B_{1u}$
2.84	0.0000	^1A_g	2.74	0.0000	^1A_g	2.32	0.0014	Q ^1A_u	2.10	0.0009	Q $^1B_{3u}$
2.95	0.0000	^1A_g	2.84	0.0000	^1A_g	2.34	0.0000	^1A_g	2.35	0.0005	Q $^1B_{2u}$
3.04	0.0024	B ^1A_u	2.89	0.0247	B ^1A_u	2.83	0.0052	B ^1A_u	2.88	0.0002	B $^1B_{2u}$
3.10	0.0077	B ^1A_u	2.92	0.0117	B ^1A_u	2.85	0.0020	B ^1A_u	2.92	0.0005	B $^1B_{3u}$
3.17	0.0000	^1A_g	2.95	0.0000	^1A_g	2.98	0.0050	^1A_u	3.04	0.0046	$^1B_{3u}$

Table 7.3: Excited state analysis as the porphycene slipping angle θ varies from 0° to 90°, as calculated at the TD-ωB97XD//TZVP level of theory.

Porphycene Monomer			0°			15°			30°		
E (eV)	f	State	E (eV)	f	State	E (eV)	f	State	E (eV)	f	State
2.14	0.1616	Q ^1B_u	2.07	0.0000	^1A_g	2.06	0.4668	Q ^1A	1.98	0.0000	^1A
2.26	0.2394	Q ^1B_u	2.07	0.3861	Q ^1A_u	2.08	0.0001	^1A	2.05	0.3481	Q ^1A
3.57	0.0000	^1A_g	2.20	0.5094	Q ^1A_u	2.20	0.4479	Q ^1A	2.14	0.0004	^1A
3.59	0.0387	N ^1B_u	2.21	0.0000	^1A_g	2.21	0.0003	^1A	2.18	0.3589	Q ^1A
3.97	0.7774	B(N) ^1B_u	3.45	0.0000	^1A_g	3.38	0.0253	^1A	2.60	0.0066	^1A
4.05	0.8852	B(N) ^1B_u	3.46	0.0064	^1A_u	3.41	0.0439	^1A	2.67	0.0034	^1A
4.13	0.0000	^1B_g	3.50	0.0334	N ^1A_u	3.46	0.0198	N ^1A	2.71	0.0053	^1A
4.21	0.0000	^1A_g	3.58	0.0000	^1A_g	3.48	0.0037	^1A	2.77	0.0039	^1A
4.23	0.0000	^1A_u	3.58	0.0073	^1A_u	3.50	0.0809	N^1A	3.35	0.0051	^1A
	45°			60°			75°			90°	
E (eV)	f	State	E (eV)	f	State	E (eV)	f	State	E (eV)	f	State
1.95	0.0003	^1A	1.79	0.0000	^1A	1.56	0.0007	^1A	1.28	0.0000	^1B_g
2.02	0.0013	^1A	1.92	0.0008	^1A	1.60	0.0000	^1A	1.30	0.0000	^1B_g
2.07	0.2869	Q ^1A	2.08	0.2169	Q ^1A	2.12	0.1977	Q ^1A	2.13	0.1965	Q ^1B_u
2.21	0.2956	Q ^1A	2.20	0.2592	Q ^1A	2.23	0.1952	Q ^1A	2.28	0.2642	Q^1B_u
2.45	0.0106	^1A	2.37	0.0302	^1A	2.32	0.0929	^1A	2.31	0.0351	^1B_u
2.52	0.0122	^1A	2.46	0.0157	^1A	2.40	0.0328	^1A	2.40	0.0013	^1B_u
2.53	0.0016	^1A	2.50	0.0056	^1A	2.67	0.0002	^1A	2.68	0.0000	^1B_g
2.60	0.0035	^1A	2.59	0.0001	^1A	2.70	0.0021	^1A	2.77	0.0000	^1B_g
3.41	0.0106	N ^1A	3.30	0.0000	^1A	3.05	0.0001	^1A	2.90	0.0000	^1A_u

the transition description, are of clear Gouterman Q-type. At 45° TD-DFT predicts a flip in the state ordering, and hence aggregation type, which is at a slightly smaller angle than the 54.7° predicted by Kasha's model. The slipping of the porphycene aggregate predicts the same trend as in porphyrin at low energies. Even though the lack of symmetry means the forbidden states are not formally forbidden, states with very small oscillator strengths can be seen to flip down below the more allowed states at 30°.

When looking at the states in the Soret-region for the dimers with small slipping angles ($\theta = 0^\circ - 30^\circ$) there is evidence of interesting orbital mixing in the Soret-type states of the aggregates, creating N-type transitions. Even though transitions with N-type densities are seen here in the porphyrin monomer using the ωB97XD functional, they are mixed in to a predominantly Soret-type state which is found in the correct region, rather than seen as a pure N-type state, denoted as a Soret(N)-state in Table 7.2. Even though there is no direct experimental evidence of these types of transitions in the porphyrin monomer, there are clear evidence of such bands in covalently bound porphyrin oligomers [276]. As these oligomers have similar orientation with respect to the macrocyclic π-systems as do the aggregates with low slipping angle presented in Table 7.2, the position of the N-transitions in between the Q- and Soret-bands seen here reflect the experimental absorption trends well. The B-bands of porphycene differ from porphyrin in general, as mentioned at the start of this section, in that the main transitions in the B-region are in fact suggested to be made up of N-type transitions, and not be described well with the Gouterman set. Indeed, the transition into the 3^1B_u state in the monomer is predominantly of N-type and neither of the strong transitions into the Soret-region (4^1B_u and 4^1B_u at 3.97 and 4.05 eV) are of pure Soret-type, but have N-type density components (denoted Soret(N) in Table 7.3). As the aggregation angle increases there is a small trend in the number of clear N-states. At small angles an investigation of the NTOs indicate that the contribution from configurations involving the orbitals with density on the pyrrole moieties are more important than at larger angles. Hence porphycene follows the same trend as porphyrin, in that N-type states vary in their importance along the aggregation coordinate.

It will certainly be interesting to see results using other methods than TD-DFT on the N-type transitions and their position upon aggregation of porphyrins. As the

pyrrolic regions of porphyrinic macrocycles are routinely functionalised in synthesis the position of the N-bands could be utilised to improve on absorption characteristics of porphyrin aggregates, and oligomers, to improve on the applications of these systems.

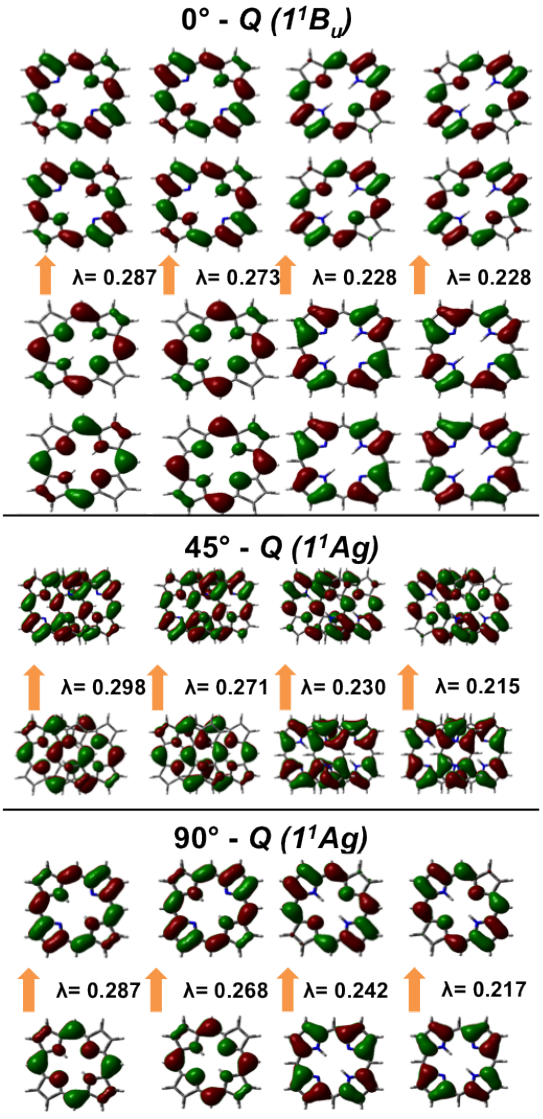

Figure 7.5: Transitions in the porphyrin aggregates as represented by their NTO pair and associated eigenvalue λ.

7.3.2.2 Absorption in T-shaped aggregates

The T-shaped porphyrin aggregate has been investigated previously on the ground state surface [238, 248], and it is therefore of great interest to evaluate the absorption spectra for the various geometries in Figure 7.2, at the TD-ωB97XD//TZVP level of theory, for the first time. This is especially true when considering the topical applications and the development of concise aggregation-absorption schemes. Absorption spectra for the porphyrin and porphycene T-shaped aggregates are presented in Figure 7.6 and Figure 7.7.

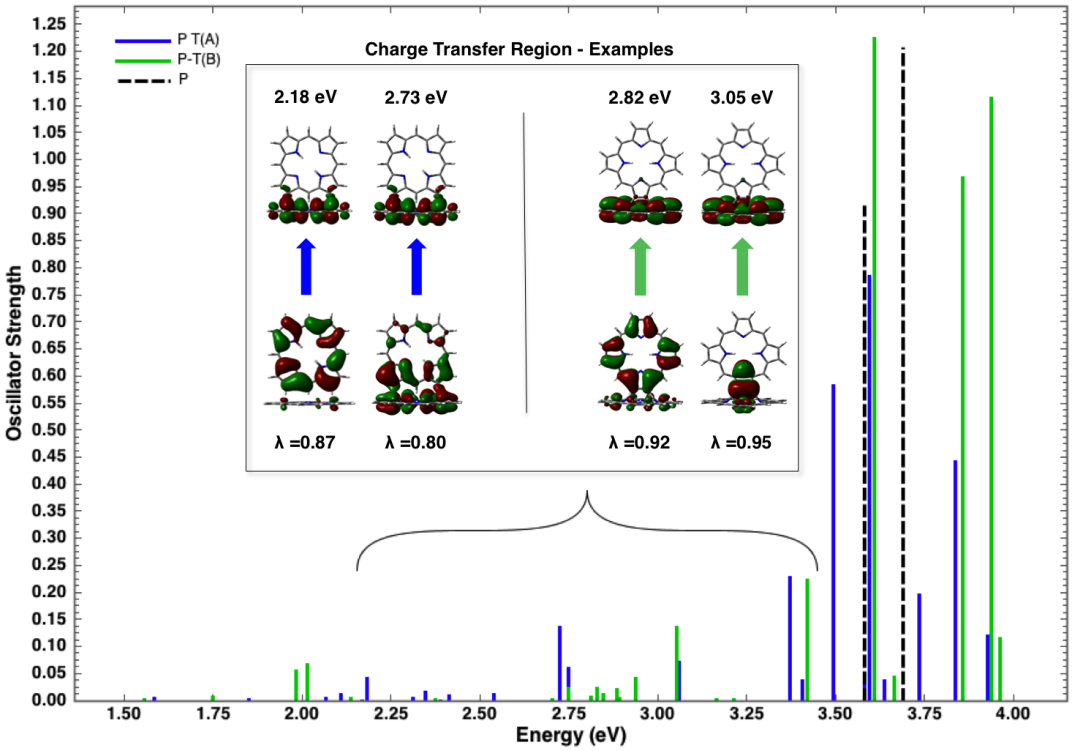

Figure 7.6: Transitions in the porphyrin T-shaped aggregates at the TD-ωB97XD//TZVP level of theory. Key examples of charge transfer transitions are represented by their NTO pair and associated eigenvalue λ. The porphyrin monomer spectrum is added (black dashed line) for comparison.

As in the case of the Slipping Excitation investigation, the use of NTOs greatly aids the characterisation of each state for both of the T-shaped porphyrin conformations. With the rings orientated as in the **P-T(B)** example, where the pyrrole moiety of

one ring is pointing towards the macrocyclic plane of the other, the transitions are separated to each ring in both the B- and the Q-region. The classic Gouterman orbitals are easily recognised when looking at the NTOs and each transition is clearly separated into transitions in one ring, meaning that no charge transfer from one monomer to the other is seen in either regions for **P-T(B)**. The orientation where the side of one macrocycle points towards the plane of the other, as in **P-T(A)**, affords greater overlap and both Q- and Soret-transitions involve a mixture of distorted Gouterman orbitals, N-type orbitals, as well as $\pi - \sigma$ type orbitals involving the C-H σ bonds overlapping with the π-cloud of the macrocycle. Looking in the medium energy region (at $2.00\text{eV} - 3.45\text{eV}$), charge transfer from Gouterman type orbitals between the rings as well as N-type orbitals are seen for both conformations, as shown in Figure 7.6. The precise position of these charge transfer bands is however difficult to asses, as they could be artificially stabilised due to the use of a long-range corrected functional as discussed earlier.

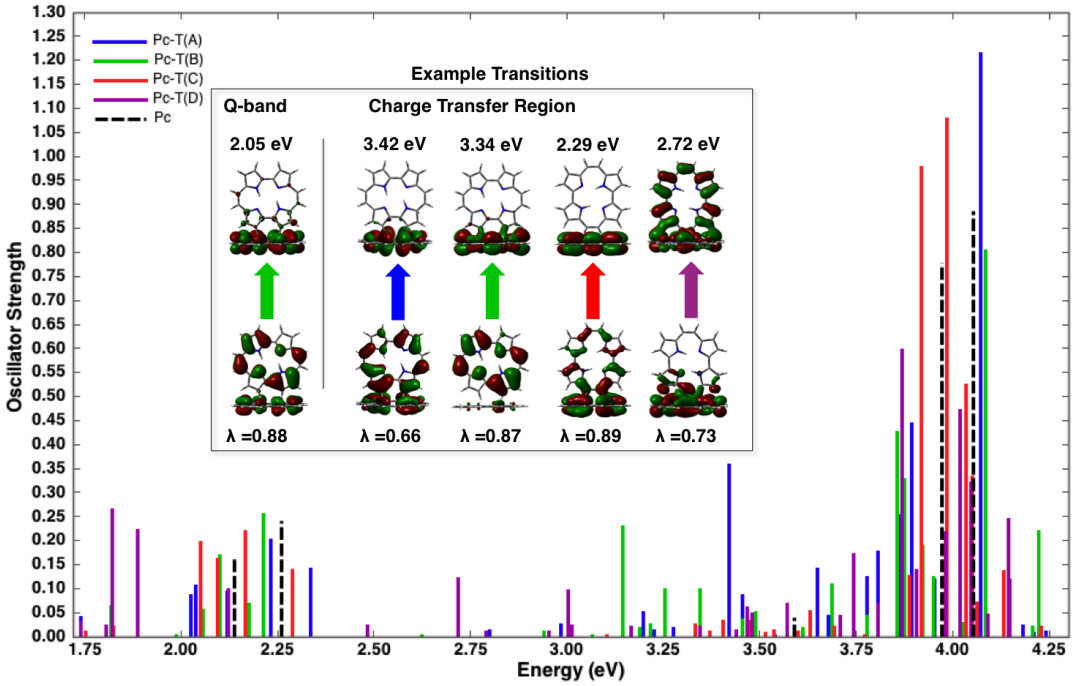

Figure 7.7: Transitions in the porphycene T-shaped aggregates at the TD-ωB97XD//TZVP level of theory. Important charge transfer transitions are represented by their NTO pair and associated eigenvalue λ. The monomer spectrum is added (black dashed line) for comparison.

Due to the elongation of the π-system in the porphycene macrocycle, the orientation of the monomers in the T-shaped geometries is especially important to consider when analysing the absorption behaviour. The **Pc-T(A)**,**(C)** and **(D)** orientations behave in a similar manner as the **P-T(A)**, with clearly separated transitions in the Q- and Soret-bands not involving any charge transfer. The **Pc-T(B)** however, has the longer sides and edges of the elongated π-systems pointing towards each other, leading to larger overlap. This leads to mixed transitions in both the Q- and the Soret-band (one Q-type transition is represented in Figure 7.7). The charge transfer region, in between the Soret- and Q-regions, are analogous to the porphyrin case, and involve transfer between the monomers. Exemplary transitions are presented in Figure 7.7.

7.3.3 Absorption in Optimised Aggregates

After carrying out the slipping-angle and T-shaped geometry investigations, the ground state structure from the aggregation optimisation section with the lowest minimum and largest binding energies, **P-ScF**$_{taut}$ for porphyrin and **Pc-ScF**$_{taut}$ for porphycene, were investigated with the TD-ωB97XD functional and TZVP basis set. The vertical excitation energies were plotted for the first 20 states and simulated stick spectra were drawn (Figure 7.8 and 7.9 for porphyrin and porphycene respectively). The equivalent transitions for the respective monomers were included for comparison.

The porphyrin spectrum is presented in Figure 7.8, where the NTO's with significant values of λ for the main transitions are indicated. When comparing to the investigation into the slipping angle the appearance of bands with significant oscillator strengths are seen in between the Q- and B-regions, at 2.8 - 3.5 eV. These absorptions are made up of exciton-type transitions between configurations that involve the Gouterman orbitals of one monomer to a Gouterman orbital of the other, and are responsible for the well known broadening of absorption spectra upon aggregation seen in experiment. The canonical orbitals for these transitions are very difficult to interpret, but the NTO's show clear charge transfer between the two monomeric units, as seen in Figure 7.8. A comparison can be made with the NTO's from the slipping angle investigation for $\theta = 60^{\circ}$ and the transition into the same region (the ^1A_u state at 2.89 eV) in Figure 7.10. Unlike the transition seen here, the orbital densities do not

show any clear charge transfer. The parameters for **P-ScF**$_{taut}$ are $\theta = 68^{\circ}$, $\theta_{\perp} = 72^{\circ}$ and an interplanar distance of $r = 3.22\mathring{A}$. As the slipping angle investigation was carried out at $\theta_{\perp} = 90^{\circ}$, any transitions from one monomeric unit to the other would be of equal and opposite direction, and hence no net charge transfer is seen, whilst at the ground state geometry the unsymmetrical overlap leads to a promotion of these types of transitions. This charge transfer promotion could rationalise why this arrangement, with porphyrins offset in θ as well as $\theta_{\perp}$, is in fact favoured in many important porphyrinic chromophores found in nature where charge transfer is utilised for functions such as the funnelling of energy to redox-active molecules, such as light-harvesting aggregates in photosynthetic bacteria [243, 277]. In the B-region at higher energies, the main transition, 3.73 eV, can be seen to include N-type densities, and no clear Gouterman-type B-transitions are seen. As discussed in the slipping angle investigation, the importance of N-type orbitals in the description of these states is unclear, but experiments as well as computational work has suggested that they are present in this region in porphyrin oligomers [276].

The simulated absorption spectrum for the porphycene minimum energy structure (**Pc-ScF**$_{taut}$ in Table 7.1) is presented in Figure 7.9. As in the monomer, the transitions in the Q-region of the aggregates are strong, due to non-degenerate LUMO and LUMO-1 leading to a non-cancellation in composite Gouterman-type transitions into this region. Clear charge transfer from one monomer to the other is observed, but contrary to the porphyrin case, there is a preference in the transitions going from one monomer to the other. For example left to right in the transition at 2.30 eV, as indicated by the large λ value of 0.80. The lowest lying minimum in the porphycene aggregate involves a twist of the macrocyclic core, as well as a displacement along θ and $\theta_{\perp}$, which leads to an uneven density distribution in the Gouterman set. This makes the characterisation of the states challenging, especially using canonical orbitals. Investigation of the NTO's however makes it possible to recognise both the Gouterman set and the presence of N-type orbitals in the transition at 4.04 in the B-region. As seen in Figure 7.9, the N-type densities are shifted towards one end of the aggregate, where the overlap is maximised. The importance of N-bands in the description of the porphycene monomer is already well known, and analogous to porphyrin, these states become even more important to consider for a balanced description of absorptions when an aggregate is formed [115].

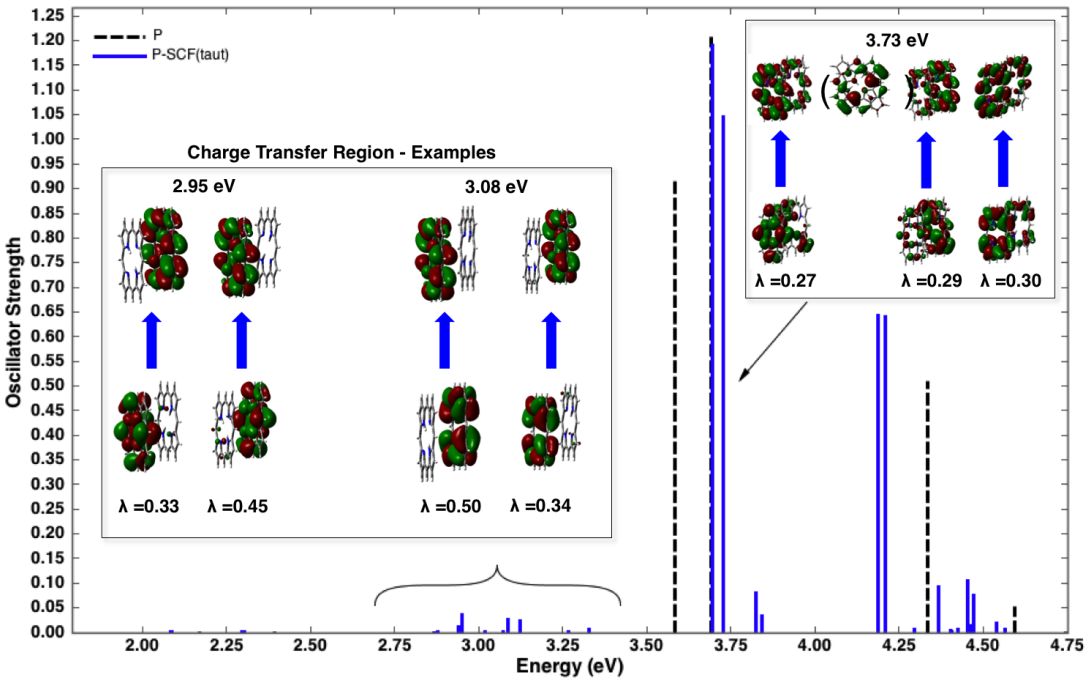

Figure 7.8: Transitions in the porphyrin ground state aggregate with lowest energy minimum (**P-ScF**$_{taut}$) (blue). Key transitions are represented by their NTO pair and associated eigenvalue λ. The orbital for the N-type transition component ($\lambda = 0.29$) is also shown from a face-on view, in brackets. The porphyrin monomer spectraum is added (black dashed line) for comparison.

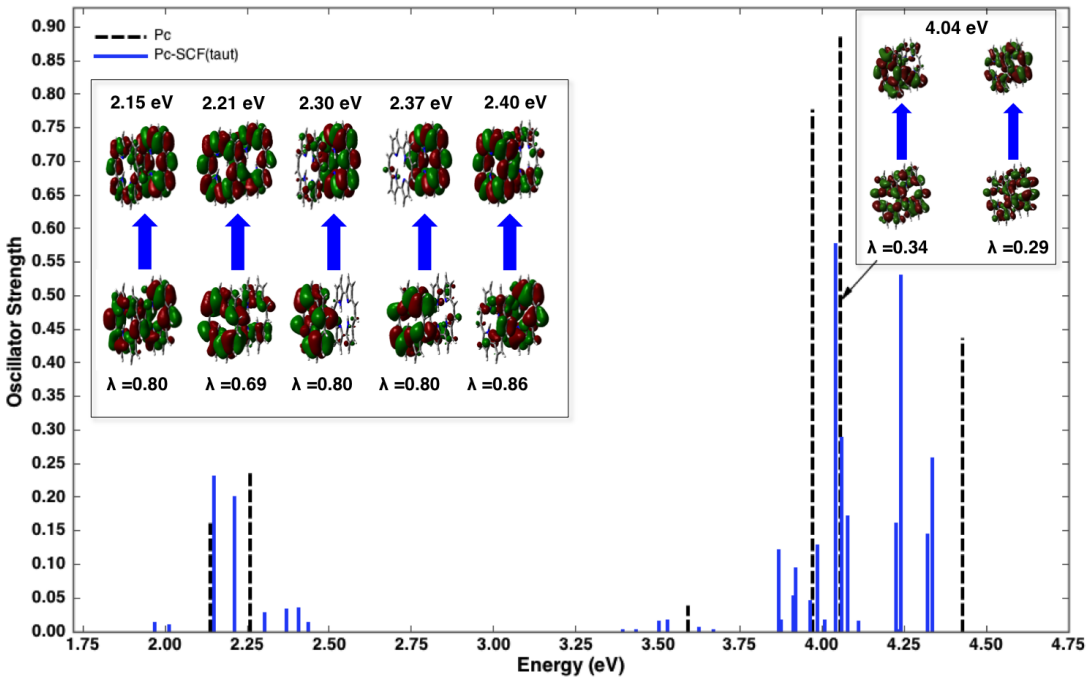

Figure 7.9: Transitions in the porphycene ground state aggregate, **Pc-ScF**$_{taut}$ (blue). NTO pairs and associated eigenvalue λ highlight important transitions. The porphycene monomer spectrum is added for comparison (black dashed line)

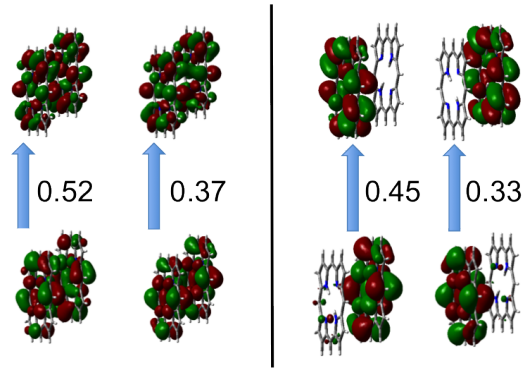

Figure 7.10: NTO pair and associated eigenvalue λ for the ^1A_u state at 2.89 eV for the $\theta = 60^\circ$ aggregate (on left) and the ^1A state of **Pc-ScF**$_{taut}$ at 420 nm / 2.95 eV (on right).

7.4 Conclusion

This chapter introduced the electronic structure of porphyrin and porphycene aggregates. The addition of dispersion, as in the B97-D functional, was crucial in order to predict bound aggregate dimers on the ground state surface. The TD-DFT study of the effect of the slipping angle on the absorption characteristics of the aggregates yielded interesting results. Due to the size of the systems, TD-DFT is the go to method, and its behaviour for these types of systems is important to evaluate. In this study the results reflected well Kasha's model of exciton coupling, and the use of NTOs rather than canonical Kohn-Sham orbitals were a useful, if not crucial, tool for state characterisations. Intriguing bands due to N-type transitions were found to be located in the region as expected from experimental absorptions in oligomeric porphyrinic systems. As wavefunction methods develop further and can take on the task of modelling large aggregates, it will certainly be interesting to see further studies on aggregation in molecules as large, and as topical with respect to applications, as porphyrins. This is especially important considering the improvement in absorption characteristics, as well as the evaluation, and possible manipulation, of excited state relaxation pathways, leading to a possible mimicking of nature, where the broadening aspects of the spectra upon aggregation is being utilised without it becoming a loss process.

Chapter 8

Excited State Relaxation in Macrocycles

8.1 Introduction

So far in this thesis we have seen how response theory on a DFT reference can be used on molecules the size of **P**s to predict the electronic spectra for both one and two photon absorption processes. As the development of photosensitisers for use in PDT involves many more challenges from the synthetic chemistry community, any input from computational chemists can help the advancement of this promising technique. One major component of PDT that is crucial for a successful photosensitiser is efficient relaxation dynamics from the excited state manifold, ultimately generating a triplet state that can be quenched by singlet oxygen. The processes of IC and ISC are illustrated in Figure 8.1. As was introduced in Chapter 3, these processes are ultrafast in nature and a computational insight is not only helpful but in fact sometimes crucial for a deeper understanding of these pathways.

When moving on from small heteroaromatics, such as imidazole and indole, to system the size of **P** there are a number of issues that needs to be considered. In this chapter a strategy for the the theoretical description of processes such as the IC and ISC in **P** and **Pc** is presented.

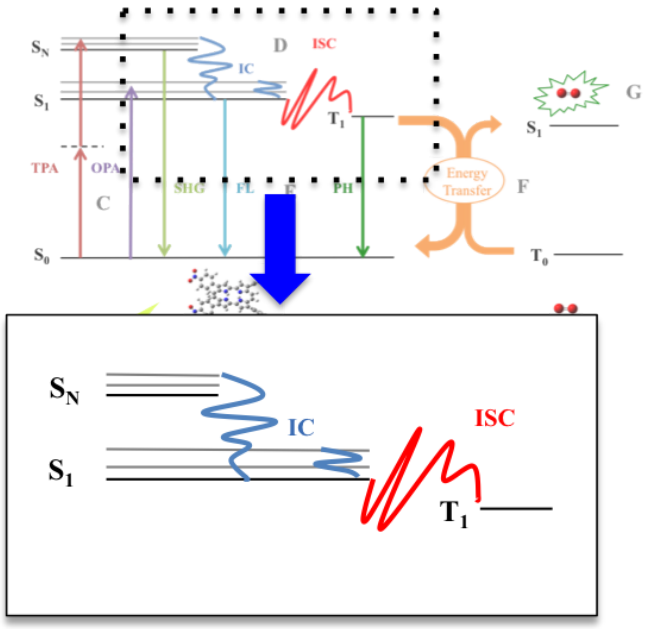

Figure 8.1: We have now reached the part of the PDT jablonski diagram that describes relaxation pathways that need to be efficient in an ideal photosensitiser.

8.2 Excited States Modelling Using Multiconfigurational Techniques

The modelling of reaction paths that cross multiple surfaces, such as IC and ISC, have been studied both experimentally and theoretically for number of years, and the understanding of the pathways involved in the photochemistry of small molecules, such as those introduced in Chapter 3, have reached great depth.[278] When it comes to the description of surface crossings of larger molecules, the use of TD-DFT would be ideal with respect to computational cost. However, response theory requires the use of a reference state that can be well described using one configuration (i.e. have no static correlation issues). This means that the topology of excited surfaces can only be investigated in dept in areas where the ground state is well defined, which removes both the flexibility of investigating the full geometrical space of the excited states in question as well as the investigation into crossing points with the ground state itself. Multiconfigurational approaches are therefore required. At the moment

the practical limit of the use of CASSCF lies in the region of 16 active electrons in 16 active orbitals. In order to look at chromophores that require an active space larger than that, or are contained within a larger system, there are two options remaining: either the computational method must be truncated, or the molecule itself must be truncated to a representative model system. Bearpark et al, investigated a collection of photochemical reactions involving multi-state processes using a CASSCF starting point.[279] Methods that can combine a quantum mechanical method (QM) with a Molecular Mechanics method (MM) (which determines molecular properties through the use of empirically built force fields) are generally referred to as hybrid methods. Hybrid methods, such as ONIOM investigated by Bearpark et al., rely on the fact that some parts of the molecule are more crucial in the representation of the chemical reaction we want to study, whilst the remainder are viewed as playing a minor role. This method was found to be appropriate for excited state potential energy surfaces, provided the chromophore could be accurately separated from the full molecule. This highlights the general trend, which is that these models are important in the investigations of chromophores in for example a protein or solvent environment.[280]

When it comes to molecules where the chromophore is essentially the entire system however, these methods were not always appropriate. This is a key factor when dealing with photosensitisers for use in PDT, as they normally are of a large structure incorporating many aromatic features, such as **P**s, where the whole system is crucial for the modelling of its photochemistry. For molecules such as this the strategy would be to turn to models where the method itself, rather than the molecular structure, has been truncated, such as the RASSCF approach.[198, 281] The RASSCF method is analogous to CASSCF but the active space has been divided into smaller parts (RAS1, RAS2 and RAS3 as introduced in Chapter 2) in order to reduce the total number of electron configurations generated. Even though the method is highly system-dependent, just like CASSCF, the partitioning of the system in this manner has been shown to be adequate and small errors when modelling the excited state surfaces, when compared to CASSCF, on a 14-electron system.[279]

We have investigated the use of RASSCF for analysis of the photochemistry of molecules the size of common photosensitiser molecules. Previous work has mainly been focused on the use of RASSCF to predict the vertical absorption of **P**, and construct quantitatively correct absorption spectra.[60, 282, 283] In this chapter we

are however focusing on the fact that analytical gradients exist and are well defined for both CASSCF and RASSCF within the Gaussian program.[284] This means that we do have access to both geometry and CIn optimisations. The correct partitioning of the subspaces in RASSCF is a core issue, and this work is focused on the selection of the orbitals and electrons to be included in the RAS spaces. The standard nomenclature for Gaussian RASSCF description (of the form CAS(n,m,RAS(a,b,c,d)) introduced in the Theoretical Background chapter) is used throughout for the discussion of the results obtained using the Gaussian 03 software.[160, 285]

8.2.1 RASSCF Orbital Selection

The issue of how to build an accurate RAS2 (or a CAS active space) is important not only for accurate qualitative descriptions of crossing points, but also for situations where the RAS/CAS wavefunction is used as a reference for further improvements. Addition of an MP2 electron correlation term (in the so called CASPT2 or RASPT2 approach) for example adds important dynamical correlation effects and has been shown to give excellent qualitative and quantitative vertical excitation results for a range of molecules, including **P**.[61, 286, 287] The RASPT2 method is very sensitive to the form of the underlying wavefunction, meaning that an accurate RASSCF wavefunction is crucial when predicting absorption spectra. When looking into relaxation pathways, an accurate wavefunction is even more important, especially when considering that it must be balanced with respect to the states that are of interest. When selecting how to divide the MO space, and selecting which of the orbitals that are to be included in the RAS2 space, the main consideration is hence to include orbitals that are relevant for the states under consideration. For crossing points for example, the MOs that constitutes the leading configuration that describes the involved states of interest must be included to make sure the wavefunction is not biased towards a specific state.

8.2.2 The Gouterman Approach for Porphyrins

In the case of **P** and **Pc** it is well known that the two dominating absorption bands in the spectrum (the Soret- and Q-bands) arise from excitation from the HOMO and the HOMO -1 to the LUMO and the LUMO+1 in the GFO model. The use of

these frontier MOs can therefore be expected to be crucial for an accurate RASSCF wavefunction for these types of systems, and can provide a good starting point for modelling the states involved in these dominating absorption bands. After a single point HF calculation, the full π-system is of the form as shown in Figure 8.2.

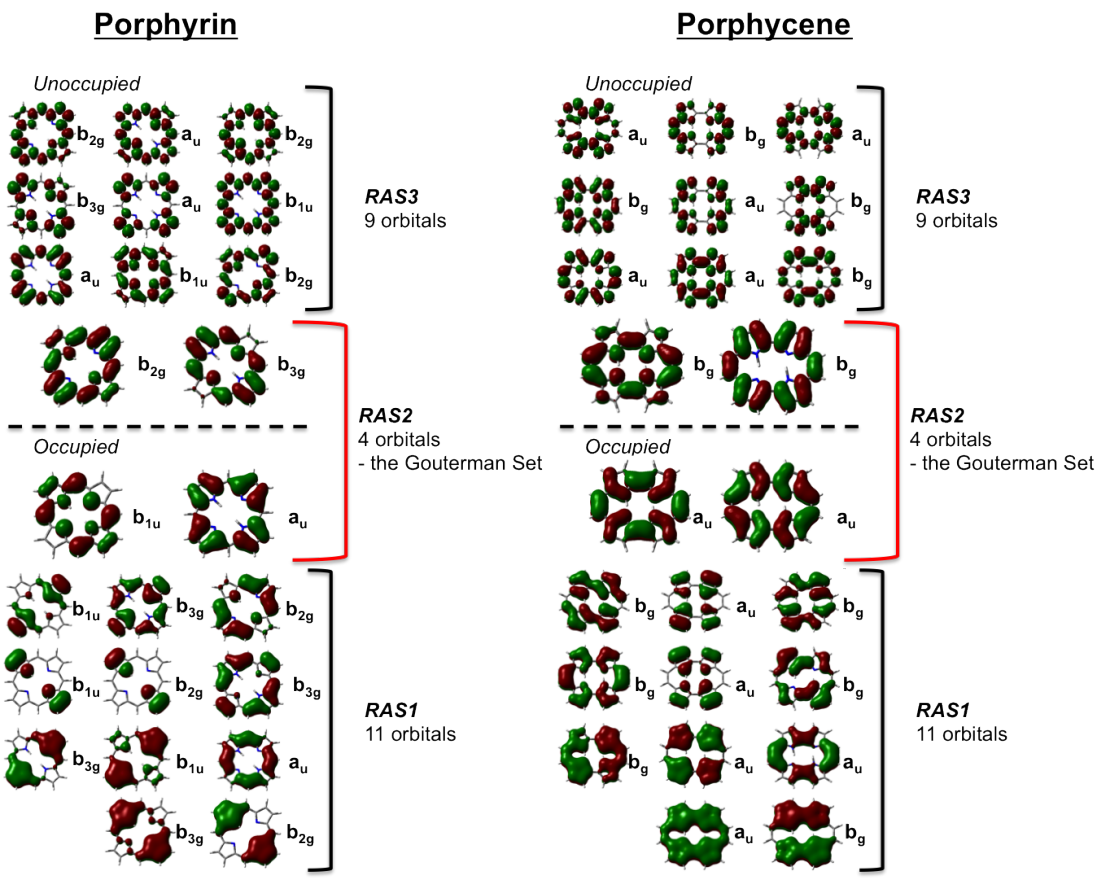

Figure 8.2: The HF orbitals of **P** and **Pc**. The partitioning used when examining the Gouterman set of orbitals as RAS2 is shown

The symmetry labels used here can be useful as a reference point, but it is important to note that the actual calculation is carried out without the use of symmetry, in order to avoid the software rotating the molecules and destroying the RAS space, and thereby also allow more flexible descriptions that break symmetry. This is especially important when looking at the topology of excited state potential energy surfaces, which can incorporate geometries away from the symmetric structure at the FC re-

gion. As the orbitals are optimised in the SCF procedure, the labels will also loose significance but can still be used as a reference point for the cases where there is visual resemblance, as well as a clear nodal pattern, in the orbitals before and after the optimisation procedure.

The first port of call was to compare the CAS(4,4) to the CAS(26,24,RAS(a,11,c,9)), with varying degree of occupations allowed in RAS1 (a) and RAS3 (b). The RAS space comprises the full π-system, and RAS2 contains the GFOs, as do the CAS active space.

As RASSCF in the method used here has analytical gradients available for geometry optimisations, the RHF structures were optimised on their CASSCF and RASSCF surfaces and compared with each other and with optimised CAM-B3LYP (with 6-31G* basis) structures. As evident from the previous chapters in this thesis, it is well known that DFT results preforms well with the optimisation of these types of systems at a low computational cost, and was therefore used as ground state reference. The singlet ground state optimised geometries for CAS(4,4) and CAS(26,24,RAS(2,11,2,9)), using the 6-31G* basis set, are presented in Figure 8.3. The optimised geometries of **P** from all the methods on the ground state surface were all planar, aromatic macrocycles, with bond lengths as indicated. When comparing the geometries with the RHF ground state optimised structure that was used for the orbital selection it becomes clear that, in order to achieve the correct symmetry group, the geometries needs to altered. It is known that **P** and **Pc** belong to the D_{2h} and C_{2h} point groups respectively, with a fully delocalised pyrrole-type moieties. In order for RHF to find a minimum on these surfaces however, the structure needs to be compressed generating C-C bonds as short as 1.22 Å. This deformation is especially evident in **Pc**, where the rectangular central cavity is elongated and compressed along the ethylene bridges. This is due to the fact that the RHF method lacks any correlation effects, and has been discussed earlier with respect to RASSCF. [198] The CAS(4,4) results generate a correct structure, to within 0.05 Åof the CAM-B3LYP minimum, whilst also being estimated to be in the correct point group, as is evident from the orbital shape. Clearly the inclusion of the GFOs is crucial in order to predict the correct ground state geometry.

Ground state RAS2/active space for **P** and **Pc** are introduced in Figure 8.4. These figures also serves as an illustration as to how the results are being analysed.

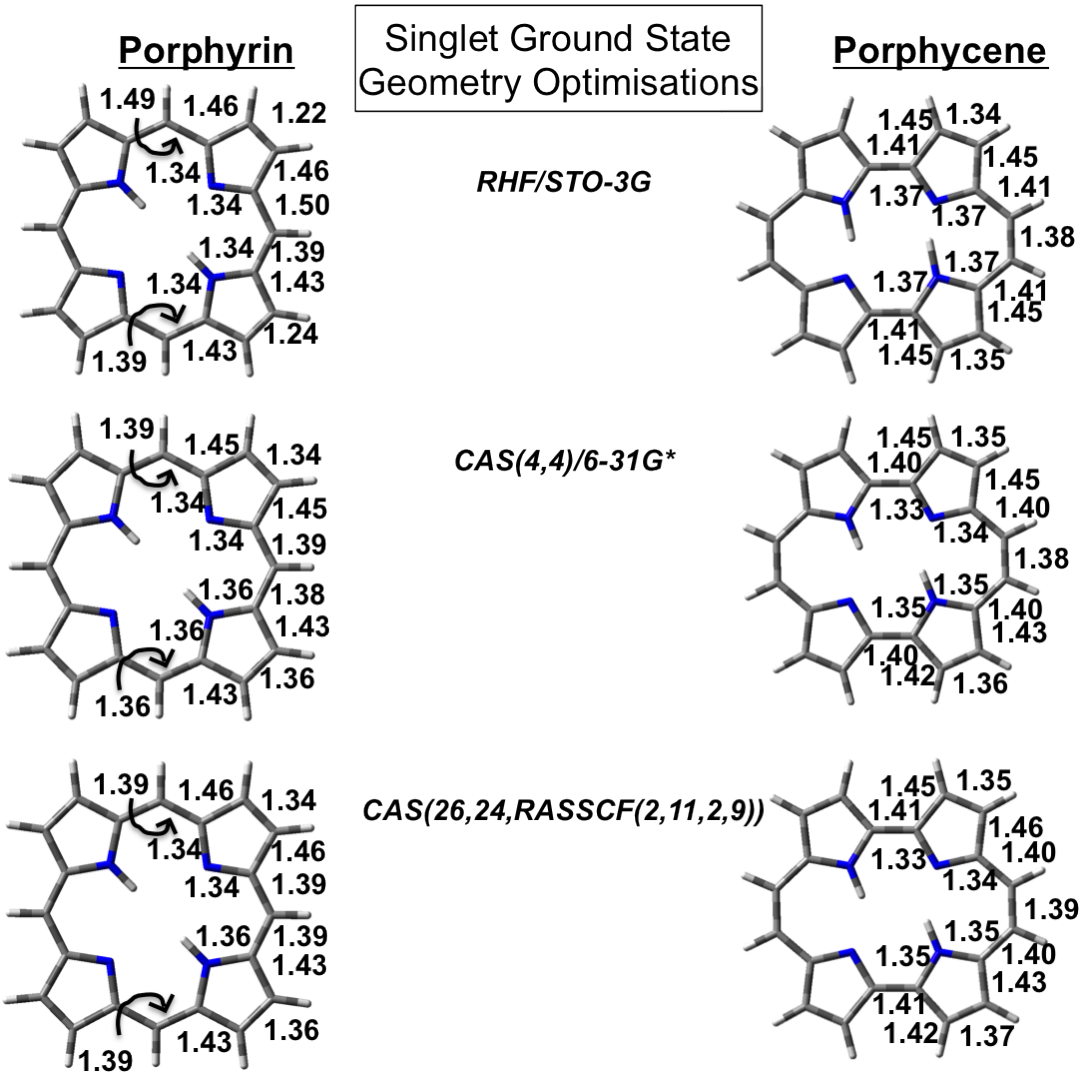

Figure 8.3: Ground state optimised geometries for **P** and **Pc**

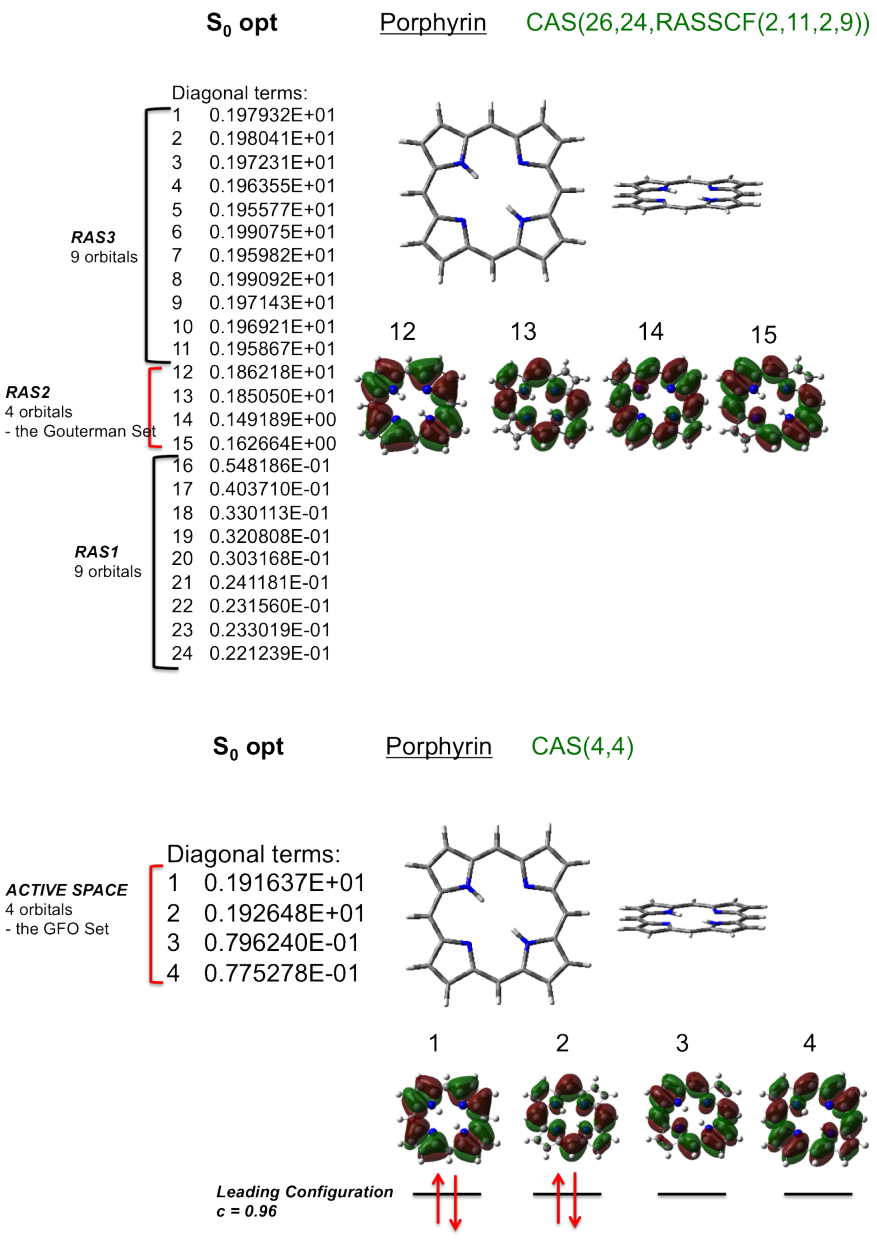

Figure 8.4: These are the variables which describes the ground state RAS and CASSCF wavefunctions of **P**. The diagonal terms are for the natural orbital optimisation (as introduced in the Theoretical Background chapter) and hence describe the orbital occupations.

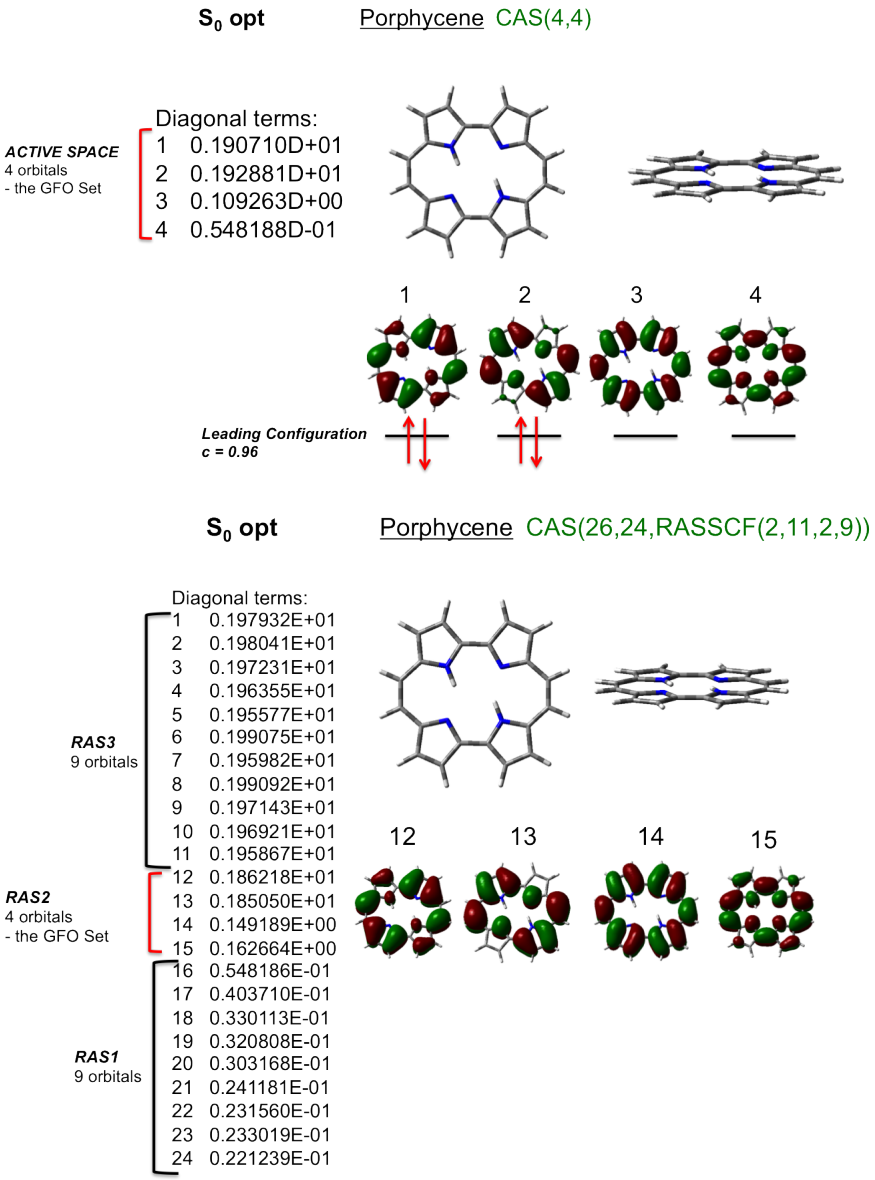

Figure 8.5: These are the variables which describes the ground state RAS and CASSCF wavefunctions of **P**. The diagonal terms are the orbital occupations of the natural orbitals.

Table 8.1: Resulting parameters for the ground state optimisation of **P** and **Pc** with CAS(4,4), CAS(26,24,RAS(1,11,1,9)) and CAS(26,24,RAS(2,11,2,9)) methods using the 6-31G* basis set. The orbital description for the leading configuration is estimated visually, as the calculations were carried out without symmetry constrains. The ΔE for the triplet states that converged are with respect to the singlet ground states using the same active space.

Method	Leading Configuration	Coefficient	Δ E (eV)
	P		
Singlet state			
CAS(4,4)	$(B_{1u})^2(A_u)^2$	0.96	5.65
CAS(26,24,RAS(1,11,1,9))	$(B_{1u})^2(A_u)^2$	0.89	4.15
CAS(26,24,RAS(2,11,2,9))	$(B_{1u})^2(A_u)^2$	0.85	0
Triplet state			
CAS(4,4)		0.96	1.40
	Pc		
Singlet state			
CAS(4,4)	$(A_u)^2(A_u)^2$	0.96	5.68
CAS(26,24,RAS(1,11,1,9))	$(A_u)^2(A_u)^2$	0.89	4.19
CAS(26,24,RAS(2,11,2,9))	$(A_u)^2(A_u)^2$	0.85	0

The first thing that can be seen when comparing the orbitals generated at the RHF level of theory is that the orbitals have been optimised to an alternative form, especially evident in the case of **Pc**. This form is more accurate, when comparing to higher level of theories, and also highlight the difficulties that conventional RHF has in reproducing the correct aromaticity pattern.

Looking at the RAS and CAS results in Table 8.1, it becomes clear that some $\pi-\pi$-dynamical correlation is crucial for predicting the geometry with the best energetics. Including the full π-system and allowing single occupations/holes in RAS3/RAS1 leads to a ground state energy improvement of 1.5 eV in **P** and **Pc**, compared with RHF. The largest improvement is however seen when allowing double occupations/holes in RAS3/RAS1. The energy goes down with a further 4.15 and 4.18 eV for **P** and **Pc** respectively. Clearly a degree of $\pi-\pi$-dynamical correlation is important for a qualitative description of energetics of the states in **P**-type systems, as expected. Using RASSCF on smaller systems, such as butadiene, has in fact been shown to be an efficient means to investigate important $\pi-\sigma$-dynamical correlation effects.

In small systems the full π-space can be incorporated, receiving a full-CI treatment, whilst the RAS1 and RAS3 spaces can account for important σ-orbitals.[288]

The RASSCF triplet states had convergence issues that unfortunately were not fully addressed before the completion of this thesis. The CASSCF results were however obtained, and the lowest energy triplet sate for **P** and Pc were found at 1.39 and 0.67 eV above the singlet state, respectively. The orbital optimisation for the triplet state lead to the orbitals being heavily localised, and so no orbital symmetry could be determined confidently.

It is important to point out at this stage that the aim of this section of work is to create a *qualitatively* correct wavefunction that has the attributes of a balanced description of excited states.

8.2.2.1 Vertical Adiabatic Energies

The vertical energy differences were measured at the FC region using the CAS(4,4) and CAS(26,24,RAS(2,11,2,9)) optimised minimum structures. **P** results are presented in Table 8.2 and **Pc** results in Table 8.3. When analysing results of RASSCF data it would be very valuable to have access to the correct indices of the leading configurations in the excited states. However, the creation of an indexed list as such is incredibly complex for RASSCF (due to the restricted nature of the RAS1 and RAS3) and the software used is currently unable to produce one.[284] The configuration numbers and coefficients are however listed in Table 8.2 . In order to characterise each state, traditional symmetry arguments have been used with respect to the visual assignment of the orbital occupations for the principal configurations in the active space of the CAS(4,4) calculation.

Both the third and fourth vertical excited states for **P** in Table 8.2 was difficult to converge on the CAS(4,4) surface, and the criteria had to be lowered to 10^5 and 10^4 respectively for the energy change in the SCF procedure. This was probably due to the fact that they mix with nearby states, which is seen in the coefficients for the configurations of the CAS(4,4). In the $2B_{2u}$ state for example, there are two configurations of B_{1g} character with coefficients of 0.2. The orbital description for the CAS(4,4) in State 4 is also not rigorous, as the orbitals are optimised during the procedure, but still behave largely as the irreducible representation indicated. As

Table 8.2: Resulting parameters for the vertical energies of **P** with the CAS(4,4) and CAS(26,24,RAS(2,11,2,9)) methods using the 6-31G* basis set. The orbital representation notation for the leading configuration is estimated visually, as the calculations were carried out without symmetry constrains. Δ eV are with respect to the ground state energy. [a] Only configurations with coefficients above 0.20 shown.

Method	Leading Configurations	Coefficient	Δ E (eV)
	P		
State 1 $1B_{3u}$			
CAS(4,4)	$(B_{1u})^1(A_u)^2(B_{2g})^1(B_{3g})^0$	0.75	3.52
	$(B_{1u})^2(A_u)^1(B_{2g})^0(B_{3g})^1$	0.63	
CAS(26,24,RAS(2,11,2,9))	c_{11}	0.62	2.58
	c_2	-0.59	
State 2 $1B_{2u}$			
CAS(4,4)	$(B_{1u})^2(A_u)^1(B_{2g})^1(B_{3g})^0$	0.77	3.74
	$(B_{1u})^1(A_u)^2(B_{2g})^0(B_{3g})^1$	0.62	
CAS(26,24,RAS(2,11,2,9))	c_7	0.66	3.46
	c_4	0.58	
State 3 $2B_{2u}$			
CAS(4,4)	$(B_{1u})^1(A_u)^2(B_{2g})^1(B_{3g})^0$	0.72	5.19
	$(B_{1u})^2(A_u)^1(B_{2g})^0(B_{3g})^1$	-0.57	
	$(B_{1u})^1(A_u)^1(B_{2g})^2(B_{3g})^0$	0.20	
	$(B_{1u})^0(A_u)^1(B_{2g})^2(B_{3g})^1$	0.20	
State 3			
CAS(26,24,RAS(2,11,2,9))	c_{12}	-0.50	4.46
	c_{16}	0.50	
	c_9	0.50	
State 4 $3B_{2u}$ [a]			
CAS(4,4)	$(B_{1u})^1(A_u)^2(B_{2g})^0(B_{3g})^1$	0.62	5.62
	$(B_{1u})^2(A_u)^1(B_{2g})^1(B_{3g})^0$	0.58	
	$(B_{1u})^2(A_u)^0(B_{2g})^1(B_{3g})^1$	0.27	
	$(B_{1u})^2(A_u)^1(B_{2g})^0(B_{3g})^1$	0.22	
State 4 $2B_{3u}$			
CAS(26,24,RAS(2,11,2,9))	c_4	-0.63	4.84
	c_7	0.55	

Table 8.3: Resulting parameters for the vertical energies of **Pc** with CAS(4,4) and CAS(26,24,RAS(2,11,2,9)) methods using the 6-31G* basis set. The orbital description for the leading configuration is estimated visually, as the calculations were carried out without symmetry constrains. Δ eV are with respect to the ground state energy. [a] Only configurations with coefficients above 0.30 shown.

Method	Leading Configurations	Coefficient	Δ E (eV)
	Pc		
State 1 $1B_u$			
CAS(4,4)	$(A_u)^2(A_u)^1(B_g)^1(B_g)^0$	0.90	3.45
	$(A_u)^1(A_u)^2(B_g)^1(B_g)^0$	0.41	
CAS(26,24,RAS(2,11,2,9))	c_{11}	-0.45	2.58
	c_2	-0.72	
State 2 $2B_u$			
CAS(4,4)	$(A_u)^2(A_u)^1(B_g)^0(B_g)^1$	0.84	3.69
	$(A_u)^1(A_u)^2(B_g)^0(B_g)^1$	0.45	
CAS(26,24,RAS(2,11,2,9))	c_7	0.81	3.30
	c_4	0.34	
State 3 $1A_g$			
CAS(4,4)	$(A_u)^2(A_u)^1(B_g)^0(B_g)^1$	0.42	5.12
	$(A_u)^2(A_u)^2(B_g)^0(B_g)^0$	0.39	
	$(A_u)^2(A_u)^0(B_g)^1(B_g)^1$	0.36	
	$(A_u)^2(A_u)^0(B_g)^2(B_g)^0$	0.34	
	$(A_u)^1(A_u)^1(B_g)^1(B_g)^1$	-0.32	
CAS(26,24,RAS(2,11,2,9))	c_{16}	-0.50	4.61
	c_{12}	0.50	
	c_{19}	-0.50	

only the first two Q-states and one of the Soret-states could be identified among the first four states, it is likely that State 4 is in fact a so-called N-type state, which is expected to be the $3B_{2u}$ state. This rationalises why a CAS space including the Gouterman set only is unsuitable and needs to be expanded.

For the CAS(4,4) calculation of the **Pc** macrocycle State 2 and State 3 the software was giving warnings for large orbital rotations, which is an indication of a bad set of starting orbitals. A look at the optimised shape and symmetries of the orbitals reveals that they are indeed now slightly weighted towards one end of the macrocyclic core in both states. This is expected, as it has been suggested in the previous chapters, due to the fact that the GFO model has been suggested to fail for some states of **Pc**.

The CAS(26,24,RAS(2,11,2,9)) for the **P** calculation did not have any convergence issues for the first four states and, using only energy arguments, the states could be suggested to be the Q- and the two Soret-bands respectively. The fact that the orbital optimisation step produces orbitals that still have the same shape as well as symmetry as they do the ground state further supports this. However, State 3, here assigned as the $2B_{2u}$ state based on the CAS(4,4) orbital occupancy, has a set of NO occupation numbers that does suggest a state where all RAS2 orbitals are singly occupied in the leading configurations, indicating a state of *gerade* symmetry, and hence a forbidden state in an OPA process. The position of these states are important with respect to TPA applications, as they are not dark to these processes. Looking into the dynamics relaxation processes of this state could therefor be important for the advancement of TPA PDT. For **Pc**, using CAS(26,24,RAS(2,11,2,9)), State 3 has the same issue with respect to the NO numbers. The CAS(4,4) in this case also converges to a state where four of the five leading configurations have gerade symmetry.

In order to expand the RAS2/Active space in a systematic manner, two approaches were attempted, which both bear in mind that CAS/RASSCF is invariant to the starting set of orbitals (due to the orbital optimisation step): First, NO occupation numbers were used to evaluate the most relevant HF molecular orbitals. The natural orbitals diagonalise the density matrix, meaning that their eigenvalues will be equal to the occupation of the orbital. This gives a tool for evaluating the multi-reference character of each orbital, and hence evaluate its importance in the RAS2/active

space. This method has been used by Sauri et al. to construct qualitatively sound wavefunctions for use in RASPT2 for the vertical energies of **P**. The results obtained the current study is introduced in the NO Approach section below.

The second approach was to design the RAS2/Active Space based on the Kohn-Sham orbitals resulting from a DFT calculation. There is a lot of debate what the KS orbitals and their eigenvalues actually represent, and as far as the response theory results introduced in this thesis are concerned, we have been careful to refer to the NTO representation when analysing absorption transitions. Some studies argues that, when care is taken when identifying order, symmetry and shape of the orbitals they can in fact be used as one-electron orbitals for *qualitative* chemical analysis.[289] In the case of TD-DFT, there is no actual need for orbitals in the first place. The results are exact with respect to the density. However, the method of implementing DFT does use orbitals that, using a good functional, are very well behaved with respect to experiment. It is therefore interesting to see what insight can be gained from the symmetry and shape of the KS orbitals that describe particular states. This approach to building a RAS/CAS wavefunction is introduced in the KS Approach section below.

8.2.3 NO Approach

In the work presented here, the NO occupation method was attempted for both **P** and **Pc** vertical energies, as well as as a measure to construct a wavefunction to be used for a CIn optimisations. In this NO approach, each vertical excited state, calculated using the CAS(26,24,RAS(2,11,2,9)) wavefunction, had the occupation numbers tabulated. A cutoff of $0.1 \leq p_{ii} \leq 1.9$ was used to decide which orbitals, if any, needed to be incorporated into the wavefunction for each specific state. When calculating the energy differences between states, such as excitation energy from the ground state and surface intersections, as well as CIn optimisations all wavefunctions have to be built considering the occupation numbers of both states, in order to avoid wavefunction bias to a particular state.

In the results presented in Table 8.4, State 6 is included as an example. This state, and also State 7 and 10, did converge vertically, but could not be characterised due to the fact that the orbital optimisation step resulted in orbital shapes and symmetries that were far removed from the original set. In work carried out by Sauri et al., which

Table 8.4: Natural Occupation Numbers for key molecular orbitals of the lowest $\pi - \pi^*$ states in **P**. The symmetry description in the left column refers to state1, 2 and 3 only, where nodal patterns could be used to categorise to orbitals.

Orbital	State 1	State 2	State 3	State 4	State 6
b2g	1.96	1.94	1.96	1.96	1.96
b3g	**1.93**	1.96	**1.93**	1.96	**1.91**
b2g	1.99	1.98	1.99	1.99	1.99
b1u	1.95	1.96	1.96	1.95	1.94
b1u	1.99	1.98	1.99	1.99	1.99
b2g	1.97	1.96	1.97	1.96	1.98
b1u	1.97	1.96	1.96	1.96	1.98
b3g	1.94	1.96	**1.94**	1.95	**1.94**
au	1.45	1.40	1.03	1.45	0.96
b1u	1.48	1.53	1.03	1.36	1.22
b2g	0.53	0.60	0.97	0.55	0.38
b3g	0.58	0.48	0.97	0.65	1.49
au	0.07	0.06	0.08	0.06	0.12
b1u	0.04	0.03	0.04	0.04	0.04
b2g	0.03	0.03	0.03	0.03	0.03
b3g	0.03	0.03	0.03	0.03	0.03

Table 8.5: Natural Occupation Numbers for key molecular orbitals of the lowest $\pi - \pi^*$ states in **Pc**. The symmetry description in the left column refers to state1, 2 and 3 only, where nodal patterns could be used to categorise to orbitals.

Orbital	State 1	State 2	State 3	State 5
bg	1.937990	1.964020	1.934260	1.94052
bg	1.964700	1.948330	1.962880	1.96395
bg	1.992010	1.985070	1.990110	1.98956
au	1.992290	1.985790	1.990110	1.98958
au	1.970870	1.967960	1.969660	1.96914
au	1.996637	1.972380	1.965830	1.96508
au	1.959510	1.963300	1.962960	1.96066
bg	1.943210	1.963590	1.944800	1.93556
au	1.648120	1.146440	1.029990	1.03657
au	1.270320	1.782880	1.043510	1.04064
bg	0.760379	0.882999	0.985126	0.988114
bg	0.354102	0.224748	0.961960	0.956839
au	0.066445	0.056257	0.078178	0.0746174
au	0.053607	0.044553	0.055768	0.0631236
bg	0.036682	0.035740	0.039650	0.0394697
au	0.028373	0.028489	0.029252	0.0289844
bg	0.030785	0.028595	0.031063	0.0325363

used symmetry, the orbitals were constrained to optimise to stay within the irreducible representation elements they originated in. This lead to NO occupation numbers in the order of 1.25 being found in the RAS1 set of a CAS(26,24,RAS(2,11,2,9)) wavefunction for states above the Q- and Soret-states.[60] But here, State 6 have NO occupations well within the cutoff range, as do states 7 and 10. Clearly the cutoff needs to be lowered when orbital flexibility is introduced. The **Pc** results using this approach is listed in Table 8.5. As discussed earlier, it is well known that the GFO model is not suitable for **Pc**. However, it is seen here that the occupation numbers are even more within the suggested cut off value. The converged State 5 is also included here, but was not characterised due to orbital optimisations.

In order to investigate whether a higher cut off value could be used, such as $0.10 \leq p_{ii} \leq 1.95$, State 1 and 3 of **P** were both attempted incorporating the b_3g orbitals (indicated in **bold** in Table 8.4) into the RAS2 space. The results are summarised in Figure 8.6 and Table 8.6

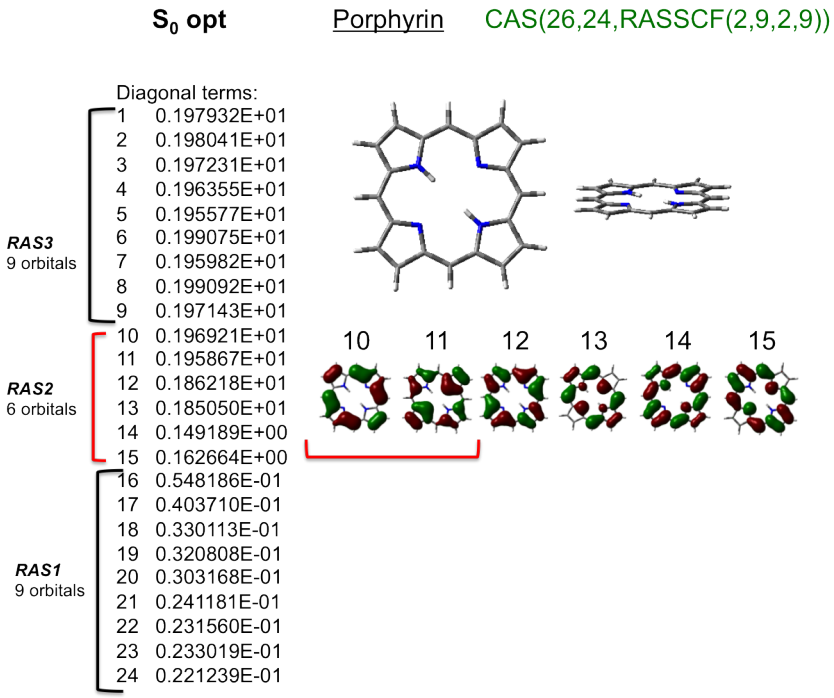

Figure 8.6: Expanded RASSCF set, as determined from the NO approach.

Table 8.6: Resulting parameters for the vertical energies of **P** with the CAS(26,24,RAS(2,9,2,9)) method, selected with NO approach, using the 6-31G* basis set. Δ eV are with respect to the CAS(26,24,RAS(2,11,2,9)) energies.

Method	Leading Configurations	Coefficient	Δ E (eV)
	P		
Ground State			
CAS(26,24,RAS(2,9,2,9))	c_1	0.89	0.09
State 1			
CAS(26,24,RAS(2,9,2,9))	c_7	0.57	0.29
	c_4	0.59	

The change in energy of the ground state is in the order of only 0.09 eV, and the geometries are identical. When it comes to the excited state that converged however, a larger change is seen, as the state is stabilised by 0.29 eV, approaching the experimental value of the first Q-state. Clearly the addition of two extra orbitals and two electrons improved the description. Unfortunately, as the RASSCF configurations are not indexed, it can not be seen how the specific orbitals that were selected in this approach caused the stabilisation of this specific state.

8.2.4 KS Approach

Vertical TD-DFT outputs, using B3LYP and the 6-31G** basis set, was analysed with respect to the single excitations and their KS orbital description. As the macrocycle is not expected to be heavily delocalised, the B3LYP functional without long range correction was considered suitable. For **P**, the results indicate, as illustrated in Figure 8.7, that two orbitals outside the GFO set should be incorporated into the RAS2 space of the CAS(26,24,RAS(2,11,2,9)) in order to describe State 3 and 5 accurately.

In Table 8.7 the resulting energies are compared with the energies obtained using the GFO set. There is little or no change in the energies and configurations, and the orbitals still behave largely as the irreducible representations they belong to upon inspection.

The KS approach was also attempted for **Pc**, using the same method as in **P**. Unfortunately the **Pc** states were very difficult to converge to vertical states using a RAS space the size of CAS(26,24,RAS(2,11,2,9)).

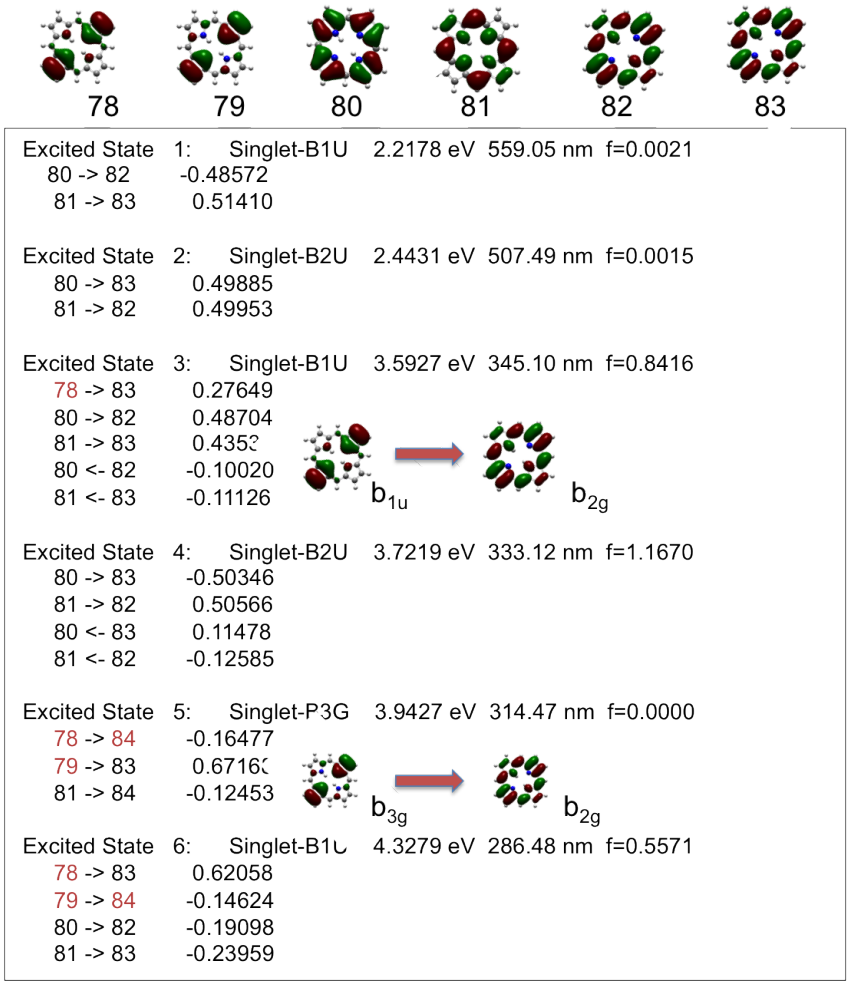

Figure 8.7: The top line indicates the orbitals that were chosen after inspection of the KS orbitals

Table 8.7: Resulting parameters for the vertical energies of **P** with the CAS(26,24,RAS(2,9,2,9)) method, selected with KS approach, using the 6-31G* basis set. Δ eV are with respect to the CAS(26,24,RAS(2,11,2,9)) energies using the same approach.

Method	Leading Configurations	Coefficient	Δ E (eV)
	P		
Ground State			
CAS(26,24,RAS(2,9,2,9))	c_1	0.84	0.36
State 1			
CAS(26,24,RAS(2,9,2,9))	c_7	0.59	0.25
	c_4	0.57	
State 2			
CAS(26,24,RAS(2,9,2,9))	c_{11}	0.64	0.15
	c_2	-0.57	
State 3			
CAS(26,24,RAS(2,9,2,9))	c_9	-0.50	0.09
	c_{16}	-0.50	
	c_{12}	0.50	
State 4			
CAS(26,24,RAS(2,9,2,9))	c_9	-0.50	0.09
	c_{16}	-0.50	
	c_{12}	0.50	

Table 8.8: Resulting parameters for the ground state of **Pc** with the CAS(26,24,RAS(2,9,2,9)) method, selected with KS approach, using the 6-31G* basis set. Δ eV are with respect to the CAS(26,24,RAS(2,11,2,9)) energies using the same approach.

Method	Leading Configurations	Coefficient	Δ E (eV)
	Pc		
Ground State			
CAS(26,24,RAS(2,9,2,9))	c_1	0.84	0.36

8.3 Optimised Excited States

Excited state optimisations were carried out for all converged vertical states. As far as the state could be accurately characterised, both geometries and energies were compared with TD-DFT optimised states at the CAM-B3LYP//6-31G* level of theory. The results are presented in Figure 8.8

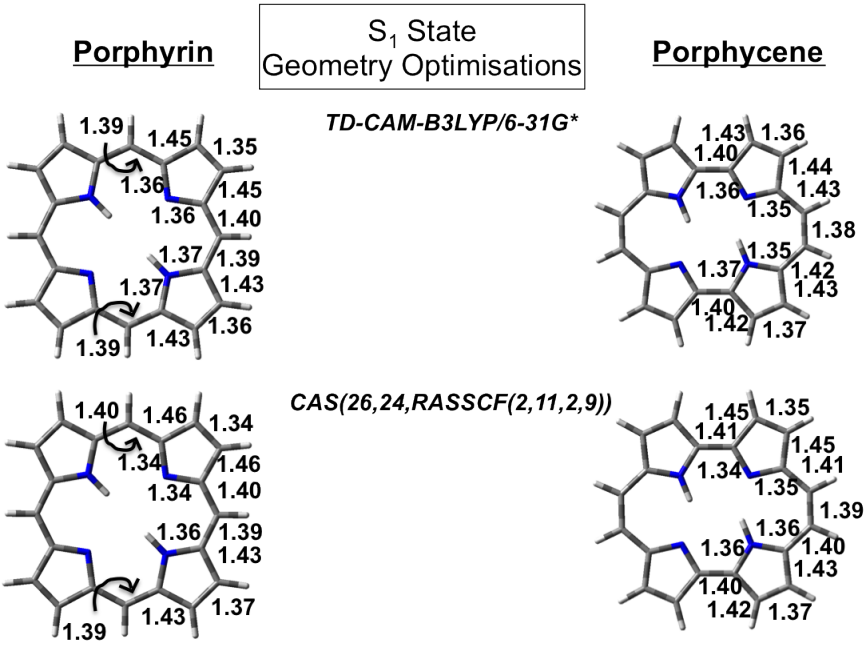

Figure 8.8: Optimised parameters, compared to a TD-DFT optimised excited state minimum

Porphyrin has its first CAS(26,24,RAS(2,11,2,9) excited state at nearly exactly vertically from its ground state geometry, and only shows changes of the order of 0.01 Å. The **Pc** geometry did also only have a very small change, in the pyrrole moieties, with an elongation in the N-C bonds in the order of 0.01 Å. Comparing with TD-DFT reference, we can see that this wavefunction is very good for describing the geometry at the first excited state minimum energy. The geometries are nearly identical, apart from a slight elongation of the C-N double bond.

8.4 Excited State Relaxation

For all converged states, CIn intersections were attempted. The basis set was downsized to a 4-31G set as a starting point, due to the exploratory nature of the preliminary optimisations. It is well known that pyrrole type molecules (such as of the type introduced in Chapter 3 of this Thesis) have two dominating coordinates that couple the first excited state and the ground state: the $\pi - \sigma*$ state coupling through elongation of the N-H bond, and a $\pi - \pi*$ state coupling through an envelope puckering movement in the C-N-C plane. The first approach was therefore to set CIn optimisations to start from either an N-H elongated or a C-N-C puckered geometry. These geometries were altered manually. Within the time limit of the completion of this Thesis, only one CI was successfully characterised, between the first excited singlet state, 1^1B_u, and the ground state, ^1A_g, in **Pc** (Figure 8.9).

The coordinates that lift the degeneracy, the branching space coordinates x_1 and x_2 introduced in the Theory section, are both in the plane of the macrocycle, which is still in its planar geometry at the intersection. The localisation of the mode in one part of the **Pc** structure in this manner is commonly seen in large aromatic moieties, such as denrimes, which could indicate a successful intersection optimisation.[290] One interesting note is that the RAS2 has a highly localised orbital. This orbital would not have been found using a CAS(4,4) wavefunction, as the orbitals are only allowed to mix within the active space. It would not have been found within the restrictions of symmetry either, which highlights the importance of a flexible wavefunction when localising crossing points. Clearly localised orbitals are needed to describe intersections of this type, where the modes that facilitate crossing are localised as well.

8.5 Conclusion

This chapter introduced a section of exploratory work carried out using the CASSCF and RASSCF methods as implemented in the Gaussian software. As this program has access to analytical gradients that are well defined for the RASSCF wavefunction, ground state optimisations were carried out successfully, reproducing expected symmetries and geometries. Instead of focusing on vertical excitations, the first aim was to, select a stable wavefunction that could describe excited, as well as ground

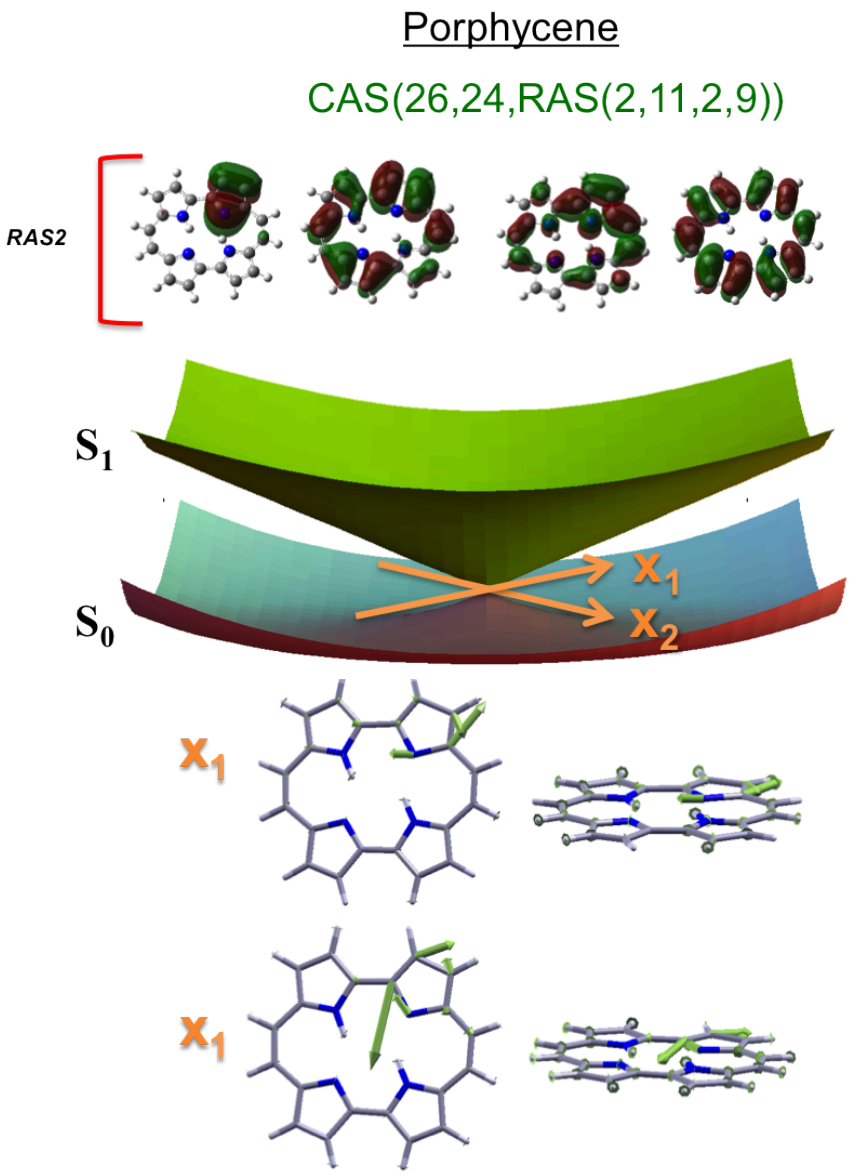

Figure 8.9: Conical intersection found between the first excited and the ground state.

state, in a robust manner. The use of NO occupation numbers was successful in the localisation of the first couple of states. The second aim of this chapter was to use the wavefunctions for the calculation of relaxation pathways between the states. The intersection that was found show a relaxation pathway that proceeds through one localised mode, which highlight the need for a flexible wavefunction.

Overall, the results presented here, even though they are very preliminary, seem promising. The code does however need to be fully developed before more through analysis of results can be carried out. Apart from indexing of the configurations, as mentioned in the text, the evaluation of the $\langle S^2 \rangle$ eigenvalue would have been incredibly useful. Especially for evaluation of crossing points as to being IC or ISCs. The present convergence in the optimisations are also very time consuming and needs to be developed further. The use of RASSCF does however come across as having the potential to be very powerful, and the future is certainly bright for excited state calculations of compounds with applications as topical as PDT.

Chapter 9

My Conclusions

In this thesis, computational chemistry techniques are used as a tool for both the interpretation of experimental data on existing systems, and investigations into new systems and dynamics pathways. The main problem of the thesis is centered on the various photochemical phenomena that take place during the photosensitisation pathway of PDT. Studying the efficiency of absorption of light by both small and large heteroaromatic systems, and following the relaxation pathways from the excited states, this thesis highlight the complexity of the overall problem from a computational chemistry point of view. Not only does the molecular systems at hand have to be considered when choosing a computational method, but the character of the photochemical processes themselves have to be well understood.

In chapter 3, high level CC methods as well as multiconfigurational techniques were used to successfully characterise the absorption as well as relaxation dynamics of indole and imidazole. The presence of $\pi\sigma^*$ states is an important aspect of these types systems, and the use of computation is shown here to be very important for the characterisation of these states, as they are optically dark.

Chapter 4, as well as chapter 5 and 6, focuses on the non-linear optical effects of large heteroaromatics. For these studies DFT and TD-DFT needs to be used, due to the size of the systems. The use of the CAM-B3LYP functional in conjunction with quadratic response theory, predicts the TPA behaviour of a large set of substituted porphycenes that could be promising for their use as PDT photosensitises. The effect of the core electronic structure of a large set of macrocycles on the TPA is also presented. Substitution of a pyrrole unit for a furan moiety, indicates that a

very small effect in the OPA can still afford large TPA changes, due to resonance enhancement of the signal. The same functional and method also concurs with experimental evidence that substitution pattern has a large impact on SHG processes in porphyrin and porphycene, even when used without accounting for solvent effects.

From the results in chapter 7 is is clear that DFT with added dispersion is crucial when dealing with ground and excited states when there are more than one molecule in an isolated system. As this is the case in most biologically pertinent situations, this is a very important concept to consider. Especially as DFT can be used for systems of considerable size. The study shows that the TD-DFT calculations behave well in accordance with Kasha's rule for exciton coupling, and also highlight the usefulness of NTOs to describe transitions.

The final chapter of this thesis deals with the relaxation dynamics of large heteroaromatics. As in chapter 3, multiconfigurational techniques are applied. Unlike the CASSCF strategy used for smaller systems, the RASSCF method needed for these systems is not as robust and well characterised for relaxation dynamics. In the exploratory work carried out here, it is however evident that it is possible to build a stable wavefunction for many of the excited states available. This wavefunction also seems useful for the optimisation of both ground and excited states, as well as location of crossing points.

9.1 Future Work

Overall in this thesis there are a lot of very interesting research avenues that could be further investigated. In the work on TPA especially, future research should aim at incorporating TPA solvent studies. This is true in case of the PCM method, as well as the use of more specific models, such as QM/MM in order to fully appreciate the extent of these effects. It would also be interesting to see how well current dispersion functionals can predict TPA.

Using RASSCF for ISC crossing points can also be complemented by the application of the DFT hybrid singlet-triplet crossing method as developed by Harvey et al.[135] This method has been shown to give accurate ISC points for the phenyl cation amongst others, and could have potential for macrocycles as well.

For the overall issue of PDT as a whole the main hurdle left is the interaction of the system with molecular oxygen in the sensitisation process. As this involves calculations of a system open shell character, the use of flexible methods such as RASSCF and higher order wavefunction methods is needed, and recent work such as that of Barbatti et al, is very promising for the field.[291]

The field of heteroaromatic photochemistry in general, and that of PDT in particular, is very involved and requires intimate knowledge of many highly specialised computational tools. The work introduced in this thesis highlights that, even though there are many aspects still to be considered, computations can have a part to play in the development of PDT as a treatment technique. It can also play a crucial role in interpreting experimental data for these type of systems. As computational hardware and software continues to develop, there seems to be a bright future for the computational contribution to the understanding of the photochemistry of heteroaromatics.

Appdx A

Benchmark of vertical excited states in the porphyrin monomer, comparing Experiment, EOM-CCSD and RASPT2 results with a range of TD-DFT functionals and with state charcterisation.

EOM-CCSD/aug-cc-pVDZ

Excitation Energy (eV)	Symmetry	Character	*Comment*
2.1937	B1u	GFO	*Q*
2.6076	B2u	GFO	*Q*
3.848	B1u	GFO	*B*
3.9537	B2u	GFO	*B*
4.0825	B3g	GFO (+HOMO-3)	*N*

RASPT2/cc-pVDZ

Excitation Energy (eV)	Symmetry	Character	*Comment*
2.18	B1u	GFO	*Q*
2.38	B2u	GFO	*Q*
3.21	B1u	GFO	*B*
3.23	B2u	GFO	*B*

Experiment [a]

Excitation Energy (eV)	Symmetry	Character	*Comment*
1.98-2.02	b1u	GFO	*Q*
2.33-2.42	b2u	GFO	*Q*
3.13-3.33	b1u	GFO	*B*
3.13-3.33	b2u	GFO	*B*

Figure 1: RASPT2 results as well as experimental results are reported in Reference [61].

B97D/ TZVP

Excitation Energy (eV)	Symmetry	Character	*Comment*
2.1628	B1u	GFO	*Q*
2.2923	B2u	GFO	*Q*
2.9534	B3g	HOMO-2 LUMO+1	*N*
2.992	B1u	GFO and HOMO-3	*N*
3.0072	Ag	HOMO-2 LUMO	
3.032	B2u	GFO and HOMO-3	*N*

B97D/ 6-31G*

Excitation Energy (eV)	Symmetry	Character	*Comment*
2.1703	B1u	GFO	*Q*
2.3026	B2u	GFO	*Q*
2.9506	B3g	HOMO-2 LUMO+1	*N*
2.9958	B1u	GFO and HOMO-3	*N*
3.0034	Ag	HOMO-2 LUMO	

B97D/ 6-311G*

Excitation Energy (eV)	Symmetry	Character	*Comment*
2.1664	B1u	GFO	*Q*
2.2917	B2u	GFO	*Q*
2.9533	B3g	HOMO-2 LUMO+1	*N*
2.9913	B1u	GFO and HOMO-3	*N*
3.0091	Ag	HOMO-2 LUMO	

Figure 2: B97D results with varying basis sets

CAM-B3LYP/ TZVP

Excitation Energy (eV)	Symmetry	Character	*Comment*
2.2277	B1U	GFO	*Q*
2.4402	B2U	GFO	*Q*
3.5852	B1U	GFO (+HOMO-3)	*N*
3.6905	B2U	GFO	*B*
3.9524	B3G		
4.3048	B1U		

CAM-B3LYP/ 6-31G*

Excitation Energy (eV)	Symmetry	Character	*Comment*
2.24	B1U	GFO	Q
2.4648	B2U	GFO	Q
		GFO (+ HOMO -3, HOMO-2, LUMO+2)	
3.6184	B1U		N
3.7517	B2U	GFO	B
3.9648	B3G		

CAM-B3LYP/ 6-311G*

Excitation Energy (eV)	Symmetry	Character	*Comment*
2.229	B1U	GFO	Q
2.4392	B2U	GFO	Q
		GFO (+ HOMO -3, HOMO-2, LUMO+2)	
3.5961	B1U		N
3.7196	B2U	GFO	B
3.9576	B3G		

Figure 3: CAM-B3LYP results with varying basis sets

PBE0/ TZVP

Excitation Energy (eV)	Symmetry	Character	*Comment*
2.3414	B1U	GFO	*Q*
2.5002	B2U	GFO	*Q*
3.4458	B1U	GFO (+HOMO-3)	*N*
3.5833	B2U	GFO (+HOMO-3)	*N*
3.5883	B3G		

PBE0/ 6-31G*

Excitation Energy (eV)	Symmetry	Character	*Comment*
2.3536	B1U	GFO	*Q*
2.52	B2U	GFO	*Q*
3.4677	B1U	GFO (+HOMO-3)	*N*
3.5979	B3G	N	
3.6336	B2U	GFO (+HOMO-3)	*N*
3.8221	AG		

PBE0/ 6-311G*

Excitation Energy (eV)	Symmetry	Character	*Comment*
2.3453	B1U	GOF	*B*
2.5017	B2U	GFO	*B*
3.452	B1U	GFO (HOMO-3)	*N*
3.5939	B3G		
3.6073	B2U	GFO (HOMO-3)	*N*
3.8099	AG		

Figure 4: PBE0 functional with varying basis sets

wB97XD/ TZVP

Excitation Energy (eV)	Symmetry	Character	*Comment*
2.1678	B1U	GFO	*Q*
2.3906	B2U	GFO	*Q*
3.5818	B1U	GFO (+HOMO-3)	*N*
3.6895	B2U	GFO	*B*
3.9739	B3G		
3.9739	B3G		

wB97XD/6-31G*

Excitation Energy (eV)	Symmetry	Character	*Comment*
2.1827	B1U	GFO	*Q*
2.4164	B2U	GFO	*Q*
3.6166	B1U	GFO (HOMO-3)	*N*
3.751	B2U	GFO	*B*
3.9849	B3G		

wB97XD/ 6-311G*

Excitation Energy (eV)	Symmetry	Character	*Comment*
2.1706	B1U	GFO	*Q*
2.3902	B2U	GFO	*Q*
3.5954	B1U	GFO (HOMO-3)	*N*
3.7207	B2U	GFO	*B*
3.9805	B3G		

Figure 5: ωB97XD results with varying basis sets

References

[1] N.J. Turro, V. Ramamurthy, and J.C. Scaiano. *Modern molecular photochemistry of organic molecules*. University Science Books, 2010. 2, 47

[2] J. March. *Advanced organic chemistry: reactions, mechanisms, and structure*. A Wiley-Interscience Publication. Wiley, 1985. 2

[3] M. R. Wasielewski. Photoinduced electron transfer in supramolecular systems for artificial photosynthesis. *Chem. Rev.*, 92(3):435–461, 1992. 3

[4] C. W. Cody, D. C. Prasher, W. M. Westler, F. G. Prendergast, and W. W. Ward. Chemical structure of the hexapeptide chromophore of the aequorea green-fluorescent protein. *Biochemistry*, 32(5):1212–1218, 1993. 3

[5] W. Kaiser and C. G. B. Garrett. Two-photon excitation in caf2: Eu2+. *Phys. Rev. Lett.*, 7:229–231, 1961. 3

[6] C.E. Crespo-Hernndez, B. Cohen, P. M. Hare, and B. Kohler. Ultrafast excited-state dynamics in nucleic acids. *Chem. Rev.*, 104(4):1977–2020, 2004. 3, 57

[7] C. T. Middleton, K. de La Harpe, C. Su, Y. K. Law, C. E. Crespo-Hernndez, and B. Kohler. Dna excited-state dynamics: From single bases to the double helix. *Ann. Rev. Phys. Chem.*, 60(1):217–239, 2009. 3

[8] C.Z. Bisgaard, H. Satzger, S. Ullrich, and A. Stolow. Excited-state dynamics of isolated dna bases: A case study of adenine. *ChemPhysChem*, 10(1):101–110, 2009. 5, 57

[9] R. Bonnett. *Chemical Aspects of Photodynamic Therapy*. Advanced chemistry texts. Taylor & Francis, 2000. 5, 7, 55, 152

[10] Niels Ryberg Finsen. *Om Bekæmpelse af Lupus vulgaris med en Redegørelse for de i Danmark opnaaede Resultater*. Gyldendalske boghandels forlag, 1902. 7

[11] M. Ethirajan, Y. Chen, P. Joshi, and R. K. Pandey. The role of porphyrin chemistry in tumor imaging and photodynamic therapy. *Chem. Soc. Rev.*, 40: 340–362, 2011. 7

[12] R. R Allison, G. H Downie, R. Cuenca, X-H. Hu, C. JH Childs, and C. H Sibata. Photosensitizers in clinical {PDT}. *Photodiag. Photodynam. Therapy*, 1(1):27 – 42, 2004. 7, 9

[13] E. D Sternberg, D. Dolphin, and C. Brckner. Porphyrin-based photosensitizers for use in photodynamic therapy. *Tetrahedron*, 54(17):4151 – 4202, 1998. 7

[14] T.J. Dougherty, J.E. Kaufman, A. Goldfarb, K.R. Weishaupt, D. Boyle, and A. Mittleman. Photoradiation therapy for the treatment of malignant tumors. *Cancer Res.*, 38(8):2628–2635, 1978. 8

[15] Jonathan P. Celli, Bryan Q. Spring, Imran Rizvi, Conor L. Evans, Kimberley S. Samkoe, Sarika Verma, Brian W. Pogue, and Tayyaba Hasan. Imaging and photodynamic therapy: Mechanisms, monitoring, and optimization. *Chem. Rev.*, 110(5):2795–2838, 2010. 8, 55, 97

[16] R. Bonnett. Photodynamic therapy in historical perspectives. *Reviews in Contemporary Pharmacotherapy*, 10(1):1–17, 1999.

[17] R. R. Allison and C. H. Sibata. Oncologic photodynamic therapy photosensitizers: A clinical review. *Photodiag. Photodynam. Therapy*, 7(2):61 – 75, 2010. 8

[18] C. M. Brackett and S. O. Gollnick. Photodynamic therapy enhancement of anti-tumor immunity. *Photochem. Photobiol. Sci.*, 10:649–652, 2011. 8

[19] J. P. Hubschman, S. Reddy, and S. D. Schwartz. Age-related macular degeneration: current treatments. *Clin Ophthalmol*, 3:155–166, 2009. 8

[20] J. Moan and Q. Peng. An outline of the hundred-year history of pdt. *Anticancer Res*, 23(5A):3591–3600, 2003. 9

[21] J.C. Kennedy, R.H. Pottier, and D.C. Pross. Photodynamic therapy with endogenous protoporphyrin: Ix: Basic principles and present clinical experience. *J. Photochem. Photobiol. B*, 6(12):143 – 148, 1990. ISSN 1011-1344. 9

[22] C.A. Morton, K.E. McKenna, and L.E. Rhodes. Guidelines for topical photodynamic therapy: update. *Brit. J. Dermatol.*, 159(6):1245–1266, 2008. ISSN 1365-2133. 9

[23] M. L. Elsaie, S. Choudhary, and K. Nouri. Photodynamic therapy in dermatology: a review. *Laser Med. Sci.*, 24(6):971–980, 2009. ISSN 0268-8921. 9

[24] D. Dolphin, E. D. Sternberg, and C. Bruckner. Porphyrin-based photosensitizers for use in photodynamic therapy. *Tetrahedron*, 54(17):4151–4202, 1998. ISSN 0040-4020. 9

[25] J. C. Sutherland. Biological effects of polychromatic light. *Photochem. Photobiol.*, 76(2):164–170, 2002. ISSN 1751-1097. 9, 10

[26] K. Plaetzer, B. Krammer, J. Berlanda, F. Berr, and T. Kiesslich. Photophysics and photochemistry of photodynamic therapy: fundamental aspects. *Lasers Med. Sci.*, 24(2):259–268, 2009. ISSN 0268-8921. 9

[27] K. Szacilowski, W. Macyk, A. Drzewiecka-Matuszek, M. Brindell, and G. Stochel. Bioinorganic photochemistry. frontiers and mechanisms. *Chem. Rev.*, 105(6):2647–2694, 2005. 10

[28] A. Hagfeldt, G. Boschloo, L. Sun, L. Kloo, and H. Pettersson. Dye-sensitized solar cells. *Chem. Rev.*, 110(11):6595–6663, 2010.

[29] A. W. Hains, Z. Liang, M. A. Woodhouse, and B. A. Gregg. Molecular semiconductors in organic photovoltaic cells. *Chem. Rev.*, 110(11):6689–6735, 2010.

[30] A. J. Esswein and D. G. Nocera. Hydrogen production by molecular photocatalysis. *Chem. Rev.*, 107(10):4022–4047, 2007.

[31] M. L. Marin, L. Santos-Juanes, A. Arques, A. M. Amat, and M. A. Miranda. Organic photocatalysts for the oxidation of pollutants and model compounds. *Chem. Rev.*, 112(3):1710–1750, 2012.

[32] H. Imahori, T. Umeyama, K. Kurotobi, and Y. Takano. Self-assembling porphyrins and phthalocyanines for photoinduced charge separation and charge transport. *Chem. Commun.*, 48:4032–4045, 2012.

[33] S. M.B. Costa, S. M. Andrade, D. M. Togashi, P. M.R. Paulo, C. A.T. Laia, Isabel V. M., and A. M. Gonalves da Silva. Optical spectroscopy and photochemistry of porphyrins and phthalocyanines. *J. Porphyr. Phthalocya.*, 13: 509–517, 2009.

[34] J. Barber. Photochemistry: A quantum step towards artificial photosynthesis. *Nature*, 307:596, 1984. 10

[35] P. K. Frederiksen, M. Jorgensen, and P. R. Ogilby. Two-photon photosensitized production of singlet oxygen. *J. Am. Chem. Soc.*, 123(6):1215–1221, 2001. 11

[36] J. D. Bhawalkar, N. D. Kumar, C. F. Zhao, and P. N. Prasad. Two-photon photodynamic therapy. *J. Clin. Laser Med. Surg.*, 15(5):201–204, 1997.

[37] A. Karotki, M. Khurana, J. R. Lepock, and B. C. Wilson. Simultaneous two-photon excitation of photofrin in relation to photodynamic therapy. *Photochem. Photobiol.*, 82(2):443–452, 2006. 11

[38] W. G. Fisher, WP Partridge, Jr, C. Dees, and E. A. Wachter. Simultaneous two-photon activation of type-i photodynamic therapy agents. *Photochem. Photobiol.*, 66(2):141–155, Aug 1997. 11

[39] P. C. Jha, B. Minaev, and H. Agren. One- and two-photon absorptions in asymmetrically substituted free-base porphyrins: A density functional theory study. *J. Chem. Phys.*, 128:074302, 2008. 11

[40] E. Dahlstedt, H.A. Collins, M. Balaz, M. K. Kuimova, M. Khurana, B. C. Wilson, D. Phillips, and H. L. Anderson. One- and two-photon activated phototoxicity of conjugated porphyrin dimers with high two-photon absorption cross sections. *Org. Biomol. Chem.*, 7(5):897–904, Mar 2009. 11

[41] M. Drobizhev, F. Q. Meng, A. Rebane, Y. Stepanenko, E. Nickel, and C. W. Spangler. Strong two-photon absorption in new asymmetrically substituted porphyrins: Interference between charge-transfer and intermediate-resonance pathways. *J. Phys. Chem. B*, 110(20):9802–9814, 2006. 11

[42] J. D. Baker and M. C. Zerner. Applications of the random phase approximation with the indo/s hamiltonian: Uv–vis spectra of free base porphin. *Chem. Phys. Lett.*, 175(3):192–196, 1990.

[43] S. J. A. van Gisbergen, A. Rosa, G. Ricciardi, and E. J. Baerends. Time-dependent density functional calculations on the electronic absorption spectrum of free base porphin. *J. Chem. Phys.*, 111:2499–2506, 1999. 80, 88

[44] B. Minaev, Y.-H. Wang, C.-K. Wang, Y. Luo, and H. Agren. Density functional theory study of vibronic structure of the first absorption qx band in free-base porphin. *Spectrochim. Acta, Part A*, 65(2):308–323, 2006. 80, 120

[45] M. Drobizhev, Y. Stepanenko, Y. Dzenis, A. Karotki, A. Rebane, P. N. Taylor, and H. L. Anderson. Understanding strong two-photon absorption in pi-conjugated porphyrin dimers via double-resonance enhancement in a three-level model. *J Am Chem Soc*, 126:15352–15353, 2004.

[46] B. Minaev and H. Agren. Theoretical dft study of phosphorescence from porphyrins. *Chem. Phys.*, 315(3):215–239, 2005. 48

[47] D. Sundholm. Interpretation of the electronic absorption spectrum of free-base porphin using time-dependent density-functional theory. *Phys. Chem. Chem. Phys.*, 2:2275–2281, 2000. 11

[48] M. Johnsen, M. J. Paterson, J. Arnbjerg, O. Christiansen, C. B. Nielsen, M. Jorgensen, and P. R. Ogilby. Effects of conjugation length and resonance enhance-

ment on two-photon absorption in phenylene-vinylene oligomers. *Phys. Chem. Chem. Phys.*, 10:1177–1191, 2008. 11, 124

[49] W.-H. Lee, M. Cho, S.-J. Jeon, and B. R. Cho. Two-photon absorption and second hyperpolarizability of the linear quadrupolar molecule. *J. Phys. Chem. A*, 104(47):11033–11040, 2000.

[50] X. Zhou, J. Feng, and A.-M. Ren. Theoretical investigation on the one- and two-photon absorption properties of multi-branched oligomers with truxenone center and flourene branches. *Chem. Phys. Lett.*, 397:500–509, 2004.

[51] M. Albota, D. Beljonne, J.-L. Brdas, J. E. Ehrlich, J.-Y. Fu, A. A. Heikal, S. E. Hess, T. Kogej, M.D. Levin, S. R. Marder, D. McCord-Maughon, J. W. Perry, H. Rckel, M. Rumi, G. Subramaniam, W. W. Webb, X.-L. Wu, and C. Xu. Design of organic molecules with large two-photon absorption cross sections. *Science*, 281(5383):1653–1656, 1998.

[52] J. Shen, W.-D. Cheng, D.-S. Wu, Y.-Z. Lan, F.-F. Li, S.-P. Huang, H. Zhang, and Y.-J. Gong. Theoretical study of two-photon absorption in donor-acceptor chromophores tetraalkylammonium halide/carbon tetrabromide. *J. Phys. Chem. A*, 110(34):10330–10335, Aug 2006.

[53] M. Drobizhev, A. Karotki, M. Kruk, and A. Rebane. Resonance enhancement of two-photon absorption in porphyrins. *Chem. Phys. Lett.*, 355(1-2):175–182, 2002.

[54] G. S. He, L.-S. Tan, Q. Zheng, and P. N. Prasad. Multiphoton absorbing materials: molecular designs, characterizations, and applications. *Chem. Rev.*, 108(4):1245–1330, 2008.

[55] K. Ogawa and Y. Kobuke. Recent advances in two-photon photodynamic therapy. *Anticancer Agents Med. Chem.*, 8(3):269–279, 2008.

[56] P. C. Ray and Z. Sainudeen. Very large infrared two-photon absorption cross section of asymmetric zinc porphyrin aggregates: Role of intermolecular interaction and donor-acceptor strengths. *J. Phys. Chem. A.*, 110(44):12342–12347, 2006.

[57] O. Rubio-Pons, Y. Luo, and H. Agren. Effects of conjugation length, electron donor and acceptor strengths on two-photon absorption cross sections of asymmetric zinc-porphyrin derivatives. *J. Chem. Phys.*, 124(9):94310, 2006. 11

[58] P. Juzenas, W. Chen, Y.-P. Sun, M. A. N. Coelho, R. Generalov, N. Generalova, and I. L. Christensen. Quantum dots and nanoparticles for photodynamic and radiation therapies of cancer. *Adv. Drug Deliv. Rev.*, 60(15):1600 – 1614, 2008. 12

[59] A. B. Ormond and H. S. Freeman. Dye sensitizers for photodynamic therapy. *Materials*, 6(3):817–840, 2013. 12

[60] Vi. Sauri, L. Serrano-Andres, A. R. M. Shahi, L. Gagliardi, St. Vancoillie, and K. Pierloot. Multiconfigurational second-order perturbation theory restricted active space (raspt2) method for electronic excited states: A benchmark study. *J. Chem. Theo. Comput.*, 7:153–168, 2011. 12, 168, 183

[61] L. Serrano-Andres, M. Merchan, M. Rubio, and B. O. Roos. Interpretation of the electronic absorption spectrum of free base porphin by using multiconfigurational second-order perturbation theory. *Chem. Phys. Lett.*, 295:195–203, 1998. 88, 169

[62] Y. Tokita, J. Hasegawa, and H. Nakatsuji. Sac-ci study on the excited and ionized states of free-base porphin. rydberg excited states and effect of polarization and rydberg functions. *J. Phys. Chem. A*, 102(10):1843–1849, 1998.

[63] S. R. Gwaltney and R. J. Bartlett. Coupled-cluster calculations of the electronic excitation spectrum of free base porphin in a polarized basis. *J.Chem. Phys.*, 108(16):6790–6798, 1998. 88

[64] M. Gouterman. Study of the effects of substitution on the absorption spectra of porphin. *J. Chem. Phys.*, 30(5):1139–1161, 1959. 48

[65] M. A. Robb, M. Garavelli, M. Olivucci, and F. Bernardi. *A Computational Strategy for Organic Photochemistry*, pages 87–146. John Wiley & Sons, Inc., 2007. 12, 58

[66] P.W. Atkins and R. Friedman. *Molecular Quantum Mechanics*. OUP Oxford, 2011. 14

[67] L. S. Cederbaum. The exact molecular wavefunction as a product of an electronic and a nuclear wavefunction. *J. Chem. Phys.*, 138(22):224110, 2013. 18

[68] L. Piela. *Ideas of Quantum Chemistry*. Elsevier Science, 2013. 19, 20, 37

[69] A. Szabo and N.S. Ostlund. *Modern Quantum Chemistry: Introduction to Advanced Electronic Structure Theory*. Dover Books on Chemistry. Dover Publications, 2012. 21, 22, 27

[70] C. C. J. Roothaan. New developments in molecular orbital theory. *Rev. Mod. Phys.*, 23:69–89, 1951. 24

[71] J. C. Slater. Atomic shielding constants. *Phys. Rev.*, 36:57–64, Jul 1930. 25

[72] Tomoyuki Hamada. Rydberg basis set effects on ab initio second hyperpolarizabilities of h2, {C6H6} and {CS2} molecules. *Chem. Phys.*, 211(13):171 – 178, 1996. 26

[73] W. J. Hehre, R. Ditchfield, and J. A. Pople. Selfconsistent molecular orbital methods. xii. further extensions of gaussiantype basis sets for use in molecular orbital studies of organic molecules. *J.Chem. Phys.*, 56(5):2257–2261, 1972. 26, 80, 101

[74] A. Schafer, C. Huber, and R. Ahlrichs. Fully optimized contracted gaussian basis sets of triple zeta valence quality for atoms li to kr. *J. Chem. Phys.*, 100 (8):5829–5835, 1994. 146

[75] F. Weigend. Accurate coulomb-fitting basis sets for h to rn. *Phys. Chem. Chem. Phys.*, 8:1057–1065, 2006. 26

[76] T. H. Dunning. Gaussian basis sets for use in correlated molecular calculations. i. the atoms boron through neon and hydrogen. *J. Chem. Phys.*, 90(2):1007–1023, 1989. 27

[77] R. A. Kendall, T. H. Dunning, and R. J. Harrison. Electron affinities of the first-row atoms revisited. systematic basis sets and wave functions. *J. Chem. Phys.*, 96(9):6796–6806, 1992. 27

[78] P. A. M. Dirac. The quantum theory of the emission and absorption of radiation. *Proceedings of the Royal Society of London. Series A*, 114(767):243–265, 1927. 29

[79] F. Jensen. *Introduction to Computational Chemistry*. Wiley, 2006. 30

[80] J. A. Pople, R. Seeger, and R. Krishnan. Variational configuration interaction methods and comparison with perturbation theory. *Int. J. Qant. Chem.*, 12 (S11):149–163, 1977. 30

[81] P. E. M. Siegbahn. Generalizations of the direct ci method based on the graphical unitary group approach. i. single replacements from a complete ci root function of any spin, first order wave functions. *J. Chem. Phys.*, 70(12): 5391–5397, 1979. 31

[82] B. O. Roos, P. R. Taylor, and P. E.M. Siegbahn. A complete active space scf method (casscf) using a density matrix formulated super-ci approach. *Chem. Phys.*, 48(2):157 – 173, 1980. 31

[83] P. A. Malmqvist, A. Rendell, and B. O. Roos. The restricted active space self-consistent-field method, implemented with a split graph unitary group approach. *J. Phys. Chem.*, 94(14):5477–5482, 1990. 33

[84] J. A. Pople, R. Krishnan, H. B. Schlegel, and J. S. Binkley. Electron correlation theories and their application to the study of simple reaction potential surfaces. *Int. J. Quant. Chem.*, 14(5):545–560, 1978. 34

[85] R.J. Bartlett and G. D. Purvis. Many-body perturbation theory, coupled-pair many-electron theory, and the importance of quadruple excitations for the correlation problem. *Int. J. Quant. Chem.*, 14(5):561–581, 1978. 34

[86] L. H. Thomas. The calculation of atomic fields. *Proc. Cambridge Phil. Soc.*, 23:542–548, 1 1927. 35

[87] P. Hohenberg and W. Kohn. Inhomogeneous electron gas. *Phys. Rev.*, 136: B864–B871, 1964. 36

[88] W. Kohn and L. J. Sham. Self-consistent equations including exchange and correlation effects. *Phys. Rev.*, 140:A1133–A1138, 1965. 37

[89] J. P. Perdew and Y. Wang. Accurate and simple analytic representation of the electron-gas correlation energy. *Phys. Rev. B*, 45:13244–13249, 1992. 39

[90] A. D. Becke. Density-functional exchange-energy approximation with correct asymptotic behavior. *Phys. Rev. A*, 38:3098–3100, 1988. 39

[91] Chengteh Lee, Weitao Yang, and Robert G. Parr. Development of the colle-salvetti correlation-energy formula into a functional of the electron density. *Phys. Rev. B*, 37:785–789, 1988. 39

[92] J. P. Perdew. Density-functional approximation for the correlation energy of the inhomogeneous electron gas. *Phys. Rev. B*, 33:8822–8824, 1986. 39

[93] A. D. Becke. Density functional thermochemistry. iii. the role of exact exchange. *J. Chem. Phys.*, 98(7):5648–5652, 1993. 39, 80, 104

[94] Y. Zhao and D. G. Truhlar. A new local density functional for main-group thermochemistry, transition metal bonding, thermochemical kinetics, and non-covalent interactions. *J. Chem. Phys.*, 125(19), 2006. 39

[95] Y. Zhao and D. G. Truhlar. *Theor. Chem.iAcc.*, 120(1-3):215–241, 2008. ISSN 1432-881X. 40, 104

[96] C. Moller and M. S. Plesset. Note on an approximation treatment for many-electron systems. *Phys. Rev.*, 46:618–622, 1934. 40

[97] Q. Wu and W. Yang. Empirical correction to density functional theory for van der waals interactions. *J. Chem. Phys.*, 116(2):515–524, 2002. 40, 144

[98] U. Zimmerli, M. Parrinello, and P. Koumoutsakos. Dispersion corrections to density functionals for water aromatic interactions. *J.Chem. Phys.*, 120(6): 2693–2699, 2004.

[99] S. Grimme. Accurate description of van der waals complexes by density functional theory including empirical corrections. *J. Comput. Chem.*, 25(12):1463–1473, 2004. 142, 146

[100] I. Bayach, J.C. Sancho-Garca, F. Di Meo, J.-F.F. Weber, and P. Trouillas. - stacked polyphenolic dimers: A case study using dispersion-corrected methods. *Chem. Phys. Lett.*, 578:120–125, 2013. 40, 141, 144

[101] S. Grimme. Semiempirical gga-type density functional constructed with a long-range dispersion correction. *J. Comput. Chem.*, 27(15):1787–1799, 2006. 40, 144

[102] J. P. Perdew and K. Schmidt. Jacobs ladder of density functional approximations for the exchange-correlation energy. *AIP Conference Proceedings*, 577(1): 1–20, 2001. 40

[103] G. A. Worth and L. S. Cederbaum. Beyond born-oppenheimer: Molecular dynamics through a conical intersection. *Ann. Rev. Phys. Chem.*, 55(1):127–158, 2004. 41, 42

[104] S. Matsika and P. Krause. Nonadiabatic events and conical intersections. *Ann. Rev. Phys. Chem.*, 62(1):621–643, 2011. 58

[105] W. Domcke, D.R. Yarkony, and H. Köppel. *Conical Intersections: Theory, Computation and Experiment*. Advanced series in physical chemistry. World Scientific Publishing Company, 2011. 41

[106] D. R. Yarkony. Conical intersections: diabolical and often misunderstood. *Acc. Chem. Res.*, 31(8):511–518, 1998. 42

[107] M. J. Paterson, M. J. Bearpark, M. A. Robb, L. Blancafort, and G. A. Worth. Conical intersections: A perspective on the computation of spectroscopic jahn-teller parameters and the degenerate 'intersection space'. *Phys. Chem. Chem. Phys.*, 7:2100–2115, 2005. 42, 58

[108] M. J. Paterson, M. A. Robb, L. Blancafort, and A. D. DeBellis. Mechanism of an exceptional class of photostabilizers: A seam of conical intersection parallel to

excited state intramolecular proton transfer (esipt) in o-hydroxyphenyl-(1,3,5,)-triazine. *J. Phys. Chem. A*, 109(33):7527–7537, 2005. 43, 53

[109] W. Domcke and D. R. Yarkony. Role of conical intersections in molecular spectroscopy and photoinduced chemical dynamics. *Annu. Rev. Phys. Chem.*, 63(1):325–352, 2012. 43

[110] P. Norman and K. Ruud. Microscopic theory of nonlinear optics. In ManthosG. Papadopoulos, AndrzejJ. Sadlej, and Jerzy Leszczynski, editors, *Non-Linear Optical Properties of Matter*, volume 1 of *Challenges and Advances in Computational Chemistry and Physics*, pages 1–49. Springer Netherlands, 2006. 44

[111] P. Norman. A perspective on nonresonant and resonant electronic response theory for time-dependent molecular properties. *Phys. Chem. Chem. Phys.*, 13: 20519–20535, 2011. 46, 80, 93

[112] M. Gouterman. Spectra of porphyrins. *J. Mol. Spectrosc.*, 6(0):138 – 163, 1961. ISSN 0022-2852. 48, 88

[113] H. Shimakoshi, K. Sasaki, Y. Iseki, and Y. Hisaeda. Synthesis and photosensitizing properties of porphycene with imidazolium tag. *JPP*, 16:530–536, 2012. 49

[114] J. Arnbjerg, A. Jimenez-Banzo, M. J. Paterson, S.i Nonell, J. I. Borrell, O. Christiansen, and P. R. Ogilby. Two-photon absorption in tetraphenylporphycenes: are porphycenes better candidates than porphyrins for providing optimal optical properties for two-photon photodynamic therapy? *J. Am. Chem. Soc.*, 129(16):5188–5199, 2007. 49, 77, 117

[115] J. Hasegawa, K. Takata, T. Miyahara, S. Neya, M. J. Frisch, and H. Nakatsuji. Excited states of porphyrin isomers and porphycene derivatives: a sac-ci study. *J. Phys. Chem. A*, 109(14):3187–3200, 2005. 49, 88, 114, 162

[116] L. T. Bergendahl and M. J. Paterson. Two-photon absorption-molecular structure investigation using a porphycene chromophore with potential in photodynamic therapy. *J. Phys. Chem. B*, 116(39):11818–11828, 2012. 49, 117

[117] J. R. Platt. Classification of spectra of cata-condensed hydrocarbons. *J. Chem. Phys.*, 17(5):484–495, 1949. 49, 59

[118] E. Runge and E. K. U. Gross. Density-functional theory for time-dependent systems. *Phys. Rev. Lett.*, 52:997–1000, 1984. 50

[119] M.E. Casida and M. Huix-Rotllant. Progress in time-dependent density-functional theory. *Annu. Rev. Phys. Chem.*, 63(1):287–323, 2012. 50

[120] Mark E. Casida. Time-dependent density-functional theory for molecules and molecular solids. *J. Mol. Str. THEOCHEM*, 914(13):3 – 18, 2009. 50

[121] Ulf Bast, R.and E., B. Gao, T. Helgaker, K. Ruud, and A. J. Thorvaldsen. The ab initio calculation of molecular electric, magnetic and geometric properties. *Phys. Chem. Chem. Phys.*, 13:2627–2651, 2011. 51, 80

[122] P. Salek, O. Vahtras, J. Guo, Y. Luo, T. Helgaker, and H. gren. Calculations of two-photon absorption cross sections by means of density-functional theory. *Chem. Phys. Lett.*, 374(56):446 – 452, 2003. 80

[123] H. Koch and P. Jorgensen. Coupled cluster response functions. *J. Chem. Phys.*, 93(5):3333–3344, 1990.

[124] J. F. Stanton and R. J. Bartlett. The equation of motion coupled-cluster method. a systematic biorthogonal approach to molecular excitation energies, transition probabilities, and excited state properties. *J. Chem. Phys.*, 98(9): 7029–7039, 1993. 51, 61

[125] O. Christiansen, H. Koch, and P. Jo/rgensen. Perturbative triple excitation corrections to coupled cluster singles and doubles excitation energies. *The Journal of Chemical Physics*, 105(4):1451–1459, 1996. 51

[126] M. K. Shukla and J. Leszczynski. Comprehensive evaluation of medium and long range correlated density functionals in td-dft investigation of dna bases and base pairs: gas phase and water solution study. *Mol. Phys.*, 108(21-23): 3131–3146, 2010. 51

[127] D. J. Tozer, R. D. Amos, N. C. Handy, B. O. Roos, and L. Serrano-Andres. Does density functional theory contribute to the understanding of excited states of unsaturated organic compounds? *Mol. Phys.*, 97(7):859–868, 1999. 51

[128] L. Bernasconi, M. Sprik, and J. Hutter. Time dependent density functional theory study of charge-transfer and intramolecular electronic excitations in acetonewater systems. *J.Chem. Phys.*, 119(23):12417–12431, 2003.

[129] A. Dreuw and M. Head-Gordon. Failure of time-dependent density functional theory for long-range charge-transfer excited states. the zincbacteriochlorin-bacteriochlorin and bacteriochlorophyll-spheroidene complexes. *J. Am. Chem. Soc.*, 126(12):4007–4016, 2004. 51

[130] T. Yanai, D. P. Tew, and N. C. Handy. A new hybrid exchangecorrelation functional using the coulomb-attenuating method (cam-b3lyp). *Chem. Phys. Lett.*, 393(13):51 – 57, 2004. 52, 99, 101, 146

[131] M. J. G. Peach, T. Helgaker, P. Salek, T. W. Keal, O. B. Lutnaes, D. J. Tozer, and N. C. Handy. Assessment of a coulomb-attenuated exchange-correlation energy functional. *Phys. Chem. Chem. Phys.*, 8:558–562, 2006. 52, 99

[132] M. J. Paterson, O. Christiansen, F. Pawlowski, P. Jorgensen, C. Httig, T. Helgaker, and P. Salek. Benchmarking two-photon absorption with cc3 quadratic response theory, and comparison with density-functional response theory. *J. Chem. Phys.*, 124(5), 2006. 52, 105

[133] L. Goerigk and S. Grimme. Double-hybrid density functionals provide a balanced description of excited 1la and 1lb states in polycyclic aromatic hydrocarbons. *J. Chem. Theory Comput.*, 7(10):3272–3277, 2011. 52

[134] Miquel Huix-Rotllant and Nicolas Ferr. Triplet state photochemistry and the three-state crossing of acetophenone within time-dependent density-functional theory. *The Journal of Chemical Physics*, 140(13):134305, 2014. 52

[135] J. N. Harvey, M. Aschi, H. Schwarz, and W. Koch. The singlet and triplet states of phenyl cation. a hybrid approach for locating minimum energy crossing points

between non-interacting potential energy surfaces. *Theor. Chem. Acc.*, 99(2): 95–99, 1998. 52, 192

[136] M. J. Paterson, M. J. Bearpark, M. A. Robb, and L. Blancafort. The curvature of the conical intersection seam: An approximate second-order analysis. *J. Chem. Phys.*, 121(23):11562–11571, 2004. 53

[137] D.W.E. Al, W. Domcke, D.R. Yarkony, and H. Köppel. *Conical Intersections: Theory, Computation and Experiment*. Advanced Series in Physical Chemistry Series. World Scientific Publishing Company, Incorporated, 2011. 53

[138] A. Dreuw and M. Head-Gordon. Single-reference ab initio methods for the calculation of excited states of large molecules. *Chem. Rev.*, 105(11):4009–4037, 2005. 53

[139] R. L. Martin. Natural transition orbitals. *J. Chem. Phys.*, 118:4775–4777, 2003. 54, 117, 153

[140] M. R. Detty, S. L. Gibson, and S. J. Wagner. Current clinical and preclinical photosensitizers for use in photodynamic therapy. *J. Med. Chem.*, 47(16): 3897–3915, Jul 2004. 55, 115, 142

[141] A. Weiss, H. van den Bergh, A. W. Griffioen, and P. Nowak-Sliwinska. Angiogenesis inhibition for the improvement of photodynamic therapy: the revival of a promising idea. *Biochim Biophys Acta*, 1826(1):53–70, Aug 2012. 55

[142] J.M. Berg, J.L. Tymoczko, and L. Stryer. *Biochemistry*. Number pts. 1-34 in Biochemistry. W.H. Freeman, 2002. 55

[143] C.E. Housecroft and A.G. Sharpe. *Inorganic Chemistry*. Pearson Prentice Hall, 2005. 55

[144] P. Meredith and T. Sarna. The physical and chemical properties of eumelanin. *Pigm. Cell Res.*, 19(6):572–594, 2006. 57

[145] A. Huijser, A. Pezzella, and V. Sundstrom. Functionality of epidermal melanin pigments: current knowledge on uv-dissipative mechanisms and research perspectives. *Phys. Chem. Chem. Phys.*, 13:9119–9127, 2011. 57

[146] C. Canuel, M. Mons, F. Piuzzi, B. Tardivel, I. Dimicoli, and M. Elhanine. Excited states dynamics of dna and rna bases: Characterization of a stepwise deactivation pathway in the gas phase. *J. Chem. Phys.*, 122(7):074316, 2005. 58

[147] H. Kang, K. T. Lee, B. Jung, Y. J. Ko, and S. K. Kim. Intrinsic lifetimes of the excited state of dna and rna bases. *J. Am. Chem. Soc.*, 124(44):12958–12959, 2002.

[148] S. Ullrich, T. Schultz, M. Z. Zgierski, and A. Stolow. Direct observation of electronic relaxation dynamics in adenine via time-resolved photoelectron spectroscopy. *J. Am. Chem. Soc.*, 126(8):2262–2263, 2004. 58

[149] P R Callis. Electronic states and luminescence of nucleic acid systems. *Annu. Rev. Phys. Chem.*, 34(1):329–357, 1983. 58

[150] W. Domcke, D. Yarkony, and H. Köppel. *Conical Intersections: Electronic Structure, Dynamics & Spectroscopy*. Advanced series in physical chemistry. World Scientific, 2004. 58

[151]

[152] M. J. Paterson, O. Christiansen, F. Jensen, and P. R. Ogilby. Overview of theoretical and computational methods applied to the oxygen-organic molecule photosystem. *Photochem. Photobio.*, 82(5):1136–1160, 2006. 58

[153] J. Kupper, D. W. Pratt, W. Leo Meerts, C. Brand, J. Tatchen, and M. Schmitt. Vibronic coupling in indole: Ii. investigation of the 1la-1lb interaction using rotationally resolved electronic spectroscopy. *Phys. Chem. Chem. Phys.*, 12: 4980–4988, 2010. 59

[154] C. Brand, J. Kupper, D. W. Pratt, W. Leo M., D. Krugler, J. Tatchen, and M. Schmitt. Vibronic coupling in indole: I. theoretical description of the 1la-1lb interaction and the electronic spectrum. *Phys. Chem. Chem. Phys.*, 12: 4968–4979, 2010. 59, 68

[155] A. L. Sobolewski, W. Domcke, C. Dedonder-Lardeux, and C. Jouvet. Excited-state hydrogen detachment and hydrogen transfer driven by repulsive 1[small pi][sigma]* states: A new paradigm for nonradiative decay in aromatic biomolecules. *Phys. Chem. Chem. Phys.*, 4:1093–1100, 2002. 60, 65, 68, 69

[156] M. N. R. Ashfold, G. A. King, D. Murdock, M.G. D. Nix, T. A. A. Oliver, and A. G. Sage. [small pi][sigma]* excited states in molecular photochemistry. *Phys. Chem. Chem. Phys.*, 12:1218–1238, 2010.

[157] G. M. Roberts, D. J. Hadden, L. T. Bergendahl, A. M. Wenge, S. J. Harris, T. N. V. Karsili, M. N. R. Ashfold, M. J. Paterson, and V. G. Stavros. Exploring quantum phenomena and vibrational control in [sigma]* mediated photochemistry. *Chem. Sci.*, 4:993–1001, 2013. 60, 69

[158] A. L. Sobolewski and W Domcke. Ab initio investigations on the photophysics of indole. *Chem. Phys. Lett.*, 315(34):293 – 298, 1999. 60, 65, 68

[159] C.J. Cramer. *Essentials of Computational Chemistry: Theories and Models*. Wiley, 2005. 60

[160] M. J. Frisch, G. W. Trucks, H. B. Schlegel, G. E. Scuseria, M. A. Robb, J. R. Cheeseman, G. Scalmani, V. Barone, B. Mennucci, G. A. Petersson, H. Nakatsuji, M. Caricato, X. Li, H. P. Hratchian, A. F. Izmaylov, J. Bloino, G. Zheng, J. L. Sonnenberg, M. Hada, M. Ehara, K. Toyota, R. Fukuda, J. Hasegawa, M. Ishida, T. Nakajima, Y. Honda, O. Kitao, H. Nakai, T. Vreven, J. A. Montgomery, Jr., J. E. Peralta, F. Ogliaro, M. Bearpark, J. J. Heyd, E. Brothers, K. N. Kudin, V. N. Staroverov, R. Kobayashi, J. Normand, K. Raghavachari, A. Rendell, J. C. Burant, S. S. Iyengar, J. Tomasi, M. Cossi, N. Rega, J. M. Millam, M. Klene, J. E. Knox, J. B. Cross, V. Bakken, C. Adamo, J. Jaramillo, R. Gomperts, R. E. Stratmann, O. Yazyev, A. J. Austin, R. Cammi, C. Pomelli, J. W. Ochterski, R. L. Martin, K. Morokuma, V. G. Zakrzewski, G. A. Voth, P. Salvador, J. J. Dannenberg, S. Dapprich, A. D. Daniels, . Farkas, J. B. Foresman, J. V. Ortiz, J. Cioslowski, and D. J. Fox. Gaussian 09 revision a.01, . Gaussian Inc. Wallingford CT 2009. 61, 74, 80, 117, 146, 169

[161] Dalton, a molecular electronic structure program, release 2.0 (2005), see http://www.kjemi.uio.no/software/dalton/dalton.html. 61, 74, 80, 117

[162] A. L. Sobolewski and W. Domcke. Computational studies of the photophysics of hydrogen-bonded molecular systems. *J. Phys. Chem. A*, 111(46):11725–11735, 2007. 61, 65, 68

[163] T. A. A. Oliver, G. A. King, and M. N. R. Ashfold. Position matters: competing o-h and n-h photodissociation pathways in hydroxy- and methoxy-substituted indoles. *Phys. Chem. Chem. Phys.*, 13:14646–14662, 2011. 61, 63

[164] J. Hager and S. C. Wallace. Laser spectroscopy and photodynamics of indole and indole-van der waals molecules in a supersonic beam. *J. Phys. Chem.*, 87 (12):2121–2127, 1983. 63

[165] Y. Nibu, H. Abe, N. Mikami, and M. Ito. Electronic spectra of hydrogen-bonded indoles in a supersonic free jet. *J. Phys. Chem.*, 87(20):3898–3901, 1983.

[166] J. W. Hager, D. R. Demmer, and S. C. Wallace. Electronic spectra of jet-cooled indoles: evidence for the 1la state. *J. Phys. Chem.*, 91(6):1375–1382, 1987. 63

[167] Y. Huang and M. Sulkes. Anomalously short fluorescence lifetimes in jet cooled 4-hydroxyindole. evidence for excited state tautomerism and proton transfer in clusters. *Chem. Phys. Chem.*, 254(34):242 – 248, 1996. 63

[168] R. Livingstone, O. Schalk, A. E. Boguslavskiy, G. Wu, L.T. Bergendahl, A. Stolow, M. J. Paterson, and D. Townsend. Following the excited state relaxation dynamics of indole and 5-hydroxyindole using time-resolved photoelectron spectroscopy. *J. Chem. Phys.*, 135(19), 2011. 63, 66

[169] O. Schalk, A. E. Boguslavskiy, and S. Albert. Substituent effects on dynamics at conical intersections: Cyclopentadienes. *J. Phys. Chem. A*, 114(12):4058–4064, 2010. 65

[170] B. Valeur and G. Weber. Resolution of the fluorescence excitation spectrum of indole into the 1la and 1lb excitation bands. *Photochem. Photobio.*, 25(5): 441–444, 1977. 65

[171] R. L. Rich, Y. Chen, D. Neven, M. Negrerie, F. Gai, and J. W. Petrich. Steady-state and time-resolved fluorescence anisotropy of 7-azaindole and its derivatives. *J. Phys. Chem.*, 97(9):1781–1788, 1993.

[172] E. Jalviste and N. Ohta. Stark absorption spectroscopy of indole and 3-methylindole. *J. Chem. Phys.*, 121(10):4730–4739, 2004. 65

[173] N. Glasser and H. Lami. Nonradiative decay of indoles under collison-free conditions. *J. Chem. Phys.*, 74(11):6526–6527, 1981. 65

[174] M. G. D. Nix, A. L. Devine, B. Cronin, and M. N. R. Ashfold. High resolution photofragment translational spectroscopy of the near uv photolysis of indole: Dissociation via the 1[small pi][sigma]* states. *Phys. Chem. Chem. Phys.*, 8: 2610–2618, 2006. 65

[175] D. J. Hadden, K. L. Wells, G. M. Roberts, L. T. Bergendahl, M. J. Paterson, and V. G. Stavros. Time resolved velocity map imaging of h-atom elimination from photoexcited imidazole and its methyl substituted derivatives. *Phys. Chem. Chem. Phys.*, 13:10342–10349, 2011. 69, 72, 75

[176] A. T. J. B. Eppink, B. J. Whitaker, E. Gloaguen, B. Soep, A. M. Coroiu, and D. H. Parker. Dissociative multiphoton ionization of no2 studied by time-resolved imaging. *J. Chem. Phys.*, 121(16):7776–7783, 2004. 69

[177] A. Iqbal and V. G. Stavros. Active participation of 1* states in the photodissociation of tyrosine and its subunits. *J. Phys. Chem. Lett.*, 1(15):2274–2278, 2010. 69

[178] M. Barbatti, H. Lischka, S. Salzmann, and C. M. Marian. Uv excitation and radiationless deactivation of imidazole. *J. Chem. Phys.*, 130(3):034305, 2009. 70, 73

[179] A. Iqbal. *PhD Thesis*. PhD thesis, University of Warwick, 2010. 71

[180] K.A. Holbrook, M. J. Pilling, and S.H. Robertson. *Unimolecular Reactions*. John Wiley and sons, Chichester UK, 1996. 73

[181] M. G. D. Nix, A. L. Devine, B. Cronin, R. N. Dixon, and M. N. R. Ashfold. High resolution photofragment translational spectroscopy studies of the near ultraviolet photolysis of phenol. *J. Chem. Phys.*, 125(13):133318, 2006. 73

[182] M. Schreiber, M. R. Silva-Junior, S. P. A. Sauer, and W. Thiel. Benchmarks for electronically excited states: Caspt2, cc2, ccsd, and cc3. *J. Chem. Phys.*, 128(13):134110, 2008. 74

[183] J. C. Stockert, M. Caete, A. Juarranz, A. Villanueva, R. W. Horobin, J. I. Borrell, J. Teixid, and S. Nonell. Porphycenes: facts and prospects in photodynamic therapy of cancer. *Curr. Med. Chem.*, 14(9):997–1026, 2007. 77

[184] V. Gottfried, R. Davidi, C. Averbuj, and S. Kimel. In vivo damage to chorioallantoic membrane blood vessels by porphycene-induced photodynamic therapy. *J. Photochem.Photobiol. B*, 30(23):115 – 121, 1995. ISSN 1011-1344. 77

[185] M. Vogel, E.and Kocher, H. Schmickler, and J. Lex. Porphycene, a novel porphin isomer. *Angew. Chem. Int. Ed.*, 25(3):257–259, 1986. 77, 114

[186] M. Pawlicki, H.A. Collins, R.G. Denning, and H.L. Anderson. Two-photon absorption and the design of two-photon dyes. *Angew. Chem. Int. Edit.*, 48 (18):3244–3266, 2009. 77

[187] D. Sanchez-Garcia and J. L. Sessler. Porphycenes: synthesis and derivatives. *Chem. Soc. Rev.*, 37(1):215–232, Jan 2008. 77

[188] K. S. Kim, Y. M. Sung, T. Matsuo, T. Hayashi, and D. Kim. Investigation of aromaticity and photophysical properties in [18]/[20] porphycene derivatives. *Chemistry*, 17(28):7882–7889, 2011. 77

[189] J. Almlof, T. H. Fischer, P. G. Gassman, A. Ghosh, and M. Haeser. Electron correlation in tetrapyrroles: ab initio calculations on porphyrin and the tautomers of chlorin. *J. Phys. Chem.*, 97:10964–10970, 1993. 80

[190] A. Ghosh. First-principles quantum chemical studies of porphyrins. *Accounts Chem. Res.*, 31:189–198, 1998. 80, 118

[191] R. Improta, C. Ferrante, R. Bozio, and V. Barone. The polarizability in solution of tetra-phenyl-porphyrin derivatives in their excited electronic states: a pcm/td-dft study. *Phys. Chem. Chem. Phys.*, 11(22):4664–4673, Jun 2009. 80

[192] J. Tomasi, B. Mennucci, and R. Cammi. Quantum mechanical continuum solvation models. *Chem. Rev.*, 105(8):2999–3093, 2005. 80

[193] P. C. Hariharan and J. A. Pople. The influence of polarization functions on molecular orbital hydrogenation energies. *Theor. Chim. Acta*, 28:213–222, 1973. 80

[194] D. Andrae, U. Haussermann, M. Dolg, H. Stoll, and H. Preuss. Energy-adjusted ab initio pseudopotentials for the second and third row transition elements. *Theor. Chim. Acta*, 77:123–141, 1990. 80

[195] M. J. Paterson, J. Kongsted, O. Christiansen, K. V. Mikkelsen, and C. B. Nielsen. Two-photon absorption cross sections: an investigation of solvent effects. theoretical studies on formaldehyde and water. *J. Chem. Phys.*, 125 (18):184501, Nov 2006. 81

[196] L. Ferrighi, L. Frediani, E. Fossgaard, and K. Ruud. Two-photon absorption of [2.2]paracyclophane derivatives in solution: a theoretical investigation. *J. Chem. Phys.*, 127(24):244103, Dec 2007. 105

[197] Y. Luo, P. Norman, P. Macak, and H. Agren. Solvent-induced two-photon absorption of a push pull molecule. *J. Phys. Chem. A*, 104(20):4718–4722, 2000. 81, 105

[198] M. Merchan, E. Orti, and B. O. Roos. Ground-state free-base porphin - c2v or d2h symmetry - a theoretical contribution. *Chem. Phys. Lett.*, 221(1-2): 136–144, 1994. 88, 168, 171

[199] A. B. J. Parusel and A. Ghosh. Density functional theory based configuration interaction calculations on the electronic spectra of free-base porphyrin, chlorin, bacteriochlorin, and cis- and trans-isobacteriochlorin. *J. Phys. Chem. A*, 104 (11):2504–2507, 2000. 88

[200] L. Edwards, D.H. Dolphin, M. Gouterman, and A.D. Adler. Porphyrins xvii. vapor absorption spectra and redox reactions: Tetraphenylporphins and porphin. *J. Mol. Spectrosc.*, 38(1):16 – 32, 1971. 88

[201] K. Kristensen, J. Kauczor, T. Kjaergaard, and P. Jorgensen. Quasienergy formulation of damped response theory. *J. Chem. Phys.*, 131(4):044112, 2009. 93

[202] K. Kristensen, J. Kauczor, A. J. Thorvaldsen, P. Jorgensen, T. Kjaergaard, and A. Rizzo. Damped response theory description of two-photon absorption. *J. Chem. Phys.*, 134(21):214104, 2011. 93

[203] F. Terenziani, C. Katan, E. Badaeva, S. Tretiak, and M. Blanchard-Desce. Enhanced two-photon absorption of organic chromophores: Theoretical and experimental assessments. *Adv. Mater.*, 20:4641–4678, 2008. 93

[204] P. Macak, Y. Luo, and H. Agren. Simulations of vibronic profiles in two-photon absorption. *Chem. Phys. Lett.*, 330:447 – 456, 2000.

[205] N. Lin, Y. Luo, K. Ruud, X. Zhao, F. Santoro, and A. Rizzo. Differences in two-photon and one-photon absorption profiles induced by vibronic coupling: The case of dioxaborine heterocyclic dye. *Chem. Phys. Chem.*, 12:3392–3403, 2011. 93

[206] N. S. Venkataramanan, A. Suvitha, H. Nejo, Hi. Mizuseki, and Y. Kawazoe. Electronic structures and spectra of symmetric meso-substituted porphyrin: Dft and tddft-pcm investigations. *Int. J. Quantum Chem.*, 111:2340–2351, 2011. 94

[207] J. E. Lopez-Duarte, I.and Reeve, I.and Depotter G. Perez-Moreno, J.and Boczarow, J. Fleischhauer, K. Clays, and H.L. Anderson. "push-no-pull" porphyrins for second harmonic generation imaging. *Chem. Sci.*, 4:2024–2027, 2013. 97, 99

[208] J. E. Reeve, H. A. Collins, K. De Mey, M. M. Kohl, K. J. Thorley, O. Paulsen, K. Clays, and H. L. Anderson. Amphiphilic porphyrins for second harmonic generation imaging. *J. Am. Chem. Soc.*, 131(8):2758–2759, 2009. 97, 98

[209] P. A. Franken, A. E. Hill, C. W. Peters, and G. Weinreich. Generation of optical harmonics. *Phys. Rev. Lett.*, 7:118–119, 1961. 97

[210] M. J. Frisch, G. W. Trucks, H. B. Schlegel, G. E. Scuseria, M. A. Robb, J. R. Cheeseman, G. Scalmani, V. Barone, B. Mennucci, G. A. Petersson, H. Nakatsuji, M. Caricato, X. Li, H. P. Hratchian, A. F. Izmaylov, J. Bloino, G. Zheng, J. L. Sonnenberg, M. Hada, M. Ehara, K. Toyota, R. Fukuda, J. Hasegawa, M. Ishida, T. Nakajima, Y. Honda, O. Kitao, H. Nakai, T. Vreven, J. A. Montgomery, Jr., J. E. Peralta, F. Ogliaro, M. Bearpark, J. J. Heyd, E. Brothers, K. N. Kudin, V. N. Staroverov, R. Kobayashi, J. Normand, K. Raghavachari, A. Rendell, J. C. Burant, S. S. Iyengar, J. Tomasi, M. Cossi, N. Rega, J. M. Millam, M. Klene, J. E. Knox, J. B. Cross, V. Bakken, C. Adamo, J. Jaramillo, R. Gomperts, R. E. Stratmann, O. Yazyev, A. J. Austin, R. Cammi, C. Pomelli, J. W. Ochterski, R. L. Martin, K. Morokuma, V. G. Zakrzewski, G. A. Voth, P. Salvador, J. J. Dannenberg, S. Dapprich, A. D. Daniels, . Farkas, J. B. Foresman, J. V. Ortiz, J. Cioslowski, and D. J. Fox. Gaussian 09 revision c.01, . Gaussian Inc. Wallingford CT 2009. 101

[211] Kestutis Aidas, Celestino Angeli, Keld L. Bak, Vebjrn Bakken, Radovan Bast, Linus Boman, Ove Christiansen, Renzo Cimiraglia, Sonia Coriani, Pl Dahle, Erik K. Dalskov, Ulf Ekstrm, Thomas Enevoldsen, Janus J. Eriksen, Patrick Ettenhuber, Berta Fernndez, Lara Ferrighi, Heike Fliegl, Luca Frediani, Kasper Hald, Asger Halkier, Christof Httig, Hanne Heiberg, Trygve Helgaker, Alf Christian Hennum, Hinne Hettema, Eirik Hjertens, Stinne Hst, Ida-Marie Hyvik, Maria Francesca Iozzi, Branislav Jansk, Hans Jrgen Aa. Jensen, Dan Jonsson, Poul Jrgensen, Joanna Kauczor, Sheela Kirpekar, Thomas Kjrgaard, Wim Klopper, Stefan Knecht, Rika Kobayashi, Henrik Koch, Jacob Kongsted, Andreas Krapp, Kasper Kristensen, Andrea Ligabue, Ola B. Lutns, Juan I. Melo, Kurt V. Mikkelsen, Rolf H. Myhre, Christian Neiss, Christian B. Nielsen, Patrick Norman, Jeppe Olsen, Jgvan Magnus H. Olsen, Anders Osted, Martin J. Packer, Filip Pawlowski, Thomas B. Pedersen, Patricio F. Provasi, Simen Reine, Zilvinas Rinkevicius, Torgeir A. Ruden, Kenneth Ruud, Vladimir V. Rybkin, Pawel Saek, Claire C. M. Samson, Alfredo Snchez de Mers, Trond Saue, Stephan P. A. Sauer, Bernd Schimmelpfennig, Kristian Sneskov, Arnfinn H. Steindal,

Kristian O. Sylvester-Hvid, Peter R. Taylor, Andrew M. Teale, Erik I. Tellgren, David P. Tew, Andreas J. Thorvaldsen, Lea Thgersen, Olav Vahtras, Mark A. Watson, David J. D. Wilson, Marcin Ziolkowski, and Hans gren. The dalton quantum chemistry program systems. *Wiley Interdisciplinary Reviews Computational Molecular Science*, 4(3):269–284, 2014. 101

[212] C. Adamo and V. Barone. Toward reliable density functional methods without adjustable parameters: The pbe0 model. *J. Chem. Phys.*, 110(13):6158–6170, 1999. 104, 146

[213] J. L. Sessler, E. A. Brucker, S. J. Weghorn, M. Kisters, M. Schafer, J. Lex, and E. Vogel. Corrphycene: A new porphyrin isomer. *Angew. Chem. Int. Ed.*, 33 (22):2308–2312, 1994. 114, 119

[214] M. O. Senge. Extroverted confusion? linus pauling, melvin calvin, and porphyrin isomers. *Angew. Chem. Int. Ed.*, 50:4272–4277, 2011. 114

[215] P. J. Chmielewski, L. Latos-Grazynski, K. Rachlewicz, and T. Glowiak. Tetra-p-tolylporphyrin with an inverted pyrrole ring: A novel isomer of porphyrin. *Angew. Chem. Int. Ed.*, 33:779–781, 1994. 115

[216] Hi. Furuta, T. Asano, and T. Ogawa. "n-confused porphyrin": A new isomer of tetraphenylporphyrin. *J. Am. Chem. Soc.*, 116(2):767–768, 1994. 115

[217] A. Srinivasan and H. Furuta. Confusion approach to porphyrinoid chemistry. *Acc. Chem. Res.*, 38:10–20, 2005. 115, 129

[218] H. Furuta, H. Maeda, and A. Osuka. Doubly n-confused porphyrin. a new complexing agent capable of stabilizing higher oxidation states. *J. Am. Chem. Soc.*, 122:803–807, 2000. 115

[219] T. D. Lash, A. D. Lammer, and G. M. Ferrence. Neo-confused porphyrins, a new class of porphyrin isomers. *Angew. Chem. Int. Ed.*, 50:9718–9721, 2011. 115

[220] D. G. Hilmey, M. Abe, M. I. Nelen, C. E. Stilts, G. A. Baker, S. N. Baker, F. V. Bright, S. R. Davies, S. O. Gollnick, A. R. Oseroff, S. L. Gibson, R. Hilf,

and M. R. Detty. Water-soluble, core-modified porphyrins as novel, longer-wavelength-absorbing sensitizers for photodynamic therapy. ii. effects of core heteroatoms and meso-substituents on biological activity. *J. Med. Chem.*, 45 (2):449–461, 2002. 115

[221] G. Karthik, M. Sneha, V. P. Raja, J. M. Lim, D. Kim, A. Srinivasan, and T. K. Chandrashekar. Core-modified meso aryl hexaphyrins with an internal thiophene bridge: Structure, aromaticity, and photodynamics. *Chem. Eur. J.*, 19:1886–1890, 2013. 115

[222] H. Rath, J. Sankar, V. PrabhuRaja, T.e K. Chandrashekar, A. Nag, and D. Goswami. Core-modified expanded porphyrins with large third-order nonlinear optical response. *J. Am. Chem. Soc.*, 127:11608–11609, 2005. 115

[223] J. S. Lee, J.M. Lim, M. Toganoh, Hi. Furuta, and D. Kim. Comparative spectroscopic studies on porphyrin derivatives: electronic perturbation of n-confused and n-fused porphyrins. *Chem. Commun.*, 46:285–287, 2010. 117

[224] D. K. Maity, R. L. Bell, and T. N. Truong. Mechanism and quantum mechanical tunneling effects on inner hydrogen atom transfer in free base porphyrin a direct ab initio dynamics study. *J. Am. Chem. Soc.*, 122(5):897–906, 2000. 117

[225] J. Baker, P. M. Kozlowski, A. A. Jarzecki, and P. Pulay. The inner-hydrogen migration in free base porphyrin. *Theor. Chem. Acc.*, 97:59–66, 1997.

[226] H. H. Schlabach, M.and Limbach, E. Bunnenberg, A. Y. L. Shu, B. R. Tolf, and C. Djerassi. Nmr study of kinetic hh/hd/dh/dd isotope effects on the tautomerism of acetylporphyrin: evidence for a stepwise double proton transfer. *J. Am. Chem. Soc.*, 115(11):4554–4565, 1993. 117

[227] A. L. Sobolewski, M. Gil, J. Dobkowski, and J. Waluk. On the origin of radiationless transitions in porphycenes. *J. Phys. Chem. A*, 113(27):7714–7716, 2009. 118, 146

[228] Y.-D. Wu, K. W. K. Chan, C.-P. Yip, E. Vogel, D. A. Plattner, and K. N. Houk. Porphyrin isomers: Geometry, tautomerism, geometrical isomerism, and stability. *J. Org. Chem.*, 62(26):9240–9250, 1997. 118

[229] A. Ghosh and J. Almloef. Structure and stability of cis-porphyrin. *J. Phys. Chem.*, 99(4):1073–1075, 1995. 118

[230] J. Frenkel. On the transformation of light into heat in solids. ii. *Phys. Rev.*, 37:1276–1294, May 1931. 141

[231] V. V. Egorov. Theory of the j-band: From the frenkel exciton to charge transfer. *Physics Procedia*, 2(2):223 – 326, 2009. 141

[232] M. Kasha, H. R. Rawls, and M. A. El-Bayoumi. The exciton model in molecular spectroscopy. *Pure Appl. Chem.*, 11:371–392, 1965. 141, 151

[233] Z.-Y. Zhou, G.-G. Shan, Y.-L. Zhu, X.-J. Yu, Y.-H. Dong, and J.-Y. Zhao. Theoretical studies on excited state proton transfer tautomerism reaction and spectroscopic properties of 8-hydroxyquinoline monomers and dimers. *J Struct. Chem.*, 50(4):606–612, 2009. 141

[234] R. Verzeni, O. M, A. Cimas, I. Corral, and M. Yez. Ms-caspt2 study of the low-lying electronic excited states of di-thiosubstituted formic acid dimers. *Theor. Chem. Acc.*, 132(3):1–10, 2013.

[235] Maciej Kolaski, C. R. Arunkumar, and Kwang S. Kim. Aromatic excimers: Ab initio and td-dft study. *J. Chem. Theory Comput.*, 9(1):847–856, 2013.

[236] G. Olaso-Gonzalez, M. Merchan, and L. Serrano-Andres. The role of adenine excimers in the photophysics of oligonucleotides. *J. Am. Chem. Soc.*, 131(12): 4368–4377, 2009.

[237] R. Fukuda and M. Ehara. Theoretical study of the electronic excitations of free-base porphyrinar2 van der waals complexes. *J.Chem. Phys.*, 139(7):074303–10, 2013.

[238] J. Rezac, J.c, J. Fanfrlik, D. Salahub, and P. Hobza. Semiempirical quantum chemical pm6 method augmented by dispersion and h-bonding correction terms reliably describes various types of noncovalent complexes. *J. Chem. Theory Comput.*, 5(7):1749–1760, 2009. 141, 143, 159

[239] S. R. Stoyanov, C.-X. Yin, M. R. Gray, J. M. Stryker, S. Gusarov, and A. Kovalenko. Computational and experimental study of the structure, binding preferences, and spectroscopy of nickel(ii) and vanadyl porphyrins in petroleum. *J. Phys. Chem. B*, 114(6):2180–2188, 2010. 141

[240] Mi. Maj, J. Jeon, R. W. Gra, and M. Cho. Induced optical activity of dna-templated cyanine dye aggregates: Exciton coupling theory and td-dft studies. *J. Phys. Chem. A*, 117(29):5909–5918, 2013.

[241] R. Huenerbein and S. Grimme. Time-dependent density functional study of excimers and exciplexes of organic molecules. *Chem. Phys.*, 343(23):362 – 371, 2008. 141, 142, 145

[242] J.-D. Chai and M. Head-Gordon. Systematic optimization of long-range corrected hybrid density functionals. *J.Chem. Phys.*, 128(8):084106, 2008. 142, 145

[243] J. L. McHale. Hierarchal light-harvesting aggregates and their potential for solar energy applications. *J. Phys. Chem. Lett.*, 3(5):587–597, 2012. 142, 152, 162

[244] A. Kay and M. Graetzel. Artificial photosynthesis. 1. photosensitization of titania solar cells with chlorophyll derivatives and related natural porphyrins. *J. Phys. Chem.*, 97(23):6272–6277, 1993. 142

[245] M. Kawasaki and S. Aoyama. High efficiency photocurrent generation by two-dimensional mixed j-aggregates of cyanine dyes. *Chem. Commun.*, pages 988–989, 2004. 142

[246] P. L. Marek, H. Hahn, and T. S. Balaban. On the way to biomimetic dye aggregate solar cells. *Energy Environ. Sci.*, 4:2366–2378, 2011. 142

[247] E. E. Jelley. Spectral absorption and fluorescence of dyes in the molecular state. *Nature*, 138:1009–1010, 1936. 142, 143

[248] C. Mck-lichtenfeld and S. Grimme. Structure and binding energies of the porphine dimers. *Mol. Phys.*, 105(19-22):2793–2798, 2007. 143, 148, 159

[249] M. Pitonak, P. Neogrady, J. Rezac, P. Jurecka, M. Urban, and P. Hobza. Benzene dimer. high-level wave function and density functional theory calculations. *J. Chem. Theory Comput.*, 4(11):1829–1834, 2008. 143, 145, 149

[250] M. J. Allen and D. J. Tozer. Helium dimer dispersion forces and correlation potentials in density functional theory. *J. Chem. Phys.*, 117(24):11113–11120, 2002. 144

[251] T. van Mourik and R. J. Gdanitz. A critical note on density functional theory studies on rare-gas dimers. *J.Chem. Phys.*, 116(22):9620–9623, 2002. 144

[252] N. Kurita, H. Inoue, and H. Sekino. Adjustment of perdew-wang exchange functional for describing van der waals and {DNA} base-stacking interactions. *Chem. Phys. Lett.*, 370(12):161 – 169, 2003. 144

[253] M. J. G. Peach and D. J. Tozer. Overcoming low orbital overlap and triplet instability problems in tddft. *J. Phys. Chem. A*, 116(39):9783–9789, 2012. 144

[254] J.-D. Chai and M. Head-Gordon. Long-range corrected hybrid density functionals with damped atom-atom dispersion corrections. *Phys. Chem. Chem. Phys.*, 10:6615–6620, 2008. 145

[255] S. Grimme, S. Ehrlich, and L. Goerigk. Effect of the damping function in dispersion corrected density functional theory. *J. Comput. Chem.*, 32(7):1456–1465, 2011. 145

[256] T. Janowski and P. Pulay. High accuracy benchmark calculations on the benzene dimer potential energy surface. *Chem. Phys. Lett.*, 447(13):27 – 32, 2007. 145

[257] J. Rezac and P. Hobza. Benzene dimer: Dynamic structure and thermodynamics derived from on-the-fly ab initio dft-d molecular dynamic simulations. *J Chem. Theory Comput.*, 4(11):1835–1840, 2008. 149

[258] M. O. Sinnokrot and C. D. Sherrill. Substituent effects in pi-pi interactions. sandwich and t-shaped configurations. *J. Am. Chem. Soc.*, 126(24):7690–7697, 2004. 146

[259] A. D. Boese, J. M. L. Martin, and N. C. Handy. The role of the basis set: Assessing density functional theory. *J.Chem. Phys.*, 119(6):3005–3014, 2003. 146

[260] S.F. Boys and F. Bernardi. The calculation of small molecular interactions by the differences of separate total energies. some procedures with reduced errors. *Mol. Phys.*, 19(4):553–566, 1970. 146

[261] M. Boronat, E. Ort, P.M. Viruela, and F. Toms. Theoretical study of the n-h tautomerism in free base porphyrin. *J. Mol. Struct.*, 390(13):149 – 156, 1997. 146

[262] C. A. Hunter, J. K.M. Sanders, and A. J. Stone. Exciton coupling in porphyrin dimers. *Chem. Phys.*, 133(3):395 – 404, 1989. 149, 152

[263] C. A. Hunter and J. K. M. Sanders. The nature of pi-pi interactions. *J. Am. Chem. Soc.*, 112(14):5525–5534, 1990. 149

[264] A. Osuka and K. Maruyama. Synthesis of naphthalene-bridged porphyrin dimers and their orientation-dependent exciton coupling. *J. Am. Chem. Soc.*, 110(13): 4454–4456, 1988. 152

[265] Y. Nakamura, N. Aratani, and A. Osuka. Cyclic porphyrin arrays as artificial photosynthetic antenna: synthesis and excitation energy transfer. *Chem. Soc. Rev.*, 36:831–845, 2007.

[266] P.J. Goncalves, D.S. Correa, P.L. Franzen, L. De Boni, L.M. Almeida, C.R. Mendonca, I.E. Borissevitch, and S.C. Zlio. Effect of interaction with micelles on the excited-state optical properties of zinc porphyrins and j-aggregates formation. *Scpectrochim. Acta Mol. Biomol. Spectros.*, 112(0):309 – 317, 2013.

[267] N. C. Maiti, S. Mazumdar, and N. Periasamy. J- and h-aggregates of poprhyrin-surfactant complexes: Time-resolved fluoresence and other spectroscopic stidies. *J. Phys. Chem. B*, 102(9):1528–1538, 1998. 153

[268] R. F. Pasternack, P. R. Huber, P. Boyd, G. Engasser, L. Francesconi, E. Gibbs, P. Fasella, G. Cerio Venturo, and L. deC. Hinds. Aggregation of meso-

substituted water-soluble porphyrins. *J. Am. Chem. Soc.*, 94(13):4511–4517, 1972.

[269] N. C. Maiti, M. Ravikanth, S. Mazumdar, and N. Periasamy. Fluorescence dynamics of noncovalently linked porphyrin dimers, and aggregates. *J. Phys. Chem.*, 99(47):17192–17197, 1995.

[270] K. Kano, K. Fukuda, H. Wakami, R. Nishiyabu, and R. F. Pasternack. Factors influencing self-aggregation tendencies of cationic porphyrins in aqueous solution. *J. Am. Chem. Soc.*, 122(31):7494–7502, 2000. 152

[271] Z. El-Hachemi, C. Escudero, F. Acosta-Reyes, M. T. Casas, V. Altoe, S. Aloni, G. Oncins, A. Sorrenti, J. Crusats, J. L. Campos, and J. M. Ribo. Structure vs. properties - chirality optics and shapes - in amphiphilic porphyrin j-aggregates. *J. Mater. Chem. C*, 1:3337–3346, 2013. 152

[272] P W Bohn. Aspects of structure and energy transport in artificial molecular assemblies. *Annu. Rev. Phys. Chem.*, 44(1):37–60, 1993. 153

[273] T. Fournier, T.-H. Tran-Thi, N. Herlet, and C. Sanchez. Charge transfer dynamics of porphyrinphthalocyanine heterodimers in hybrid solgel films. *Chem. Phys. Lett.*, 208(12):101 – 105, 1993.

[274] G. Giancane and L. Valli. State of art in porphyrin langmuirblodgett films as chemical sensors. *Adv. Colloid Interface Sci.*, 171172:17 – 35, 2012. 153

[275] P.J. Goncalves, N.M. Barbosa Neto, G.G. Parra, L. de Boni, L.P.F. Aggarwal, J.P. Siqueira, L. Misoguti, I.E. Borissevitch, and S.C. Zlio. Excited-state dynamics of meso-tetrakis(sulfonatophenyl) porphyrin j-aggregates. *Opt. Mat.*, 34(4):741 – 747, 2012. 153

[276] Z.-L. Cai, M. J. Crossley, J. R. Reimers, R. Kobayashi, and R. D. Amos. Density functional theory for charge transfer. the nature of the n-bands of porphyrins and chlorophylls revealed through cam-b3lyp, caspt2, and sac-ci calculations. *J. Phys. Chem. B*, 110(31):15624–15632, 2006. PMID: 16884287. 157, 162

[277] J. Deisenhofer, O. Epp, K. Miki, R. Huber, and H. Michel. X-ray structure analysis of a membrane protein complex: Electron density map at 3 resolution and a model of the chromophores of the photosynthetic reaction center from rhodopseudomonas viridis. *J. Mol. Bio.*, 180(2):385 – 398, 1984. 162

[278] A. H. Zewali. Femtochemistry: Past, present and future. *Pure Appl. Chem*, 72:2219 – 2231, 2000. 167

[279] M. J. Bearpark, F. Ogliaro, T. Vreven, M. Boggio-Pasqua, M. J. Frisch, S. M. Larkin, M. Morrison, and M. A. Robb. {CASSCF} calculations for photoinduced processes in large molecules: Choosing when to use the rasscf, {ONIOM} and {MMVB} approximations. *J. Photochem. Photobiol. A*, 190(23):207 – 227, 2007. 168

[280] A. Toniolo, G. Granucci, and T. J. Martnez. Conical intersections in solution: a qm/mm study using floating occupation semiempirical configuration interaction wave functions. *The Journal of Physical Chemistry A*, 107(19):3822–3830, 2003. 168

[281] J. Olsen, B. O. Roos, P. Jorgensen, and H. J. Aa. Jensen. Determinant based configuration interaction algorithms for complete and restricted configuration interaction spaces. *J. Chem. Phys.*, 89(4):2185–2192, 1988. 168

[282] A. Kerridge. A rasscf study of free base, magnesium and zinc porphyrins: accuracy versus efficiency. *Phys. Chem. Chem. Phys.*, 15:2197–2209, 2013. 168

[283] M. Rubio, B. O. Roos, L. Serrano-Andrs, and M. Merchn. Theoretical study of the electronic spectrum of magnesium-porphyrin. *J. Chem. Phys.*, 110(15): 7202–7209, 1999. 168

[284] M. Klene, M. A. Robb, L. Blancafort, and M. J. Frisch. A new efficient approach to the direct restricted active space self-consistent field methods. *J. Chem. Phys.*, 119(2):713–728, 2003. 169, 176

[285] M. J. Frisch, G. W. Trucks, H. B. Schlegel, G. E. Scuseria, M. A. Robb, J. R. Cheeseman, J. A. Montgomery, Jr., T. Vreven, K. N. Kudin, J. C. Burant, J. M.

Millam, S. S. Iyengar, J. Tomasi, V. Barone, B. Mennucci, M. Cossi, G. Scalmani, N. Rega, G. A. Petersson, H. Nakatsuji, M. Hada, M. Ehara, K. Toyota, R. Fukuda, J. Hasegawa, M. Ishida, T. Nakajima, Y. Honda, O. Kitao, H. Nakai, M. Klene, X. Li, J. E. Knox, H. P. Hratchian, J. B. Cross, V. Bakken, C. Adamo, J. Jaramillo, R. Gomperts, R. E. Stratmann, O. Yazyev, A. J. Austin, R. Cammi, C. Pomelli, J. W. Ochterski, P. Y. Ayala, K. Morokuma, G. A. Voth, P. Salvador, J. J. Dannenberg, V. G. Zakrzewski, S. Dapprich, A. D. Daniels, M. C. Strain, O. Farkas, D. K. Malick, A. D. Rabuck, K. Raghavachari, J. B. Foresman, J. V. Ortiz, Q. Cui, A. G. Baboul, S. Clifford, J. Cioslowski, B. B. Stefanov, G. Liu, A. Liashenko, P. Piskorz, I. Komaromi, R. L. Martin, D. J. Fox, T. Keith, M. A. Al-Laham, C. Y. Peng, A. Nanayakkara, M. Challacombe, P. M. W. Gill, B. Johnson, W. Chen, M. W. Wong, C. Gonzalez, and J. A. Pople. Gaussian 03, revision c.02, . Gaussian, Inc., Wallingford, CT, 2004. 169

[286] K. Andersson, P. A. Malmqvist, B. O. Roos, A. J. Sadlej, and K. Wolinski. Second-order perturbation theory with a casscf reference functions. *J. Phys. Chem.*, 94(14):5483–5488, 1990. 169

[287] P. . Malmqvist, K. Pierloot, A. R. M. Shahi, C. J. Cramer, and L. Gagliardi. The restricted active space followed by second-order perturbation theory method: Theory and application to the study of cuo2 and cu2o2 systems. *J. Chem. Phys.*, 128(20):204109, 2008. 169

[288] M. Boggio-Pasqua, M. J. Bearpark, M. Klene, and M. A. Robb. A computational strategy for geometry optimization of ionic and covalent excited states, applied to butadiene and hexatriene. *J. Chem. Phys.*, 120(17):7849–7860, 2004. 176

[289] R. Stowasser and R. Hoffmann. What do the kohnsham orbitals and eigenvalues mean? *J. Am. Chem. Soc.*, 121(14):3414–3420, 1999. 180

[290] S. Schumacher, A. Ruseckas, N.A. Montgomery, P. J. Skabara, A.L. Kanibolotsky, M. J. Paterson, I. Galbraith, G. A. Turnbull, and I. D. W. Samuel. Effect of exciton self-trapping and molecular conformation on photophysical properties of oligofluorenes. *J. Chem. Phys.*, 131(15), 2009. 188

[291] D. Asturiol and M. Barbatti. Electronic states of porphycene-o2 complex and photoinduced singlet o2 production. *J. Chem. Phys.*, 139(7):074307, 2013. 193